CRANFIELD UNIVERSITY

JUSTIN BOUVET

STEAM OXIDATION OF HEAT EXCHANGER MATERIALS FOR THE NEW GENERATION OF POWER PLANTS

SCHOOL OF WATER, ENERGY AND ENVIRONMENT

PhD
Academic Years: 2015 - 2018

Supervisor: Dr JOY SUMNER
Associate Supervisor: PROF NIGEL SIMMS
November 2018

CRANFIELD UNIVERSITY

SCHOOL OF WATER, ENERGY AND ENVIRONMENT

PhD

Academic Years 2015 - 2018

JUSTIN BOUVET

STEAM OXIDATION OF HEAT EXCHANGER MATERIALS FOR THE NEW GENERATION OF POWER PLANTS

Supervisor: DR JOY SUMNER
Associate Supervisor: PROF NIGEL SIMMS
November 2018

This thesis is submitted in partial fulfilment of the requirements for the degree of PhD

ABSTRACT

Energy production over recent decades has emitted CO_2, linked to an increase in global average temperatures and climate change. Part of the solution to tackle this is through improved power plant flexibility to enable renewable integration, and enhanced generator efficiency. Fossil fuel-based generators' efficiencies can be improved by increasing steam working temperatures and pressures inside power plants. However, these more severe working conditions can accelerate degradation phenomena, for example, by steam oxidation.

To assess the simulate steam oxidation processes at the elevated temperatures required for high efficient power plants, various austenitic steels and nickel-based alloys were exposed to pure steam between 650 and 800°C for up to 10,000 hours. Effects of pressure and surface finish were also investigated.

It was observed that, for the different materials, oxide formation increased with increasing oxidation time and steam temperature. Oxidized TP347HFG samples (18.4%$_w$Cr and 11.5%$_w$Ni) exhibit multi-layered oxide scales susceptible to spallation. Surface finishes applying high compressive stresses drastically enhanced oxidation resistance and promoted chromia layer formation even at elevated temperatures and longer exposure times. Other prepared surfaces, with low compressive stresses, induced increased oxidation resistance only at early exposure times. Sanicro 25 (22.5%$_w$Cr and 25%$_w$Ni) and nickel-based alloys naturally possess very high oxidation resistances, which results from ready formation of chromia formation on their surfaces; these alloys were not affected by surface preparation. Exposing different materials to increasing pressure in laboratory experiments increased oxidation rates. However, in service exposed materials show the opposite pressure effect. Isotope exposure tests revealed that up to 20% of the anionic species in the oxide layers were hydroxides and/or hydrogen, showing their significant influence on the steam oxidation mechanisms.

Finally, models describing mass change and oxide growth for the different materials and surface finishes were developed to contribute to better power plant management.

Keywords:

Pure steam, surface finish, high temperature, pressure effect, isotope exposure, ferritic steels, austenitic steels, nickel-based alloys.

ACKNOWLEDGEMENTS

I wish to address my gratitude to my supervisors Dr Joy Sumner and Prof. Nigel Simms for this great scientific opportunity, and for the precious help and guidance they provided throughout my research.

I would also like to thank all the technical staff at Cranfield University who have helped me in the various stages of my project: Christine Kimpton, Euan Hakon, and Peter West.

Special thanks to all my office counterparts with whom I have spent many great momenta and shared many laughs: Chiara, Andrew, Blessing, Laurie, John, Stefano, Andy, and Victor.

Lastly, I would like to express my gratitude to my family and Marine for their support and love which have kept me going during the difficult moments.

TABLE OF CONTENTS

LIST OF FIGURES

LIST OF TABLES

LIST OF EQUATIONS

LIST OF ABBREVIATIONS

BSE	Backscatter electron
COP21	21st yearly cession of the conference of the parties
CTE	Coefficient of thermal expansion
EBSD	Electron backscatter diffraction
EDX	Energy dispersive X-ray
EPSRC	Engineering and physical sciences research council
ESEM	Environmental scanning electron microscope
EU	European Union
FIB	Focussed iron beam
Gt	Gigatonnes
IEA	International energy agency
INDC	Intended nationally determined contribution
Mtoe	Million tonnes of oil equivalent
NPL	National physical laboratory
OFN	Oxygen free nitrogen
SE	Secondary electron
SEM	Scanning electron microscope
SIMS	Secondary ion mass spectrometry
UK	United Kingdom
XRD	X-ray diffraction

Nomenclature

A	Area $[m]^2$
c	Concentration $[mol.m^{-3}]$
C_p	Specific heat $[J.m^{-2}.K^{-4}]$
d	Tube diameter $[m]$
D	Diffusion coefficient $[m^2.s^{-1}]$
D_0	Standard diffusion coefficient $[m^2.s^{-1}]$
E	Radiation emission $[W.m^{-2}]$
ε	Emissivity factor
h	Convection heat transfer coefficient $[W.m^{-2}.K^{-1}]$
j	Diffusion flux $[mol.m^{-2}.s^{-1}]$
k	Thermal conductivity $[W.m^{-1}.K^{-1}]$
k_l	Linear oxidation rate $[mg.cm^{-2}.h^{-1}]$
k_p	Parabolic oxidation rate $[(mg.cm^{-2})^2.h^{-1}]$
L	Unit of length $[m]$
$\dot{m}$	Fluid mass flow $[kg.s^{-1}]$
Nu	Nusselt number
η	Dynamic viscosity $[kg.m^{-1}.s^{-1}]$
P	Pressure $[bars]$
Pr	Prandtl number
ρ	Fluid density $[kg.m^{-3}]$
φ	Heat flux $[W]$
Q	Activation energy $[J.mol^{-1}]$
R	Gas constant $[J.mol^{-1}.K^{-1}]$
Re	Reynolds number
σ	Stefan-Boltzmann constant $[W.m^{-2}.K^{-4}]$
T	Temperature $[K]$
u	Fluid velocity $[m.s^{-1}]$
x	Linear position $[m]$

1. Introduction

1.1. Energy generation

The world's population relies on energy supply and, more precisely, electricity. The increasing world population along with rising living standards is accompanied by an increase in energy demand. Since the industrial age, the energy generation industry has tried to meet the population's requirements. Unfortunately the effects of energy production on the environment have only recently been taken into consideration, such that globally there is a critical environmental situation linked to climate change and characterised by a rise in the world's average temperature. To avoid severe and irreversible impacts of climate change it is necessary to hold the increase in average global temperature below 2°C and urgent actions are being undertaken to ensure this [1].

In March 2007, the European Union adopted a strategy to improve energy security and to tackle climate change. It was decided that, by 2020, 20% of the EU's (European Union) energy should come from renewable sources. The European Council also underlined the importance of making consequent improvements in generation efficiency and clean fossil fuel technologies [1]. For the UK, a specific goal was decided which states that by 2020 15% of its energy should come from renewable sources. The UK's final energy consumption from renewable sources increased steadily from 7.0% in 2014 to 10.2% in 2017. This is now getting close to the goal set in 2015 [2,3]. As a continuation of the strategy promoting the use of renewable energy sources, the EU countries set their INDC (Intended Nationally Determined Contribution) during the COP21 (21st yearly cession of the conference of the parties) in December 2015. Furthermore, it was agreed that the share of renewable energy should be at least 27% by 2030 and that energy efficiency of power plants should also be improved by at least 27% [4]. Finally, long term objectives agreed by the EU are to cut greenhouse gas emissions by at least 80% by 2050 compared with 1990 levels [4,5].

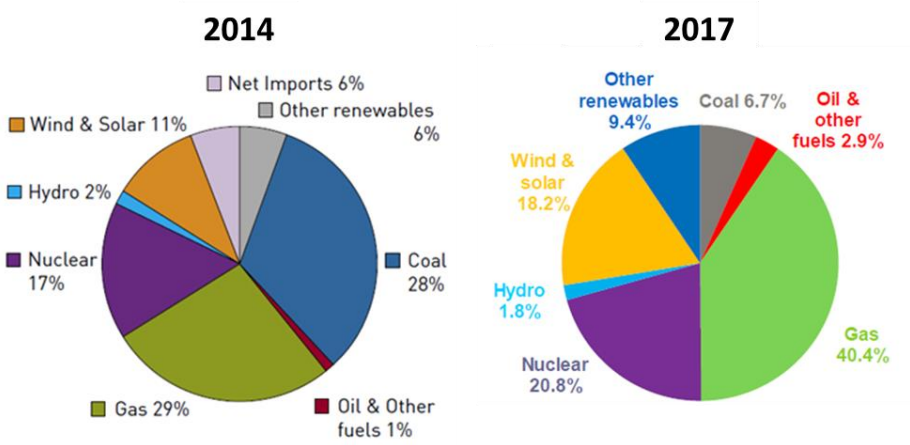

Figure 1-1: Electricity supplied by fuel type in the UK in 2014 [2] and 2017 [3].

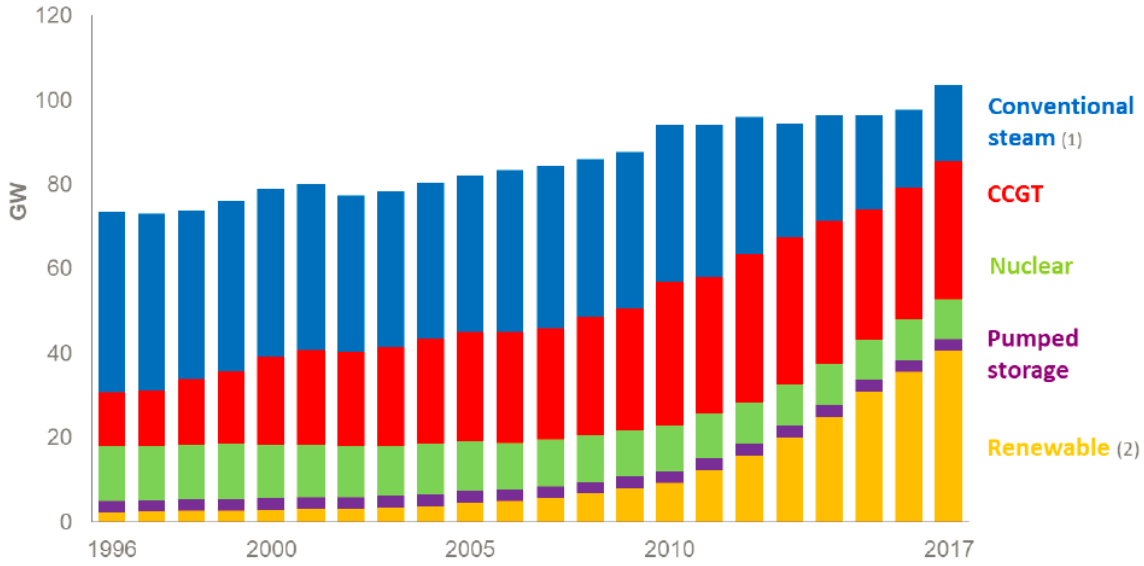

Figure 1-2: Electricity capacity of different technologies used in the UK between 1996 and 2017 [3] ((1)Mainly coal, includes gas turbines, oil engines mixed/dual fired and co-firing. (2) Included power plants run with biomass.)

Figure 1-1 and Figure 1-2 show the electricity supply by fuel type in the UK and the capacity installed for each technology used to produce electricity. Coal and steam cycle technologies are an important part of the electricity generation industry in the UK. In the UK, between 2014 and 2017, the share of electricity produced from coal dropped from 28% to 6.7% and the share of the installed capacity from conventional steam cycles dropped from 26% to 17%. These figures do not take into account the electricity produced from biomass using steam cycle technology. Even though the share of electricity produced from coal has drastically decreased in the UK, coal still

constitutes a significantly used source of primary energy in the world and its share will continue to be substantial globally for years to come as shown in Figure 1-3.

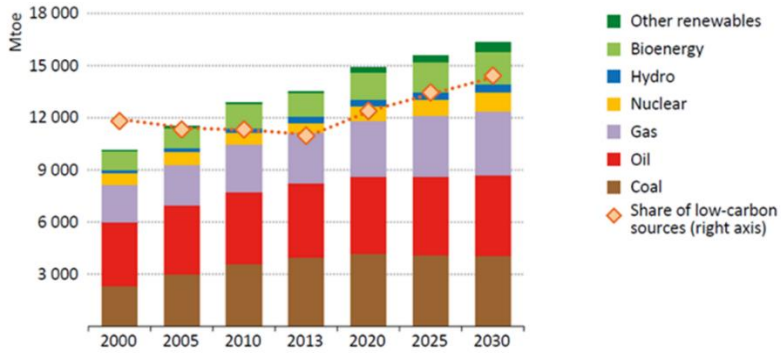

Figure 1-3: Evolution of global primary energy demand in Mtoe (million tonnes of oil equivalent) by fuel type according to the INDC set at COP21 [4].

The International Energy Agency (IEA) developed a strategy, called Bridge, identifying possible areas for achieving the INDC strategy put in place during the COP21. Figure 1-4 displays the possible areas for CO_2 emission savings from the power sector. Coal represents the fuel with the largest potential for CO_2 emission savings and one of the policy drivers for reducing CO_2 emissions power plants is to improve the coal efficiency. The IEA report [4] explains that inefficient coal use should be avoided, which means the uptake of new generation coal power plants with higher efficiency. In parallel, the increasing share in intermittent energy production from renewable sources induce a need for more flexibility of the conventional power plants to assure the reliability of the energy supply [4].

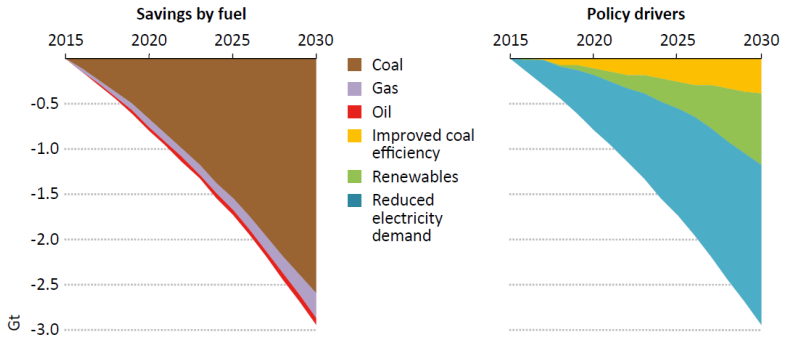

Figure 1-4: Global energy related CO_2 emissions savings in Gt (gigatonnes) from the power sector in the "Bridge" scenario relative to the "INDC" scenario [4]**.**

1.2. Project background

The power generation industry faces new challenges to increase the flexibility and the performances of power plants. There are various aspects regarding the power plant flexibility that need to be improved. Firstly, the plants should be flexible both in term of fuel used and power output. Indeed, to meet the EU objective of producing 20% of energy from renewable sources, co-firing coal and biomass plants as well as the use of biomass-only fired plants should be developed more [1]. Moreover, flexibility in terms of power output is necessary to follow energy demand variation and to counter the fluctuations in energy produced from renewable sources [1–3].

The power generation industry uses conventional steam turbines or combined heat and power stations to produce energy from coal and renewable fuels [2,3]. The steam follows a Rankine cycle to create electrical energy from the combustion of solid fuels [6]. In developing countries, low efficiency subcritical power plants are still in use [4], but in the UK, to raise power generation efficiency, plants use supercritical conditions [6] characterized by steam temperatures and pressures in the heat exchangers of 566°C and 248 bars respectively. The future technological trend is to use power plants with advanced ultra-supercritical conditions to further increase plant efficiency [7]. Thus, CO_2 generation per unit of energy produced will be reduced and the decarbonisation of the combustion gases could become economically viable. A proposed advanced ultra-supercritical plant works under steam conditions such as 345 bars and 760°C. This means the power plant can achieve a net plant efficiency of 45% or more, compared with a classic supercritical power plant which has an efficiency of 38% [8]. However, improving the power plants' performances is accompanied with the heat exchangers being exposed to higher temperatures which results in several issues including more severe oxidation of the inner surface of the heat exchanger tubes due to the new higher temperature, higher pressure steam conditions [7]. Sustaining component life require study, and is needed to insure the economic viability of this power generation technology.

1.3. Aims and objectives

The aim of the project is to improve the understanding and quantification of high temperature steam oxidation of candidate heat exchanger materials under different exposure conditions. To do this the following objectives must be met:

1. To investigate the long-term temperature sensitivity of steam oxidation degradation mechanisms for candidate materials [9,10].
2. To improve the understanding of different factors such as surface finish and steam pressure, in affecting the oxidation mechanisms [8,9,11–13].
3. To develop quantitative models describing steam oxidation processes and the damage associated. Such a tool can be used to calculate the boundaries of safe operating windows for the different candidate materials.

1.4. PhD activities

This PhD was funded alongside an EPSRC project Flex-E-Plan (see Appendix A).

Specific activities related to the project were:

- Materials with different composition have been exposed to different steam exposure conditions (objective 1 and 2). The evolution of the sample's mass, oxide scale morphology and scale thickness has been used to extract useful information about oxidation mechanisms, kinetics and scale spallation (objective 3).
- Steam paths, hydrogen embrittlement, and oxygen diffusion, in the different materials and their oxide scales was observed to understand details of the oxidation processes occurring (objective 2).
- The effect of different surface finish (grinding, polishing, machining and shot-peening) have been evaluated to understand how to influence on the steam oxidation resistance of the different alloys (objective 1, 2 and 3).

- The effect of pressure have been assessed to obtain more information regarding its influence upon the oxidation process and to link industrial and laboratory data (objective 2 and 3).

The academic interests are oriented towards the understanding of the steam oxidation phenomenon by identifying the different types of oxides formed and the exposure conditions leading to their appearance as well as the transport mechanisms inside the different oxides formed using isotope doped steam.

The industrial interests of this study are in the development of a quantitative model describing the growth of the different oxides taking into account the effects of surface finish, and pressure.

1.5. Thesis structure

This thesis is separated in different chapters. Chapter 1 introduces the energy generation industry background, as well as the different aims and objectives of the project. Chapter 2 gathers the literature review associated with the thesis. The different experimental and analysis devices are presented alongside the methodology used for samples' preparation and exposure tests in Chapter 3. Then the results from the steam exposure tests performed and the discussions associated with them are detailed in Chapter 4 followed by a general discussion in Chapter 5. Finally, the conclusions regarding the different objectives set for this project followed by suggestions for further work are presented in Chapter 6 and Chapter 7 respectively.

2. Literature review

2.1. Power-plant background

Large-scale coal and biomass power plants are associated with the generation of steam in order to produce energy (electricity and heat). The energy generation process is entirely dependent from the exchange of heat from a hot gas stream, resulting from the combustion of a fuel, to a steam cycle [6]. To generate energy, the simplest thermodynamic steam cycle in term of design is the Rankine cycle Figure 2-1 and Figure 2-2 [14].

Large-scale solid fuel fired power stations traditionally use pulverized coal systems to produce energy [6]. However, the targets set by the European Union to promote the use of renewable fuels have been accompanied with the introduction of biomass and waste fuel fired power plants which increasingly used for energy generation and are usually used for small scale heat generators [6]. The interest in the introduction of these new fuels is explained by the fact that their combustion results in a decrease of the net CO_2 emissions compared with conventional coal power plants [6]. Waste represents a potentially sustainable and renewable type of fuel since some waste products are revived from biomass [6]. Even if biomass can be co-fired with coal in traditional pulverized coal-fired power plants without large modification of the industrial equipment, changing the fuels affects every aspect of the power plants since it affects the combustion conditions and the composition of the combustion gas in the boiler [6,15]. The fireside and steam-side conditions are important parameters to be considered when selecting heat exchanger materials because the chosen materials should possess both good steam-side and fireside corrosion resistance. The apparition of oxides inside and outside the heat exchangers, and the deposits appearing on the fireside of the heat exchangers have a large influence on the heat transfer and heat flux phenomena which are linked with the steam conditions [16].

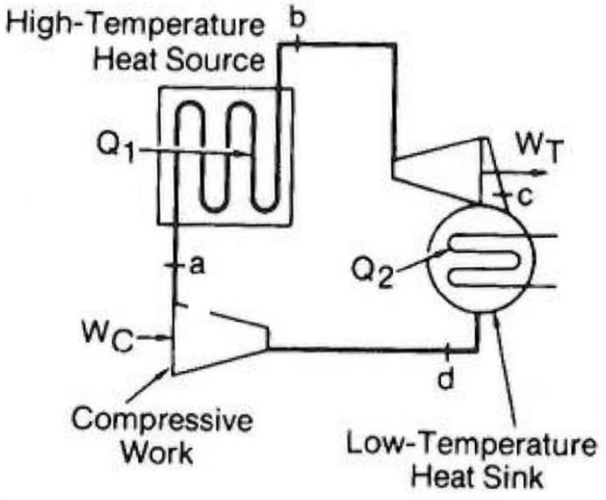

Figure 2-1: Simplified schematic diagram of the water/steam path for simple combustion plant [14]**.**

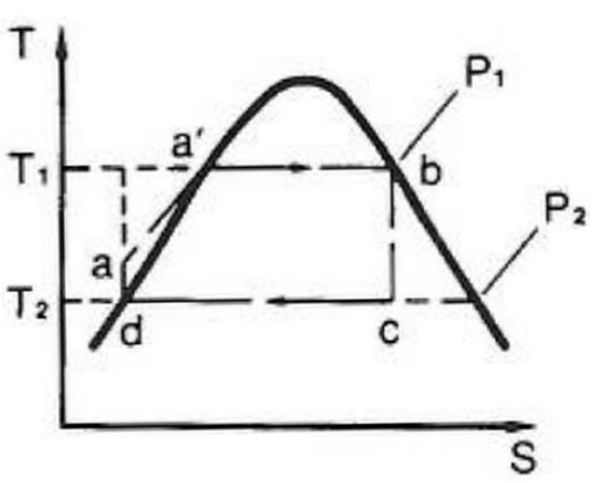

Figure 2-2: Entropic diagram associated with simple Rankine cycle for a steam cycle [14]**.**

To increase the energy production efficiency some modifications have been added to the simple Rankine cycle [14] and are shown in Figure 2-3:

- Economiser: The role of this component is to bring the liquid entering the boiler closer to its saturation state by increasing its temperature. This lowers the irreversibility of the Rankine cycle associated and increases the thermal efficiency using heat generated in the condenser or in the coolest part of the hot gas stream to heat up the compressed liquid.
- Superheater: This component heats the steam above its saturated state, leading to an increase in energy production efficiency. It also lowers the amount of moisture present in the steam after being heated in the boiler, decreasing corrosion and erosion of the steam turbine.
- Reheater: This component increases the temperature of the steam after a first stage of energy extraction in the steam turbine. At this stage, steam is still above the saturated vapour state and it prevents the formation of moisture before it enters the latest stage of the steam turbine. Power plants running under supercritical pressures use a two-stage reheat to increase the energy production efficiency.

Figure 2-3 and Figure 2-4 present respectively a schematic diagram of the water/steam path and an entropic diagram associated to the Rankine cycle for a steam cycle associated with a coal power plant with supercritical boiler [6]. Electrical energy is recovered from the electrical generator which is linked with the steam turbine.

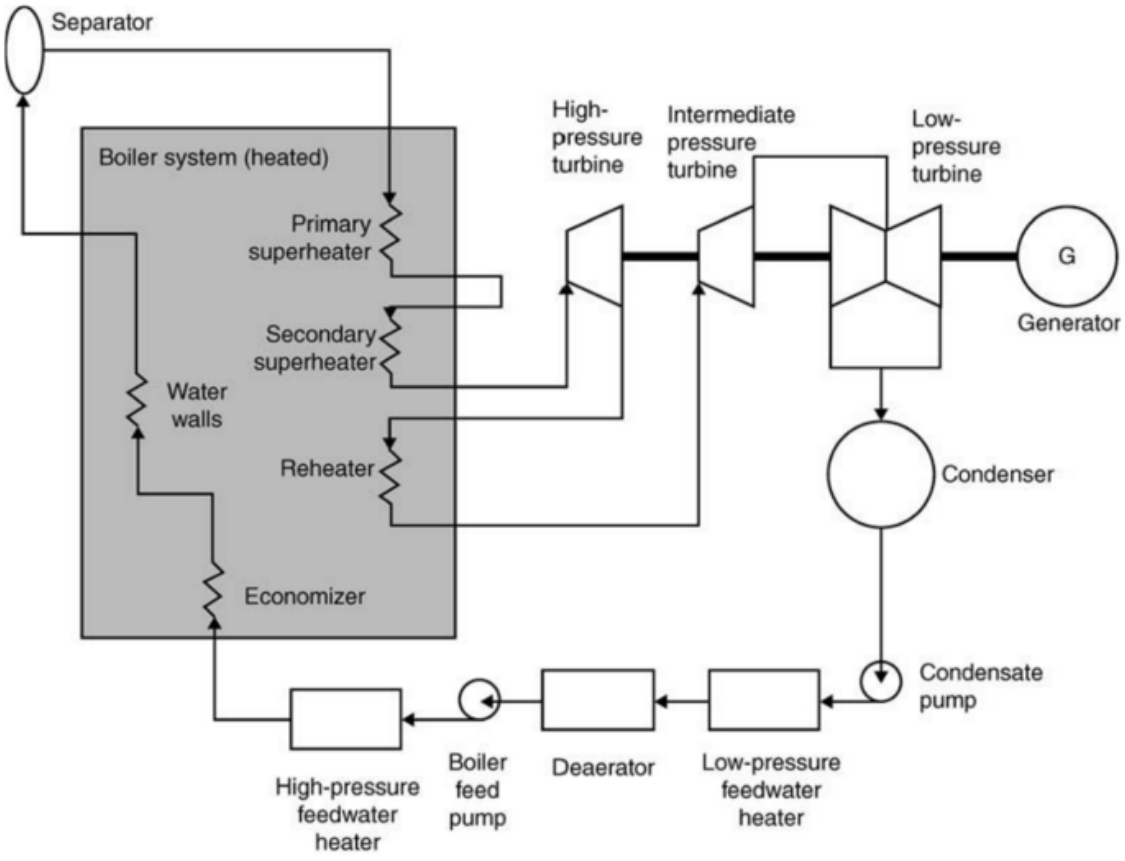

Figure 2-3: Simplified schematic diagram of the water/steam path for a coal power plant [6]**.**

The advantages of using supercritical cycles, with steam above its critical pressure, are that the running conditions allow reaching the highest thermodynamic efficiency possible to be reached and there is no need for a moisture separator. The use of multiple energy extraction stages in the steam turbine increases the energy conversion efficiency by transferring the maximum heat generated during the fuel combustion to the steam for the generation of energy [14].

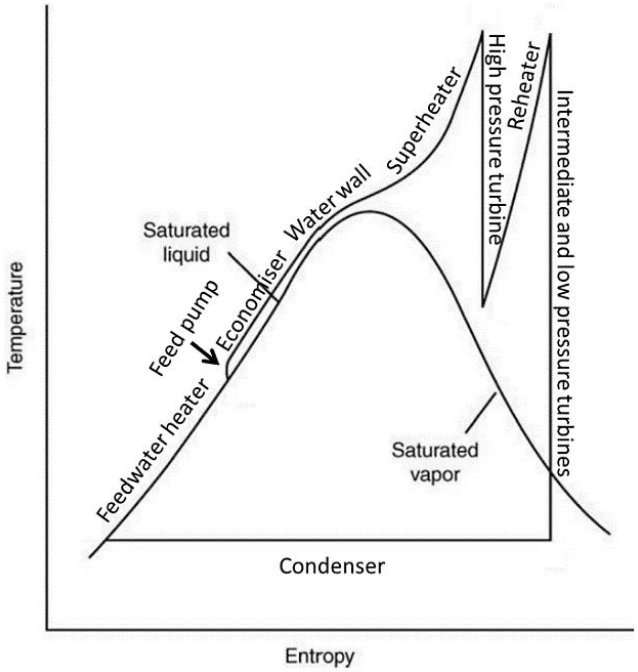

Figure 2-4: Entropic diagram associated with Rankine cycle for a steam cycle associated with a supercritical boiler [6]**.**

2.2. Heat exchangers and heat transfer

2.2.1. Heat exchangers

The role of heat exchangers is to transfer heat between two fluids at different temperatures separated by a solid wall [17].

Different types of heat exchangers can be found with different configuration [17]. The simplest configuration is to use concentric tubes in which the cold and hot fluids move inside them with a parallel-flow (Figure 2-5) or counterflow arrangement (Figure 2-6). Cross-flow arrangements can also be used; these consist of mixed or unmixed fluids moving in perpendicular directions to one another (Figure 2-7) [17]. Shell-and-tube heat exchangers (Figure 2-8) are another common configuration in which the turbulence of the fluids and their velocity can be enhanced by modifying the flow paths [17]. Shell-and-tube heat exchanger's mode of operation combines cross-flow and

counterflow. To obtain a high heat transfer surface per unit of volume when at least one of the fluids is in the gaseous state, compact heat exchangers can be used [17]. This type of heat exchanger is composed of a dense array of tubes with small flow passages. In real power plant designs, compact cross-flow heat exchangers are used to transfer heat from the hot flue gas to steam.

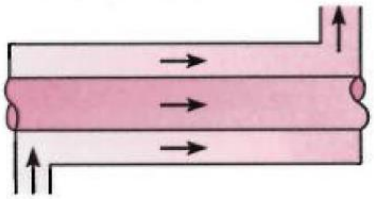

Figure 2-5: Concentric tube heat exchanger with a parallel flow arrangement [17]**.**

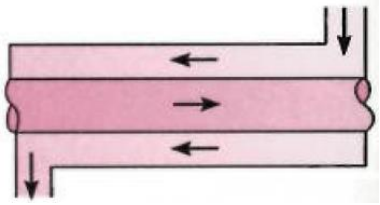

Figure 2-6: Concentric tube heat exchanger with a counterflow arrangement [17]**.**

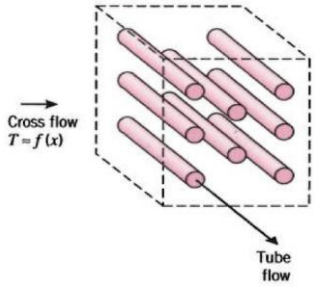

Figure 2-7: Cross-flow heat exchanger [17]**.**

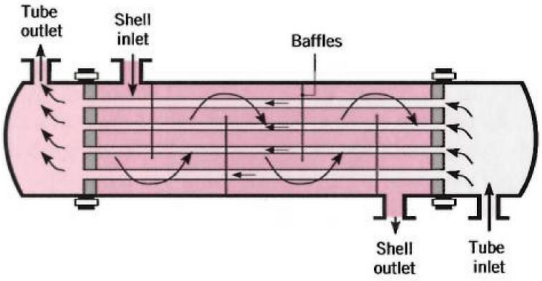

Figure 2-8:Shell-and-tube heat exchanger [17]**.**

2.2.2. Heat transfer

Heat transfer corresponds to the transition of energy due to a temperature difference inside one medium or between different media [17,18]. The transfer of heat can happen through different processes:

- Conduction: happens with the presence of a temperature gradient inside one medium.
- Convection: when there is heat transfer between a surface and a moving fluid at different temperatures.
- Thermal radiation: correspond to the transfer of energy as electromagnetic waves between to surfaces at different temperatures.

Figure 2-9 and Figure 2-10 present the composition of the heat exchanger interface allowing the transfer of heat from the hot flue gas to steam. From these figures, it is possible to visualize that different heat transfer processes take place at different locations around heat exchangers [19]:

- Conduction process through the different oxide layers and heat exchanger wall.
- Convection process between the hot flue gas and the fireside oxidation layer and ash deposit, as well as between the steam and the steamside oxidation layer.
- Radiation process between the outer part of the heat exchanger tube and the hot flue gas.

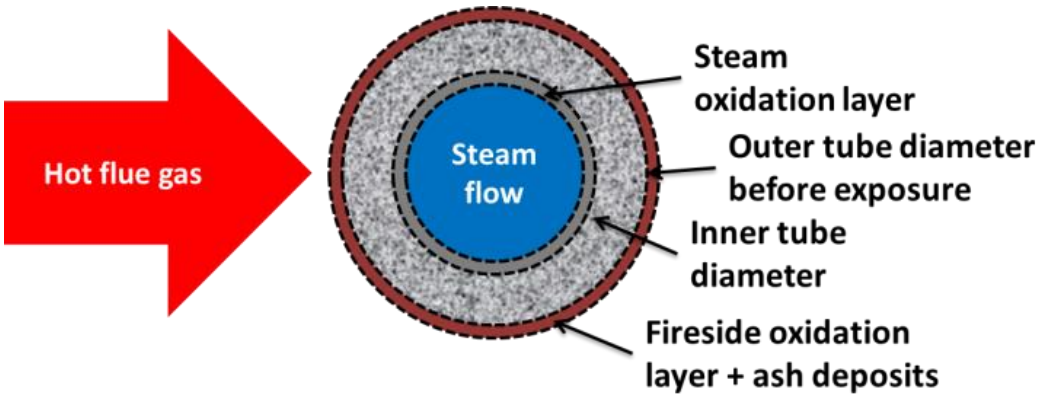

Figure 2-9: Schematic of a heat exchanger tube in service showing the different oxide and deposit layers (adapted from [16]**).**

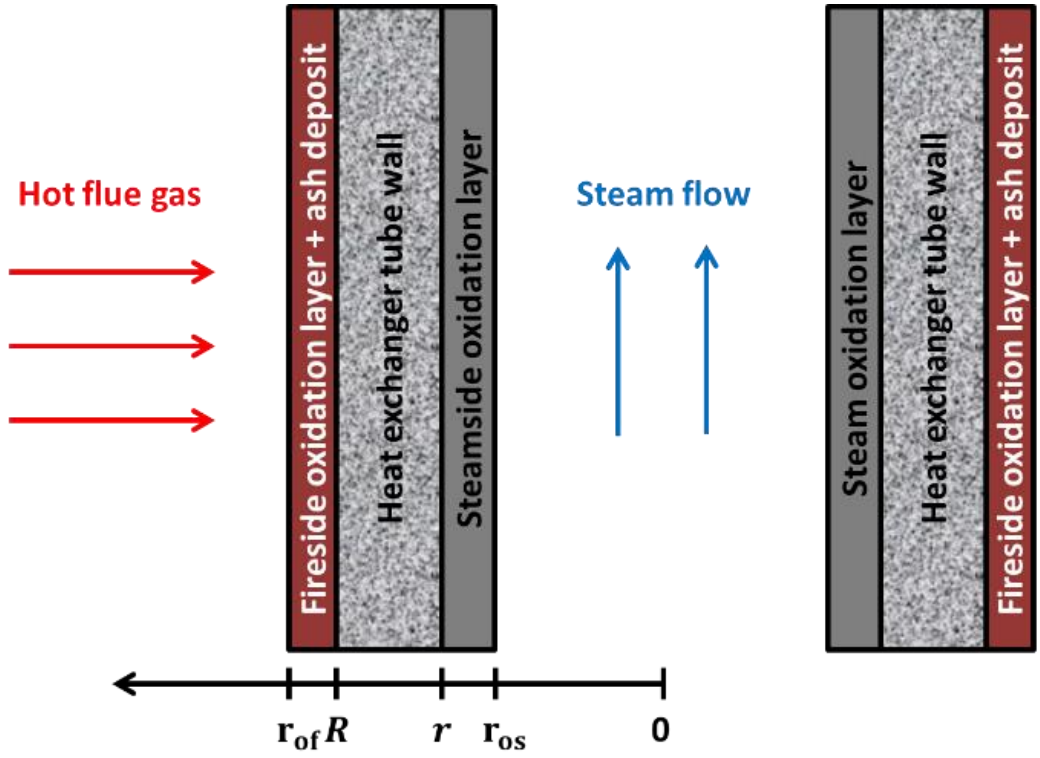

Figure 2-10: Cross-sectional schematic of a heat exchanger tube in service showing the different oxide and deposit layers [19]**.**

2.2.2.1. Conduction

Conduction accounts for the way heat is transferred through a static medium in presence of a temperature gradient. Conduction can be found in solids, stationary liquids or stationary gases. In these media, the heat is transferred through the transfer of energy from highly energetic to lower energetic particles [17]. Thermal conduction for an established regime can be described using Fourier's law [17].

$$\vec{\varphi} = -Ak\,\overrightarrow{grad}(T) \qquad \textbf{(2-1)}$$

Where $\vec{\varphi}$ is the heat flux vector [W], A is the area through which the heat is exchanged [m^2], T is the temperature [K], and k is the thermal conductivity [$W.m^{-1}.K^{-1}$].

For the case studied in this project where conduction happens in cylindrical heat exchanger along the radial direction, the heat flux equation can be written as follows [17]:

$$\varphi = -Ak\frac{\partial T}{\partial r} \quad \textbf{(2-2)}$$

Where φ is the radial heat flux $[W]$, A is the area through which the heat is exchanged $[m^2]$, T is the temperature $[K]$, r is the radial position $[m]$, and k is the thermal conductivity $[W.m^{-1}.K^{-1}]$.

When Equation (2-2) is applied to the heat exchanger tube wall, the heat flux can be written as follows [17]:

$$\varphi = -2\pi L k_{met}\frac{T_R - T_r}{\ln\left(\frac{R}{r}\right)} \quad \textbf{(2-3)}$$

Where φ is the radial heat flux $[W]$, L is the length of the heat exchanger tube $[m]$, T_r and T_R are the temperatures at the inner and outer wall of the heat exchanger $[K]$, r and R are the radius or the inner and outer walls of the heat exchanger tube $[m]$, and k_{met} is the thermal conductivity $[W.m^{-1}.K^{-1}]$.

2.2.2.2. Convection

Heat transfer by convection happens when a fluid is moving at the surface of a solid wall in presence of a temperature gradient between the two media. The fluid in motion and the surface interact in a thin region at the interface between them call the boundary layer. In the boundary layer the temperature of the fluid depends on it position from the solid surface thus thermal diffusion and fluid motion contribute to the transfer of heat. The heat exchangers used in power plants are subject to forced convection processes, since the fluids inside and around the tubes are in motion driven by fans and pumps (Figure 2-9 and Figure 2-10). Convective is heat flux is expressed from Newton's low of cooling [17,18]:

$$\varphi = Ah(T_s - T_f) \quad \textbf{(2-4)}$$

Where φ is the heat flux [W], h is the convection heat transfer coefficient [$W.m^{-2}.K^{-1}$], A is the area through which the heat is exchanged [m^2], T_s and T_f are the solid surface and fluid temperatures [K].

Studying and calculating convective heat flux mainly consists of determining the convection heat transfer coefficients. The mathematical expression of this coefficient depends on the conditions in the boundary layer such as the surface geometry; the fluid thermodynamic properties and the fluid movements, whether the fluid is heating or cooling etc [17].

Different boundary layers are involved in the convective heat transfer process [17]:

- Velocity boundary layer: where the fluid motion is affected by the solid surface.
- Thermal boundary layer: where the fluid temperature is affected by the solid surface temperature.
- Concentration boundary layer: where the fluid composition is affected by a chemical reaction at the solid surface.

The thermal and velocity boundary layers are of interest for the calculation of the convection heat transfer coefficient. Different dimensionless coefficients have been introduced to quantify the different physical phenomena happening within the different boundary layers. These are the Nusselt number, the Reynolds number and the Prandtl number, which are discussed hereafter.

The Nusselt number is directly linked with the convection heat transfer coefficient and can be interpreted as the ratio between the total heat transfer and the heat transferred by diffusion in the thermal boundary layer. The Nusselt number is written [17]:

$$Nu = \frac{hL}{k} \quad \textbf{(2-5)}$$

Where h is the convection heat transfer coefficient [$W.m^{-2}.K^{-1}$], L is the characteristic length of the contact interface [m], and k is the fluid thermal conductivity [$W.m^{-1}.K^{-1}$]. As the convection is happening inside and outside a cylindrical tube, the characteristic length is the diameter of the tube.

Figure 2-9 and Figure 2-10 show that the geometries of the interaction areas between the heat exchanger tube and the internal fluid, and between the heat exchanger tube and the external fluid are different. In the first case there is a fully developed turbulent flow in a smooth circular tube and in the second there is a fully developed turbulent cross flow around a tube [17,19]. Since the geometry of the two different interfaces is different, the Nusselt number is calculated with different empirical equations having for parameters the Reynolds and Prandtl numbers [17].

The Reynolds number could be interpreted as the ratio between the inertia and the viscous forces of the fluid [17]:

$$Re = \frac{\rho u L}{\eta} = \frac{4\dot{m}}{\pi d \eta} \quad \textbf{(2-6)}$$

Where ρ is the fluid density [$kg.m^{-3}$], u is the fluid velocity [$m.s^{-1}$], L is the characteristic length of the contact interface [m], and η is the dynamic viscosity [$kg.m^{-1}.s^{-1}$]. Because of the fluid is flowing inside or outside a cylindrical tube, the characteristic length is the diameter of the tube d [m]. For the flow inside the tube it is possible to use the fluid mass flow $\dot{m}$ [$m^3.s^{-1}$] to calculate the Reynolds number.

The Prandtl number describes the ration between the momentum diffusivity and the thermal diffusivity [17]:

$$Pr = \frac{\eta C_p}{k} \quad \textbf{(2-7)}$$

Where C_p is the fluid specific heat [$J.kg^{-1}.K^{-1}$], k is the fluid thermal conductivity [$W.m^{-1}.K^{-1}$], and η is the dynamic viscosity [$kg.m^{-1}.s^{-1}$].

Inside heat exchanger tubes, at the interface between steam and the tube wall, the equation for the Nusselt number is given by the Dittus-Boelter Equation [17]:

$$Nu = 0.023\, Re^{\frac{4}{5}}\, Pr^{0.4} \quad \textbf{(2-8)}$$

For the calculation of the Nusselt number inside heat exchanger tubes, other possible correlations exist like the Sieder and Tate correlation which takes into considerations large flow property variations [17].

Outside the heat exchanger tube, at the interface between the hot flue gas and the tube wall, the equation for the Nusselt number is given by the Hilpert correlation [17]:

$$Nu = 0.683\ Re^{0.466}\ Pr^{\frac{1}{3}} \quad \textbf{(2-9)}$$

For the calculation of the Nusselt number outside heat exchanger tubes, other possible correlations exist like the Zhukauskas or Churchill and Bernstein correlations [17].

2.2.2.3. Radiation

Unlike the transfer of heat by conduction and convection, radiation does not need to operate in a medium [17]. Thermal radiation consists of the emission of electromagnetic waves from a hot surface, liquid or gas into its surroundings. For gases, the radiation emission is a volumetric phenomenon whereas for solids and liquids the emission is a surface phenomenon. Non-polar gases, such as O_2 and N_2, do not emit radiation unlike polar molecules, such as H_2O and CO_2, which emit radiation at various temperatures [17]. A method for determining the radiation emission from a hemispherical gas mass to a surface was developed by Hottel [17]:

$$E_g = \varepsilon_g \sigma T_g^4 \quad \textbf{(2-10)}$$

Where E_g is the emission from the gas per unit of area of the surface receiving radiation [$W.m^{-2}$], ε_g is the gas emissivity factor, σ is the Stefan-Boltzmann constant [$W.m^{-2}.K^{-4}$], and T_g is the gas temperature [K].

Gases resulting from the combustion of coal contain a mixture of O_2, N_2, H_2O and CO_2. Only the polar molecules emit radiation and the emissivity factor for the mixture could be written [17]:

$$\varepsilon_g = \varepsilon_{H_2O} + \varepsilon_{CO_2} - \Delta\varepsilon \quad \textbf{(2-11)}$$

Where ε_{H_2O} is the gas emissivity factor for H_2O, ε_{CO_2} is the gas emissivity factor for CO_2, and $\Delta\varepsilon$ is the correction factor due to the mutual absorption of radiation between the two gaseous species considered [17].

The different gas emissivity factors are determined by correlating data and depends on the gas temperature, the total pressure of the gas, the partial pressure of the radiating specie and the geometry of the system [17]. Due to the complexity of the radiation emission coefficients, heat transfer by radiation was not considered in this work [17,19].

2.2.2.4. Total heat transfer

The total heat transfer process from the hot flue gas to steam can be represented using the following equivalent thermal circuit adapted from [17]:

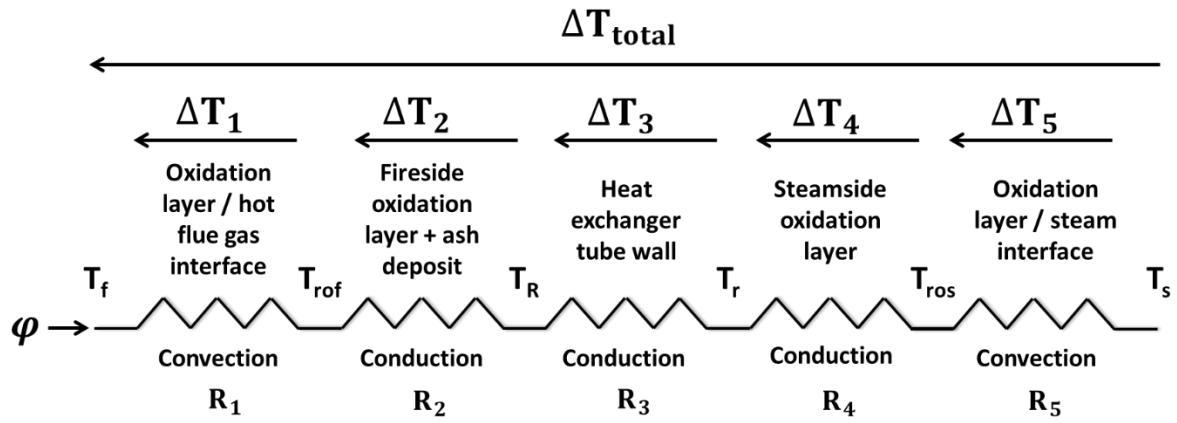

Figure 2-11: Equivalent thermal circuit for the heat transfer through a heat exchanger tube with internal and external scale layers as presented in Figure 2-10.

The heat flux can be written as the total temperature difference over the total thermal resistance of the system (see Figure 2-11) [17]:

$$\varphi = \frac{\Delta T_{total}}{R_{total}} \qquad \textbf{(2-12)}$$

Where the temperature difference $\Delta T_{total} = \Delta T_1 + \Delta T_2 + \Delta T_3 + \Delta T_4 + \Delta T_5$ and the thermal resistance is $R_{total} = R_1 + R_2 + R_3 + R_4 + R_5$.

Heat is transferred by conduction through the oxide scale layers formed at the fireside and steamside of the heat exchanger tube, and through the heat exchanger tube. Transposing Equation (2-3) for the different oxide layers, their equivalent thermal circuit heat flux are:

For the fireside oxide $\varphi = \frac{1}{R_2}\Delta T_2$ with $R_2 = -\frac{\ln\left(\frac{r_{of}}{R}\right)}{2\pi k_{of} L}$.

For the steamside oxide $\varphi = \frac{1}{R_4}\Delta T_4$ with $R_4 = -\frac{\ln\left(\frac{r}{r_{os}}\right)}{2\pi k_{os} L}$.

For the heat exchanger tube $\varphi = \frac{1}{R_3}\Delta T_3$ with $R_3 = -\frac{\ln\left(\frac{R}{r}\right)}{2\pi k_{met} L}$.

Where φ is the radial heat flux $[W]$, L is the length of the heat exchanger tube $[m]$, ΔT_i are temperatures differences $[K]$, R_i are thermal resistances, r, R, r_{of}, r_{os} are respectively the radius or the inner and outer walls of the heat exchanger tube, and of the fireside and steamside oxides $[m]$, and k_{met}, k_{of}, and k_{os} are respectively the thermal conductivity of the metal, the fireside oxide and the steamside oxide respectively $[W.m^{-1}.K^{-1}]$.

The heat flux transferred by convection between the hot flux gas and the outer part of the heat exchanger tube can be written:

$\varphi = \frac{1}{R_1}\Delta T_1$ with $R_1 = \frac{1}{Nu_{of}\, k_f\, r_{of}}$ .and $\Delta T_1 = T_{rof} - T_f$

Where k_f is the hot flue gas thermal conductivity $[W.m^{-1}.K^{-1}]$, r_{of} is the radial position of the interface between the hot flue gas and the fireside oxide $[m]$, and the Nusselt number at the surface of the fireside oxide Nu_{of} is calculated using Equation (2-9).

Similarly, the heat flux transferred by convection between the steam and the inner part of the heat exchanger tube can be written:

$\varphi = \frac{1}{R_5}\Delta T_5$ with $R_5 = \frac{1}{Nu_{os}\, k_s\, r_{os}}$ .and $\Delta T_5 = T_s - T_{ros}$

Where k_s is the steam thermal conductivity [$W.m^{-1}.K^{-1}$], r_{os} is the radial position of the interface between steam and the steamside oxide [m], and the Nusselt number at the surface of the steamside oxide Nu_{os} is calculated using Equation (2-8).

Finally, using the values obtained previously the heat flux can be written [16,19]:

$$\varphi = \frac{2\pi L\left(T_s - T_f\right)}{\frac{1}{h_f r_{of}} + \frac{\ln\left(\frac{r_{of}}{R}\right)}{k_{of}} + \frac{\ln\left(\frac{R}{r}\right)}{k_{met}} + \frac{\ln\left(\frac{r}{r_{os}}\right)}{k_{os}} + \frac{1}{h_2 r_{os}}} \quad \textbf{(2-13)}$$

2.3. Steam oxidation of metals

2.3.1. Thermodynamics and kinetics of steam oxidation of metals

High temperature corrosion represents a high economic and technical challenge to any industry relying on thermal processes whose efficiency depends on the operating temperature. Oxidation is involved in any atmosphere with an oxygen partial pressure, such as air, H_2O, CO_2 In parallel to the metal oxidation, concurrent degradation reactions can take place such as nitridation and carburization and the reaction products can be found above or below any oxide scale formed depending on the oxygen partial pressure [20]. Deposits such as ash or molten species can be present at the surface of the metal and leads to severe localized attack's mechanisms such as fireside corrosion [6,21]. Deposits are not present inside heat exchanger tubes but are affecting the outer part of the tube in contact with hot flue gas originated from fuel combustion. Although they indirectly affect the steam oxidation process, the presence of deposits can affect the transfer of heat thus changing the temperature of the metal in contact with steam.

The mechanism of high temperature oxidation for a pure metal can be written [9]:

$$M(s) + O_2(g) \leftrightarrow MO_2(s) \quad \textbf{(2-14)}$$

The equilibrium constant of this reaction is [9]:

$$K = \frac{a_{MO_2}}{a_M * P(O_2)_{eq}} \quad \textbf{(2-15)}$$

Where a_M and a_{MO_2} are the activity coefficient of the metal and the oxide and $P(O_2)_{eq}$ is the oxygen partial pressure at equilibrium [$bars$]. For solid constituents the activity coefficient is equal to 1 when the different solids are not mixed. If the bulk material and the oxide are part of a solid solution, the activity coefficient is smaller than 1. Thus the equilibrium constant K is mostly dependant on the oxygen partial pressure.

The standard free energy ΔG^0 in [$J.mol^{-1}$] is given by the condition under which the chemical reaction is in equilibrium [9].

$$\Delta G^0 = -RTln(K) = -RT \ln\left(\frac{a_{MO_2}}{a_M * P(O_2)_{eq}}\right) \quad \textbf{(2-16)}$$

Where R is the gas constant [$J.mol^{-1}.K^{-1}$] and T is the temperature [K].

The Gibbs free energy [$J.mol^{-1}$] of this oxidation reaction can be written [9]:

$$\Delta G = \Delta G^0 + RT \ln\left(\frac{a_{MO_2}}{a_M * P(O_2)}\right) \quad \textbf{(2-17)}$$

If the bulk material and the oxide are not considered to be part in a solid solution it can be assumed that $a_M = a_{MO_2} = 1$. Then the standard free energy can be written [9]:

$$\Delta G^0 = -RT \ln\left(\frac{1}{P(O_2)_{eq}}\right) \quad \textbf{(2-18)}$$

The standard free energy for the different oxidation reactions can be found in multiple thermodynamic handbooks and can also be represented in Ellingham diagrams (Figure 2-14). Thus knowing the value of the standard free energy allows the determination of the equilibrium oxygen partial pressure for the oxidation reaction (2-14) [9]:

$$p(O_2)_{eq} = \exp\left(\frac{\Delta G^0}{RT}\right) \quad \textbf{(2-19)}$$

The Gibbs free energy for the oxidation reaction can then be written [9]:

$$\Delta G = RT \ln\left(\frac{p(O_2)_{eq}}{P(O_2)}\right) \quad \textbf{(2-20)}$$

For a chemical reaction to happen its Gibbs' free energy must be negative: $\Delta G < 0$. In consequence, an oxidation reaction takes place if the oxygen partial pressure of the atmosphere, in which a metal is placed, is higher that the equilibrium oxygen partial pressure of the oxidation reaction $\left(p(O_2) > p(O_2)_{eq}\right)$ [9,22].

In a pure steam atmosphere, oxidation is possible due to water dissociation taking place at high temperature (Equation (2-21)). Being able to calculate the oxygen partial pressure under different steam conditions (i.e. temperature and pressure) is crucial to know what oxides are thermodynamically likely to forme during the oxidation process [9,22].

$$H_2O(g) \leftrightarrow H_2(g) + \frac{1}{2}O_2(g) \quad \textbf{(2-21)}$$

The equilibrium constant of this reaction is:

$$K = \frac{pO_2^{0.5} pH_2}{pH_2O} \quad \textbf{(2-22)}$$

The standard free energy is expressed as [9,22]:

$$\Delta G^0 = -RT \ln(K) \quad \textbf{(2-23)}$$

Standard free energy values for steam dissociation under different temperature and pressure conditions can be found in chemistry handbooks. The oxidizing atmosphere's temperature and pressure as well as the standard free energy for steam dissociation need to be linked with the oxygen partial pressure. To do so, the partial dissociation of 1 mole of water, giving x moles of H^2 and $\frac{x}{2}$ moles of O_2, is considered under an atmosphere at the pressure P. The different pressures can be expressed as [23]:

$$pO_2 = \frac{x}{x+2} P \quad \textbf{(2-24)}$$

$$pH_2 = \frac{2x}{2+x}P \quad \textbf{(2-25)}$$

$$pH_2O = \frac{2(1-x)}{2+x}P \quad \textbf{(2-26)}$$

The equilibrium constant can then be written as [23]:

$$K^2 = \frac{x^3}{(2+x)(1-x)^2}P \quad \textbf{(2-27)}$$

If the amount of water dissociated is very low, $x \ll 1$, then the equilibrium constant can be simplified [23]:

$$K^2 = \frac{x^3}{2}P \quad \textbf{(2-28)}$$

Using the Equations (2-24) with $x \ll 1$, and (2-28) the oxygen partial pressure can be estimated as a function of the total pressure and the equilibrium constant [23]:

$$pO_2 = \left(\frac{KP}{2}\right)^{\frac{2}{3}} \quad \textbf{(2-29)}$$

Then the partial pressure can be linked with the standard free energy of water dissociation [9,22]:

$$pO_2 = \left(\frac{\exp\left(-\frac{\Delta G^0}{RT}\right)P}{2}\right)^{\frac{2}{3}} \quad \textbf{(2-30)}$$

Figure 2-12 shows the oxygen partial pressure resulting from steam dissociation at different temperatures and pressures [23,24]. It is possible to observe that at low pressure, a slight pressure variation influences greatly the oxygen partial pressure. By contrast, at high pressure, pressure variations do not affect significantly the oxygen partial pressure. This figure also shows the stability conditions of the oxides usually

formed during the steam oxidation of iron-chromium alloys. All oxides presented here are stable at temperatures below 1000°C [24].

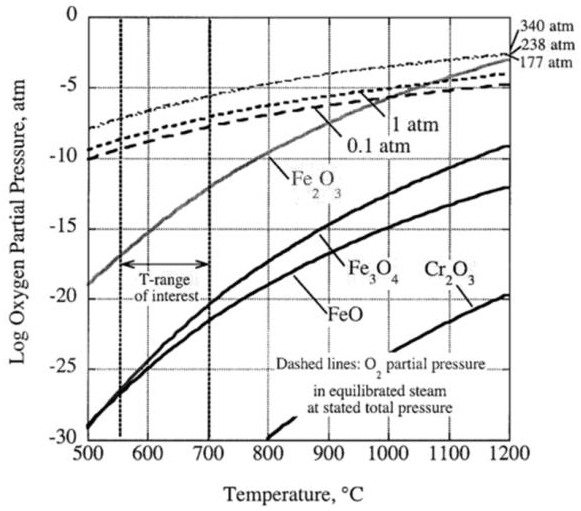

Figure 2-12: Effective oxygen partial pressures in steam and the stability of oxides [24]**.**

It appears that the presence of steam leads to higher oxidation rates than in the presence of a dry gas as shown in Figure 2-13 [25]. Ehlers et al. [25] observed that the oxidation rate was higher during wet gas exposure and that the oxides formed are less protective than the ones produced during dry oxidation, therefore the change in kinetics observed was due to faster growing oxides.

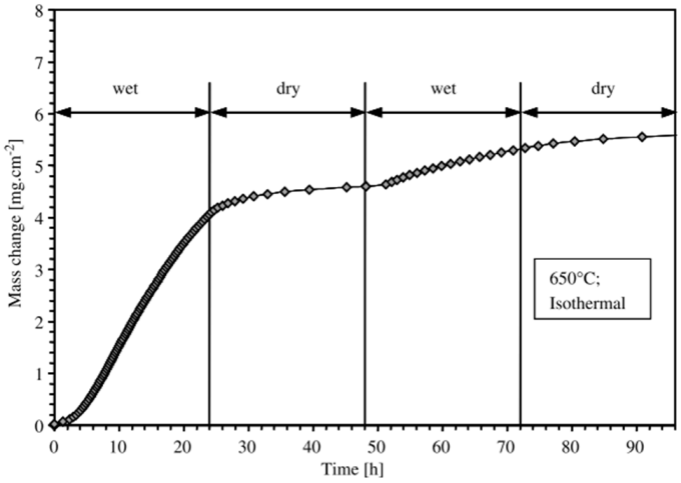

Figure 2-13: Weight gain recorded during the oxidation of P91 at 650°C switching the gas composition every 24 hours between wet ($N_2 - 1\%_{vol}O_2 - 4\%_{vol}H_2O$) and dry ($N_2 - 1\%_{vol}O_2$) gas [25]**.**

The various equations presented previously (Equation (2-14) to Equation (2-30)) explain and quantify where the oxygen comes from to oxidise a metal at high temperature [9,22]. The basic thermodynamic equations related to the oxidation of metals were presented and can be used with Ellingham diagrams (Figure 2-14) to determine which oxide can form and their stability under given steam conditions (temperature and pressure) [9,22].

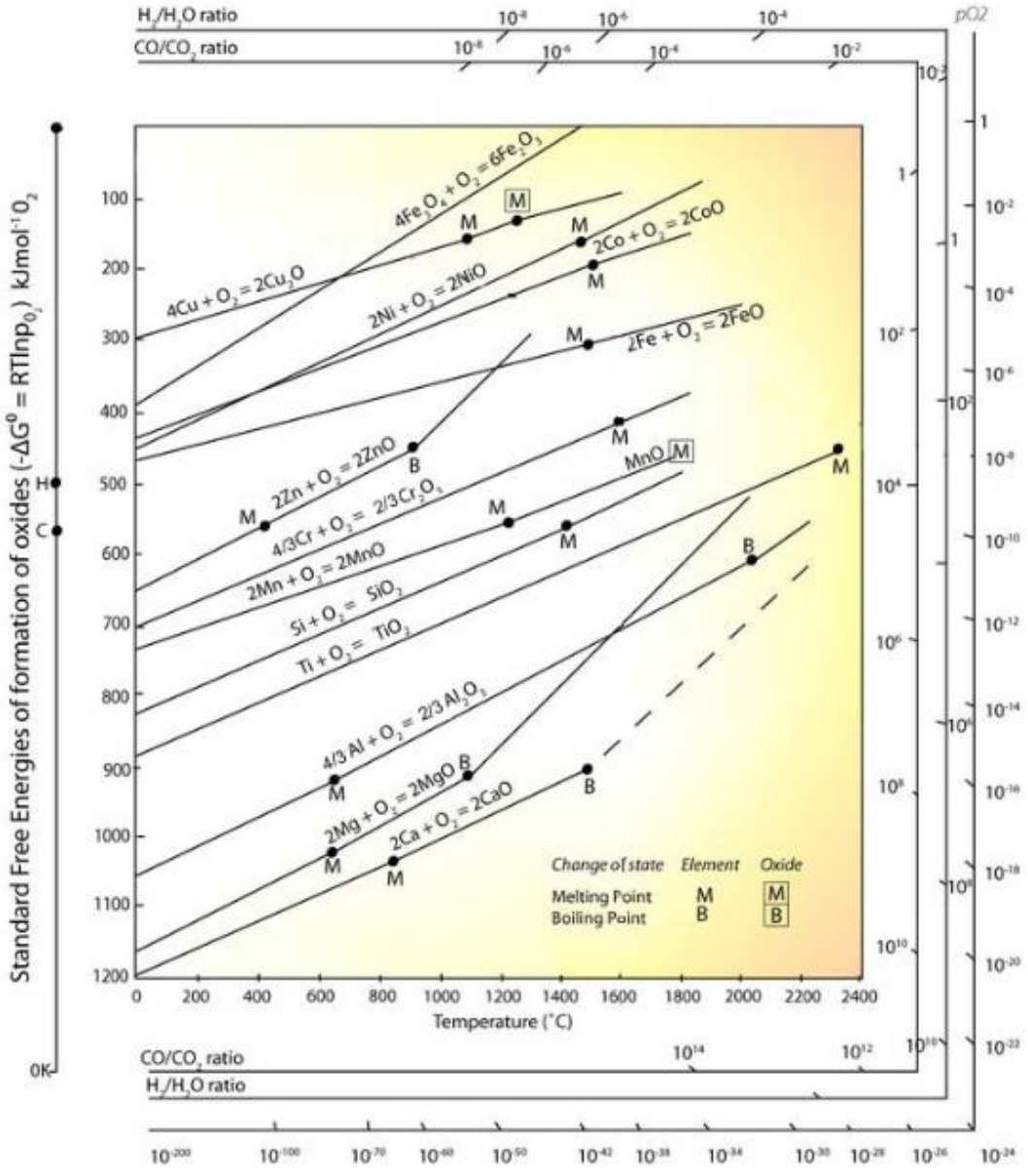

Figure 2-14: Example of Ellingham diagram for various oxides [26]**.**

The performances of various materials regarding high temperature oxidation depends on their corrosion resistance [6,27]. A material is resistant to high temperature

oxidation if the attack rate is the lowest possible, there is no localised attack (i.e. at grain boundaries), and the corrosion products formed are stable [27]. However, all metallic materials are unstable in high temperature oxidizing environments so, for the metal to possess oxidation resistances, the oxide formed needs to be protective. An oxide is considered protective if the following requirements are respected [27]:

1. High thermodynamic stability of the scale in the service environment.
2. Good resistance of the scale against impurities, deposits, ashes on the surface.
3. Impermeability against aggressive components of the environment.
4. Slow growth rates of the scale.
5. Good healing capacities regarding crack formation and scale spallation.
6. Similar thermal expansion coefficient to the metallic substrate.
7. High strain tolerance.
8. Good adhesion to the metallic substrate.
9. Good erosion resistance.
10. Low oxide vapour pressure, and resistance to volatilization.
11. High melting temperature.

The three most protective oxides are chromia Cr_2O_3, alumina Al_2O_3 and silica SiO_2. For the protective oxides to be formed, the alloy substrate should possess a sufficient amount of Cr, Si, and Al [27]. Other mixed Cr and Al containing oxides with spinel structures can also provide some oxidation protection to a metallic substrate.

Generally oxidation is a complex process divided in multiple steps which include the initial formation, then growth, and finally failure of the formed oxides. Oxide growth and failure often occur in parallel within different parts of a sample undergoing different processes, which makes the late stages of oxidation process complex to model [9,22,27].

In the initial stage of oxidation, oxygen atoms are absorbed at the surface of the metal [22,27]. Once the metal surface is saturated with absorbed oxygen, the oxygen dissolves and oxide nucleation starts. The formed nuclei are localized at the metal surface and spread alongside it until the entire surface is covered by a continuous oxide [22,27]. Oxygen absorption has been schematized in Figure 2-15. When absorbed at the surface of the material, oxygen reacts with the metal to form iron nuclei

in the case presented hereafter [28]. The consumption of iron diffusing to the surface of the material leads to the formation of iron vacancies diffusion into the substrate. Within the metal substrate, grain boundaries constitute faster oxygen diffusion paths, which leads to their preferential oxidation [28]. For a carbon containing alloy, carbides can be found at grain boundaries and for a chromium containing alloy, chromia is preferentially formed at the grain boundaries due to an enhancement of chromium diffusion [28].

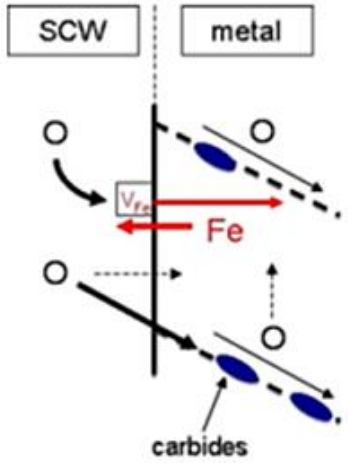

Figure 2-15: Schematic of the early oxidation stages of oxidation [29]**.**

Numerous compositions of oxide nuclei can form in the initial stages of oxidation as long as they are thermodynamically possible and stable [27]. These transient oxides depend on multiple factors such as metal substrate composition, grain orientations (Figure 2-16), temperature and pressure. The oxidation rate of the nuclei increases with oxidation time until the growth of the nuclei with different composition start to affect one another, causing the oxidation rate to decrease. Indeed, a faster growing oxide can prevent the formation of other oxides if it possesses low diffusion rates for certain species intervening in the formation of other oxides [27]. As a result, this faster oxide act as a diffusion barrier. For a metallic alloy, different oxides can form at the surface of the material and each possible oxide possesses its own growth rate. For the material to develop an oxidation resistance, it is crucial that the more protective oxides, with the slowest oxidation rate, covers the alloy surface potentially below other oxides [27]. This phenomenon is classic for iron-chromium alloys for which chromia or

chromium-rich spinel oxides can be found between the bulk material and the iron-rich oxides. For nickel-based alloys containing chromium and aluminium, a similar phenomenon can be observed with the formation of alumina bellow a chromia layer [27]. However the formation of the protective oxide layer requires that the alloy possesses a sufficient amount of the reactive metal substance to form a continuous layer.

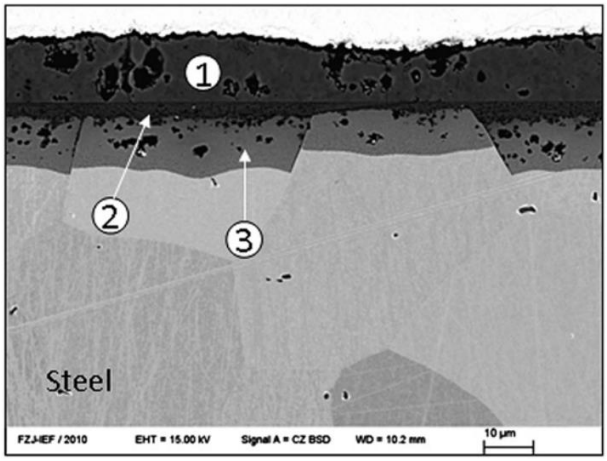

Figure 2-16: Cross-section of a ferritic steel with 17.5 w% Cr content oxidized at 550°C for 500 hours in $Ar - 4\%_{vol}H_2 - 40\%_{vol}H_2O$. (1) shows the outer oxide scale, (2) and (3) show the inner oxide scales [30]**.**

Once the initial oxide layer generated by the surface spreading of oxide nuclei is formed, the oxide layers grow in terms of thickness and forms a dense oxide scale in which the growth is controlled by solid state diffusion [9,22,27]. Solid state diffusion depends on the lack of stoichiometry of the oxide layers where defects, such as vacancies and interstitial sites, allow the transportation of the different reactants (Figure 2-17) [9,22,27]:

- Metallic ions are transported through the oxide towards the gas interface to react
- Oxygen ions are transported to the metallic substrate interface to react

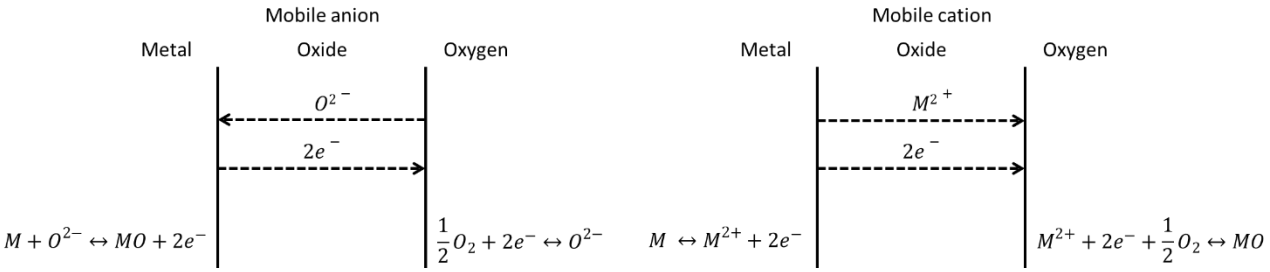

Figure 2-17: Interfacial reactions and ionic transport processes for high temperature oxidation.

If the oxide layers are highly stoichiometric and maintain electroneutrality, the defects can be categorized are Schottky or Frenkel defects [9,22,27,31]. Schottky defects describe the defects in compounds with ionic vacancies on both the cationic and anionic sub-lattices [22]. Thus anions and cations are mobile. Frenkel defects describe the defects in compounds with the presence of cations vacancies and cations in interstitial sites [22]. In this case only cations are mobile. Although Schottky and Frenkel defects are a possible explanation for ionic transport in the oxide scales, neither of them includes a mechanism for electron migration [22]. Electron migration mechanism towards the gas interface is necessary for the oxide and oxygen anions formation. In consequence, to explain the simultaneous migration of ions and electrons, oxide scales have to be considered as non-stoichiometric compounds [9,22,31]. This means the real composition of the oxide scale is not exactly the one given by the idealised formula. There are some ion interstitials or vacancies in addition to electron excess or defects which means oxides are semiconductors. Semiconductors are globally electroneutral and can exhibit negative (n-type) or positive (p-type) behaviour [9,22,31].

n-type semiconductors transfer electrical charges using negative carriers (electrons) and they possess either an excess of metal, with interstitial cations and an excess of electrons in the conduction band, or a deficit of non-metal compounds, with anion vacancies and excess of electrons in the conduction band [22].

p-type semiconductors transfer electrical charges using positive carriers and they possess a deficit of metal, with cation vacancies and deficit of electrons in the conduction band. A deficit of an electron is called an electron hole [22].

A third type of semiconductor exists, called an intrinsic semiconductor. This corresponds to materials with a high electrical conductivity due to the presence of electronic defects in large excess compared to ionic defects. Electronic defects are due to the presence of an excess of electrons in the conduction band associated with an excess of electron holes on the valence band [9,22].

Anionic transport by solid state diffusion depends on defects present in oxide scales. With regards to the types of defects that could be present in the oxide scale, diffusion through oxide scales during high temperature oxidation should be understood [9,22]. Atoms in crystalline solids are constantly migrating from one lattice site to another. Figure 2-18 shows the different diffusion mechanisms involved in crystalline solids.

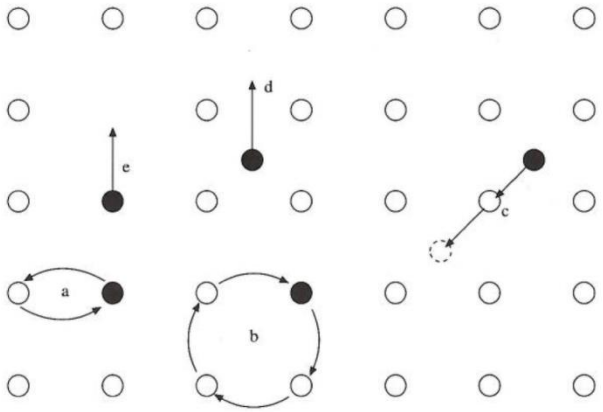

Figure 2-18: The different diffusion mechanisms in crystalline solids: (a) place exchange, (b) ring mechanism, (c) interstitialcy mechanism, (d) interstitial atom movement, (e) vacancy mechanism [9]**.**

The different diffusion mechanisms are described hereafter [9]:

(a) Place exchange: The atom's jump consists of an exchange of two neighbouring atoms.

(b) Ring mechanism: The atom's jump consists of an exchange between four neighbouring atoms in a ring.

(c) Interstitialcy mechanism: The atom's jump consists of an interstitial atom moving to an occupied lattice site, forcing the previous atom occupying the site to the next interstitial position.
(d) Interstitial atom movement: The atom's jump consists of an interstitial atom moving to another interstitial position.
(e) Vacancy mechanism: The atom jump's consists of an atom moving from a lattice site to the nearest vacant lattice site.

Considering oxide scales as semiconductors (i.e. non-stoichiometric compounds), mechanisms (c), (d), and (e) are the most important mechanisms for ionic transport. In addition, since the oxide scales are composed of multiple oxide grains short circuit diffusions paths allow faster diffusion. These short circuits for the ionic transport could be along grain boundaries, dislocations or cracks.

Transport by diffusion of an element in the oxide scale is driven by its concentration gradient over the oxide's thickness [9,32]. Fick's first law explains that a substance diffuses from high to low concentration regions [9]:

$$J = -D\ \overrightarrow{grad}(c) \tag{2-31}$$

Where J is the diffusion flux [$mol.m^{-2}.s^{-1}$], D is the diffusion coefficient [$m^2.s^{-1}$], and c is the concentration of the diffusing substance [$mol.m^{-3}$].

If the diffusion is considered to be linear, Fick's first law can be written [9,17,32]:

$$J = -D\ \frac{\partial c}{\partial x} \tag{2-32}$$

Where x is the linear position [m].

Fick's second law explains the concentration evolution of the diffusing substance over time [9,17,32]:

$$\frac{\partial c}{\partial t} = D\ \nabla^2(c) \tag{2-33}$$

Where t is the diffusion time [s], D is the diffusion coefficient [$m^2.s^{-1}$], and c is the concentration of the diffusing substance [$mol.m^{-3}$].

If the diffusion is considered to be linear, Fick's second law can be written [9,17,32]:

$$\frac{\partial c}{\partial t} = D\frac{\partial^2 c}{\partial x^2} \quad \textbf{(2-34)}$$

Where x is the linear position $[m]$.

The diffusion coefficient follows an Arrhenius law since it depends on temperature and an activation energy, which is the energy required for the atom's diffusion mechanism to take place [9].

$$D = D_0 \exp\left(-\frac{Q}{RT}\right) \quad \textbf{(2-35)}$$

Where D is the diffusion coefficient $[m^2.s^{-1}]$, D_0 is the standard diffusion coefficient $[m^2.s^{-1}]$, Q is the activation energy for diffusion $[J.mol^{-1}]$, R is the gas constant $[J.mol^{-1}.K^{-1}]$ and T is the temperature $[K]$.

Wagner [9,22,33] has provided a theory of oxidation which describes the oxidation behaviour of a metal under simplified conditions described hereafter:

1) The oxide layer is compact and perfectly adherent
2) The migration of ions or electrons across the scale is the rate controlling process
3) Thermodynamic equilibrium is established at both metal/scale and scale/gas interfaces
4) Oxide scale shows only small derivation from stoichiometry (i.e. constant ionic fluxes into the scale)
5) Thermodynamic equilibrium is established locally through the scale
6) The scale is thick compared with the distances over which space charge effect occurs (i.e. no electrical double layer formed)
7) Oxygen solubility in the metal may be neglected

Figure 2-19 and Figure 2-20 show oxide scale formation according to Wagner's theory. The different surface reactions given are dependent on either the anion or/and cation diffusion. Regarding the oxide scale, the oxide activity is considered constant over the entire oxide layer ($a'_{MO} = a''_{MO} = 1$). The overall oxidation reaction is the same as the

one described by Equation (2-14) which is associated with the free energy equation of Equation (2-16) [9,22].

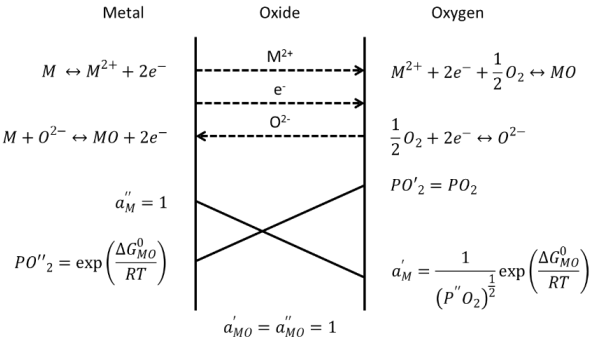

Figure 2-19: Scale formation according to Wagner's model [22]**.**

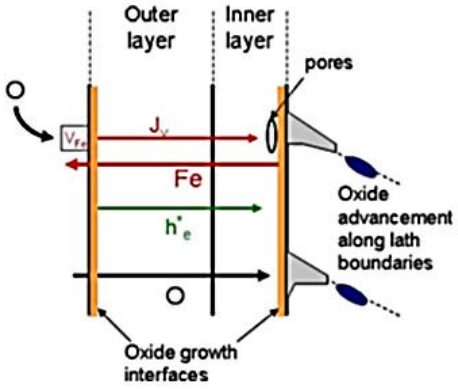

Figure 2-20: Schematic of an oxidation mechanism occuring once the oxide layers are formed [29]**.**

Considering Fick's first law and the fact that ionic diffusion is the rate-controlling process for oxide growth, it is possible to write that all the diffusing ions are transformed into oxide [22,27]. Therefore, the diffusion flux can be written:

$$J_{ion} = \frac{1}{V_{ox}}\frac{dx}{dt} = -D_{ion}\frac{\partial c_{ion}}{\partial x} \quad \textbf{(2-36)}$$

Where V_{ox} is the molar volume of the oxide $[m^3.mol^{-1}]$, x is the oxide thickness $[m]$, D_{ion} is the ion diffusion coefficient $[m^2.s^{-1}]$, and c_{ion} is the ions concentration $[mol.m^{-3}]$.

Wagner's theory and Figure 2-19 indicate that the ion concentration at the metal/oxide and at the oxide/gas interfaces are constant and given by the thermodynamic equilibrium at both interfaces. In consequence, over the concentration difference is constant over the entire oxide thickness. Then considering an oxide thickness of x and Equation (2-36), it is then possible to write that the rate of oxide growth is [27]:

$$\frac{dx}{dt} = \frac{k}{x} \quad \textbf{(2-37)}$$

Where $k = D_{ion}V_{ox}\Delta c$ is a constant. Integrating Equation (2-37) knowing that $x = 0$ at $t = 0$ it is possible to write that the oxide growth rate is parabolic:

$$x^2 = 2kt \quad \textbf{(2-38)}$$

Under Wagner's theory, the oxide layer is considered to be compact so the and homogeneous so the oxide thickness is proportional to its mass. Thus both the mass change and layer thickness associated with oxide growth follow a parabolic rate [27].

2.3.2. Steam oxidation of heat exchanger materials

For a material to be used as a heat exchanger tube, several properties are required [34,35]:

- High steam oxidation and fireside corrosion resistance
- High creep resistance
- High thermal conductivity
- Weldability
- Low cost

A large range of materials can be considered for heat exchanger tubing. These can be classified in three groups: ferritic steels, austenitic steels and nickel-based alloys. Table 2-1 lists some of the candidate materials and the temperature range of application for these different materials based on their creep resistance.

Table 2-1: Candidate materials to be used as heat exchanger tubes [10]**.**

Trade designation	Nominal composition	ASME code/code case	Preferred application(a)	Temperature of application (metal)(b)
HCM2S	2-1/4Cr-1.5W-V	2199	WW	Up to 575 °C (1050 °F)
Tempaloy F-2W	2Cr-1W-Mo-V-Nb	…	WW	
HCM12	12Cr-1Mo-1W-V-Nb	…	WW	
NF12	11Cr-2.6W-2.5Co-V-Nb-N	…	H	Up to 650 °C (1200 °F)
SAVE12	12Cr-W-Co-V-Nb-N	…	H	
NF616 (P-92)	9Cr-2W-Mo-V-Nb-N	2179	H	Up to 620 °C (1150 °F)
HCM12A (P-122)	12Cr-1.5W-Mo-V-Nb-N-Cu	2180	H	
E911	9Cr-1Mo-1W-V-Nb-N	…	H	
Austenitic steels				
SAVE25	23Cr-18Ni-Nb-Cu-N	…	T	620-675 °C (1150-1250 °F)
NF709	20Cr-25Ni-Nb-Ti-N	…	T	
Hr3C	25Cr-20Ni-Nb-N	2113	T	
Super304H	18Cr-8Ni-W-Nb-N	…	T	
347HFG	18Cr-10Ni-Nb	2159	T	
800HT	21Cr-32Ni-Al-Ti	1987	T	
HR120	Ni-33Fe-25Cr-N	2315	T	
Ni Base alloys				
INCO740	24Cr-20Co-2Ti-2Nb-V-Al	…	P, T	675-788 °C (1250-1450 °F)
230	22Cr-14W-2Mo-La	2063	P, T	
Marco alloy				
625	21.5Cr-9Mo-5Fe-3.6Nb-Al-Ti	1409	P, T	
617	22Cr-12.5Co-9Mo-1.2Al	1956	P, T	
HR6W	23Cr-6W-Nb-Ti	…	P, T	
45TM	27Cr-23Fe-2.75Si	2188	P, T	

(a) WW, water wall; T, superheater/reheater tubes; P, pipes and headers. (b) These upper limit metal temperatures are based on creep.

The following Sections will specify on how ferritic steels, austenitic steels and nickel-based alloys react to high temperature steam oxidation. More detailed information regarding the effect of surface finish, heat flux and spallation is also covered.

2.3.2.1. Ferritic steels

Chromium content has been reported to be the main material parameter affecting the steam oxidation behaviour of ferritic steels [36]. These materials are generally classified in two groups depending on their chromium content: steels with up to 2.25%$_{atm}$ Cr and steels with 9-12%$_{atm}$ Cr. Compared to the other classes of materials studied, ferritic steel possess the lowest chromium content.

Ennis and Quadakkers [37] have studied the first stages of steam oxidation of 9-10%$_{atm}$ Cr ferritic-martensitic steels between 550 and 650°C. The initial oxidation rate is reported to be very low and the more chromium in the material, the longer the initial oxidation rate stays low. Chromium-rich oxide starts to form at the oxide/bulk interface

along with FeO as a result from the oxidation of the bulk material. As the oxidation of the material continues, an inner and outer oxide layers appear (Figure 2-21). Was [36] reported that the steam oxidation of these materials leads to the apparition of a dual layer oxide, characterized by an outer iron-rich oxide layer composed of magnetite (Fe_3O_4) and an inner spinel iron-chromium oxide $(Fe,Cr)_3O_4$ layer. The spinel oxide is a partially protective layer and its breakdown leads to the rapid growth of magnetite at the oxide/steam interface. An internal oxidation zone can also be observed at the oxide/metal interface. The distribution of the different species in the oxide scales is explained by their different oxygen affinity and their diffusion rates within the different scales [38].

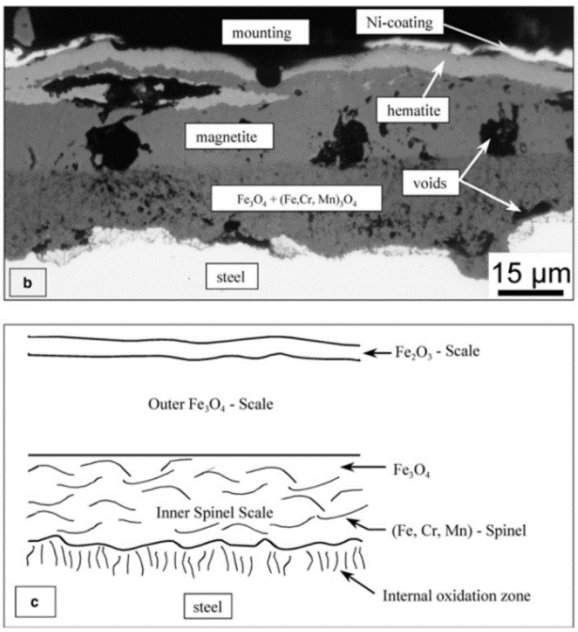

Figure 2-21: Cross-section of P91 after 100 hours of exposure to a wet gas in the temperature range 600-700°C [25]**.**

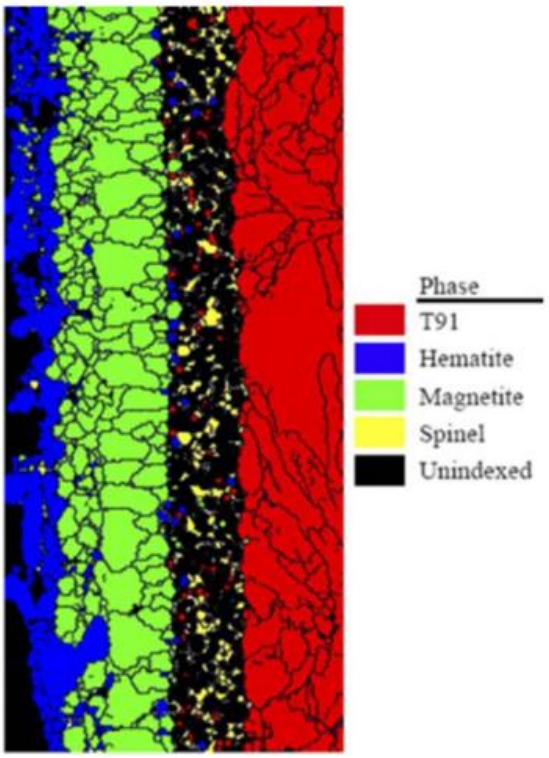

Figure 2-22: EBSD image of T91 exposed to supercritical water at 500°C for 505 hours [39]**.**

The outer layer of the multi-layered oxide scale is a porous non protective oxide layer with high iron and oxygen content mainly composed of large columnar magnetite grains oriented parallel to the direction of oxide growth (Figure 2-22) [39]. This layer is very porous and some large cracks along the oxide growth direction can be observed.

This outer layer does not show any presence of chromium [39]. Hematite (Fe_2O_3) can also be detected after 505 hours at the interface gas/outer oxide [39,40]. Ennis [37,41] did not report any hematite formation on 9-12%$_w$Cr ferritic steels after 1000 hours exposure to quasi-static gas Ar–50$_{vol}$%H_2O between 600°C and 650°C. Haematite formation is mainly observed with steam formed from non-de-oxygenated water [36]. The outer oxide's growth kinetics are driven by the outward diffusion of iron through the oxide scales [29]. The fast diffusion of the iron ions in the outer magnetite scale leads to the formation of iron vacancies when the iron supply from the bulk material is restricted by the inner oxide layer which possesses a lower iron diffusivity [37]. Throughout the oxidation process, these vacancies have been reported to coalesce into voids and then gaps. The gap formation contributes to the decrease of the iron ions transport through the outer layer. The weakening of the iron ion transport could be the reason for the appearance of haematite at the interface gas/outer scale during long term steam oxidation [37]. It has also been reported that the pores observed in the magnetite oxide act like short circuits for the diffusion of water and oxygen. Thus porosity could be a contributing factor to the increase of the oxidation rate [37,38]. The porosity could also emerge from the possible volatilisation of iron as $Fe(OH)_2$. This reaction can explain why the outer oxide layer still grow even with a large amount of pores in the scale as these can act like diffusion paths for the volatile iron hydroxide [25]. This compound is formed when the Fe reacts with H_2O and this reaction facilitates the oxygen transfer within the scales [25]. The absence of chromium in the outer oxide scale and the high porosity of the scale do not allow this oxide layer to play a protective role against steam oxidation.

The inner, more protective, layer is composed of a mix of magnetite and Fe-Cr spinel oxide. The Fe and Cr contents in the layer are not homogeneous; there are some Fe-rich and Cr-rich areas. The Fe-Cr spinel forms small equiaxed grains with fine pores (Figure 2-22). Bischoff and Motta [29] have observed the Cr-rich phases are located near the inner/diffusion layer interface (Figure 2-23), whereas the Fe-rich phases are present near the inner/outer layers interface. The growth kinetic of this oxide layer is also linked with the outward transport of iron, but the inward transport of oxygen plays a more important role in the growth of this oxide layer [29]. Thus this layer plays an important role for the protection of the bulk material. Indeed, the diffusion coefficient

of iron ions in the Fe-Cr spinel oxide is lower than in the Fe-rich phases. This phenomenon results in a decrease of the metal consumption rate. It is because, in this inner layer, the oxide growth limitation is mainly caused by limitations in iron transport [29]. The chromium content in the inner scale depends on the diffusion coefficient of the different oxidizing species. The inner layer shows some porosity due to the difference of oxide structures between $FeCr_2O_4$, which has a spinel structure, and Fe_3O_4, with an inverse spinel structure [29,42]. Porosity is also due to the presence of chromia at the early stages of oxidation, which reduces significantly the diffusion of Fe ions and thus leads to the creation of pores in the inner layers (Figure 2-23) [29]. These pores are then located in the inner layer due to the advancement of this layer in the metal. Limitation of chromium availability leads to the apparition of FeO [25].

Finally, an internal oxidation layer also called diffusion layer is observed between the inner oxide layer and the bulk material. Grain boundaries were observed to be oxidized first as they are shortcuts for oxygen diffusion towards the bulk material. The structure of the internal oxidation zone is complex due to the precipitation of different oxides (Cr_2O_3 and $FeCr_2O_4$) and the presence of matrix grains (Figure 2-23). The chromia is formed at the oxide/bulk material interface. This localized precipitation may be explained by the oxidation of the chromium carbide $Cr_{23}C_6$ initially present at the grain boundaries. Chromium depleted zones are also observed in the bulk material, near the oxidation zones, as a result of the outward diffusion of chromium to form the chromia layer. The chromia layer formation increases the corrosion resistance of the material [29,30,37,38].

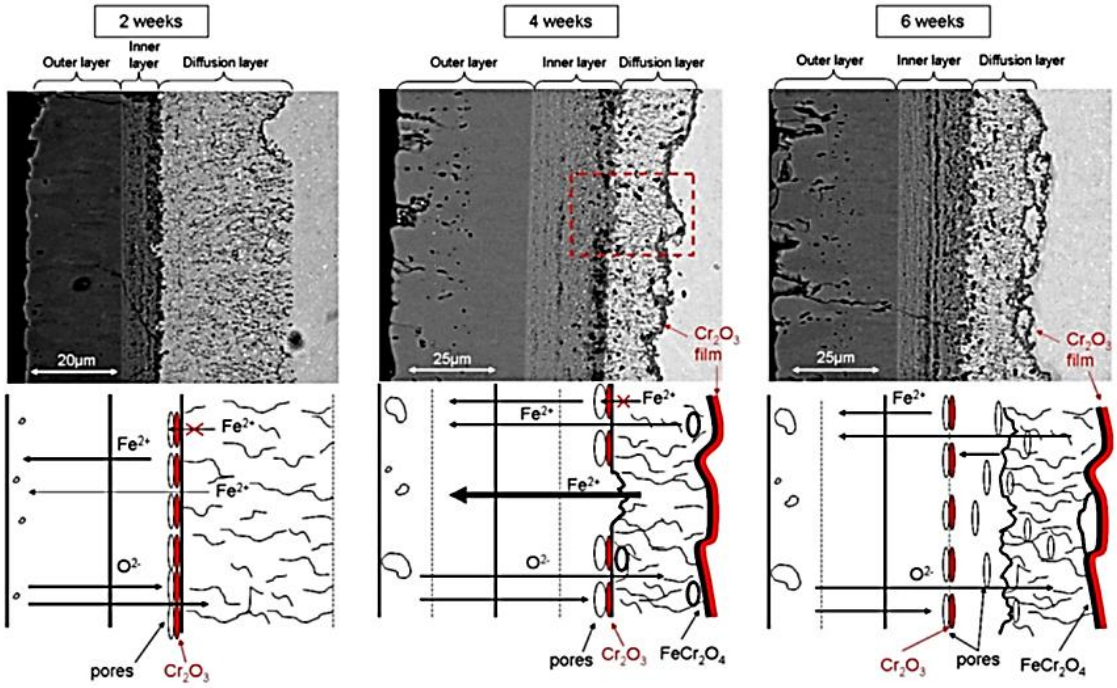

Figure 2-23: Cross-sections and schematics of 9Cr ODS (Oxide dispersion strengthened) steel oxidized in supercritical water at 600°C for 2, 4, and 6 weeks [29]**.**

It has been determined by marker experiments that the initial metal interface is located at the inner/outer scales' interface during steam oxidation of 9Cr ODS steel at 600°C [29]. This experiment also revealed that iron diffuses outwards and oxygen diffuses inwards. The outer scale growth kinetic is determined by the reaction at the gas/oxide interface and by the outward diffusion of iron ions through the oxide scales. The inner scale growth is driven by the inward diffusion of oxygen develops into the internal oxidation zone when the oxygen potential is high enough to form Cr-rich oxides.

The ferritic steels with up to 2.25% Cr follow a parabolic rate for the first 8-10 khr of steam exposure at a temperature bellow 580°C. Then, because of the exfoliation of the oxide layers, the oxidation rate is reported to become linear [24]. It has been observed that the oxidation rate does not necessarily increase with increasing temperature [30]. Indeed, at high temperature, the diffusion of chromium and silica can be higher and potentially allowing the formation of a more protective scale. This phenomenon, also reported by Young and Zurek [30], is representative of an oxidation rate controlled by solid diffusion in the oxide. Different criteria for the formation and the

maintaining of the protective chromia scale can be deducted from the Wagner's analysis. These criteria are dependent on the temperature [30].

The steam oxidation behaviour of 9-12% Cr steels in the temperature range of 550-650°C does not follow a common increase of the oxidation rate with increasing temperature [43]. The kinetics inversion observed is due to two concurring processes linked with the temperature increase: the enhanced scale diffusion processes affecting surface reaction kinetics and the enhanced Cr incorporation on the scale. These respectively increased and decreased the steam oxidation rate. The exact temperature dependence depends on the alloying elements, which affects the scale composition.

With increasing steam exposure time, the thickness of the oxide scales increases, leading to a stress increase. Moreover the inner and outer oxide layers possess different thermal expansion coefficient due to their difference in composition resulting in the creation of a weak interface between these two oxide layers. When the scale thickness or the number of defects becomes too important, or when high temperature variations occur, spallation of the oxide scale occurs (Figure 2-24) [37,38].

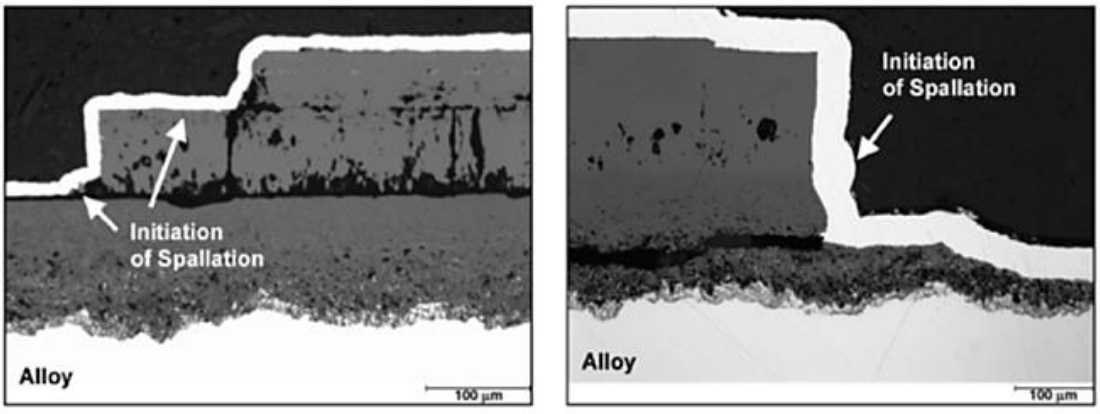

Figure 2-24: Images of oxide scale spallation of 10Cr-Mo-W steel oxidized in Ar-50%H_2O for 10,000 hours at 625 and 650°C [37]**.**

When spallation happens, the exact oxide regrowth rate, which is often assumed to be parabolic, depends on the oxide remaining at the surface of the material. Usually,

the overall oxidation rate is increased when the spallation process is triggered [24]. Ennis et al. [41] expresses that spallation can occur either at the inner-outer scale interface or oxide-alloy interface. In the case of spallation occurring at the interface between the two oxides, the oxidation process remains controlled by the iron transport in the inner spinel layer and internal oxidation zone. This oxidation rate is not changed by this kind of spallation. By contrast, spallation at the oxide-metal interface leads to an increase of the oxidation rate since the semi-protective spinel layer would have been, at least partially, removed. Since the region below the internal oxidation zone is depleted in Cr it is also more difficult to form new spinel and slow down the oxidation process again. It is reported that the buckling mode of exfoliation explains best the reason for oxide spallation, as it results from the elastic instability of thin oxides layers formed over large areas with interfacial defects [38].

2.3.2.2. Austenitic steels

Austenitic steels can be characterized by their chromium and nickel content. However, for this class of materials, their composition is not the only parameter significantly affecting the steam oxidation process, as surface preparation and grain size are observed to play a crucial role in the oxidation process [12,36,44,45].

The early stage of the steam oxidation process for austenitic steels is characterized by the formation of a protective chromia layer at the surface. The ability to form a long lasting protective chromia layer depends on the material composition and on its ability to supply chromium to the reactive interface [46]. Tuurna et al. [12] underlined the visible influence of surface finish regarding steam oxidation resistance. The rapid formation of the chromia layer depended more on the number of grain boundaries close to the materials' surface than the amount of chromium present in the bulk material. The manufacturing of fine grains materials, obtained after recrystallization by cold drawing process [47], and cold working of the surface, were solutions to produce materials with a large number of grain boundaries near the surface. Shot-peening the surface of austenitic material constitutes another solution to increase the number of

defects and dislocations near the surface of the material, allowing a higher average chromium diffusion rate towards the surface. This enhances the rapid formation of a protective chromia layer and improves the steam oxidation resistance of the material [48] as the large number of grain boundaries act as short circuit paths for chromium diffusion. Abe et al. [47] observed the enhanced formation of a chromia layer on a fine grained microstructure at the early stages of the oxidation process which increase the oxidation resistance of the tested samples. They also reported that the mechanical deformation due to cold working was diminished by annealing during the early stages of steam oxidation.

With increasing oxidation time, nodular iron-rich oxides appear as a consequence of the breakdown of the protective chromia oxide [46,47]. The nodules appearance is accompanied by a substantial increase in the mass change oxidation rate. The reason for the protective layer's breakdown is its extensive formation which create a chromium depleted zone in the metal underneath the oxide thus increasing the iron concentration which reacts with O_2 diffusing towards the bulk of the material [23,28,48,49]. The oxidizing species form by the steam dissociation can also react with the chromium present in the protective oxide layer to form volatile chromium-hydroxide and leading to the weakening of this layer [46,50].

Iron-rich nodules are forming until they cover the entire sample's surface resulting in the formation of a complex multi-layered oxide scale, of dimensions depending on the temperature and exposure time, generally composed of an iron-rich outer scale and a chromium-rich inner scale.

Lyta et al. [51] studied the oxidation of a Fe-20Cr-30Ni-2Nb (at%) austenitic steel at 800°C. They described the oxide morphology formed after ≈1.5 hours as an outer magnetite oxide layer with an inner layer composed of internal oxidation zone with a discontinuous chromia layer. Some Fe-Ni particles have been observed in the outer magnetite scale and the internal oxidation continues until the internal oxidation zone transforms into an inner oxide layer rich in chromium with chromia at the bulk material interface. After the transformation of the internal oxidation zone happening after 5 hours of exposure, there is a transition from internal to external oxidation. The inner scale is composed of a mixture of $(Fe,Cr)_3O_4$ spinel and nickel-iron compounds. Some

niobium is also detected at the chromia-metal interface. The chromium depletion in the substrate below the chromia layer is observed at longer exposure time, around 50 hours. The chromia growth rate is calculated to be parabolic. The inner and outer scales exhibit a parabolic behaviour at the early stages of steam oxidation and then the rate decreases due to the formation of the continuous and protective chromia layer. Consistent with other studies [28,46,52] indicating the chromia layer is formed initially but only lasted a few hours before the apparition of outer iron oxides. Mu et al. [46] reported that the iron oxides and the chromia grow more rapidly in a steam environment than in air.

For Sanicro 25 [53], below 700°C, only a thin chromia layer is observed after 3000 hours of steam exposure, but at 750°C, after 3000 hours, an inner chromium-rich oxide is observed with an outer magnetite layer with some hematite on the top of the scale.

In general, after breakaway oxidation when a multi-layered oxide forms at the samples' surface, the outer scale is composed of magnetite with a large number of defects and some iron-nickel compounds are also detected. After long term oxidation, hematite forms at the top of the outer scale [46]. This outer layer presents a high tendency to spall. In case of shot blasted material, spallation has been observed just before 34 khours [48]. After spallation, the new growing oxide is reported to be similar to the one growing on 9-12% ferritic steels. This change of oxide composition could be a result of the chromium depletion zone near the initial oxide-metal surface [54]. Indeed, the shot blasting treatment has improved the chromium diffusivity towards the surface of the material in order to form a protective chromium oxide this induce the formation of a chromium depletion zone. At 800°C, Fe_3O_4 is observed at the steam-metal interface and the size of the grains is larger with increasing oxidation time [51]. Zurek [53] also mentioned a chromium content decrease, below $10\%_{at}$, under the oxide-steel interface due to the formation of the protective chromia layer. A slight enrichment of copper and tungsten is signalised as well in this area.

The inner oxide appears after the transformation of the internal oxidation zone into inner oxide and its growth is then stopped by the formation of a chromia layer at the metal interface [51]. The inner oxide layer is composed of (Fe-Cr-Ni oxide) chromium-rich oxide in the bulk of oxidized grains and chromium-rich oxide in at the former grain

boundaries. For Sanicro 25, an austenitic steel with a high chromium and nickel content, Zurek [53] reported that below 700°C the inner oxide could only be composed of chromia. As a general observation, the formation of chromium-rich oxide at the grain boundaries generates a drop in chromium content in the bulk material near the formed oxide. [46] The inner layer is composed of a mixture chromium-rich oxide precipitates in an iron–chromium oxide matrix.

Jianmin and Montgomery [28,52] have tried to describe in 4 steps the oxide morphology development of TP347HFG during steam oxidation. The early stage of oxidation is described by the development of a thin chromium-rich layer into an inner iron-chromium oxide and outer iron oxide. It has also been reported the formation of Cr-Mn-Fe oxide at the surface of the material at temperature above 620°C. This protective oxide then breaks down with long exposure time, probably due to evaporation of chromium as chromium hydroxide [28].

The inner oxide expands itself inwardly through grain bulks, oxidizing them and forming a chromium-rich Fe-Cr-Ni oxide. This phenomenon continues until the oxidation front reached a grain boundary. As grain bulks are being oxidized, a Fe-Ni oxide is also formed in the outer scale.

The third stage of the oxidation process consists of the formation of a chromium-rich oxide at the grain boundaries near in internal oxidation front. This oxide acts like a protective layer and slows down the oxidation rate. This oxide is either composed of $FeCr_2O_4$ or Cr_2O_3 depending on the chromium content of the material. The protectiveness of this layer is increased by its chromium content. It has been observed that both an increase in pressure and temperature enhances the formation of a better protective layer.

The last stage of morphology development during steam oxidation corresponds to the weakening of the protective chromium-rich layer due to inward oxygen diffusion. The breakdown of the protective layer occasions the propagation of the inner oxide to other grains until the oxidation front reaches another grain boundary. The breakdown of the chromium-rich layer is linked with an increase of the oxidation rate. The different steps of morphology development proposed by Jianmin et al. are presented in Figure 2-25.

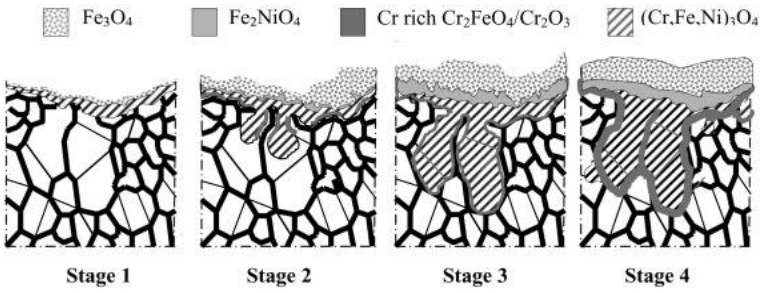

Figure 2-25 : Schematic of the oxide growth for TP347HFG [28]**.**

The kinetic of steam oxidation for this class of material appear to be parabolic but a large data scatter is observed due to spallation of the oxide layers. Because of the spallation, it is difficult to link the mass gain with the thickness growth [36].

Mu et al. [46] have investigated the hydrogen permeation of austenitic steel and it has been proven that there is a direct link between the hydrogen permeation and the oxide thickness. Moreover, hydrogen contributes to the formation of cracks and voids in the oxide scales.

Sabau et al. [55] have pointed out the limitation of mechanistic understanding of oxide growth, scale morphology evolution and spallation of this class of materials. Further investigations are also needed to understand if the iron can be transported as iron-hydroxides and-or Fe-Cr in steam. [46] This study also pointed out the need for further study of the improvement resistance of chromia forming austenitic steels. Zurek et al. [53] also reported a lack of information regarding the long term oxidation process and the microstructural changes of the material at the steam-steel interface.

2.3.2.3. Nickel-base alloys

The steam oxidation of nickel-base alloys is reported to be mostly dependent on the composition of the material. The lower the iron content, the higher the oxidation resistance. The chromium content also plays an important role in the steam oxidation resistance of this class of material but is not as critical as the iron content. Surface finish affects differently the oxidation nickel-base alloys compared to the other classes of materials studied in this project. It appears that, even if cold working the surface of

the material is reported to increase the chromia rate growth, it mainly influences the morphology of internal precipitates forming during the oxidation process [8].

The oxidation of nickel-base alloys generally consists of the appearance of external chromia and internal alumina. At low oxygen partial pressure, Ni-base alloys form a protective chromia scale and exhibit low oxidation rates [56]. At high oxygen partial pressure pressures, nickel oxide can form at the material's surface [56] and the steam oxidation can cause an increase of hydrogen injected in the alloy or increase the solid state diffusion within the oxide scale. This phenomenon increases oxygen permeability and thus lowers the ability of the alloy to form a protective chromia scale [8].

The formation of a chromium-rich oxide layer is accompanied with a chromium depletion in the bulk material near the oxide layer. Thus, if spallation occurs, the ability of the material to form a new chromia layer is lowered. The formation of internal alumina and rutile contribute to lowering the oxides growth rate [2].

The study of nickel base alloys IN617 and IN625 by Gordon et al. [57] reports that alumina and voids are formed at the same time in the scales. IN617 exhibits a nickel enrichment bellow the scale. The inner and outer regions of the formed oxides show different microstructure. The inner scale is composed of fine oxide grains with micro-pores whereas large columnar grains without pores are observed in the outer scale. The apparition of a duplex scale microstructure is due to concurrent diffusion phenomena which are the outward diffusion of cations and the inward diffusion of oxygen and hydroxyl ions. The closer to the alloy-scale interface, the larger the pores are. At the boundary, voids coalesce and their size depends on the surrounding alumina. These voids are observed after 100 hours when the alloy is exposed to a 750°C steam. Alumina filaments are often observed crossing the voids regions. Alumina forms the grain boundaries in the inner scale and this causes short circuits for the diffusion resulting in the condensation of the voids along alumina. Inner scale growth in the voids region is observed for IN625. In this case, chromia is present at the inner boundary of the voids. The outer scale also dissociates to form voids in the lower region of the scale [57].

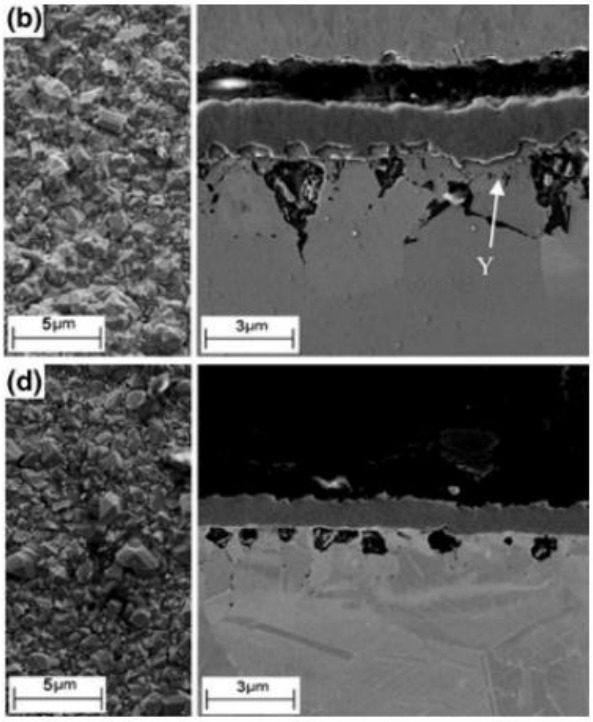

Figure 2-26: SEM images of the oxidized surface and cross-section of Alloy 617 and Alloy625 exposed to steam at 750°C and 1 atmosphere for 2000 hours [57]**.**

Ni-base alloys, such as IN740, exhibit a good microstructural stability which provides a high creep resistance which makes it suitable to be used under advanced ultra-supercritical conditions [58].

The emergence and growth of nucleated carbides in grains boundaries have been observed. The formation of inter-granular carbides is linked with the apparition of grain boundary cavities. All these phenomena cause inter-granular failures leading to possible creep-rupture failure of the material. The apparition of the Ƞ-phase (undesirable hcp Ni_3Ti) incompatible with the original metal matrix lowers the creep resistance of the material. Usually IN740 sees the apparition of the Ƴ' phase ($L1_2$ $Ni_3(Al,Ti)$) in the metal matrix which strengthens the material. But the Ƞ-phase growth instead of the Ƴ' phase near the grain boundaries results in the weakening of the grain boundaries areas [58].

[59] Chevalier et al. have studied the high temperature oxidation of pure nickel and the oxygen transport occurring during the oxidation process. Oxygen isotopes have been used to study the oxygen transport into the oxide scales and determine its diffusion

coefficient in the bulk and at the grain boundaries. Although the material studied in this paper is different from the ones studied in this project, it provides some useful information regarding the possible behaviour of oxygen in a nickel-based alloy. The paper states below 800°C the diffusion of oxygen is lower than nickel diffusion in NiO grain boundaries, thus the oxidation process leads to the formation of nickel oxide at the surface of the material. Above 800°C, O_2 diffuses via micro-cracks resulting in the apparition of a duplex oxide. The oxidation kinetics was reported parabolic until 800 C and its deviation from this rate characterizes the fact that the diffusion of species through the scale is not the determining step of oxide growth anymore.

2.3.2.4. Surface finish

Numerous types of surface finished have been used on different types of heat exchanger materials to study their effect regarding steam oxidation. A distinction can be made between surface finishes affecting the grain size and morphology of the material (heat treatments producing fine grain materials) and the ones introducing near-surface deformation (cold deformation and surface working: grinding, polishing, shot-peening, sand-blasting, machining).

Grain refinement was mentioned as a key parameter for enhancing chromium supply towards material's surface during steam oxidation. Grabke et al. [44] reported a more rapid chromium supply at the material surface for fine-grained ferritic and austenitic steels (Figure 2-27).

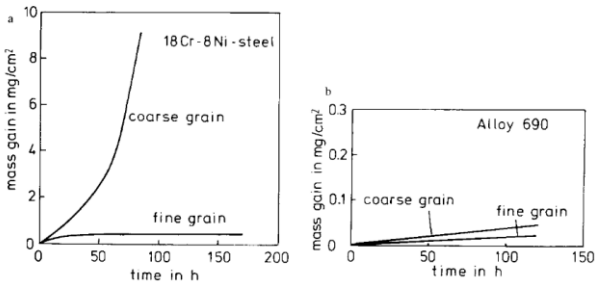

Figure 2-27: Mass change data for various materials with different grain size exposed to wet gas at 600°C [44]**.**

Surface working the materials emerged from the need to enhance chromium diffusion towards the surface of the material in order to quickly form a uniform and protective chromia layer at the early stages of steam oxidation [24,44,45,60,61]. Cold working the surface of a material generates surface deformation such as dislocations and cracks. Cold working processes most commonly studied are: grinding, polishing and shot-peening. Tuurna et al. [12] indicated more adherent and protective oxides can be observed on surfaces with strong cold working such as shot-peening (Figure 2-28), than on ground or polished surfaces.

The effect of shot-peening for ferritic steels has been investigated [13,62]. Haruyama et al. [13] reported that a protective chromia layer was formed after shot-peening the surface of ferritic steels and performing an air pre-treatment of the surface. The shot-peening process alone was not able to enhance the formation of the chromia layer. The more refine the shot-peening, the more protective the chromia layer and the chromium content at the surface can be locally increased by shot-peening with abrasive chromium shots instead of cast steel. The surface working performed had a huge impact upon the ability of the material to form a protective chromia scale. This protective scale was stable during the oxidation test in steam at 700°C and for 1000 hours. at longer exposure times, the breakdown of the chromia layer was detected and was responsible for the nodular growth of iron oxides [13].

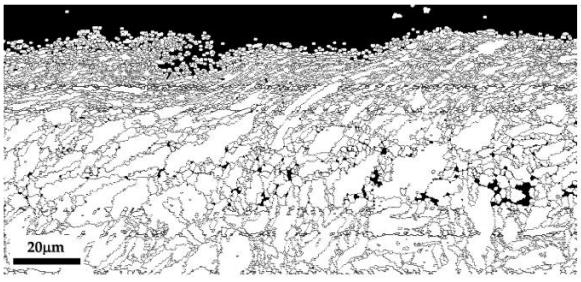

Figure 2-28: EBSD image of a shot-peened surface of NF616 steel [62]**.**

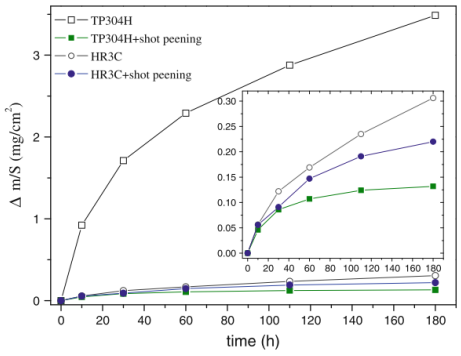

Figure 2-29: Mass change data for various austenitic steels with different surface finished exposed to steam at 650°C [63]**.**

Ren et al. [62] examined the steam oxidation process upon a shot-peened surface finish compared to an as-received surface finish. For both surface finishes a duplex

oxide layer was reported. It consisted of an outer Fe-rich layer associated with Cr-rich in the inner layer. Nevertheless, for the shot-peened sample a slightly less mass gain was monitored. Regarding species repartition in the material, chromium enrichment was detected in the inner oxide layer and in the bulk area surrounding it and was localised at grain boundaries because they act like quick diffusion paths. For the shot-peened samples, the chromium repartition was more uniform in the oxide layer and no enrichment zone was observed in the shot-peened area.

Regarding austenitic steels, Tuurna at al. [12] declared cold working the surface of the materials showed a clear influence on the early stages of the steam oxidation process, up to 1000 hours. High stress cold working, such as shot-peening, allows the formation of more adherent and thinner chromium-rich oxides than with a grinding or polishing process where a duplex oxide layer is formed [63,64]. For the ground surfaces, a nodular iron-rich oxide growth was observed and seemed to be more spread out with increasing temperatures and exposure times. The iron-rich oxide was characterized as porous and with a rapid growth kinetic. On the contrary, shot-peened surfaces exhibited a thin chromium-rich oxide layer due to faster chromium diffusion to the specimen surface achieved by the addition of diffusion paths. Eventually, it has been demonstrated that the surface finish can have a larger influence on the early stages of the steam oxidation process than the material composition [12,63].Higher peening intensity brings more surface roughness and defects enhancing an increase in Cr diffusion and thus the early formation of chromia contributing in the reduction of Fe oxide apparition [65]. Shot-peened austenitic steels TP304H exhibits a Cr-rich oxide scale after 65 hours of exposure between 650 and 770°C whereas a multilayer scale with outer iron oxide and inner iron-chromium oxide was produced on the same material without cold working. The shot-peening process showed the most significant effect at 730°C [65]. The high energy surface region formed by cold working contributes to an acceleration of the Cr diffusion allowing the formation of a Cr-rich oxide at the early stage of the oxidation[63,65,66]. This formed oxide plays a protective role again further oxidation. In the case of TP304H steel, the plastic deformation due to shot-peening results in the apparition of a martensitic phase at the surface of the material. This phase is BCC, with higher Cr diffusion properties comparing to the FCC structure of the austenitic phase [63].

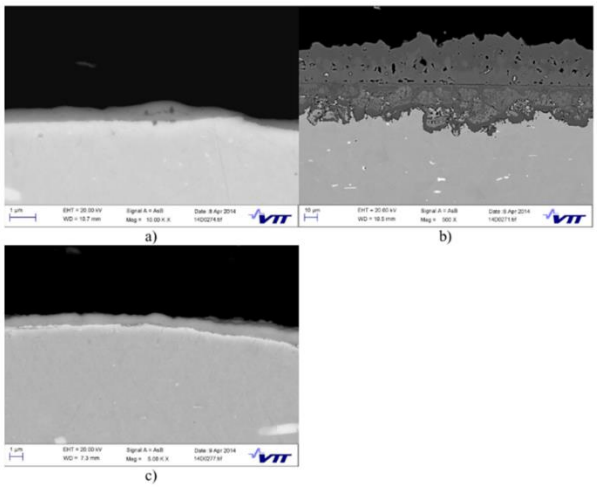

Figure 2-30: Microscope images of oxide scales formed on (a) the milled surface, (b) the polished surface, and (c) the shot-peened surface of TP347HFG after 1000 hours of steam exposure at 675°C [12]**.**

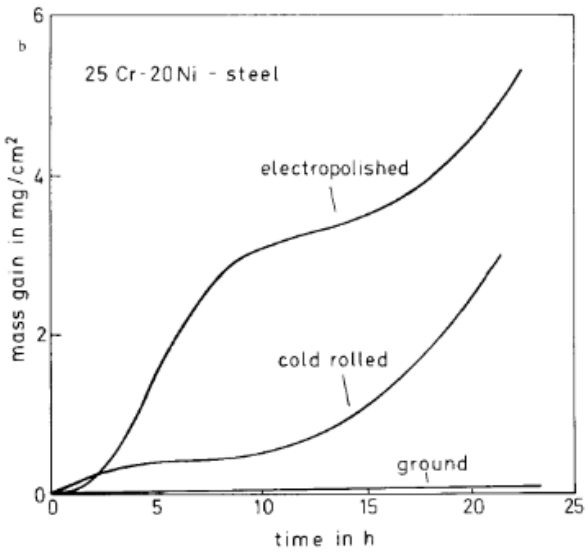

Figure 2-31: Mass change data for an austenitic steel with different surface finishes exposed to wet gas at 600°C [44]**.**

The formed chromia layer reduces the iron outward diffusion and therefore the amount of iron oxide prone to spallation [66].

Even if the increase in temperature contributes to the formation of a more protective chromia layer, shot-peening is shown to be of importance of the formation of protective chromium-rich oxides at temperatures below 700°C and at short times. With long time exposure the dislocations could disappear by recovery or recrystallization [67,68]. Thus grain boundary and bulk diffusion become the main transport mechanism which lead to the apparition of iron-rich nodules. The nodule formation is controlled by the outward diffusion of iron and inward diffusion of oxygen [44].

Steam oxidation of cold worked nickel-based materials has been studied by Cruchley et al. [69]. Shot-peened and 6µm polished RR1000 have been exposed to air oxidation between 700 and 800°C up to 8000 hours. For both surface finishes, chromia (Cr_2O_3) and rutile (TiO_2) oxides were formed in the outer layer. A Ƴ'denuded zone was detected ahead of the internal oxidation zone and alumina was present in the sub-surface. Ti-Ta-rich phases were also observed under the external oxide scale. The surface finish mainly influenced the morphology of the internal oxide precipitates.

Polished samples showed more oxidation localised at grain boundaries than in the grain itself. Moreover, alumina was found in the inter-granular and intra-granular areas whereas for shot-peened samples alumina formation is more uniform and predominant at the grain boundaries of recrystallized grains near the surface. For shot-peened samples, the oxidation depth was more uniform and was associated with the grain boundaries of small recrystallized grains.

Moreover, at 700-750°C, the rate of chromia growth is reported to be higher for shot-peened samples than for polished samples. [69,70]

After oxidation, chromium depletion was observed in and beyond the Y' denuded zone in the polished material whereas the chromium concentration is enhanced in the Y' depleted zone for the shot-peened sample.

2.3.2.5. Heat flux

In real life exposures, the super-heater and re-heater tubes are exposed to hot gas coming from fuel combustion in contact with their outer surface and steam is present in the inside. Steam is considered a cold source since the heat exchangers aim to heat the steam. As a result of the heat exchange process, a heat flux is exchanged through the tube material leading to the apparition of a thermal gradient through the tube section. In use, some oxides appear at both the steam side and the fire side of the tube and affect the heat flux and the temperature of the different parts of the super-heat or re-heater as represented Figure 2-32.

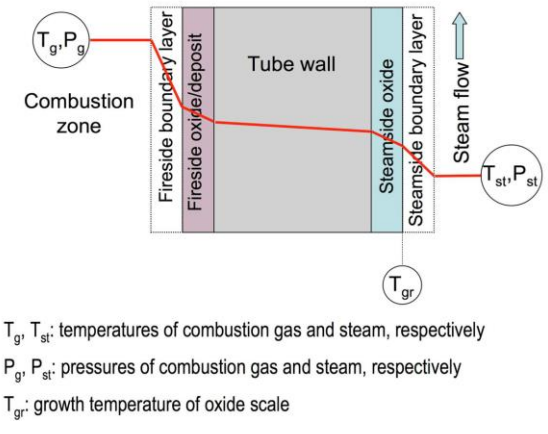

Figure 2-32 : Schematic representation of the thermal gradient through the wall of a steam tube [71]**.**

With the progressive oxide growth, a temperature increase inside the tube wall is recorded, increasing the oxide growth rate and so on. The presence of heat flux has a constant effect on the steam oxidation process.

In many studies [11,48], some differences are observed between field and laboratory data. One possible reason for the apparition of these differences could be due to the effect of heat flux involved during real life exposure. Most of the laboratory tests are performed under isothermal conditions whereas this is not the case with industrial conditions. A few comparison studies of steam oxidation with and without heat flux have been undertaken [10], nevertheless the observed effects of heat flux are characterized by an increased porosity in the oxide scales and more exfoliation. Viswanathan [10] reports that the field data recorded deviated from the parabolic behaviour observed during laboratory exposure. Jianmin [28] also reported the presence of heat flux lead to an increase of oxide pit 'size. Moreover, the oxidation kinetics also differed since the oxidation rate (in term of oxide pit depth) seemed to decrease with increasing temperature. The paper concluded that the specific effect of heat flux was unclear. Fry et al. [11] have observed that the presence of a thermal gradient across the tube wall significantly increases the oxidation kinetics. Moreover, some changes in the oxide morphology and more porosity in the oxide layers have been reported. The addition of a thermal gradient through the tube wall results of the apparition of an alternation between small and large grained oxides in the scales. The oxides created are also thicker and with different microstructures, like the one

observed with the in service materials. However, the mechanisms responsible for this effect remain unclear.

G.Holcomb [72] also reported that the presence of a thermal gradient through a tube wall can affect the O^{2-} gradient and the solubility of some species involved in the oxidation process such as nickel.

Adding heat flux as a parameter for studying steam oxidation could lead to a better understanding of the differences between the usual isothermal lab tests performed and the industrial observation of steam oxidation. Besides, tests with a thermal gradient are more realistic and aggressive, and produce more relevant oxide morphologies. [11]

2.3.2.6. Pressure

Pressure is considered to be one key parameter influencing high temperature steam oxidation along with the temperature, the material composition and the surface finish [10,23]. In terms of thermodynamics, a higher steam pressure means a higher oxygen partial pressure (Equation (2-21) which leads to a more reactive oxidation reaction as described in Equation (2-20). Another expected pressure effect concerns the solid state diffusion in the oxide scales [8,23] which is enhanced by an pressure increase. The link between the transport mechanism and the oxidation rate is given by the following equation [8] :

$$k_p \propto P^{\left(\frac{2}{3}\right)\left(\frac{b}{2a(\alpha+1)}\right)} \quad \textbf{(2-39)}$$

Where k_p is the parabolic oxidation rate [$(mg.cm^{-2})^2.h^{-1}$], *P* is the pressure [bars], a and b are respectively the metal and oxygen stoichiometry for an oxide, M_aO_b, and α is the effective charge of the metal vacancy in the oxide of interest (M_aO_b).

Pressure also affects the thermal gradient across the heat exchanger tube and the levels of stresses along the tubes [23,34].

After performing some high temperature steam oxidation tests using different steam pressures it appears that an increase of pressure only results in a slight and marginal increase of the oxidation rate [10,35]. The main effects observable were that at the lower pressure, the initiation of breakaway was delayed, and at the higher pressure more voids and cavities were formed in the oxide scales [10,23,35,73]. Ehler et al. [25] provide a link between pressure and void formation. Their work explains that porosity inside the oxide layers can be formed due to the production of volatile hydroxides such as $Fe(OH)_2$. This compound also contributes to the outward migration of iron (Figure 2-33) thus increasing the oxidation rate since the transport mechanisms are considered the rate limiting mechanism in Wagner's model [9,22,33].

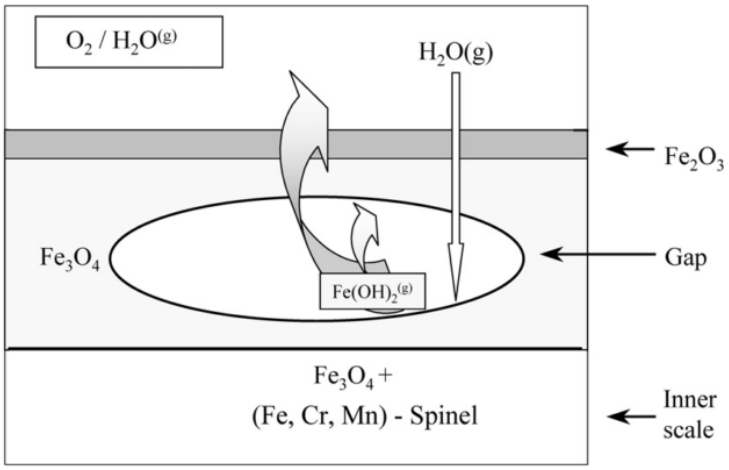

Figure 2-33: Schematic illustration of the possible mechanism for transport of iron towards the outer part of the oxide scale as the volatile hydroxide $Fe(OH)_2$ [25]**.**

However, other reports [23,28,52] show that increasing the steam pressure contributes to lower oxidation rates, which is in contradiction with what has been reported earlier. One reason for this beneficial effect of higher pressure was provided by Jianmin et al. [28,52] who observed the formation of a better protective chromia layer at higher pressure. It was suggested that due to the geometry of their experimental set up, an increase of pressure in the heat exchanger tubes leads to the thickening of the grain boundaries which enhances the diffusion of chromium towards the surface of the materials and thus creates a more protective chromia layer.

It needs to be kept in mind that most of the laboratory tests presented earlier have been performed with pressure levels significantly inferior to the operational pressures. In some cases steam is not the main gas used for the experiment but is used diluted in a gas carrier such as argon. This results in extremely low steam pressures and even lower oxygen partial pressures which causes the vapour dissociation to be rate controlling, as shown by Figure 2-12, instead of the transport mechanisms. As a result of the fact that at very high pressure the oxygen partial pressure does not vary much, some works [8,10] suggest that the increase of pressure between the old and new generations of power plant will not have a significant impact upon the steam oxidation process.

The complexity of performing high temperature steam exposure tests including the pressure parameter was presented in various reports [10,35] and doing laboratory tests closest from the operational conditions is extremely difficult. One would need a set up with flowing steam at high pressure and temperature this the presence of a heat flux. This is why in operating conditions steam pressure is observed to increase significantly the oxidation rate but that there is no clear trend reported from laboratory works.

The majorities of the studies point out a need for further investigations about the pressure effect on high temperature steam oxidation [10,24,28,35,52].

2.3.2.7. Breakaway oxidation and spallation

During the steam oxidation of the various classes of materials, presented in the precedent Sections ,a phenomenon known as breakaway oxidation happens which can either be caused by or induce spallation [10,23,30,74]. Breakaway oxidation is a term describing the enhancement of the oxidation rate due to the failure of samples' protective oxide [23,74]. Before breakaway, materials usually form a protective oxide layer, therefore the materials show slowing oxidation kinetics. However, with increasing oxidation time or changes in oxidation parameters, such as a change in temperature and pressure, nodules of less protective oxides form at the surface of the

material. This can lead to the breakdown of the initial protective oxide layer and is accompanied by an increase in oxidation kinetics [23]. Figure 2-34 illustrates the increasing oxidation kinetics accompanying breakaway oxidation. Indeed the sample with the cold rolled surface finish shows initially low oxidation kinetics, which increases significantly after 10 hours due to breakaway oxidation.

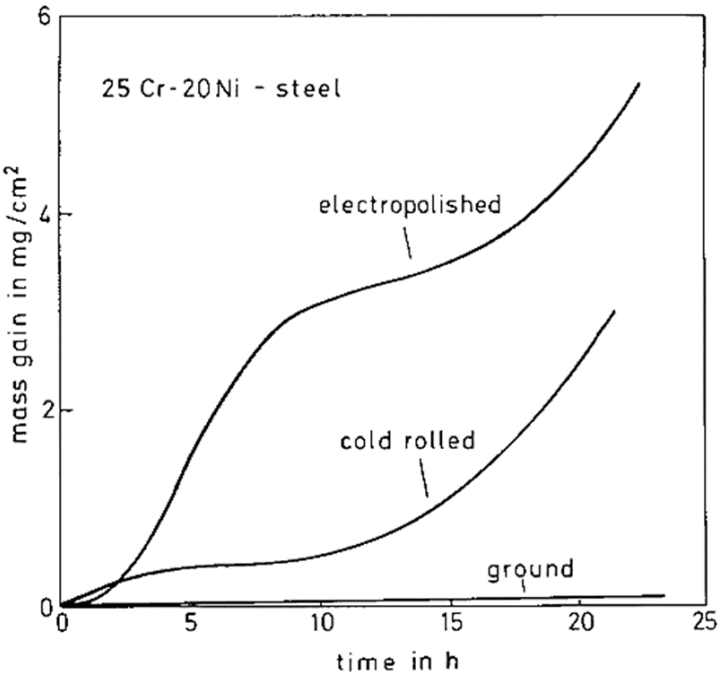

Figure 2-34: Thermogravimetric study of high temperature oxidation in a wet atmosphere of a 25Cr-20Ni austenitic steel with different surface finishes at 600°C [44].

Breakaway oxidation is caused by the mechanical [10,23] or chemical [23,30,74,75] failure of the protective oxide layer. Mechanical failure is due to crack formation across the protective oxide layer [10,23]. The cracks form preferential paths for chemical attack of the previously protected material underneath. Chemical failure arises from chromium volatilization degrading the protective chromia layer which in combination with chromium depletion underneath the surface of the material means chromium cannot be replaced. Chromium depletion is an issue because if oxygen is in contact with a material depleted of chromium, a crack appearing through the chromia layer then means the material would no longer be capable of forming more chromia and an iron-rich oxide would form instead [30,74,75].

Before breakaway, exfoliation is not a concern, but when breakaway is triggered, accompanied with an increase of the oxide thickness and with the formation of dual oxides at the surface of the oxidizing materials, exfoliation becomes a critical parameter of the steam oxidation process [23]. Oxide scale failure is cause by stresses building up in the oxide scales. Stresses originate for various reasons [9,22,27]:

- External stresses due to the component operation come from strain distribution around the heat exchanger tubes at the surface of which oxides are formed.
- The oxide growth leads to the apparition of intrinsic stresses due to the formation and development of oxides with different compositions, phases and molar volumes [23]. The multiple transport mechanisms occurring in the oxide scale, which are the inward diffusion of oxygen forming oxides at the metal interface and the outward diffusion of metallic cations forming oxides at the steam interface, contribute to the apparition of compressive stresses in the oxide layers (Figure 2-36). Pore and cracks forming in the oxide scales contribute to the formation of tensile stresses that can be described by mechanical models [76].
- The geometry of the inner surface of the heat exchanger tubes also causes a stress accumulation.
- Thermal stresses are triggered by changes in temperature due to the coefficients of thermal expansion (CTE) which are different for the base metal and the various oxides formed (Figure 2-35). Oxides with different phases show important differences in CTE [23,71,77].

All these stresses occur simultaneously in the oxide scale. They can be released by the formation of cracks and the plastic deformation of the oxide and metal substrate which eventually lead to spallation of the oxide scales (Figure 2-36).

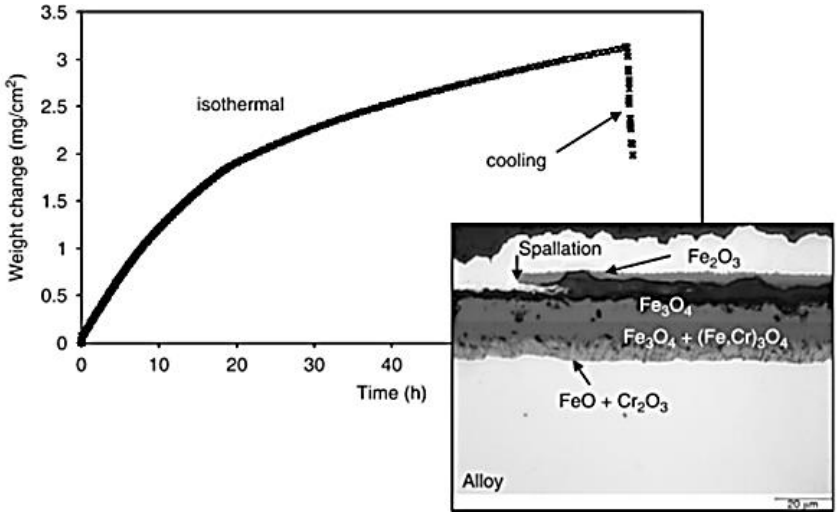

Figure 2-35: Mass change curve of a ferritic steel in a wet gas during isothermal exposure at 600°C and during cooling [37].

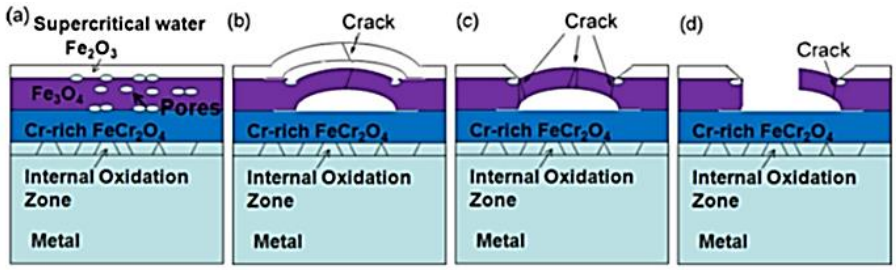

Figure 2-36: Schematic of exfoliation mechanism in presence of compressive stresses [38].

Oxide exfoliation can lead to different detrimental phenomena [23,77]. The loss of material could compromise the integrity of the tube since the remaining tube wall may not be thick enough to contain the high pressure present inside the heat exchangers. The detached oxides are abrasive and can be carried by the steam flow until the steam turbine where it can lead to the erosion of the turbine. Exfoliated oxides can accumulate in the heat exchangers tubes, typically at the bottom of a vertical loop, and cause a blockage decreasing the steam velocity at one location. Where the blockage appear, the convective coefficient is reduced and a temperature elevation happens increasing the oxidation rate and possibly leading to tube rupture due to the short term overheating of the tube where the oxide accumulation was. The flow restriction is considered the most severe phenomena caused by exfoliation of oxides, more

important than metal loss. The industry experienced and reported that blockage events happened in the first two years of operation with the use of austenitic steels as heat exchangers materials [16,55].

Sabau et al. [55] tried to develop a model describing spallation and blockage events associated. This model was based on quantitative description of certain aspects of steam oxidation such as oxide growth, scale morphologies and the identification of the exfoliated oxide's composition. These quantitative descriptions were incomplete due to limitation in mechanistic understanding especially concerning the development and growth of defects in the multi-layered oxide scales during steam exposure.

2.3.2.8. Summary

The multiple studies presented in the literature have focused on high temperature oxidation in the presence of steam, but there is a lack of studies dealing with experimental work with steam conditions similar to those used in power plants:

- Many studies [12,25,30,37,40,41,43,44,46,49,51,53,56,57] do not use steam-only atmospheres but use carrier gases or steam with oxygen at concentrations high than would be expected for equilibrium.
- The temperature and pressure ranges in the reported studies did not cover those associated with the Advanced Ultra-Supercritical conditions.
- The results reported were mainly associated with laboratory prepared surfaces, such as ground, polished and shot-peened surfaces, but there is no information regarding the actual as-received surface finish used in service.
- Studies report either long term oxidation tests with a single cycle [28,48,52] or short term and cyclic oxidation tests [30,37,43,47,64] but rarely both combined [53]. Long term cyclic oxidation tests are more of interest for the energy generation industry to understand the long term effect of the oxidation process.
- The effect of pressure is not clearly understood with opposite effects reported from the different studies (Section 2.3.2.6).

To address these gaps in knowledge about high temperature oxidation associated with the next generation of power plants, the tests reported in this thesis will use more adequate steam parameters and will allow relevant data regarding the steam oxidation process of various tubing materials to be collected. The temperatures, exposure times, steam chemistry and material's surface finishes will be selected so that the experimental work will produce extensive data. This data will fill gaps in knowledge regarding the high temperature steam oxidation process associated with Advanced Ultra-Supercritical conditions. The effect of pressure on the steam oxidation process will be assessed, however the pressure range accessible during this study remains far from the levels in real life power plants. Modelling the oxide growth for the different materials in terms of mass change and oxide thickness will be performed and will allow the quantification of spallation, which is of importance from an industrial point of view because it will allow the energy companies to predict when the heat exchanger tubes would fail, depending of the material's composition and steam conditions.

3. Experimental procedures

To tackle the remaining challenges to increase the understanding of the steam oxidation process (presented in Sections 1.3 and 2.3.2.8 dealing with the objectives and literature review) tests with different parameters have been designed. The decisions made take into account the experimental capabilities of the University and its partners in the Flex-E-Plant project as well as the objectives agreed at the beginning of the project.

3.1. Materials studied

Different materials potentially suitable to be used as heat exchanger tubes have been considered for this project. Ferritic, austenitic steels, and nickel-based alloys are three different classes of materials used in real life power plants. A minimum of one material from each class has been investigated to cover a large range of possible compositions.

The steam oxidation study of ferritic steels was performed through the study of the T 92 steel. A large collection of data already exists for this material [24,25,29,30,36–39,41,43], however not all the tests reported have been performed in a “steam only” atmosphere and it is important to gather some information allowing the calculation of oxide kinetics in a steam only atmosphere.

A large number of austenitic steels have been developed and can be used in coal power plants. Austenitic steels cover a wide range of alloy composition, so to understand how the alloy composition affects the high temperature oxidation process four different austenitic steels have been selected and exposed to high temperature steam:

- 2 low chromium and nickel content austenitic steels:
    - TP347HFG
    - Super304H
- 2 high chromium and nickel content austenitic steels:

- Sanicro 25
- HR3C

Finally, 3 nickel-based alloys have been considered and were selected due to their high temperature creep resistance:

- Alloy 263
- Alloy 617
- Alloy 740

Compositions of the different materials studied are shown in Table 3-1. Although all of the materials presented in Table 3-1 have been exposed to high temperature steam, austenitic steels Super304H and HR3C have not been investigated in detail and are not presented in this study. The choice to not investigate these materials was driven by the fact that their oxidation behaviours when in high temperature steam are close to those of TP347HFG and Sanicro 25 respectively. If a specific interest for those two materials arise in the future, the University already possesses steam exposed samples and will be able to rapidly acquire data about those samples.

Table 3-1: Alloy composition (red: ferritic steels, blue: austenitic steels, green: nickel-based alloys).

Alloy	Elemental composition (weight%)											
	Fe	Ni	Cr	Co	Mo	C	Si	Mn	Ti	Nb	Cu	W
T 92	Bal	0.4	9.5	-	0.6	0.1	0.5	0.6	-	0.1	-	2.0
TP347HFG	Bal	11.5	18.4	-	-	0.1	0.4	1.5	-	-	-	-
Super304H	Bal	8.8	18.4	-	-	0.1	0.2	0.8	-	-	3.0	-
Sanicro 25	Bal	25.0	22.5	1.5	-	0.1	0.2	0.5	-	0.5	3.0	3.6
HR3C	Bal	19.8	24.9	-	-	0.1	0.4	1.2	-	-	-	-
Alloy 263	0.7	Bal	21.0	21.0	6.1	0.1	0.4	0.6	2.4	-	0.2	-
Alloy 617	3.0	Bal	24.0	15.0	0.0	0.2	1.0	1.0	0.6	-	0.5	-
Alloy 740	0.7	Bal	25.0	20.0	0.5	0.0	0.5	0.3	1.8	2.0	-	-

3.2. Pre-exposure preparation

The different materials selected were only available in different geometries.For the austenitic steels, samples were cut from tubes (Figure 3-1 (b)) while for the ferritic steel and nickel-based alloys, samples had a cotton reel geometry (Figure 3-1 (a)). The various surfaces of the different samples were prepared to have a number of different surface finishes (Figure 3-1) as specified in the test matrixes presented in Table 3-3 and Table 3-5.

The different surface finishes applied were:

- As-received
- P1200 Ground: P1200 (European standard equivalent to 600 grit UK/USA standard [78])
- P2500 Ground: P2500 (European standard equivalent to 1000 grit UK/USA standard [78])
- Machined
- Shot-peened (SANYO and PISCO)

The as-received surface finish represents the surface commonly used by the industry, and results from the hot extrusion and pickling processes used in the manufacturing of the heat exchanger tubes when no other surface finish has been performed. The as-received surface is then located exclusively in the concave surface of the tube, which means, after the sample preparation, the as-received surface is present on one surface only. Therefore, it is not possible to obtain a sample with as-received surface finish upon each of its faces.

P1200 and P2500 ground surfaces were applied, using SiC grinding paper, on the convex and cut surfaces of the samples cut from tubes, as well as on all the surfaces of the samples cut on reel (Figure 3-1).

Machined surfaces were mechanically performed on the concave surfaces of the samples cut from tubes to try to replicate a P1200 ground surface finish, which could not be applied on this particular surface using SiC grinding paper.

Samples with shot-peened surfaces have been delivered by partners of the project. Two different shot-peening techniques were used, named SANYO and PISCO, and applied to the concave surfaces of some samples.

Before exposure, the samples were cleaned, to avoid surface contamination, and measured, to calculate the sample surface area and to form a baseline against which to measure any change in shape.

The cleaning process was composed of multiple steps:

1. Flushing samples with acetone
2. Cleaning samples in ultrasonic bath with acetone for 15 minutes
3. Flushing samples with cleaned acetone
4. Flushing samples with isopropanol
5. Cleaning samples in ultrasonic bath with isopropanol for 15 minutes
6. Flushing samples with cleaned isopropanol
7. Air drying of the samples

The specimens were then measured at the specific locations shown in Figure 3-1. Three reading were taken of each dimension to minimize the measurement error. After being measured the samples were weighed for later use in obtaining mass change.

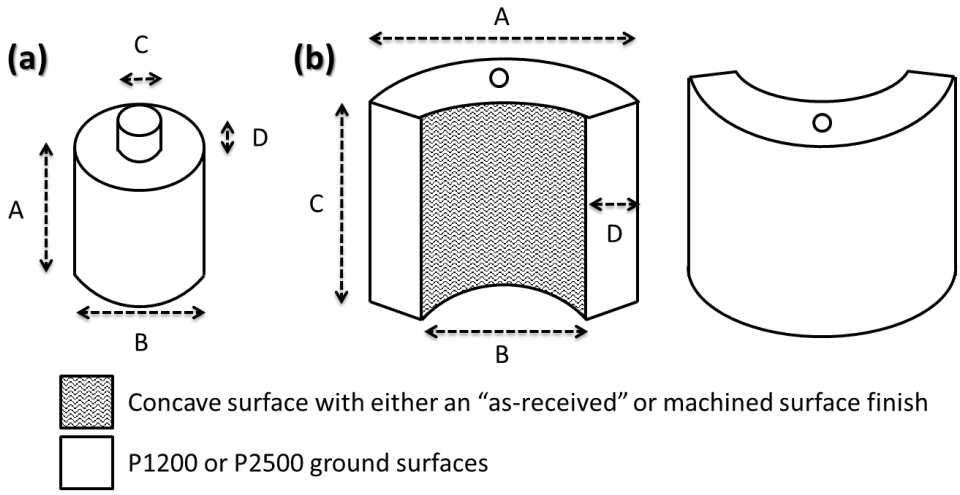

Figure 3-1: Schematic presenting the surface finishes used on the different samples' surfaces as well as the specific locations used for measuring the dimensions of the samples (a) shows the dimensions measured for cotton reels samples and (b) shows the dimensions measured for the samples cut from tubes.

3.3. Steam exposure tests

3.3.1. Steam exposure tests in isothermal furnace at atmospheric pressure

Four horizontal, high temperature and atmospheric pressure furnaces (Figure 3-2) were used to expose samples to pure steam at Cranfield University. Inside each of the furnaces, the samples were positioned in alumina crucibles. Steam was generated by heating the water pumped from a reservoir. Then, steam goes past the samples and is finally condensed after leaving the furnace. A water vessel collects the condensed water and is connected to the water pump creating a closed loop for steam generation. De-ionized water was used and a continuous de-oxygenation process was used in the water vessel by bubbling Oxygen Free Nitrogen (OFN) to reach a level of dissolved oxygen of <2 ppm (measured using HQ30 HACH portable oxygen meter). The different steam exposure tests were performed following 250 hour cycles. At the end of each cycle the furnaces were cooled down to allow weighing the different samples to monitor the evolution of their net mass change. Before and after the cycle, the furnaces were purged with OFN to avoid oxygen contamination.

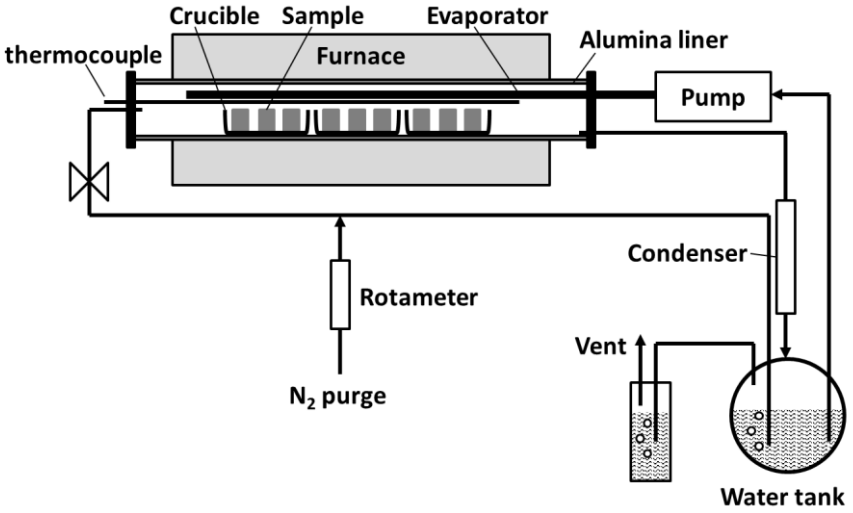

Figure 3-2: Schematic of the high temperature atmospheric isothermal steam furnace [79]**.**

To obtain some information relevant to the use of the materials (introduced earlier) under Advanced Ultra-Supercritical conditions (up to 760°C), it was decided to set the different furnaces at 650, 700, 750 and 800°C. Using these temperatures covers the temperature range of interest and keeps consistency with previous tests performed in the past years in Cranfield University. This allows data from previous tests to be used in this project. The different test conditions for are presented in Table 3-2.

Table 3-2: Test parameters for the high temperature and atmospheric pressure furnaces.

atmospheric pressure isothermal steam furnace				
	Furnace 1	Furnace 2	Furnace 3	Furnace 4
Temperature (°C)	650	700	750	800
Pressure (bars)	1	1	1	1
Steam flow ($.10^{-5}$ kg/s)	1.45	1.45	1.45	1.45
Furnace diameter (mm)	70	70	70	70
Duration of the longest test (hours)	10,000	10,000	10,000	10,000

The test matrix, Table 3-3, presents the different tests performed in the different high temperature and atmospheric pressure furnaces aiming to study the effect of temperature, surface finish and material composition of the steam oxidation process. This test matrix specifies the material tested and its surface finish as well as the time and temperature of the steam exposure test.

In order to study the mass change of the as-received surface a way to de-correlate its specific effect from the total mass change should be found. To do so, all the other surfaces should have the same finish. It has been decided to be a P1200 surface finish. Then, a sample with the P1200 surface finish only should be exposed with the same experimental conditions as the “as-received/ P1200” sample. There is no need to expose many samples with a P1200 surface finish only. Exposing only one of these samples for each material and experimental condition would give the required information regarding the mass change per surface unit over the entire steam

exposure time range. Figure 3-1 shows what the different surface finishes are on the different surfaces of a sample cut from a tube.

The shot-peened surface was also only possible to create on one surface of the samples. In order to study the specific effect of the shot-peened surface finish, the same protocol to that used for the study of as-received surface finishes was adopted.

The P2500 ground surface could be performed on every surface but the concave surface of the samples so a de-correlation is also needed to measure the specific effect of this surface finish. A fine polishing has been observed in the literature to reduce the incubation time and increase the oxidation effects at early stages [12].

The literature relates that the shot-peened surface finish is of most benefit to the austenitic steels; allowing the formation of a protective chromia layer, and increasing the steam oxidation resistance of the material [63,65]. The improved oxidation resistance does not allow significant mass change to be recorded from short exposure time to about 8000 hours [66]. Considering this observation, it has been decided to expose the shot-peened samples for no less than 10,000 hours (see Table 3-3).

Table 3-3: Test matrix associated with the tests performed at laboratory-scale in high temperature and atmospheric pressure furnaces.

finished to be continued			Steam Side Oxidation (Lab Scale)																			
			Steam Temperature (°C)																			
			650					700					750					800				
			Exposure time (hr)																			
Material Description	Type	Surface preparation	500	1500	2500	5000	10000	500	1500	2500	5000	10000	500	1500	2500	5000	10000	500	1500	2500	5000	10000
TP347HFG	Austenitic	As received				88	1				121	2				114	3	78	79	89	122	4
		Ground P1200					5					6					7					8
		Ground P2500	18	17	83	127		19	84	85			20	82	86			21	87	120	128	
		Shot peened SANYO					9					10					11					12
		Shot peened PISCO					13					14					15					16
304H	Austenitic	As received				112	40					41				119	42	77	101	113		43
		600 grit surface					49					50					51					52
		Ground P2500	45	44	102			46	103	149			47	81	104			48	118	142		
Sanicro 25	Austenitic	As received	26	27	115	90	22	28	91	124	92	23	29	93	125	94	24	30	95	136	126	25
		Ground P1200					36					37					38					39
		Ground P2500	32	31	123	129		33	139	134			34	80	153			35	137	131	130	
HR3C	Austenitic	As received				108	53				133	54				109	55	76	96	97		56
		Ground P1200																				
		Ground P2500	73	98	110			74	116	132			75	99	111			145	100	117		
Alloy 263	Nickel-base alloy	As received																				
		Ground P1200								150		67			161		68			147		69
		Ground P2500																				
Alloy 617 (mod)	Nickel-base alloy	As received																				
		Ground P1200							160	146		64			152		65	159	158	141		66
		Ground P2500							70	105				71	106			154	72	107		
Alloy 740	Nickel-base alloy	As received																				
		Ground P1200								157		61			155		62	156	151	148		63
		Ground P2500																				

3.3.2. Steam exposure tests in a high temperature and high pressure autoclave

To investigate the effect of pressure on the steam oxidation process, some samples were sent to the National Physical Laboratory (NPL) to be exposed in a high temperature and pressure steam loop associated with a static autoclave (Figure 3-3). Steam was generated by pumping the water from a reservoir into an evaporator vessel and a superheater until reaching the pressurized reaction chamber heated to the desired temperature. The exposed samples are suspended on a frame in the reaction chamber. After passing through the reaction chamber, the steam is condensed and collected in the reservoir from which a water treatment loop deionises and deoxygenates the water. Hence, the levels of dissolved oxygen in the water was 2-5 ppb [80].

The high pressure steam exposure tests were performed at 650°C and 36 bars for 1000 hours in a single cycle. To observe the pressure effect, replicas of the samples exposed at high pressure were exposed in a high temperature and atmospheric pressure furnace at 650°C for 1000 hours as well. However these tests at atmospheric pressure were separated in four cycles of 250 hours. The Table 3-4 presents the conditions under which the tests were performed and the test matrix presented in Table 3-5 brings more details on the steam exposure tests.

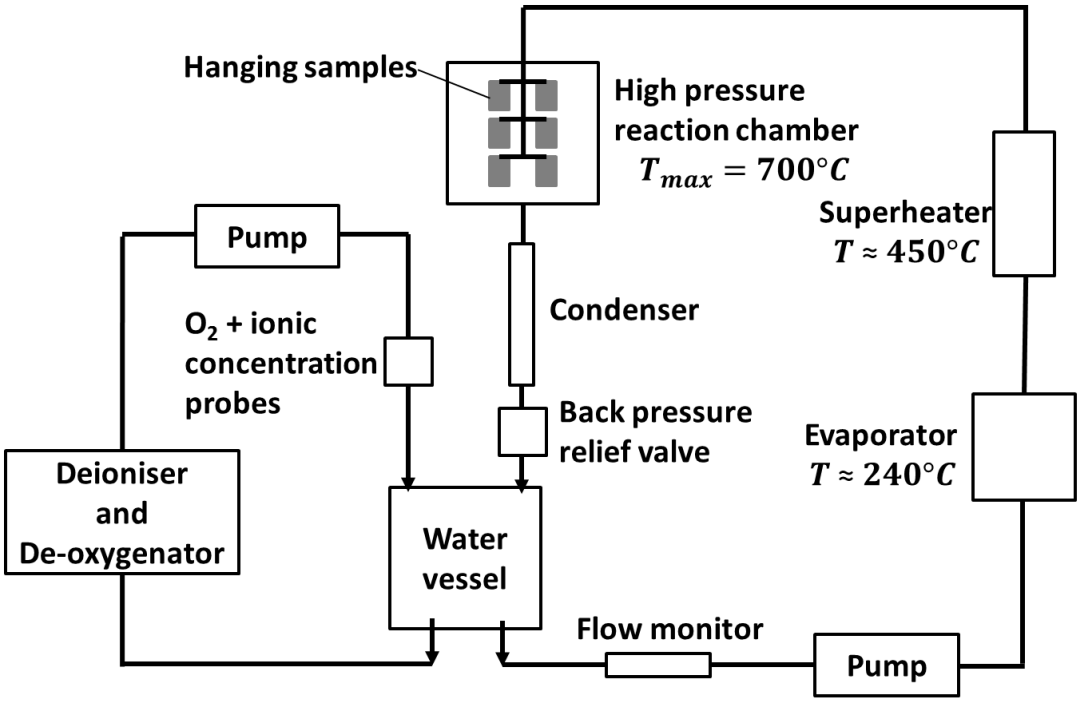

Figure 3-3: Shematic of a supercritical H_2O autoclave [81]**.**

Table 3-4: Test parameters for the study of the effect of pressure.

high pressure isothermal autoclave		
	high temperature and pressure autoclave	high temperature and atmospheric pressure furnace
temperature (°C)	650	650
pressure (bars)	36	1
steam flow (kg/s)	$1.67.10^{-4}$	$1.45.10^{-5}$
Furnace diameter (mm)	Unknown	70
exposure time (hours)	1000	1000

Table 3-5: Test matrix associated with the tests performed at laboratory-scale in a high temperature and pressure steam loop associated with a static autoclave

			Pressure study	
			Steam Temperature (°C)	
			650°C	
			Steam pressure	
			1 atm	36 bars
			Exposure time (hr)	
Material Description	Type	Surface preparation	1000	1000
T92	Ferritic	Ground P1200	140	NPL1
TP347HFG	Austenitic	As received	135	NPL3
		Ground P1200	143	NPL4
Sanicro 25	Austenitic	As received	138	NPL5
		Ground P1200	144	NPL6

3.4. Post-exposure preparation

In order to visualize and study in detail oxide scales, cross-sections of exposed samples exposed in laboratory experiments have been prepared. These cross-sections have been prepared by mounting samples using a mounting jig composed of a metal base with two holes at the bottom to place reference pins. The samples were positioned inside the metal base touching the pins and kept in position with a scalpel blade as shown in Figure 3-4. For cut on reels samples, metal rings were used to elevate the samples so that the samples' centre correspond to the jigs' centre.

Once the samples were been positioned, the jigs were filled up with a mixture composed of 40%$_{vol}$ epoxy resin, 10%$_{vol}$ hardener, and 50%$_{vol}$ ballotini. The role of the ballotini is to reduce resin shrinkage and so minimise damage to the oxide scales

during subsequent sample preparation. After vacuum de-gazing and 12 hours of hardening time, the mounted samples were cut and polished up to a 1 µm surface finish in a way that the surfaces of the cross-sections after polishing are located at the centre of the samples.

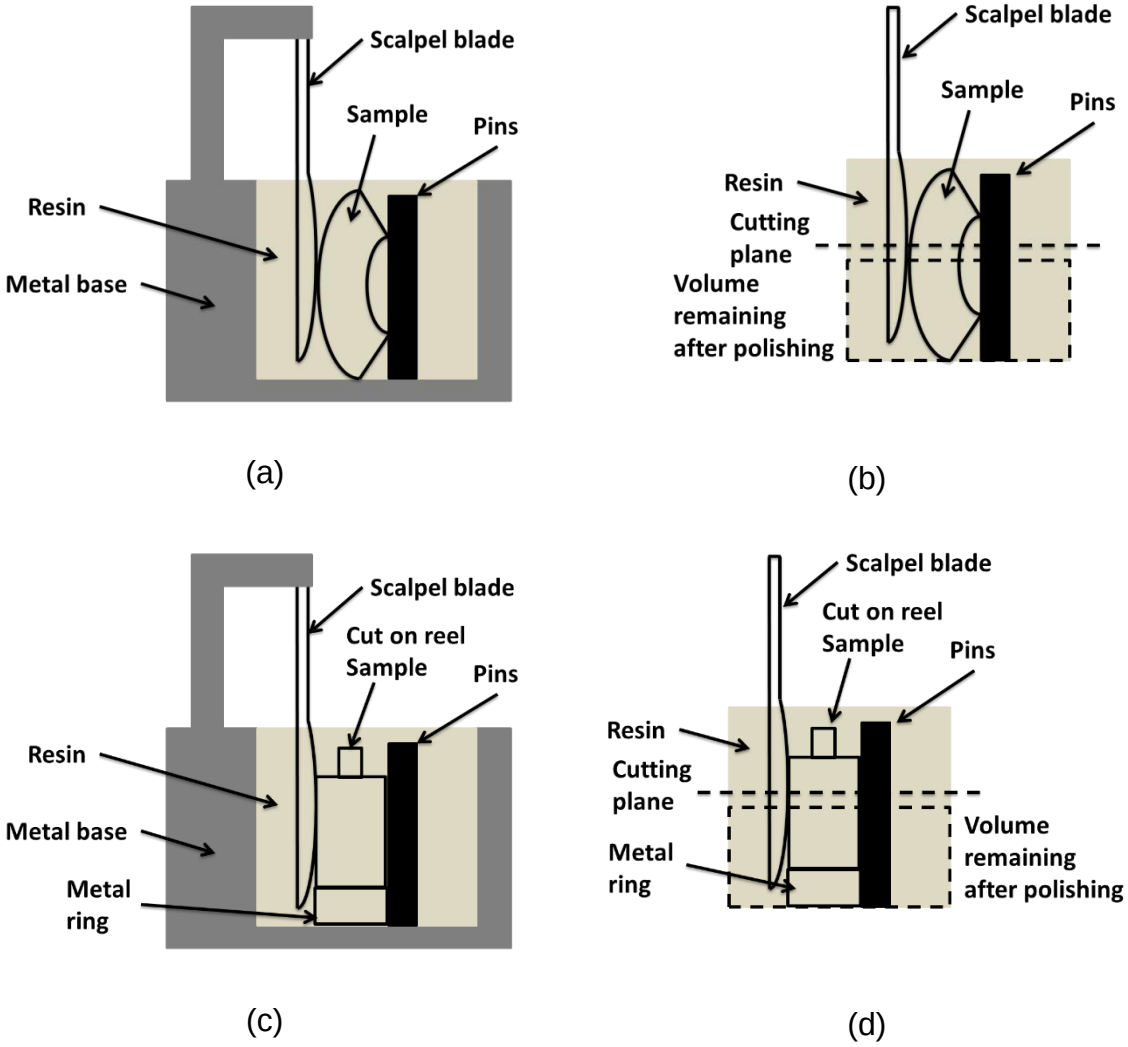

Figure 3-4: Sample mounting used to prepare cross-sections for samples cut from tubes (a) with the metal jig (b) mounted sample before cutting; for cut on reels samples (c) with the metal jig (d) mounted sample before cutting.

3.5. Data analysis and characterization

To fulfil the different objectives presented in the precedent Section, different characterization devices have been used and different data have been recorded.

On one hand, to quantify high temperature steam oxidation and to develop a quantitative model describing the effect of the steam oxidation process upon the different materials exposed, calculations of the steam oxidation kinetic parameters associated with the mass change and oxide thickness evolution for the different materials are required. On the other hand, to improve the understanding of high temperature steam oxidation, there is a necessity to observe and identify the different oxides formed at the samples' surfaces under the different steam conditions tested. Techniques such as scanning electron microscopy, X-ray diffraction and focused ion beam have contributed to the gathering of crucial data. All the different techniques used to acquire data throughout this project are presented hereafter.

3.5.1. Mass change measurements

To follow and record the mass change for the different samples exposed to high temperature steam, the Sartorius CP225D balance was used. It possesses a accuracy of 0.1 or 0.01 mg when measuring above or below 80 g respectively with a maximum of 220 g.

To monitor the mass change of the different samples exposed in the high temperature and atmospheric pressure furnaces, the exposure tests were divided in 250 hours cycles allowing the weighing of the samples and recording their mass change.

The different samples possess different surface finishes on their different surfaces. Therefore when studying the specific mass change for each of the surface finishes, a de-correlation calculation must be done. Equation (3-1) allows the calculation of the

mass change per unit of area for the sample with a P1200 uniform surface finish. The results of this equation can then be used to calculate the mass change per unit of area related to the as-received surface using Equation (3-2).

$$dm^s_{P1200} = \frac{\frac{dm_{tot}}{dt}}{A_{P1200}} \tag{3-1}$$

$$\frac{dm^s_{as}}{dt} = \frac{\frac{dm_{tot}}{dt} - \left(\frac{dm^s_{P1200}}{dt} * A_{P1200}\right)}{A_{as}} \tag{3-2}$$

Where m^s_{as} is the mass change per unit of area for the as-received surface of the sample of interest [mg.cm^2], m^s_{P1200} is the mass change per unit of area for the P1200 surface finish from the reference sample [mg.cm^2], m_{tot} is the total net mass change of the sample of interest [mg], A_{P1200} is the sample area with a P1200 surface finish [cm^2], and A_{as} is the sample area with an as-received surface finish [cm^2].

For shot-peened materials where shot-peening is only applied to the concave surface, Equation (3-2) can also be used to calculated the mass change specific to the shot-peened surface.

For P2500 ground materials with an as-received surface finish on their concave surface and a P2500 surface finish on all their other surfaces, a similar calculation can be used, as presented in Equation (3-3).

$$\frac{dm^s_{P2500}}{dt} = \frac{\frac{dm_{tot}}{dt} - \left(\frac{dm^s_{as}}{dt} * A_{as}\right)}{A_{P2500}} \tag{3-3}$$

Where m^s_{as} is the mass change per unit of area for the as-received surface of the sample of interest [mg.cm^2], m^s_{P2500} is the mass change per unit of area for the P2500 surface finish from the reference sample [mg.cm^2], m_{tot} is the total net mass change of the sample of interest [mg], A_{P2500} is the sample area with a P2500 surface finish [cm^2], and A_{as} is the sample area with an as-received surface finish [cm^2].

3.5.2. Image analysis

The image analyser Leitz microscope with Zeiss Axiocam ICc 1 and a ×20 magnifying lense that use Axiovision software was used to take pictures all around the samples while localizing the position of the different interfaces (steam/outer layer; outer layer/inner layer; inner layer/metal. The data obtained can be used to measure the oxide thickness and the metal loss for the different samples if these have been significantly oxidized. To do so, the coordinates of various points located at the outer surface of the oxide layer and at the metal / oxide interface are recorded. Thus, oxide thickness is obtained by comparing the position of the outer surface of the oxide layer with the metal / oxide interface. Metal loss data result from the difference between the original samples' dimensions and the dimensions of the metal matrix remaining after oxidation, calculated using the position data for the metal / oxide interface.

3.5.3. XRD: X-ray diffraction

The identification of the phases of the oxides formed during high temperature steam oxidation has been possible using X-Ray Diffraction (XRD). XRD spectra were obtained using a Siemens D5005 with a Cu K_α radiation source, and the identification of the different peaks was performed using the EVA software. The parameters used for the spectra acquisition are presented in Table 3-6:

Table 3-6: List of the different parameters used for the acquisition of the XRD spectra (table copied from the acquisition software).

	range #1
Scan Mode	Continuous Scan
Scan Type	Locked Coupled
Auto absorber act.	0.000000
Auto absorber deact.	0.000000
Theta [°]	10.0000
2Theta [°]	20.0000
DelayTime [s]	0.0000
Start	20.000000
Time per step [s]	1.00
Increment	0.04000
# steps	1750
Det.1 voltage [V]	861.10
Det.1 gain	300.000000
Det.1 discr.1 LL	0.500000
Det.1 discr.1 WW	1.000000
Det.1 discr.2 LL	0.000000
Det.1 discr.2 WW	0.000000
Gen.voltage [kV]	40
Gen.current [mA]	40
Theta osci-used	no
Theta osci-ampl [°]	0.0000
Theta osci-speed [°/m	0.0000
2Theta osci-used	no
2Theta osci-ampl [°]	0.0000
2Theta osci-speed [°/	0.0000

3.5.4. SEM: scanning electron microscopy

This technique is interesting to be used in parallel with XRD analysis because it gives additional information regarding the oxide composition and morphology.

Imaging oxidized surfaces, observing cross-sections and performing elemental analyses have been possible using scanning electron macroscopy. An Environmental Scanning Electron Microscope (ESEM) FEI LX30 associated with Energy Dispersive X-ray analysis (EDX) was used. The EDX was performed using the AZtec software version 2.2 and a X-max detector. This analysis technique has been mainly used to observe and analyse the surfaces and cross-sections of the convex and concave faces of the oxidized samples. When using EDX, mapping and composition analyses were performed.

Images and analyses have been done using in high vacuum mode and using an electron beam set to 20 kV. The surfaces of the samples were observed and analysed using the Secondary Electron (SE) detector with a spot size of 3. To gather information at different scales, images where taken at the following magnifications: ×2000, ×1000, ×500, ×250, ×125 and ×63. To determine the oxides observed, EDX analysis have been performed on the surfaces observed at ×2000 magnification.

Cross-sections were observed using the Backscattered Electron (BSE) detector with a spot size of 5. Five images have been taken both on the convex and concave surfaces of the samples, and some of them have been analysed using EDX. The images taken have been analysed using ImageJ to measure the thickness of the oxides formed at the different surfaces observed.

3.5.5. FIB-SIMS: focused ion beam and secondary ion mass spectrometry

For the study of oxygen and hydrogen diffusion in the oxide scales, some oxidized samples have been exposed to steam containing some oxygen and hydrogen isotopes. Mappings of the oxide scales showing how deep the different isotopes have penetrated the oxide scales was possible using a FIB-SIMS. A FEI FIB-200 SIMS workstation performed images using a gallium primary ion beam current in ion-induced secondary electron (IISEI) mode. The SIMS maps were collected for $16O^-$, $17OH^-$, $18O^-$&$18OH^-$ and $20OH^-$ isotopes.

3.6. Addressing the different objectives

The experimental and characterization devices chosen to address the different objectives are summarized in Table 3-7.

Table 3-7: Experimental and characterization devices chosen to address the difference objectives.

Objective	Experimental device		Characterization device			
	Isothermal furnace at atmospheric pressure	High temperature and high pressure autoclave	SEM-EDX	XRD	image analyser	FIB-SIMS
Study of the effect of temperature	✓		✓	✓	✓	
Study of the effect of material composition	✓		✓	✓	✓	
Study of the effect of surface finish	✓		✓	✓	✓	
Study of the effect of pressure	✓	✓	✓	✓	✓	
Study of oxygen diffusion	✓					✓

The tests described in Table 3-3, using atmospheric pressure and isothermal steam furnaces, provided a large amount of information regarding the steam oxidation at different temperatures and different exposure times. These tests allowed calculation of the oxidation kinetics of the different materials and also to observe the evolution of the scale composition and morphology through steam exposure time on a large working range of temperatures. Because of their availability and their capacity to hold a large number of samples, using these furnaces constituted the basis of the

experiments presented in this thesis. They were used to study the effect of the surface finish, and also to conduct the isotope exposure experiments.

Then, the tests with NPL's high pressure isothermal autoclave presented in Table 3-5, provided additional information allowing the understanding of the effect of pressure and enabled calculating how the oxidation rate is affected by an increase of pressure.

The gathering of the results from the two experimental steam devices have enhanced the understanding of the different parameters studied in this project.

4. Results and discussion

In this Section results associated with the characterization of the different materials before and after high temperature steam exposure are presented as well as modelling calculations.

Firstly, Section 4.1 deals with the observation and characterization of samples' surfaces before steam exposure. The Section also present the possible oxides that are predicted to form on different materials as a function of the steam exposure conditions, using of the MTdata software.

Secondly, Section 4.2 presents data from the samples exposed during the atmospheric steam exposure tests. Net mass change data, XRD, SEM images of oxidized surfaces and cross-sections, oxide thickness measurements and thickness loss are all presented and discussed. The effect of surface finish on the steam oxidation process is treated in this Section.

Section 4.3 deals with kinetic calculations for both mass change and oxide thickness evolution which are then used to build models. These models describe and predict the mass change and oxide thickness for the different materials studied as a function of the steam conditions.

In Section 4.4, the results from the high pressure tests are assessed to understand pressure's effect on the oxidation process.

Finally, the study of diffusion using isotope doped steam is discussed in Section 4.5.

4.1. Pre-exposure observations and predictions

4.1.1. Thermodynamic predictions

In order to have an idea of what oxide should be expected to form for different alloy compositions, MTdata software was used. This tool helps predicting the nature of the different species formed when a chemical reaction reaches equilibrium under different temperature and pressure conditions. The software can also quantify the various species formed in terms of mass change, partial pressure, concentration.

Different alloy compositions have been implemented into the MTdata software to perform some thermodynamic predictions of the species formed when these alloys are in contact with pure water in excess (100 kg). The various compositions tested, presented in Table 4-1, have been selected to be close to the composition of the alloys chosen to be studied in this project. The predictions have been done between 500 and 900°C at both 1 atmosphere and 36 bars. The temperature and pressure values have been chosen in accordance with the steam conditions used in the atmospheric and high pressure experimental setups.

Table 4-1: List of the different compositions tested with MTdata.

Name	Alloy targeted	Fe content (kg)	Cr content (kg)	Ni content (kg)
Alloy 1	T 92	0.0901	0.0095	0.0004
Alloy 2	TP347HFG	0.0701	0.0184	0.0115
Alloy 3	Sanicro 25	0.0525	0.0225	0.0250
Alloy 4	Alloy 617	0.003	0.024	0.073

For Alloy 1, aiming at predicting what species are formed when steam is in contact with ferritic steel T 92, is appears that the oxides expected to be formed at both steam pressures are mainly composed of magnetite (Fe_3O_4) with some Cr_2FeO_4 and a small amount of Fe_2NiO_4 (see Figure 4-1).

Figure 4-2 displays the partial pressure of the different gaseous species formed. Due to the increase of pressure, the species associated with steam dissociation (H_2O, O_2, $OH^{\bullet}$, H_2)are observed to possess a higher partial pressure. Which is expected and consistent with the calculations performed in the literature review. However, hydroxides $Fe(OH)_2$ and $Ni(OH)_2$, and oxy-hydroxides $\mathrm{CrO_2(OH)_2}$ are noted to form at 1 atmosphere and also at 36 bars but in higher quantity. Iron and nickel hydroxide possess relatively high partial pressures, meaning they are expected to be of significant importance during the steam oxidation process. $\mathrm{Fe(OH)_2}$ formation confirm the assumption of the outward transport of iron as a gaseous specie as remarked by Ehler et al. [25]. The oxy-hydroxides $\mathrm{CrO_2(OH)_2}$, generally associated with chromium evaporation possess a very low partial pressure. Thus chromium evaporation will not be a crucial reaction for the steam oxidation of ferritic steel T 92.

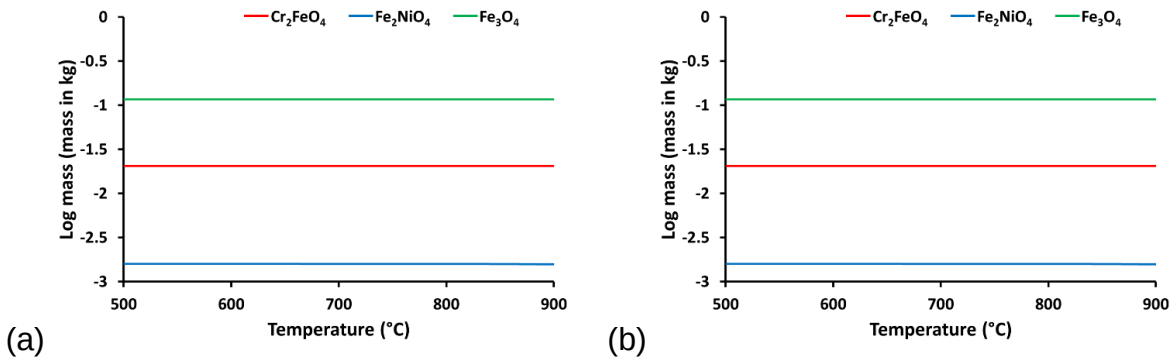

Figure 4-1: MTdata predictions for the mass of solid oxides appearing when the Alloy 1 is exposed to pure steam between 500 and 900°C at (a) 1 atmosphere and (b) 36 bars.

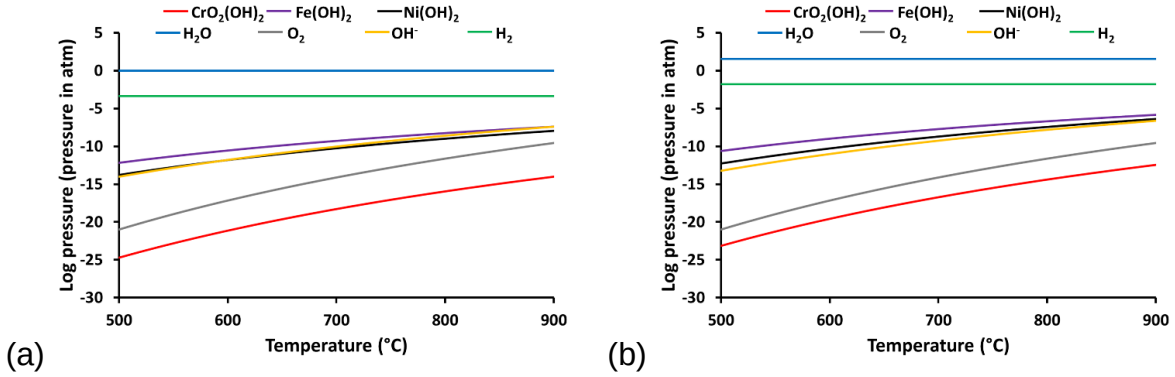

Figure 4-2: MTdata predictions for the partial pressure of gaseous species appearing when the Alloy 1 is exposed to pure steam between 500 and 900°C at (a) 1 atmosphere and (b) 36 bars.

Similarly, for TP347HFG with Alloy 2, the three different species Fe_3O_4 (magnetite), Cr_2FeO_4, and Fe_2NiO_4 are expected to form in almost the same quantity during the steam oxidation process of the alloy at atmospheric and high pressure (Figure 4-3). If can be noticed that chromia is not predicted on Figure 4-3. Even if this seems to go against what has been read in the literature review where the formation of a chromia layer can be observed [28,52], it has to be kept in mind that MTdata calculate the species present when the equilibrium of the reaction is reached. Thus the predictions do not exclude the formation of chromia but it indicates that if at some point chromia is formed, it will later disappear and probably be transformed in Cr_2FeO_4. Partial pressures of gaseous species presented in Figure 4-4 show similar results to those obtained for Alloy 1.

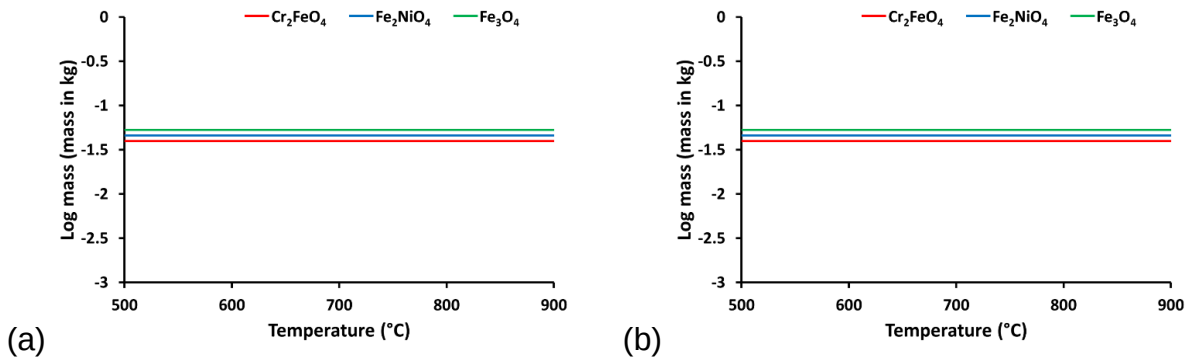

Figure 4-3: MTdata predictions for the mass of solid oxides appearing when the Alloy 2 is exposed to pure steam between 500 and 900°C at (a) 1 atmosphere and (b) 36 bars.

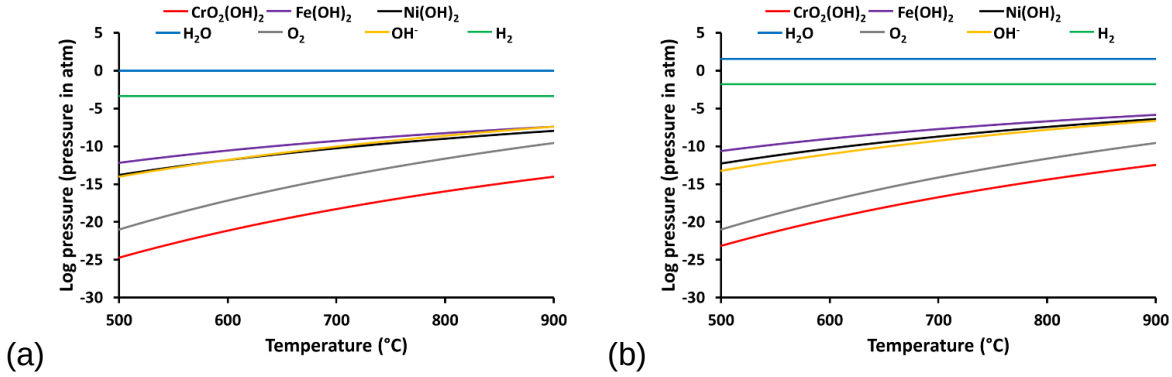

Figure 4-4: MTdata predictions for the partial pressure of gaseous species appearing when the Alloy 2 is exposed to pure steam between 500 and 900°C at (a) 1 atmosphere and (b) 36 bars.

Throughout prediction of the thermodynamically stable species using Alloy 3, it can be expected that for both pressures, unlike with the previous alloys with a quite low chromium and nickel content, the oxidation of Sanicro 25 will not lead to the formation of magnetite (Figure 4-5). At equilibrium, the expected oxides to be formed are Cr_2FeO_4, and Fe_2NiO_4 with a little NiO. Sanicro 25 seems then to form more protective oxides. Partial pressures of gaseous species presented in Figure 4-6 show similar results that what has been obtained with the two previous alloys.

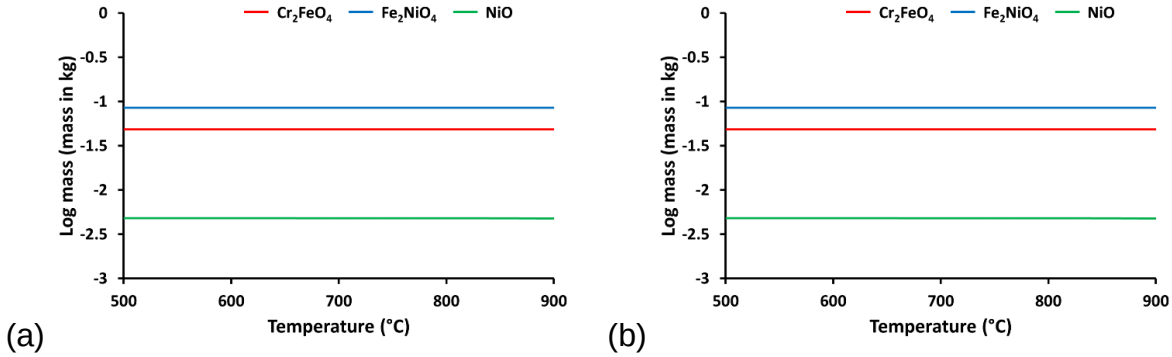

Figure 4-5: MTdata predictions for the mass of solid oxides appearing when the Alloy 3 is exposed to pure steam between 500 and 900°C at (a) 1 atmosphere and (b) 36 bars.

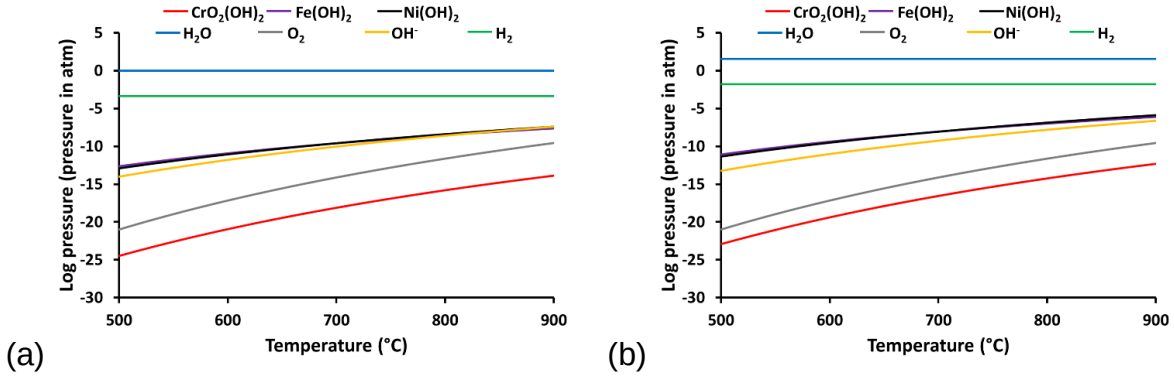

Figure 4-6: MTdata predictions for the partial pressure of gaseous species appearing when the Alloy 3 is exposed to pure steam between 500 and 900°C at (a) 1 atmosphere and (b) 36 bars.

The nickel-based alloy 617, for which prediction was performed using the composition of Alloy 4, shows large differences between the oxides formed at 1 atmosphere and 36 bars. Indeed, Figure 4-7 shows that at higher pressure there is a transition from the formation of Cr_2FeO_4 to Fe_2NiO_4 in lower quantities that the main oxides formed which are Cr_2NiO_4 and NiO. Due to the low iron concentration of this material it is quite logical that the main oxide to form is NiO. At high pressure (Figure 4-8), the partial pressure of $CrO_2(OH)_2$ is important which means chromium volatilization is a significant issue happening during the high pressure and high temperature steam oxidation of Alloy 617.

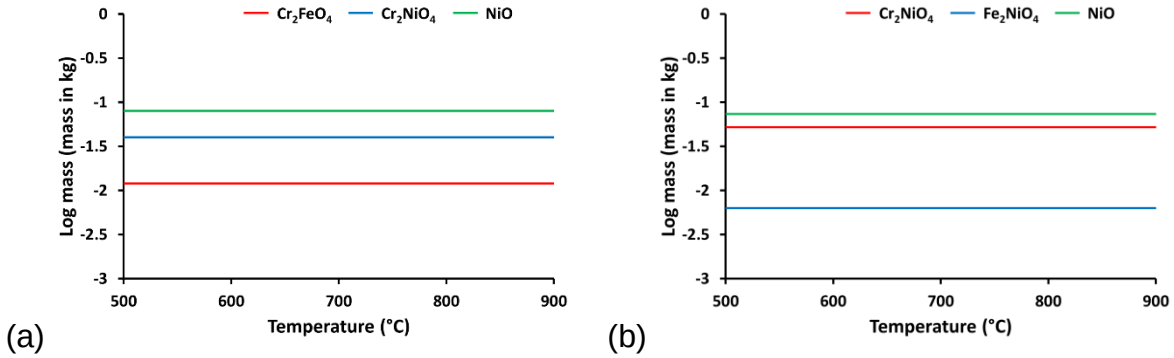

Figure 4-7: MTdata predictions for the mass of solid oxides appearing when the Alloy 4 is exposed to pure steam between 500 and 900°C at (a) 1 atmosphere and (b) 36 bars.

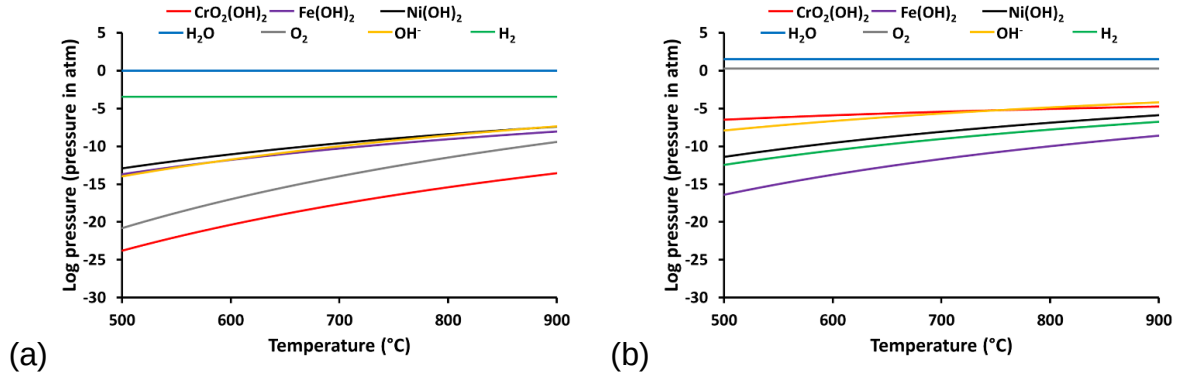

Figure 4-8: MTdata predictions for the partial pressure of gaseous species appearing when the Alloy 4 is exposed to pure steam between 500 and 900°C at (a) 1 atmosphere and (b) 36 bars.

The MTdata tool has revealed to be useful in terms of prediction of the oxides that should be formed after long steam exposure time. However, since the software calculates the species present at equilibrium, it does not allow the prediction of intermittently forming species, such as chromia, which play a crucial role in the steam oxidation process. Nevertheless, the partial pressures of the gaseous species expected to be thermodynamically stable confirm the formation of significant amounts of iron and nickel hydroxides and chromium oxy-hydroxide at high temperature for both pressures. These values allow confirming that the iron can diffuse in the oxide scales under the form of hydroxide and that chromium volatilization is important at high temperature and is one of the cause of the breakaway of the chromia layer that could be formed on some alloys.

4.1.2. Surface finish characterization

In this Section, the morphology of the surfaces prepared with various surface finishes is presented. Surface roughness residual stress measurements are also presented.

Figure 4-9 presents images of surfaces of TP347HFG prepared with various surface finishes. The images have been taken using SEM and optical microscopes. 3D images

of the different surfaces have be obtained using the confocal microscope. The confocal laser scaning Olympus Lext OLS series was used for 3D imaging the surfaces and for measuring surface roughness. The images and calculations where performed at a 20 times magnification. Table 4-2 indicates the surface roughness Ra measured using the confocal microscope.

As-received surface is observed to be very rough surfaces with many asperities. It is fair to recall that this surface finish was not prepared in Cranfield University but results from the fabrication processes used in the manufacturing of the different exchanger tubes. Thus it corresponds to the types of surface finish used in power-plants. The 3D image shows a lot of sharp peaks which are odd points obtained during the imaging of the surface.

P1200 and P2500 ground surfaces both show similar morphologies and surface roughness. Both surfaces are homogeneous with the presence of grinding and polishing marks.

Machined surfaces correspond to the surface finish applied to the concave surface to simulate a P1200 ground surface finish. It can be seen that actually the machined surface is very different from a P1200 ground surface both in terms of morphology and roughness. This observation has to be taken into account to mitigate the mass change values obtained for samples presented as having a homogeneous P1200 ground surface finish on all their surfaces.

Shot-peened surfaces are seen to possess fractures which is what is expected after this type of surface preparation [64]. The two surfaces both possess a similar morphology, however the surface roughness measured shows differences.

Table 4-2: Surface roughness for the different surfaces finishes applied on TP347HFG.

	As-received	Ground (P1200)	Ground (P2500)	Machined	Shot-peened (PISCO)	Shot-peened (SANYO)
Surface roughness (Ra - µm)	5.74	1.28	1.29	3.18	3.25	2.18

Since the roughness measurements have been performed on the prepared samples which have been cut from heat exchanger tubes, the values can be affected by the overall curved shape of the surface analysed. The roughness values obtained are then a good way of comparing the different surfaces to one another but they can be misleading when comparing with values obtained in other studies.

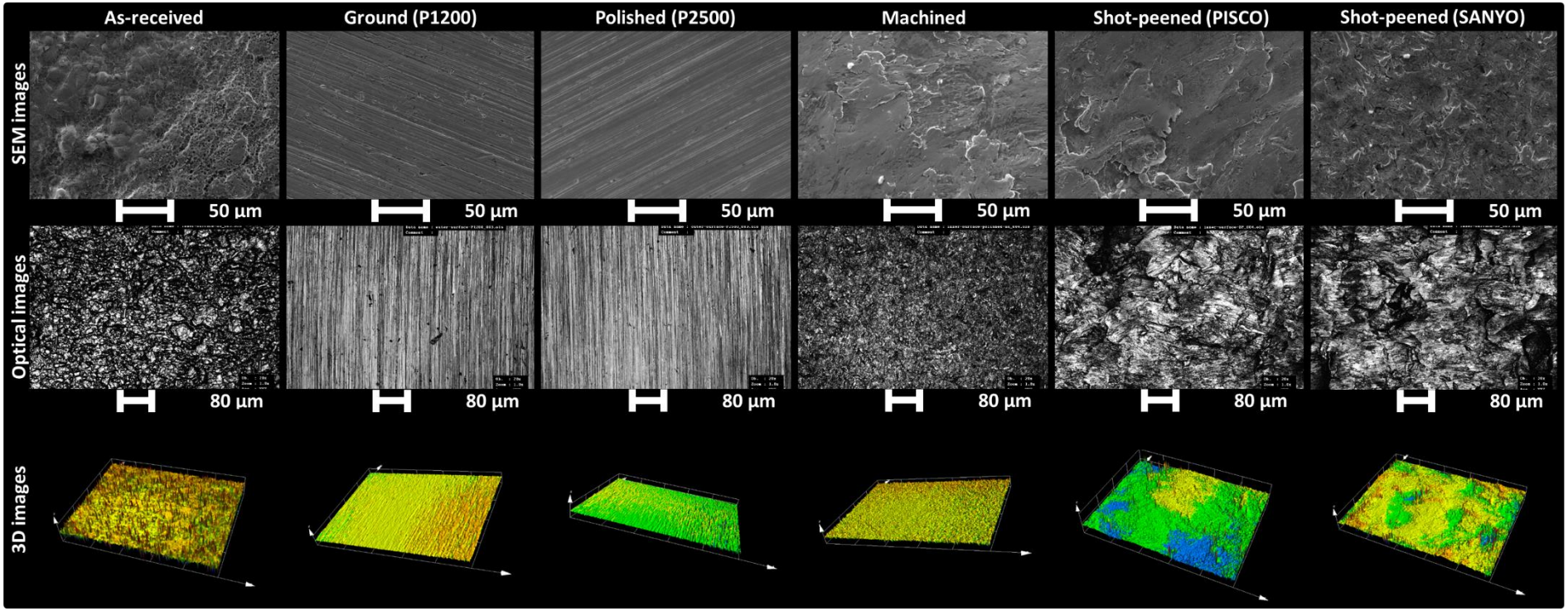

Figure 4-9: Surface imaging of different surface finishes appplied on TP347HFG before steam exposure tests.

Pulstec Miro-X360 portable X-ray residual stress analyser was used at NPL to perform residual stress measurements on different materials prepared using various surface finishes. Stress measurements for the different samples are presented separately due to the differences in geometry between the different samples analysed. Indeed, Sanicro 25 and TP347FHG samples, presented in Figure 4-10 (a) and (b) respectively, are cuts from tubes but of different dimensions and Alloy 617 samples, presented in Figure 4-11, are cut on reels. Cold working techniques such as shot-peening, grinding and machining bring compressive stresses in the materials treated which strengthen them and created dislocations at the surface of the materials.

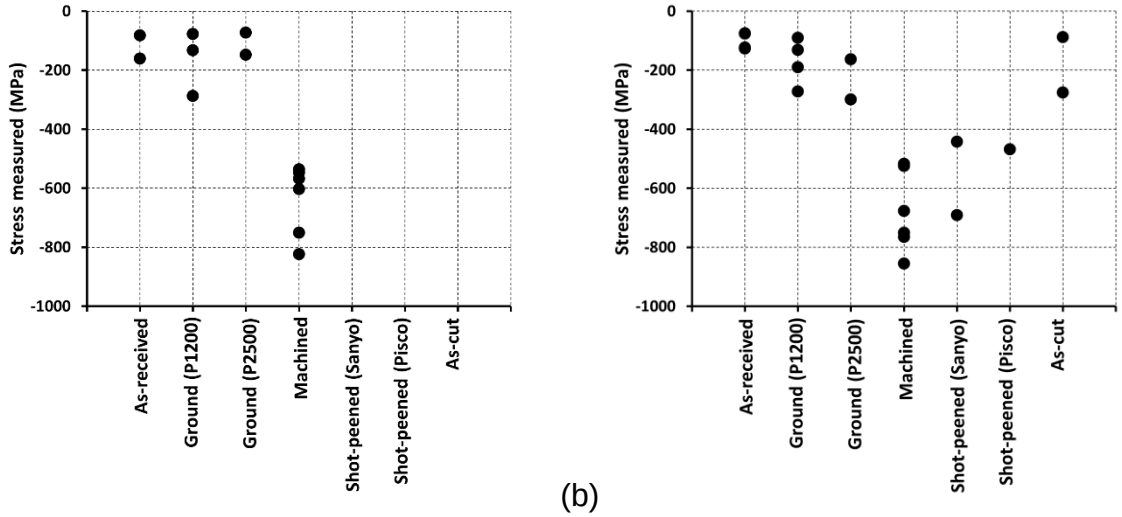

(a) (b)

Figure 4-10: Residual stress measured on different surfaces of (a) Sanicro 25 and (b) TP347HFG.

The data presented in Figure 4-10 seems to indicate that the highest compressive residual stress measurements are obtained for machined and shot-peened surfaces. Then, the remaining surface finishes presented all have similar values for residual stresses. The scatter of the data points obtained make it difficult to differentiate them from one another.

Figure 4-11 present residual stresses for Alloy 617. The only surface finishes applied to this material are P1200 and P2500 grinding. It appears that the P1200 grinding brings more compressive stresses than the P2500 grinding.

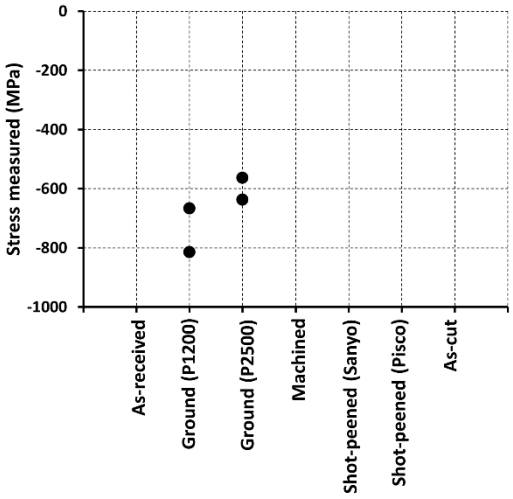

Figure 4-11: Residual stress measured on different surfaces of Alloy 617.

The residual stress measurements, have been performed on the samples' surface which are not flat. Thus the values obtained here are probably affected by the concave and convex shape of the different surfaces analysed. This is probably the reason why the values for P1200 and P2500 ground surfaces of samples cut from tubes are so different from the values obtained on cut on reels samples. Some reports presented in the literature review [12,44], have shown that the more compressive stresses are present at the surface of a material, the more dislocations are present which enhance chromium diffusion for the formation of an early and protective chromia layer.

4.2. Oxide formation during steam oxidation at atmospheric pressure

The effect of the steam temperature, exposure time, material composition and surface finish is dealt with in the following Sections. For the different materials, results are presented in terms of net mass change and oxide thickness recordings accompanied with data about oxide morphology and composition.

4.2.1. Results from atmospheric steam exposure tests

4.2.1.1. TP347HFG

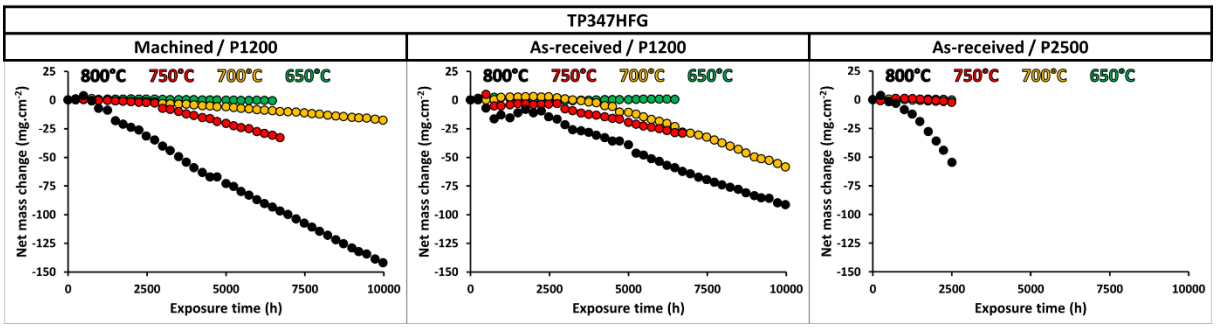

Figure 4-12: Net mass change data related to the different surface finishes of TP347HFG exposed for up to 10,000 hours.

Multiple TP347HFG samples prepared with different surface finishes have been exposed to steam and the net mass change data for the samples exposed for up to 10,000 hours is represented in Figure 4-12. The maximum mass gain stays low for the all the different samples exposed at the various temperatures. The maximum value is reached during the first 2000 hours of exposure after which mass loss is observed.

At 650°C, low exfoliation happens for all surface finishes. The oxidation process remains detrimental for the material but its integrity is maintained for a long time (>6500 hours).

First, the results presented are associated with samples having their concave surface left as-received and their convex surface ground to a P1200 grit. XRD spectra for as-received and P1200 ground surfaces of TP347HFG are presented in Figure 4-13 and Figure 4-14. SEM images for the oxidized surfaces and for cross-sections are presented in Figure 4-15 and Figure 4-16 for the as-received surfaces, and in Figure 4-17 and Figure 4-18 for the P1200 ground surfaces. Oxide thickness distributions for as-received and P1200 ground surfaces are presented in Figure 4-19. Then, the data presented deals with samples with as-received concave surfaces and P2500 ground convex surfaces. Figure 4-20 and Figure 4-21 present the XRD spectra associated with as-received and P2500 ground oxidized surfaces. Figure 4-22 and Figure 4-23 show the SEM images of the surfaces and cross-sections associated with as-received surfaces whereas Figure 4-24 and Figure 4-25 gather SEM images for surfaces and cross-sections for P2500 ground surfaces. Oxide thickness distributions measured on the as-received and P2500 ground surfaces are presented in Figure 4-26. Elemental maps obtained from EDX analyses of exposed samples are presented in Figure 4-27, Figure 4-28, and Figure 4-29. These maps allow the observation of the oxide composition of key samples with different features that can be observed with samples. Indeed, Figure 4-27 shows the elemental mapping for a thin chromia layer. Figure 4-28 shows the elemental mapping for nodules forming on a chromia layer and finally Figure 4-29, presents the elemental mapping for a multi-layered oxide scale.

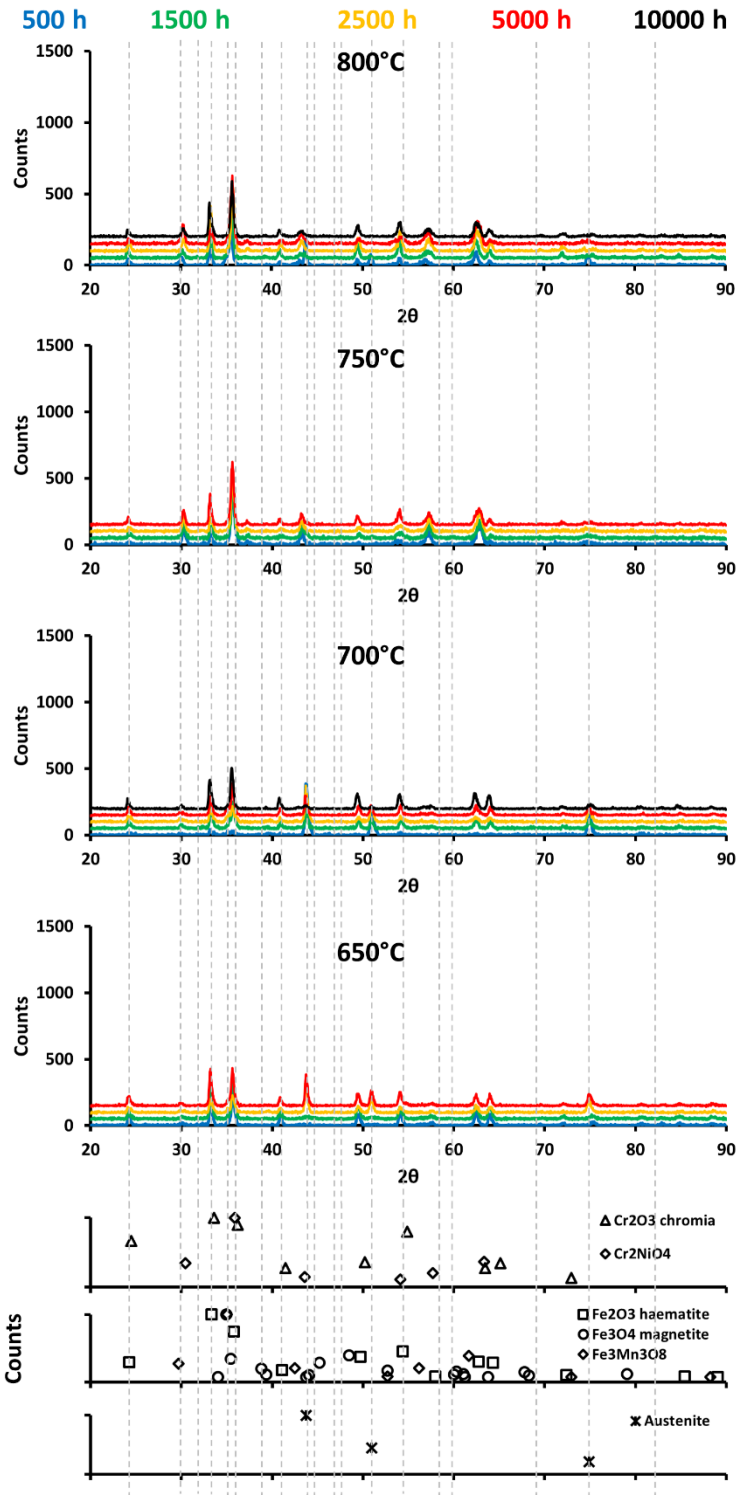

Figure 4-13: XRD spectra for P347HFG with as-received surface finish after steam oxidation at different temperatures and exposure time.

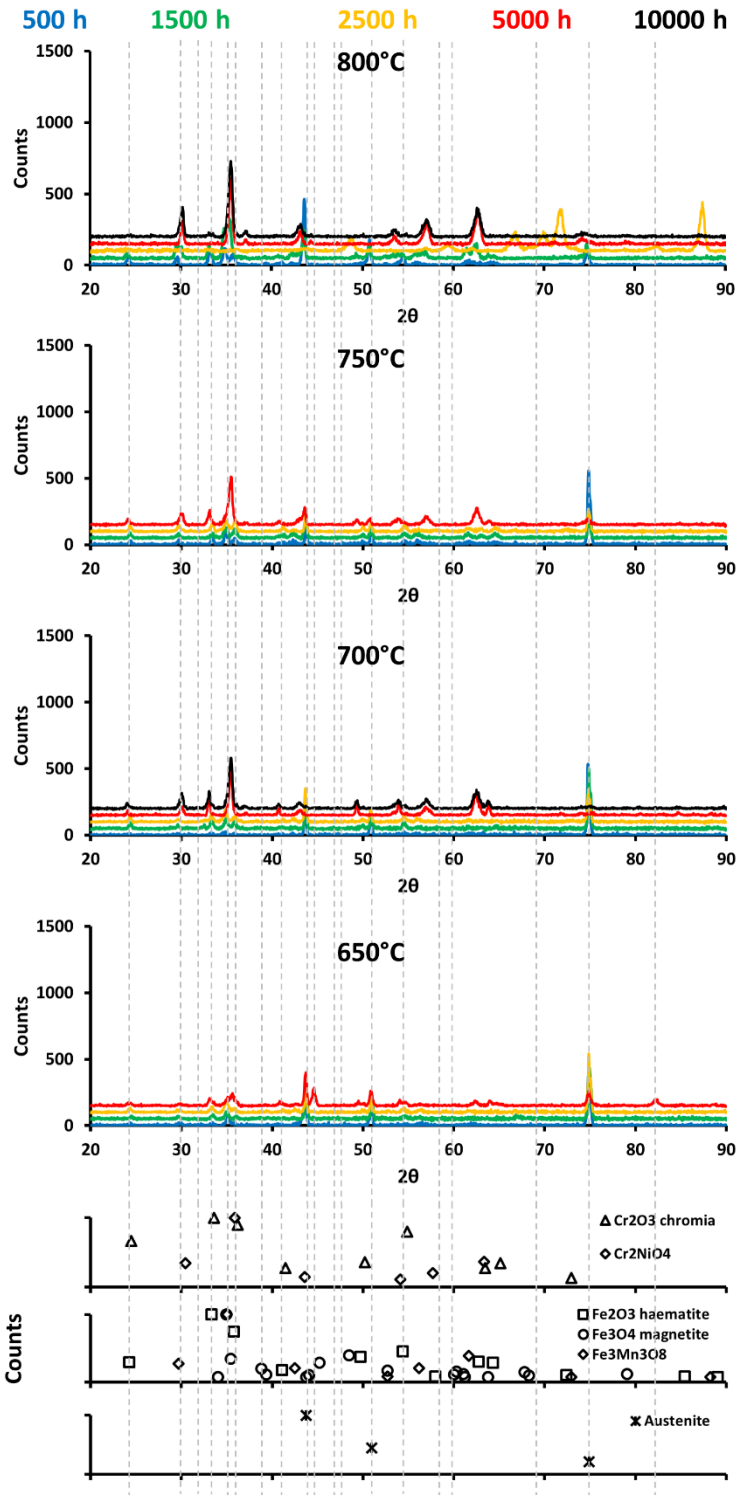

Figure 4-14: XRD spectra for TP347HFG with a P1200 ground surface finish after steam oxidation at different temperatures and exposure time.

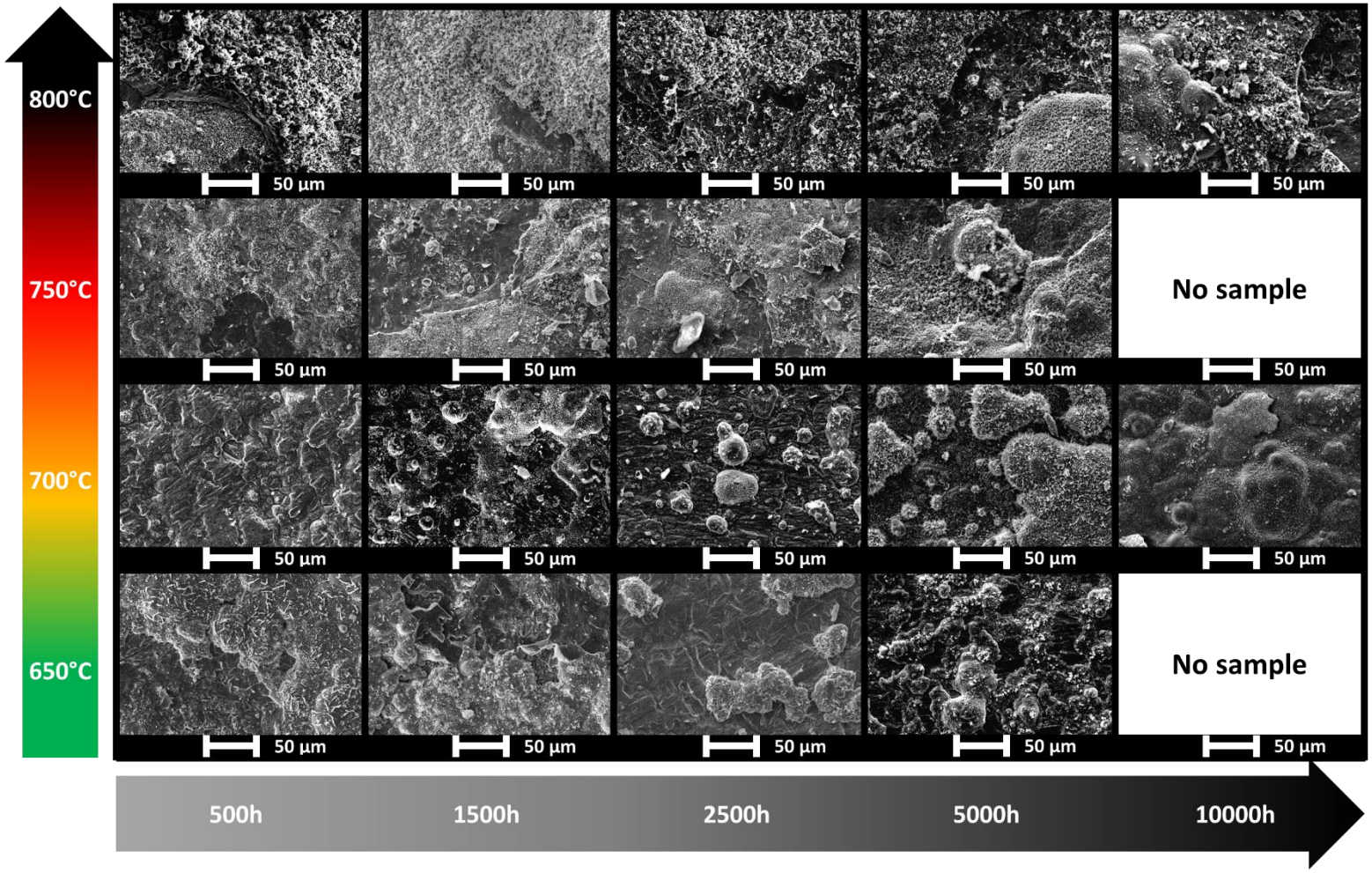

Figure 4-15: SEM images for TP347HFG with as-received surface finish after steam oxidation at different temperatures and exposure time.

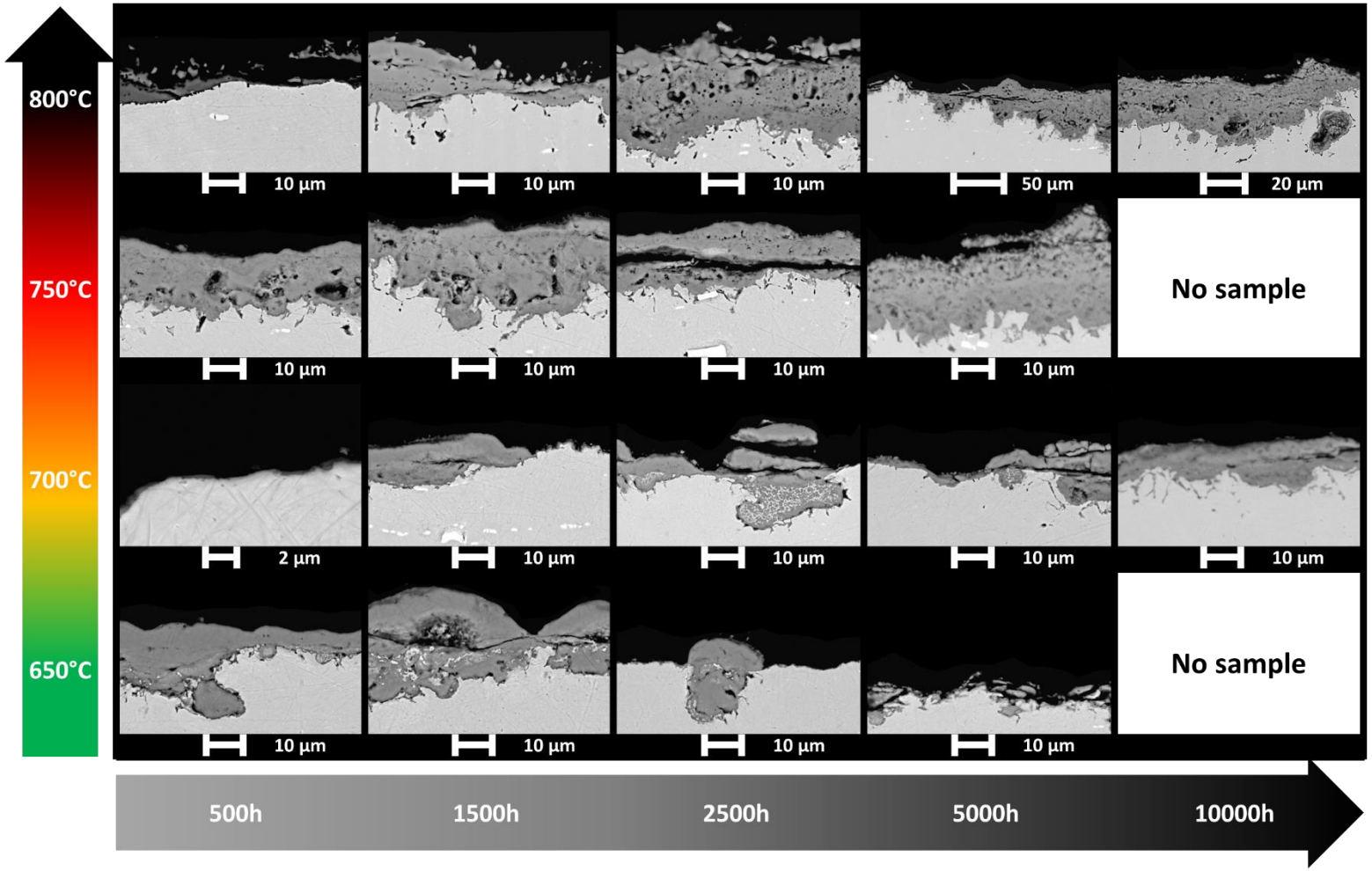

Figure 4-16: SEM images for cross-sections of TP347HFG with as-received surface finish after steam oxidation at different temperatures and exposure time.

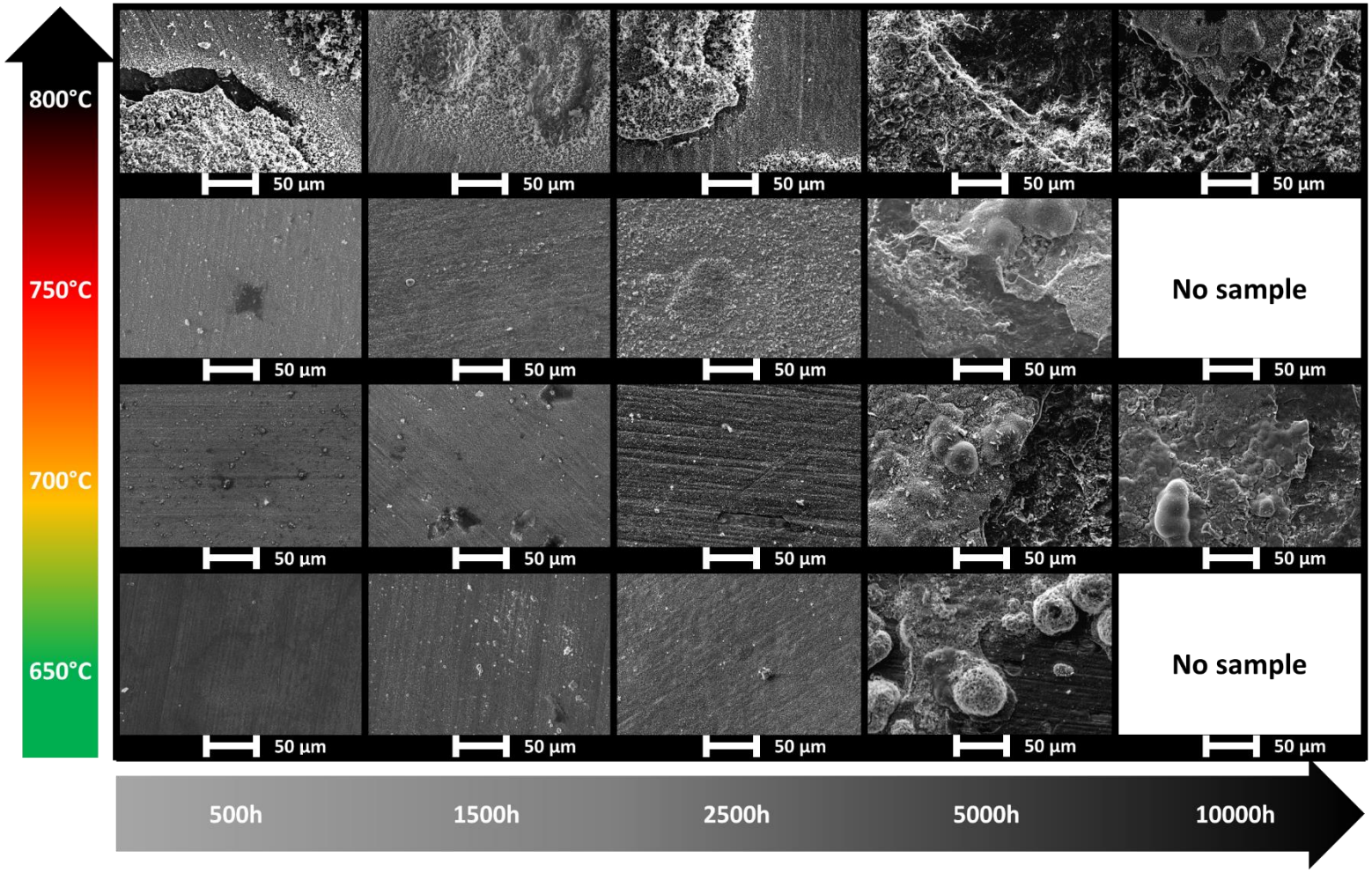

Figure 4-17: SEM images for TP347HFG with a P1200 ground surface finish after steam oxidation at different temperatures and exposure time.

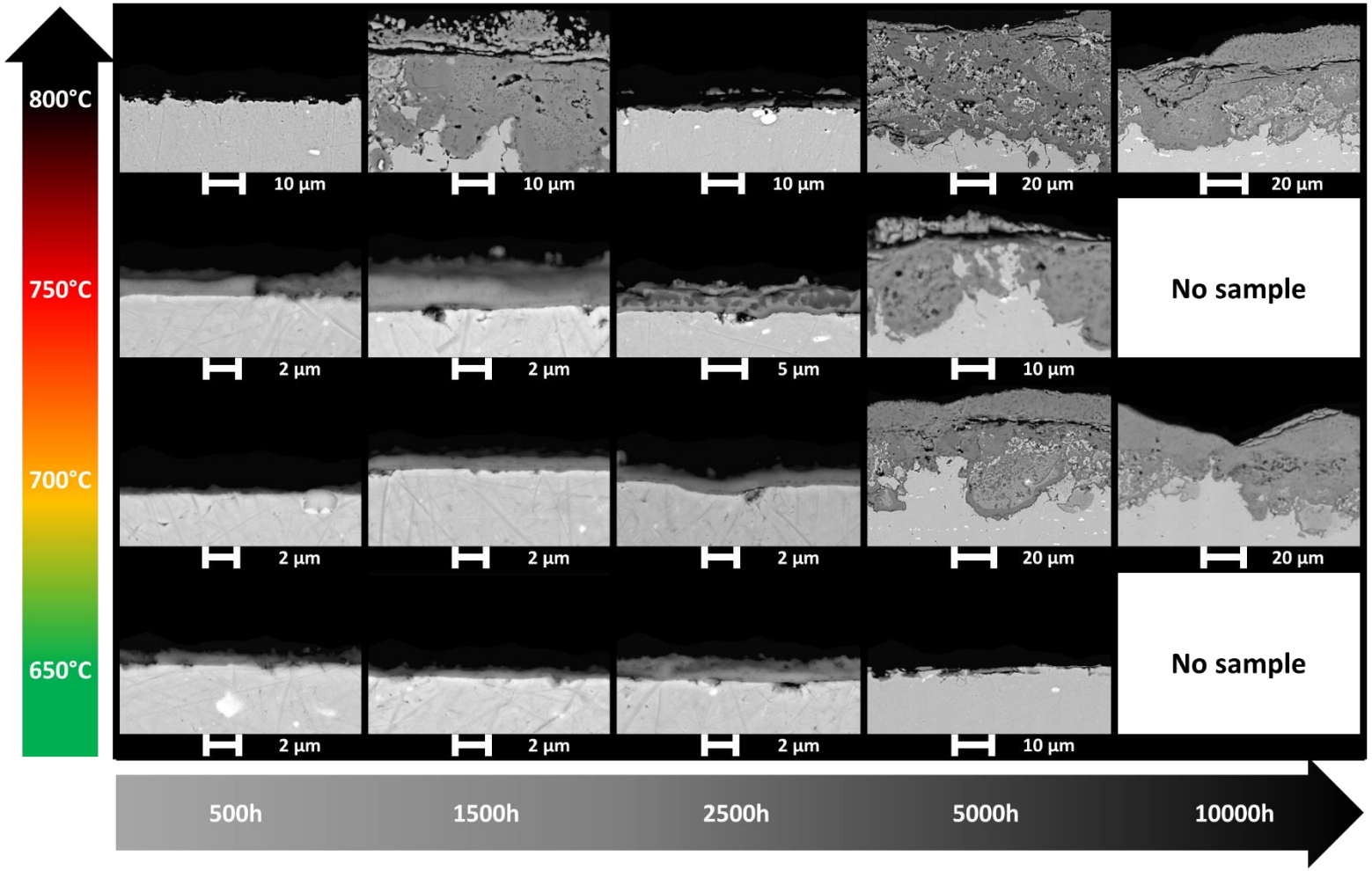

Figure 4-18: SEM images for cross-sections of TP347HFG with a P1200 ground surface finish after steam oxidation at different temperatures and exposure time.

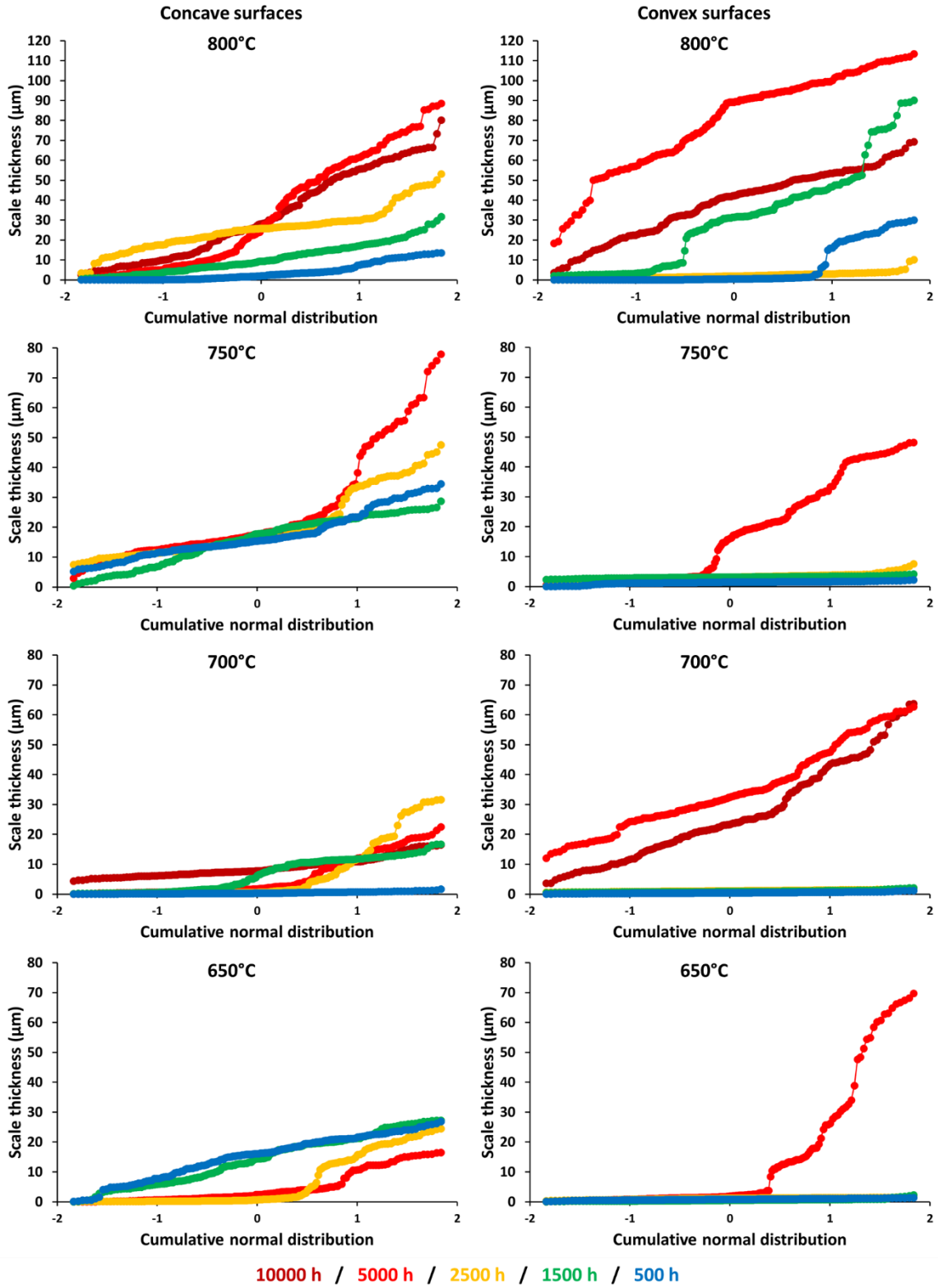

Figure 4-19: Cumulative normal distribution for the thickness of oxides formed on as-received concave surfaces and P1200 ground convex surfaces of TP347HFG after different exposure times at various temperatures.

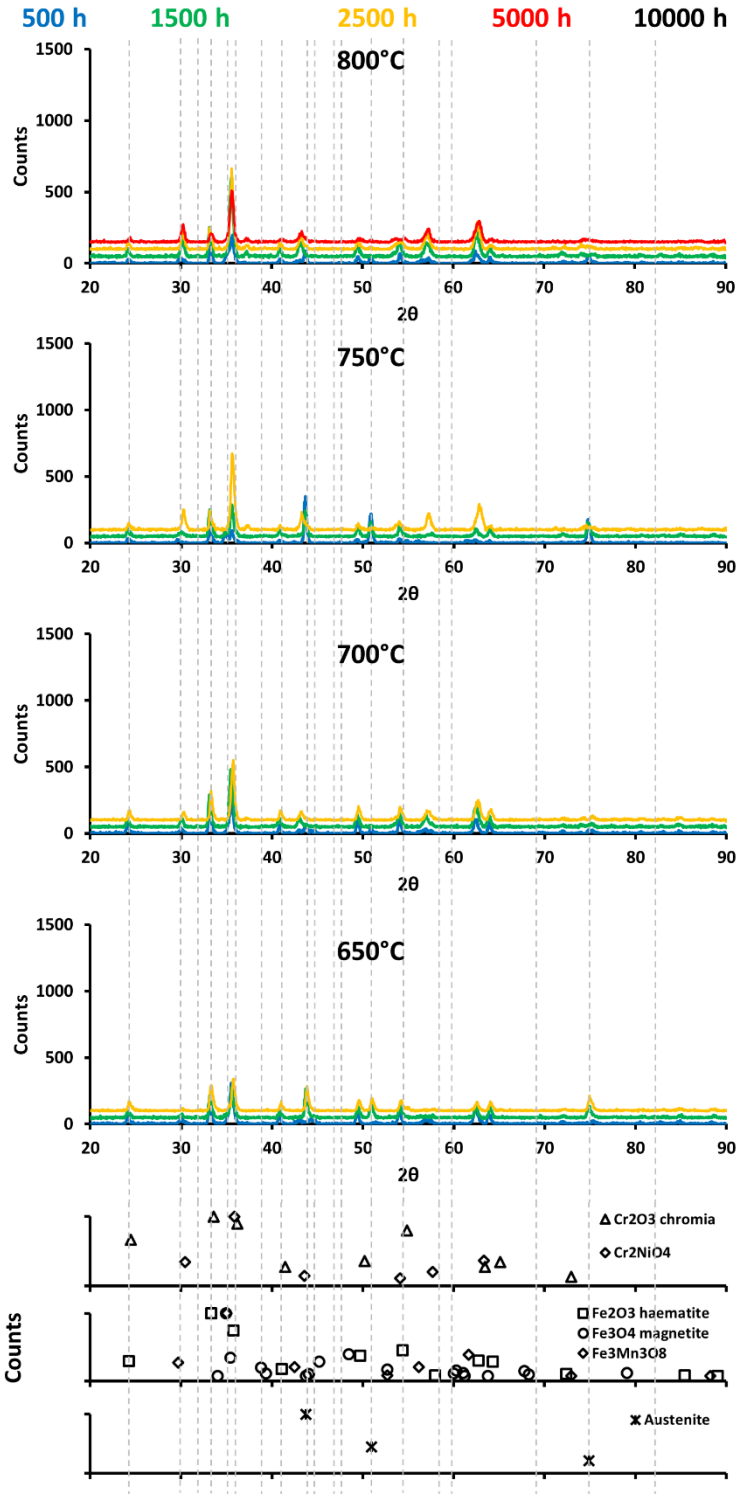

Figure 4-20: XRD spectra for P347HFG with as-received surface finish after steam oxidation at different temperatures and exposure time.

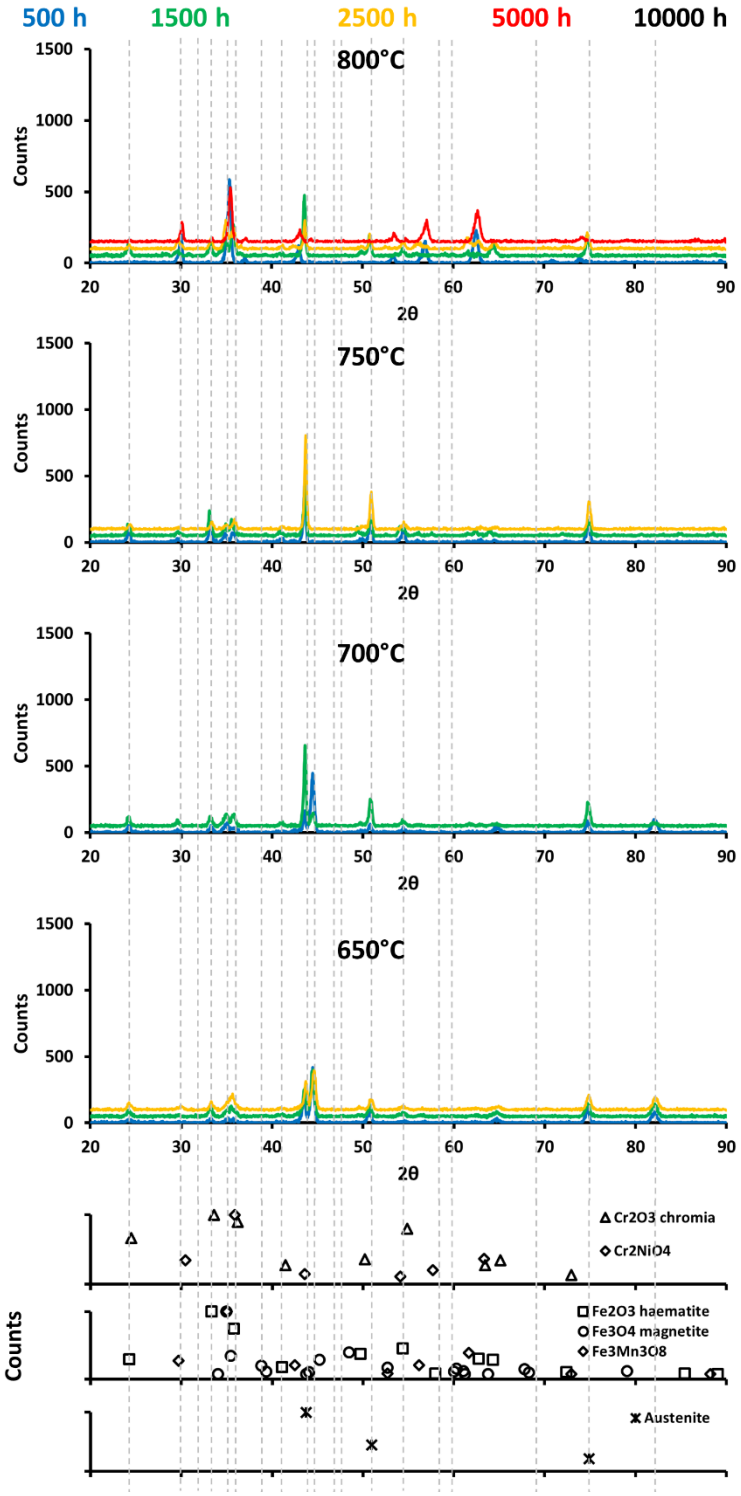

Figure 4-21: XRD spectra for TP347HFG with a P2500 ground surface finish after steam oxidation at different temperatures and exposure time.

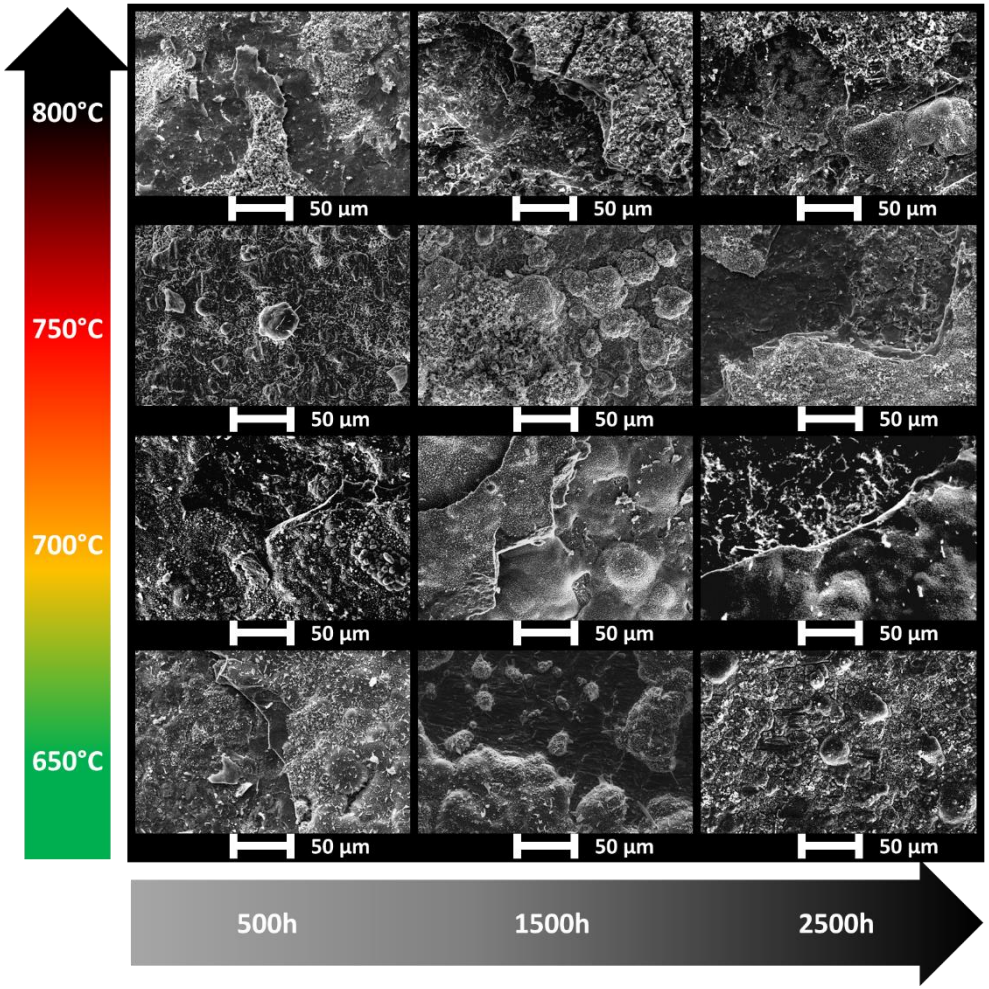

Figure 4-22: SEM images for TP347HFG with as-received surface finish after steam oxidation at different temperatures and exposure time.

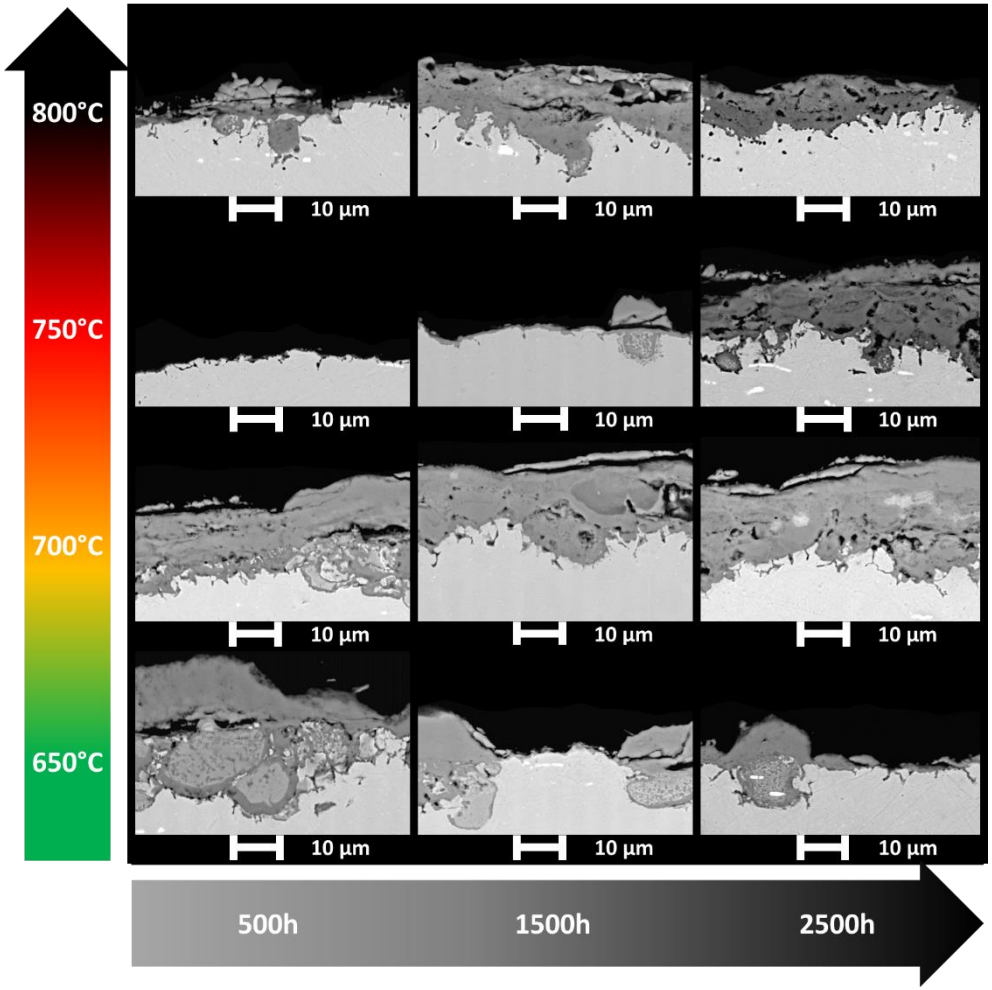

Figure 4-23: SEM images for cross-sections of TP347HFG with as-received surface finish after steam oxidation at different temperatures and exposure time.

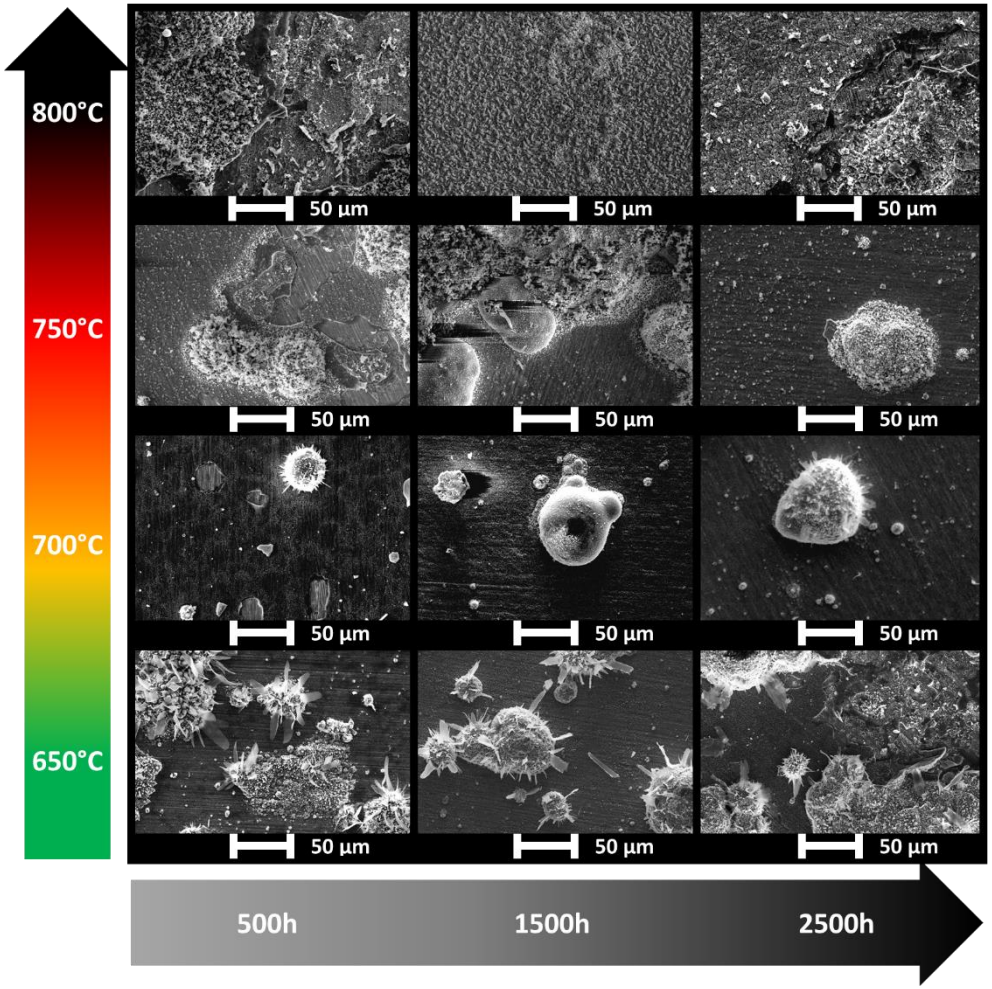

Figure 4-24: SEM images for TP347HFG with a P2500 ground surface finish after steam oxidation at different temperatures and exposure time.

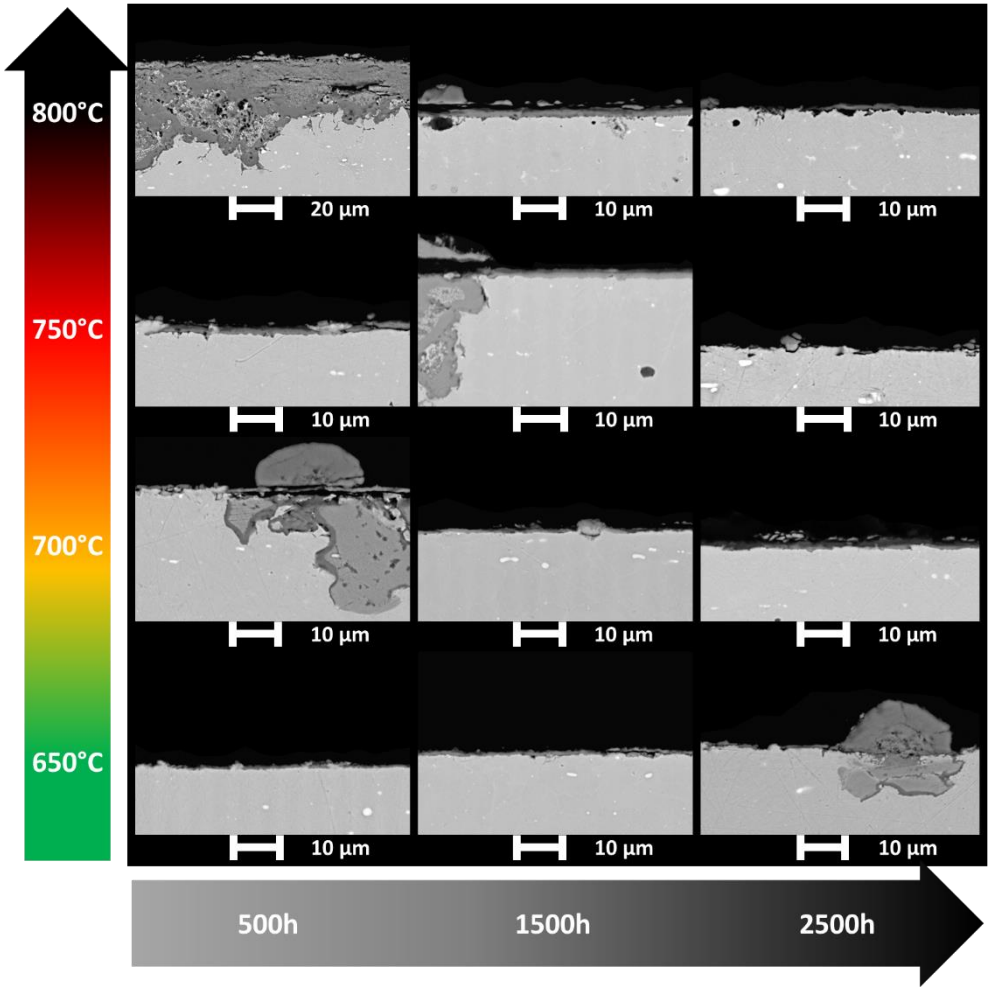

Figure 4-25: SEM images for cross-sections of TP347HFG with a P2500 ground surface finish after steam oxidation at different temperatures and exposure time.

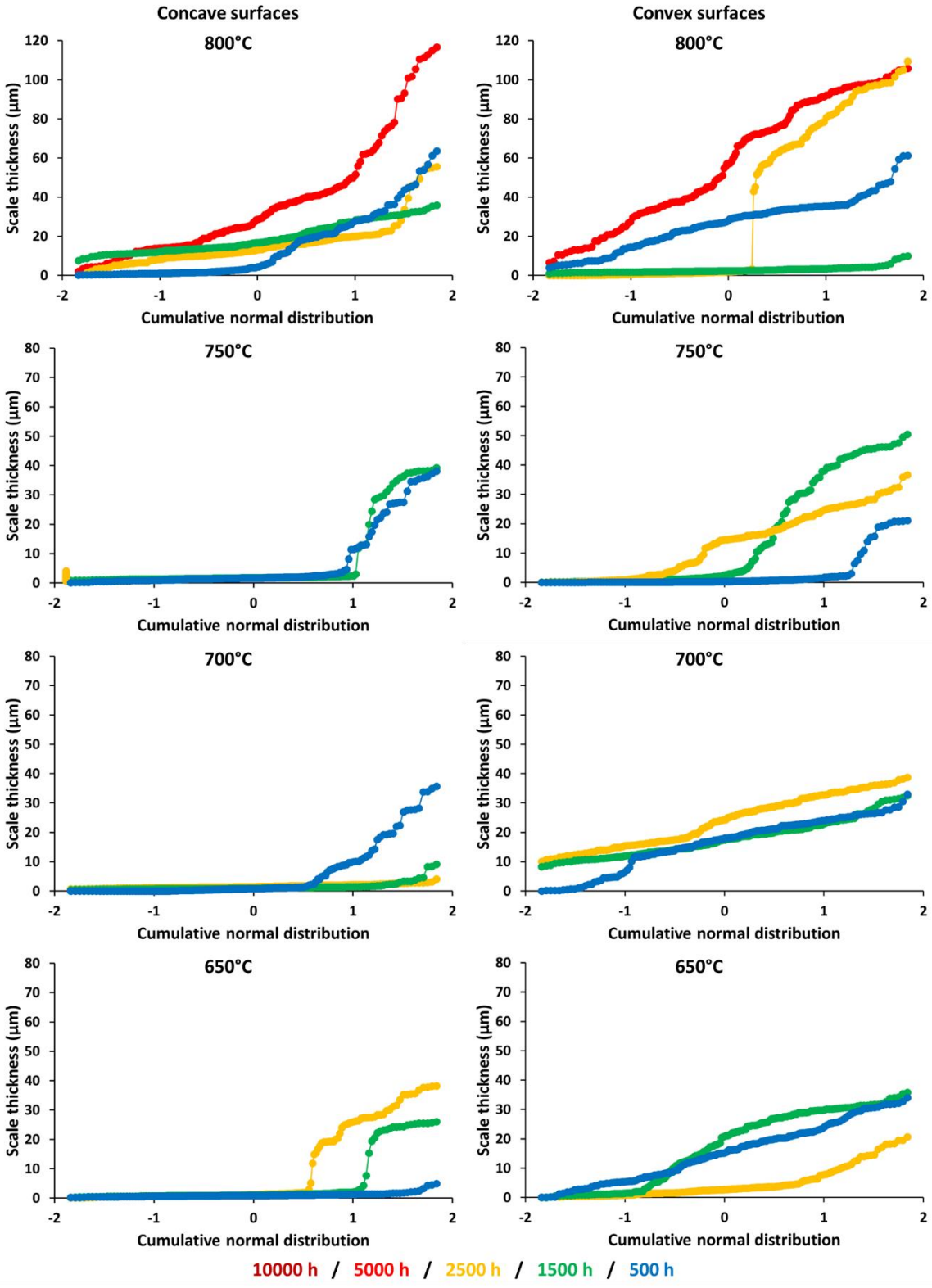

Figure 4-26: Cumulative normal distribution for the thickness of oxides formed on as-received concave surfaces and P2500 ground convex surfaces of TP347HFG after different exposure times at various temperatures.

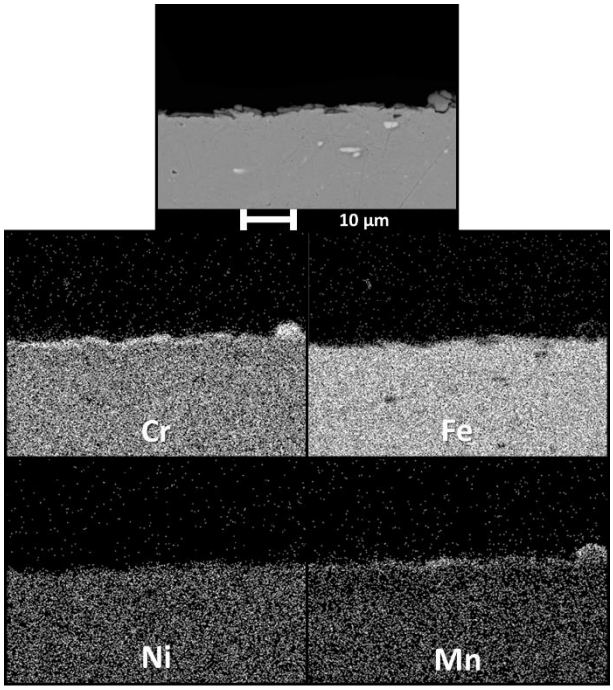

Figure 4-27: SEM image and elemental maps from EDX analysis for TP347HFG with P2500 ground surface finish after steam oxidation at 800°C for 2500 hours.

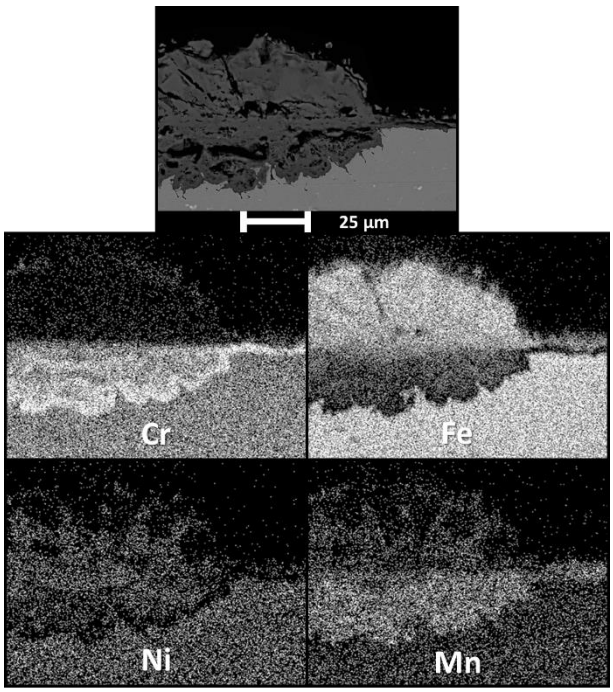

Figure 4-28: SEM image and elemental maps from EDX analysis for TP347HFG with P2500 ground surface finish after steam oxidation at 750°C for 2500 hours.

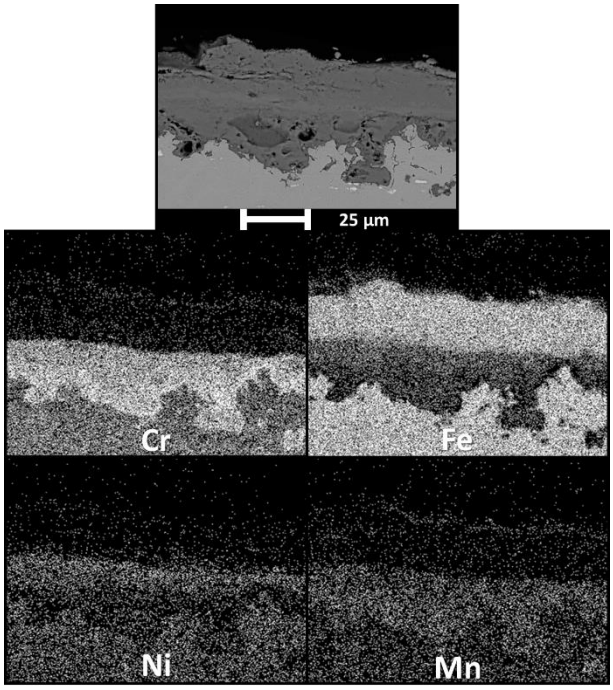

Figure 4-29: SEM image and elemental maps from EDX analysis for TP347HFG with as-received surface finish after steam oxidation at 700°C for 2500 hours.

The oxides formed on the as-received (Figure 4-15 and Figure 4-22), P2500 ground (Figure 4-24) and P1200 ground (Figure 4-17) surfaces are different in terms of composition and morphology. The XRD spectra show that the peaks related to the iron matrix are more visible on P1200 ground (Figure 4-14) and P2500 ground (Figure 4-21) surfaces compared to the as-received surfaces (Figure 4-13 and Figure 4-20) which means the oxide layer formed on those surfaces are thinner. Moreover, on as-received surfaces, the oxides formed are expected to be a mixture between iron oxides and chromium-rich oxides (Figure 4-13 and Figure 4-20). The XRD spectra are not enough to determine the exact nature of the oxides formed because the peaks for magnetite and chromia are close to one another so SEM images and EDX analysis had to be performed on the different surfaces. These images and analysis showed that on as-received surfaces (Figure 4-15 and Figure 4-22) iron oxides nodules are formed and spread on top of a chromium-rich layer similarly to what is presented in Figure 4-28. Areas where exfoliation are also visible which is in accordance with the mass data and the cross-section images. For P1200 ground surfaces (Figure 4-17),

the grinding marks are still visible which is representative of the thin thickness of the oxide layer formed. The analyses have determined this oxide layer is composed of chromia, similar to what is presented in Figure 4-27. After 5000 hours, iron-oxide nodules are formed on the surface which means the protectiveness of the chromia layer is no longer efficient (similarly to Figure 4-28). For P2500 ground surfaces (Figure 4-24), it is clear that iron-oxide nodules are forming on a thin layer of chromia at all the exposure times (Figure 4-28).

At between 700 and 800°C, after the maximum mass change point is reached, the different samples experience a spallation process which increases with increasing steam temperature and exposure time (Figure 4-12). When the steam temperature increases, the transition time at which exfoliation starts is diminishing and the slope for the loss of mass increases as well (as seen on the graph for machined surfaces). When comparing the data for the different surface finishes, it seems that at 700°C P1200 ground surfaces possess a better oxidation resistance than as-received and P2500 ground surfaces (Figure 4-12). However, at the higher temperatures it seems the as-received surfaces are more resistant. This is something that was not expected.

XRD spectra (Figure 4-14) show that for P1200 ground surfaces the peaks for the iron matrix are still detected bellow 5000 hours between 700 and 800°C. Thus the oxide layer should remain thin for those samples. However for 5000 and 10,000 samples, the oxides layers are expected to be thicker and the spectra clearly indicate the presence of iron oxides and probably chromium-rich oxide as well. At 700 and 750°C and before 5000 hours, only thin chromia layers are observed (Figure 4-17 and Figure 4-18). However, after 5000 hours a thick and multi-layered oxide can be seen, with chromium-rich oxides and iron oxides (Figure 4-29). Some iron-oxide nodules and spalled areas are also visible. The huge difference between the samples exposed until 2500 hours and those exposed for longer times may come from the preparation procedure. Indeed, the samples for 500, 1500 and 2500 hours have been exposed by a previous student at Cranfield University and it seems that he used a different grinding than the one described in the methodology. Due to a lack of time and empty slots in the steam furnaces, those samples could not have been reproduced to verify if sample preparation really was the source of the differences observed. At 800°C, grinding marks are still present on the areas where the chromia layer remains (Figure 4-17),

showing this layer is thin. Iron-oxide nodules are present and are proof the protectiveness of the chromia layer is too weak at this temperature and breakaway oxidation in quickly experienced for the material. At the longest times, exfoliation is visible and the oxide multi-layered oxides formed are really large. For the sample exposed for 5000 hours, it seam the iron-oxide layer has spalled and only the inner chromium-rich layer remains.

For the P2500 ground surfaces, XRD peaks related to the iron matrix are still present until 800°C and 1500 hours (Figure 4-21). The surface of these P2500 ground samples are thus covered with a thin oxide layer. The SEM images of the oxidized surfaces (Figure 4-24) and of the cross-sections (Figure 4-25) support the previous statement and show that even if the surface is covered with a thin chromia layer, iron-oxide nodules are present on top of it but do not entirely cover the surface. The nodules formed are experiencing spallation even when they are not present over the entire surface of the samples. At 800°C, after 1500 hours, a large and complex multi-layered oxide is visible.

When comparing the P1200 and P2500 ground surfaces, it seems the P2500 ground surface possesses a lower oxidation resistance. More nodules are visible on the P2500 ground surfaces (Figure 4-24). However, it remains better protective than the as-received surface which is fully covered with a multi-layered oxide after 700°C (Figure 4-22). The mass change data (Figure 4-12) show that at 750 and 800°C the as received surfaces possess a better oxidation resistance than the P1200 ground surfaces but this is not true and the error observed on the graphs comes from how the calculations are done for the as-received surfaces. Indeed, the samples possess both as-received and P1200 ground surfaces so to de-correlate the specific mass change for the as-received surfaces, the effect of the P1200 ground surfaces, obtained with specific samples, have been subtracted using Equation (3-2). This de-correlation affects the slopes of the mass loss observed.

Finally, for the as-received surfaces, two sets of images presented in Figure 4-15 and Figure 4-22 are showing what happens on those specific surfaces and this redundancy is interesting to see if the results, in terms of oxide composition and morphology, are reproducible. XRD data (Figure 4-13 and Figure 4-20) inform that thick oxide layers

are expected to form when exposed to steam over 700°C. Some samples exposed at 700°C still exhibit a thin chromia layer at some locations with some iron-oxide nodules. However at the higher temperatures multi-layered oxides are observed with iron oxides formed above an inner chromium-rich layer (Figure 4-15, Figure 4-16, Figure 4-22, Figure 4-23 and Figure 4-29). Spallation of the outer iron oxide can been seen and reveal the inner layer underneath it.

In terms of oxide thickness, it appears the oxide scales growing on the P1200 and P2500 ground surfaces are similar than the ones growing on the as-received surface of the sample (Figure 4-19 and Figure 4-26). The thickness distributions presented for the different surfaces finishes of TP347HFG showed large differences with the normal distribution. These differences could be explained by the exfoliation phenomenon and the nodular growth of the oxide that can be responsible for the recording of respectively lower and higher values of scale thickness compared to the normal distribution. By looking at the curve's shape, it can be deduced that the oxide scale growing on the P1200 ground surface was uniform and was affected by nodular growth and spallation only at long exposure time. The as-received surface seemed to be more affected by these phenomena even at short exposure time.

Various surface finishes have been applied on TP347HFG to assess their effect on the steam oxidation process. As-received, P1200 and P2500 ground surfaces have been previously presented and in addition a machining and two different shot-peening techniques were applied to the concave surfaces or TP347HFG. These additional surface finishes significantly increase the compressive stresses to the surface of the material (Figure 4-10 (b)) and, since shot-peening has been reported to greatly increase steam oxidation resistance for austenitic steels [13,66,69], the samples with shot-peened and machined surfaces have only been exposed for 10,000 hours. Mass change data has only been recorded for as-received, P1200 and P2500 ground surfaces and have been presented earlier. However, for machined and shot-peened surfaces, only the surface analyses and characterization have been performed which lead to oxide thickness measurements.

Figure 4-30 shows the morphology and composition of the oxides formed at surfaces originally prepared with different surface finishes, Figure 4-31 presents the cross-

sectional images associated, and Figure 4-32 presents the normal cumulative distributions associated with the oxide thickness measurements performed. Only data at 700 and 800°C have been obtained and the different samples were exposed to steam for 5000 or 10,000 hours.

At 700°C, as-received surfaces exhibit an oxidized surface covered with iron-oxide nodules under which a inner chromium-rich layer is present (similar to Figure 4-28). Low oxide thickness was measured and spallation does not seems to occur. Indeed the normal cumulative distribution for the oxide thickness measured only shows a straight line and no steps. However, at 800°C the as-received surface shows the formation of a large multi-layered oxide with some areas were spallation has occurred. P1200 ground surfaces at 700 and 800°C both show the formation of large multi-layered oxides which is subjected to spallation. P2500 ground surface at 800°C and after 5000 hours of steam exposure show the same features and composition that oxidized P1200 ground surfaces, but the oxide thickness is measured to be higher. With the exception of the as-received surface at 700°C, these three surface finishes show the formation similar oxide layers in terms of composition and morphology.

Machined surfaces have formed a thin protective chromium-rich oxide layer with nodules at 700°C. The nodules are multi-layered with inner chromium-rich oxide and iron oxide on top of it (cf. Figure 4-28). At 800°C, only a thin chromium-rich layer was observed (cf. Figure 4-27). Therefore, it seems that the machined surface was more resistant at 800°C than at 700°C, which was unexpected. Indeed, oxidation kinetics were expected to increase with increasing temperature. The apparition of nodules at 700°C and not at 800°C is a clear demonstration that, for chromia forming surfaces, higher temperatures contribute to the formation of better protective chromia layer due to the enhancement of chromium diffusion at higher temperatures.

PISCO and SANYO shot-peening procedures have both produced high oxidation resistant surfaces. Which have formed a thin chromium-rich layer on all surfaces observed except for the surface with the PISCO shot-peening at 800°C on which nodular growth is observed.

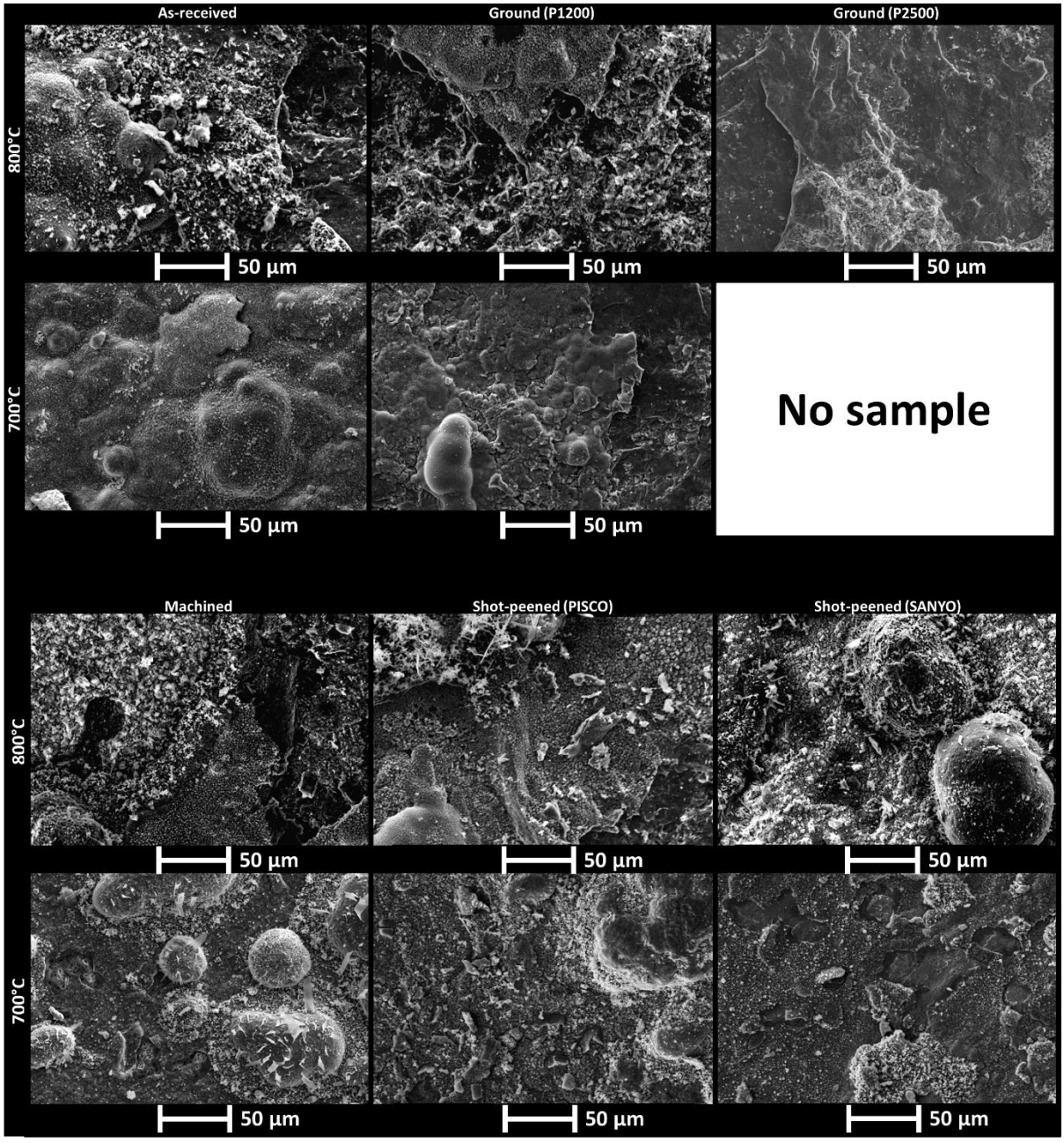

Figure 4-30: SEM images for TP347HFG with different surface finishes after 10,000 hours steam oxidation at 700 and 800°C (for the P2500 ground surface presented the exposure time is 5000 hours).

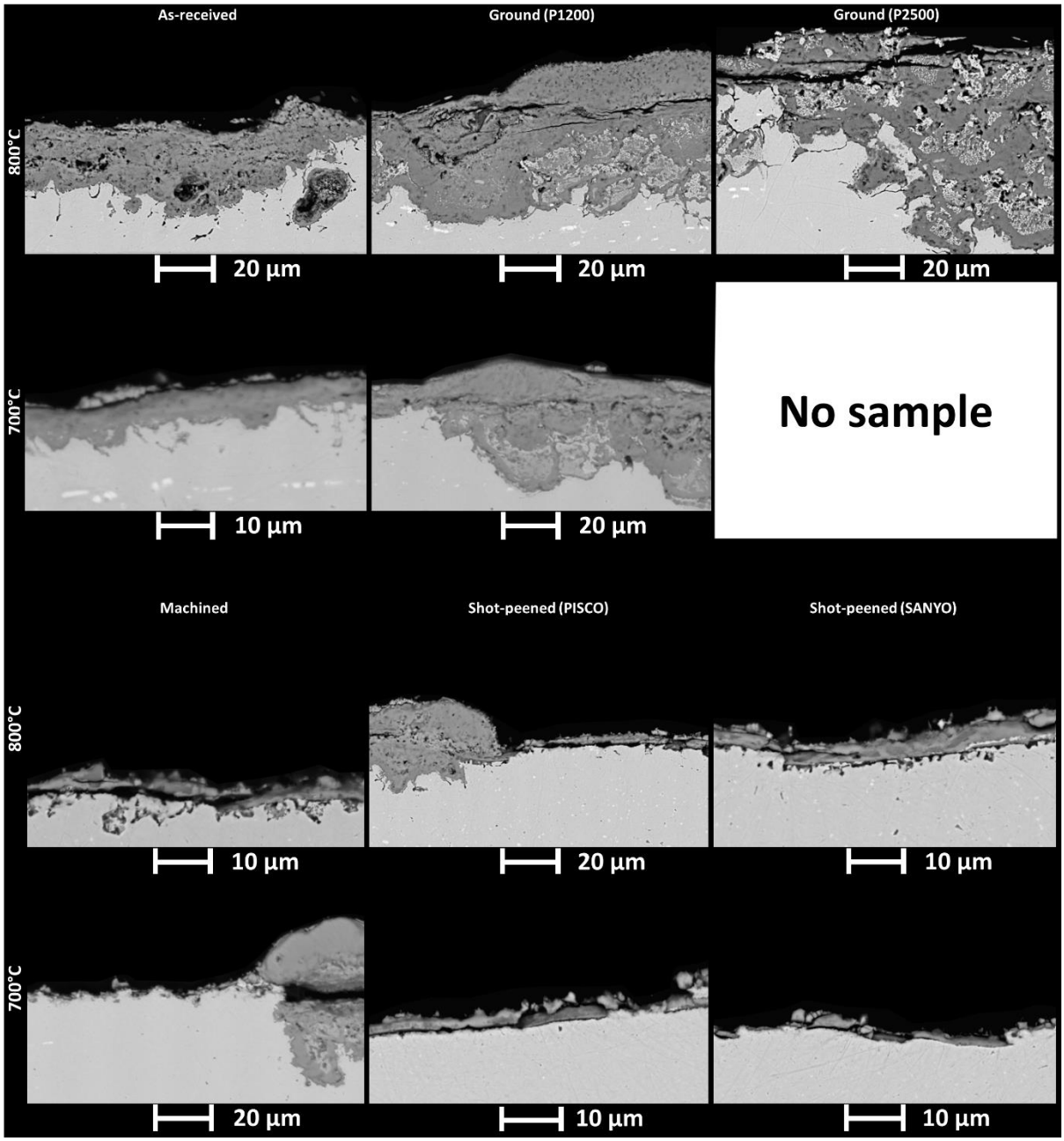

Figure 4-31: SEM images for cross-sections of TP347HFG with different surface finishes after 10,000 hours steam oxidation at 700 and 800°C (for the P2500 ground surface presented the exposure time is 5000 hours).

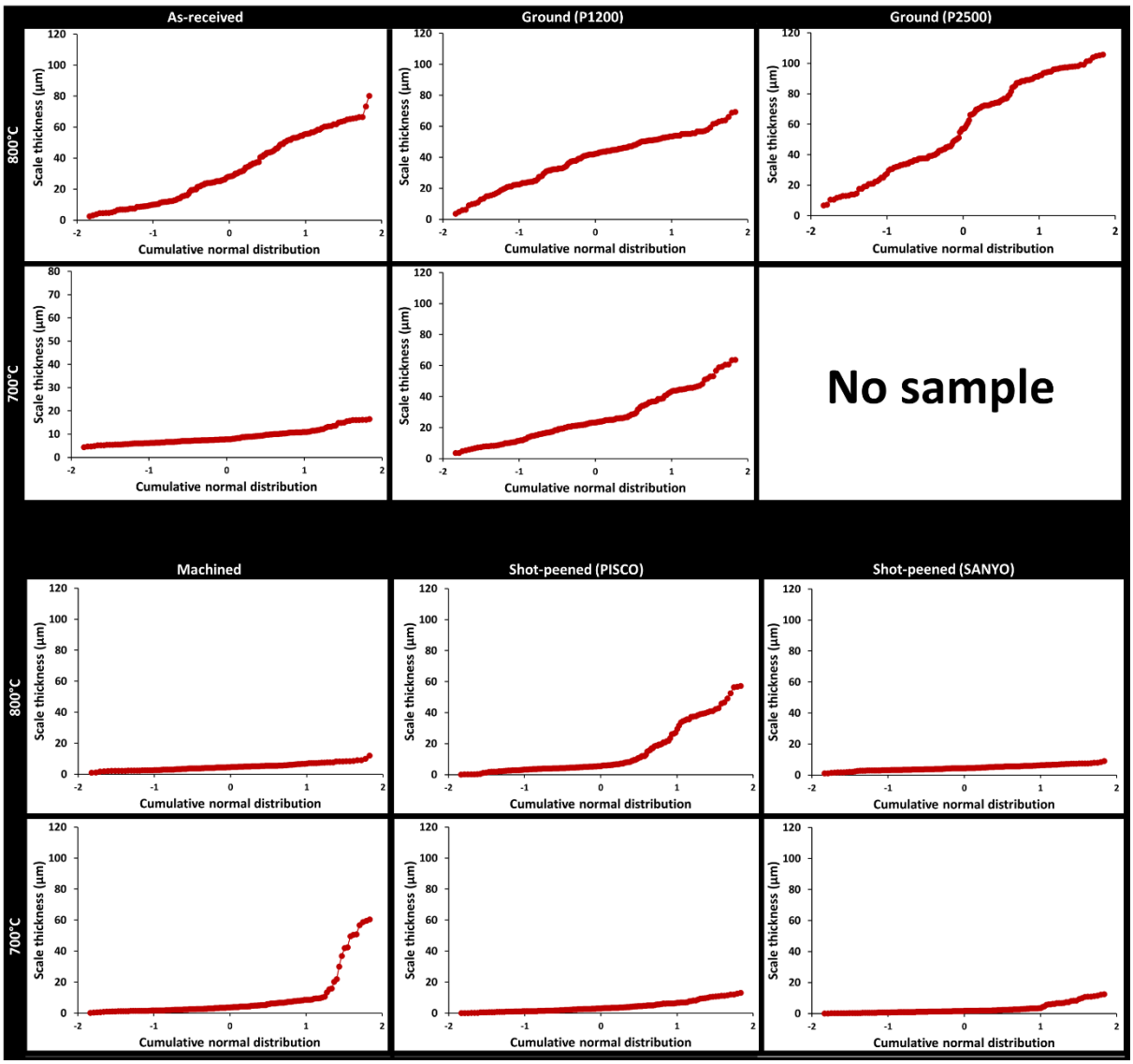

Figure 4-32: Cumulative normal distribution for the thickness of oxides formed on the various samples of TP347HFG with different surface finishes after 10,000 hours steam oxidation at 700 and 800°C (for the P2500 ground surface presented the exposure time is 5000 hours).

Figure 4-33 presents the medial oxide thickness measured, for the different surfaces exposed at 700 and 800°C, as a function of the stress levels measured on the different surfaces tested (data from Figure 4-10(b)). For both temperatures it is clear that the oxidation resistance of the different surfaces in terms of oxide growth increases significantly with increasing compressive stresses applied thanks to surface working. Even though oxide thickness seems to diminish exponentially with increasing compressive stresses, the data obtained is very scattered, especially for surfaces with

low compressive stresses, which does not allow correlating the oxide thickness with the level of stresses. Later in this report, the activation energies calculated for the different surface finishes are plotted as a function of stress levels (Figure 4-110).

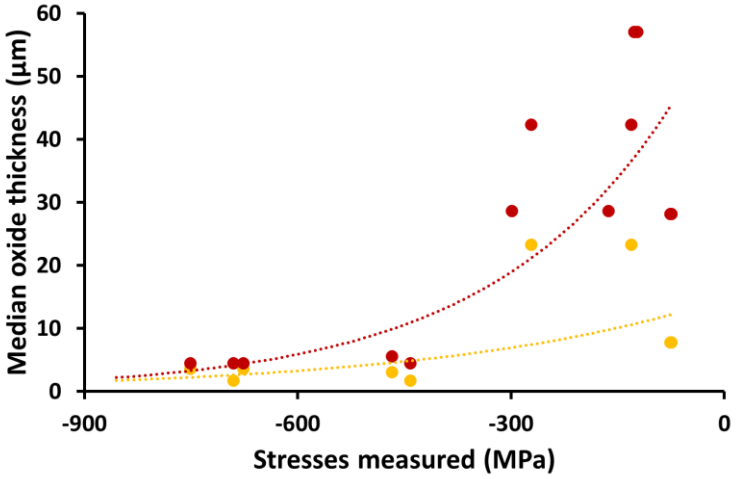

Figure 4-33: Representation of the median oxide thickness measured on TP347HFG's samples as a function of the residual stress measured on the surfaces oxidized after 10,000 hours steam oxidation at 700 and 800°.

For machined and shot-peened surfaces, only one sample was exposed for 10,000 at the different temperatures. Replica of the samples exposed would have been helpful to determine if the nodular growth, happening for some of the samples prepared with those surface finishes, is a consistent observation or not and would have helped in drawing more solid conclusion about what really happens with those particular surfaces. The absence of replica was due to the limited space available in the different furnaces used.

4.2.1.2. Sanicro 25

Sanicro 25 is a material that exhibits a very high steam oxidation resistance. Indeed, when looking at the net mass change data on Figure 4-34, the values are very low (<2mg.cm-2) and exfoliation does not seems to be significant. For P1200 ground surfaces, the mass gain increases slightly with increasing exposure time and steam

temperature (Figure 4-34). The values obtained at 750 and 800°C are similar which results from a very good high temperature steam oxidation resistance.

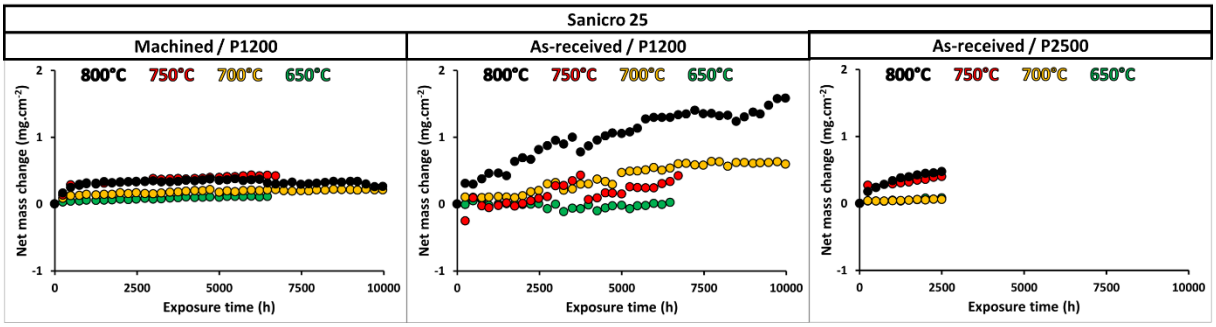

Figure 4-34: Net mass change data related to the different surface finishes of Sanicro 25 exposed for up to 10,000 hours.

Data for Sanicro 25 samples with their concave and convex surfaces having respectively an as-received and a P1200 ground surface finish is presented hereafter. XRD spectra for as-received and P1200 ground surfaces of Sanicro 25 are presented in Figure 4-35 and Figure 4-36. SEM images of the oxidized surfaces and cross-sections are presented in Figure 4-37 and Figure 4-38 for the as-received surfaces and in Figure 4-39 and Figure 4-40 for the P1200 ground surfaces. Then Figure 4-41 presents the EDX analysis performed on an oxidized surface showing the presence of a chromia layer, whereas Figure 4-42 shows the elemental mapping associated with the EDX analysis for a cross-section exhibiting a nodule and a chromia layer. The oxide thickness distributions for oxide thicknesses measured on as-received and P1200 ground surfaces are presented in Figure 4-43. Exposure data for Sanicro 25 samples with concave as-received and convex P2500 ground surfaces are presented in the following figures. Figure 4-44 and Figure 4-45 show the XRD data respectively associated with exposed as-received and P2500 ground surfaces. Pictures of oxidized surfaces and cross-sections are respectively presented in Figure 4-46 and Figure 4-47 for as-received surfaces, and in Figure 4-48 and Figure 4-49 for P2500 ground surfaces. The oxide thickness distributions obtained for the as-received and P2500 ground surfaces are shown in Figure 4-50.

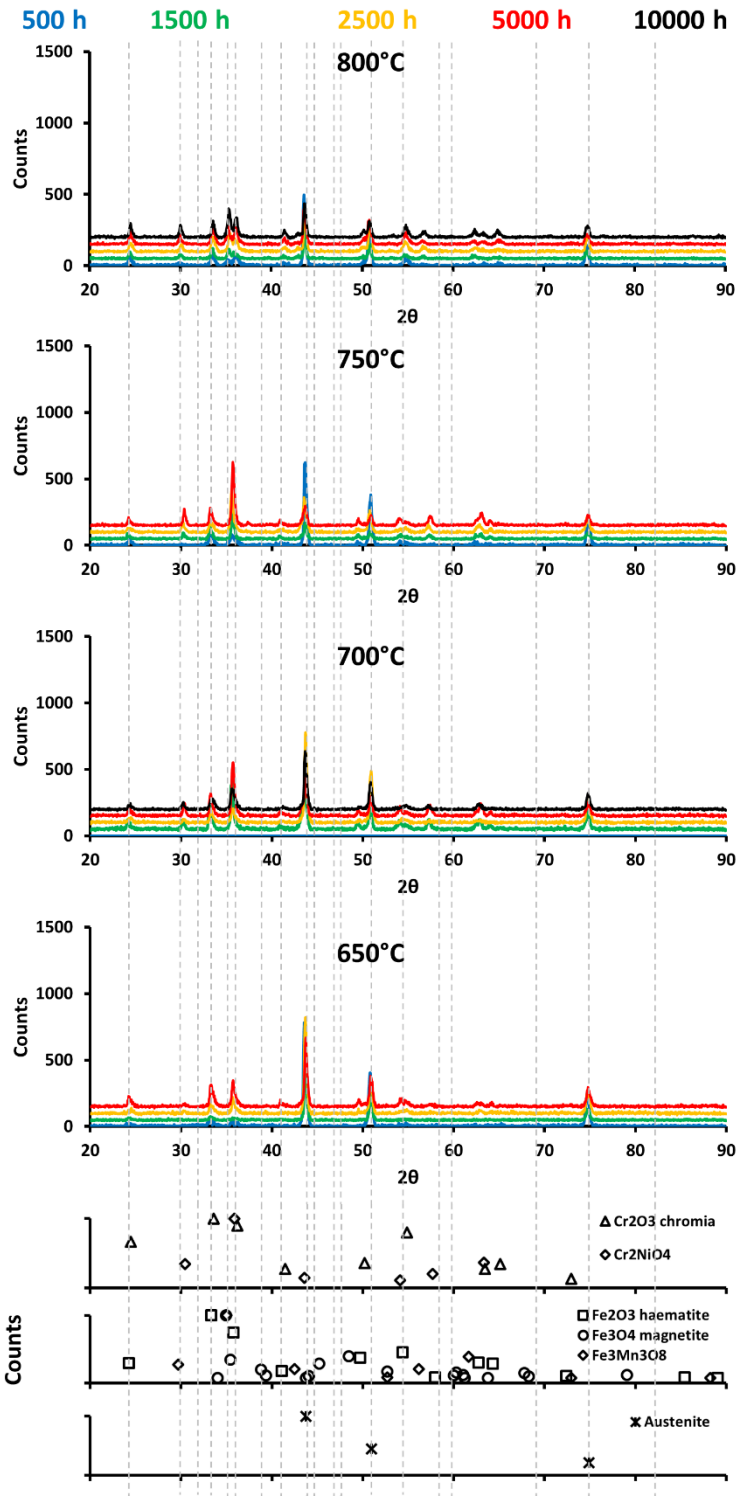

Figure 4-35: XRD spectra for Sanicro 25 with as-received surface finish after steam oxidation at different temperatures and exposure time.

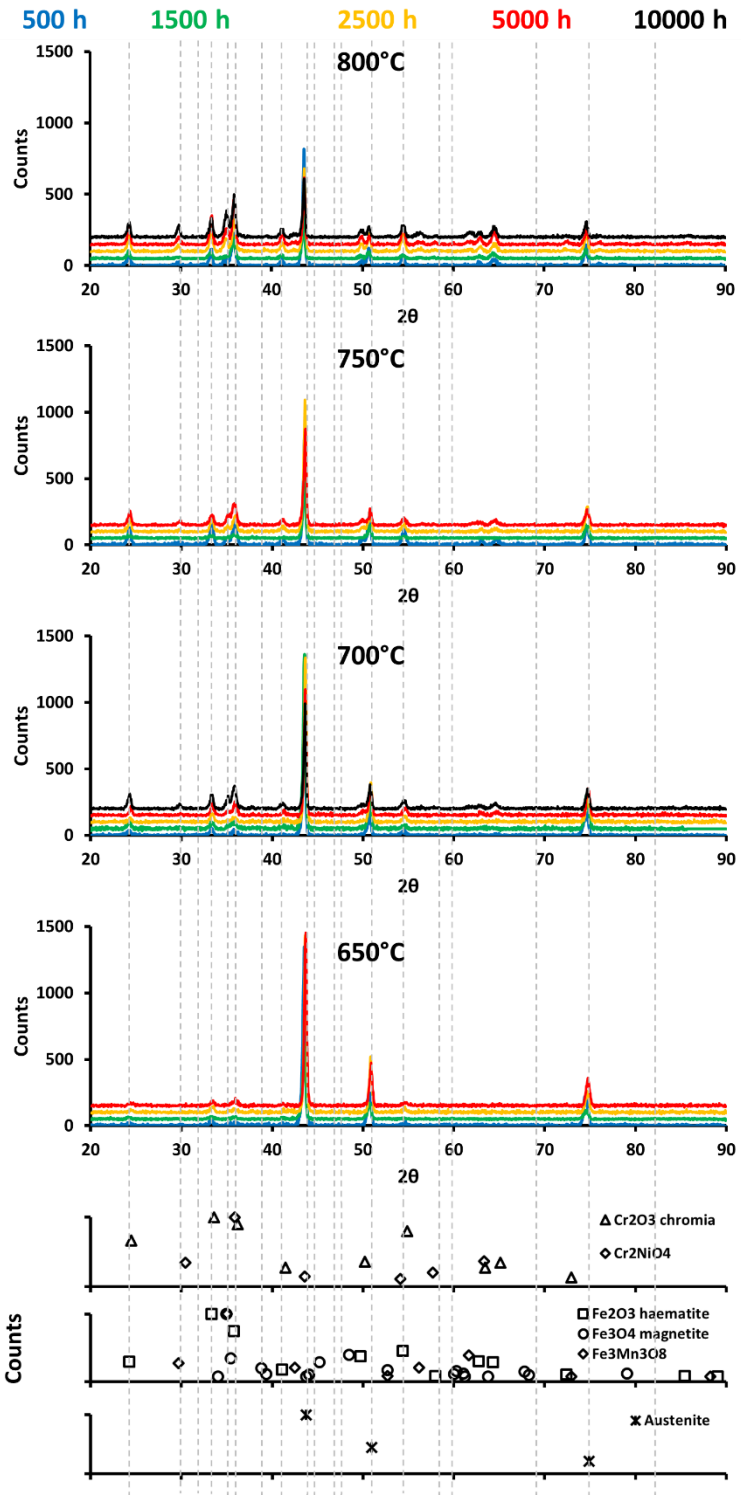

Figure 4-36: XRD spectra for Sanicro 25 with a P1200 ground surface finish after steam oxidation at different temperatures and exposure time.

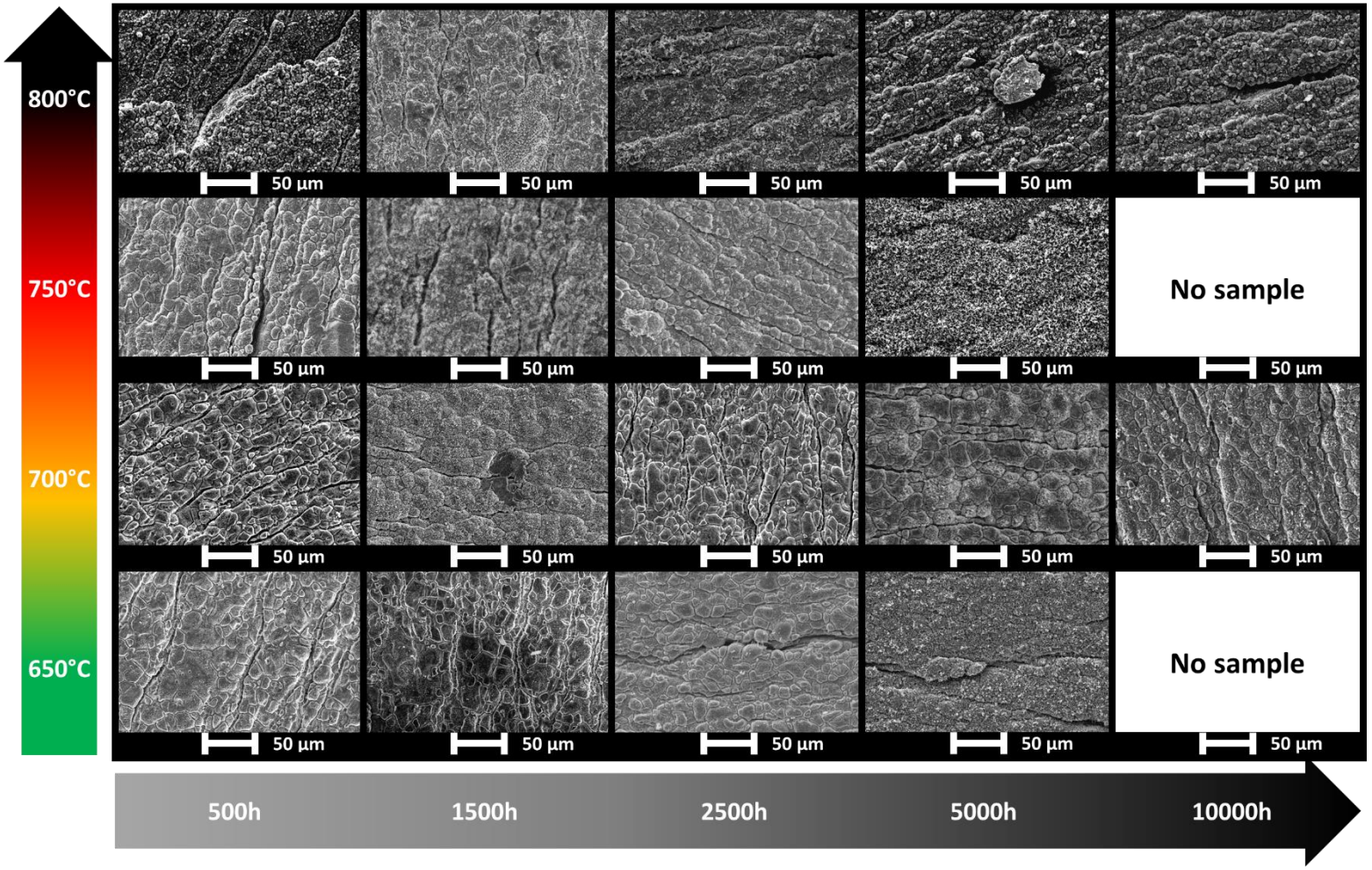

Figure 4-37: SEM images for Sanicro 25 with as-received surface finish after steam oxidation at different temperatures and exposure time.

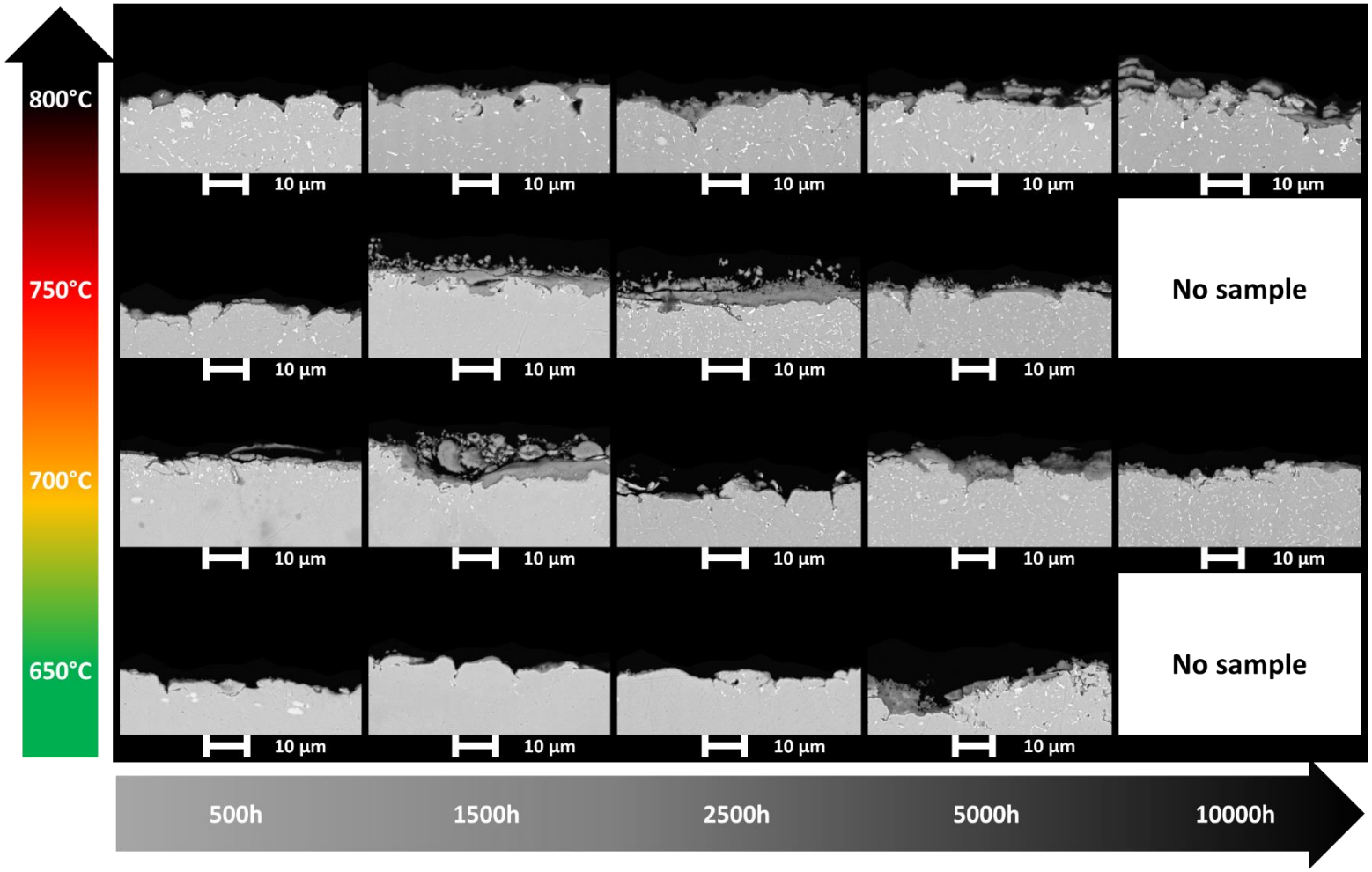

Figure 4-38: SEM images for cross-sections of Sanicro 25 with as-received surface finish after steam oxidation at different temperatures and exposure time.

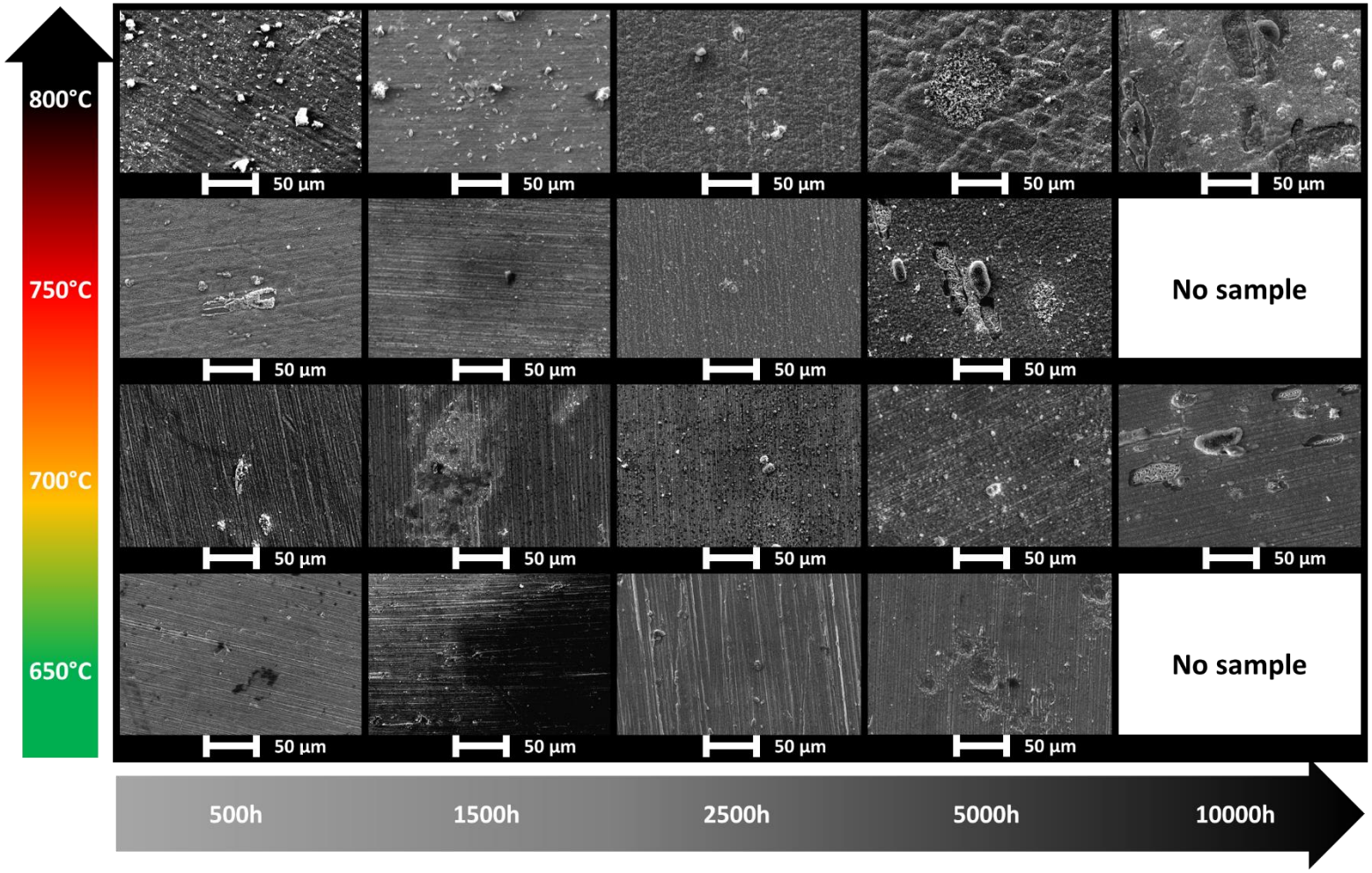

Figure 4-39: SEM images for Sanicro 25 with a P1200 ground surface finish after steam oxidation at different temperatures and exposure time.

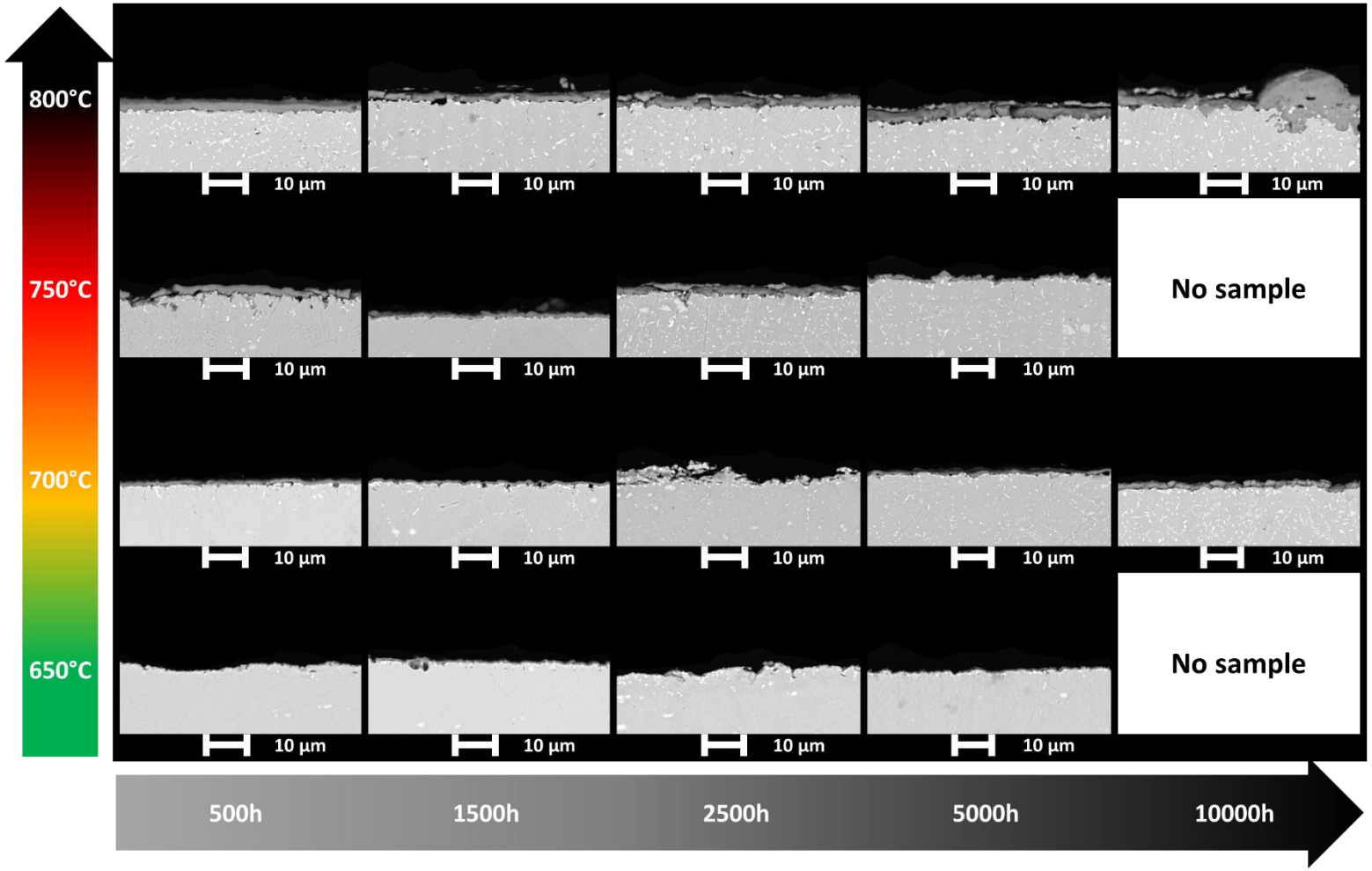

Figure 4-40: SEM images for cross-sections of Sanicro 25 with a P1200 ground surface finish after steam oxidation at different temperatures and exposure time.

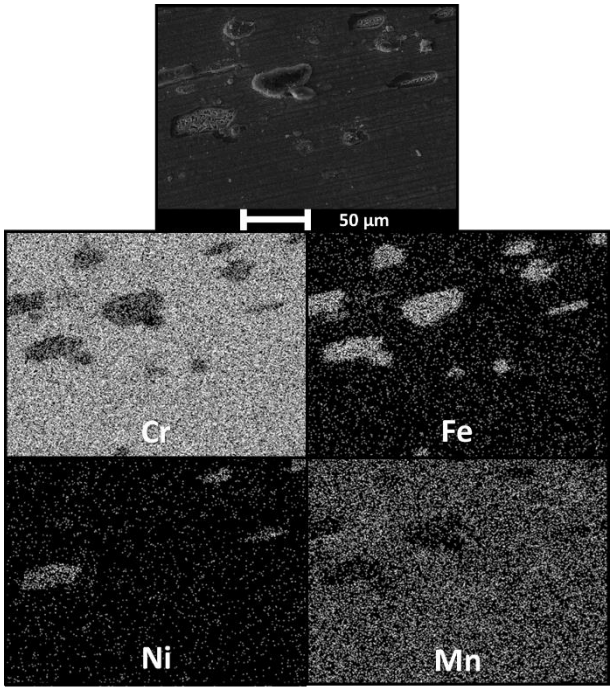

Figure 4-41: SEM image and elemental maps from EDX analysis for Sanicro 25 with P1200 ground surface finish after steam oxidation at 700°C for 10,000 hours.

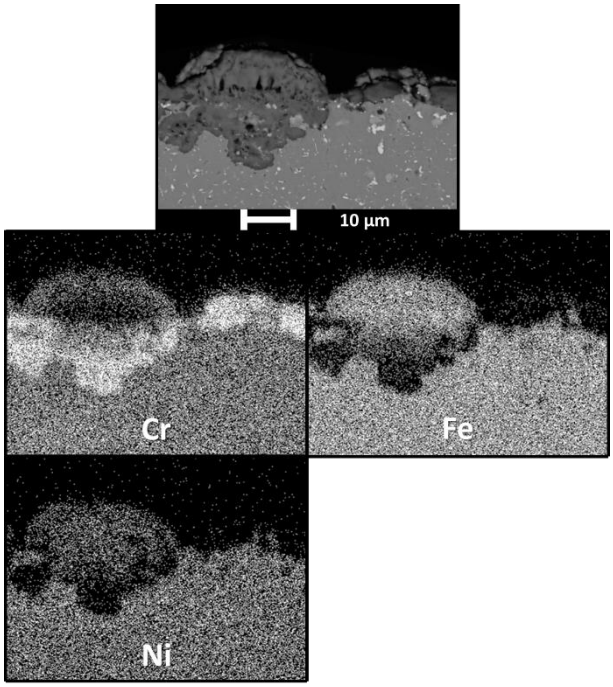

Figure 4-42: SEM image and elemental maps from EDX analysis for Sanicro 25 with P1200 ground surface finish after steam oxidation at 800°C for 10,000 hours.

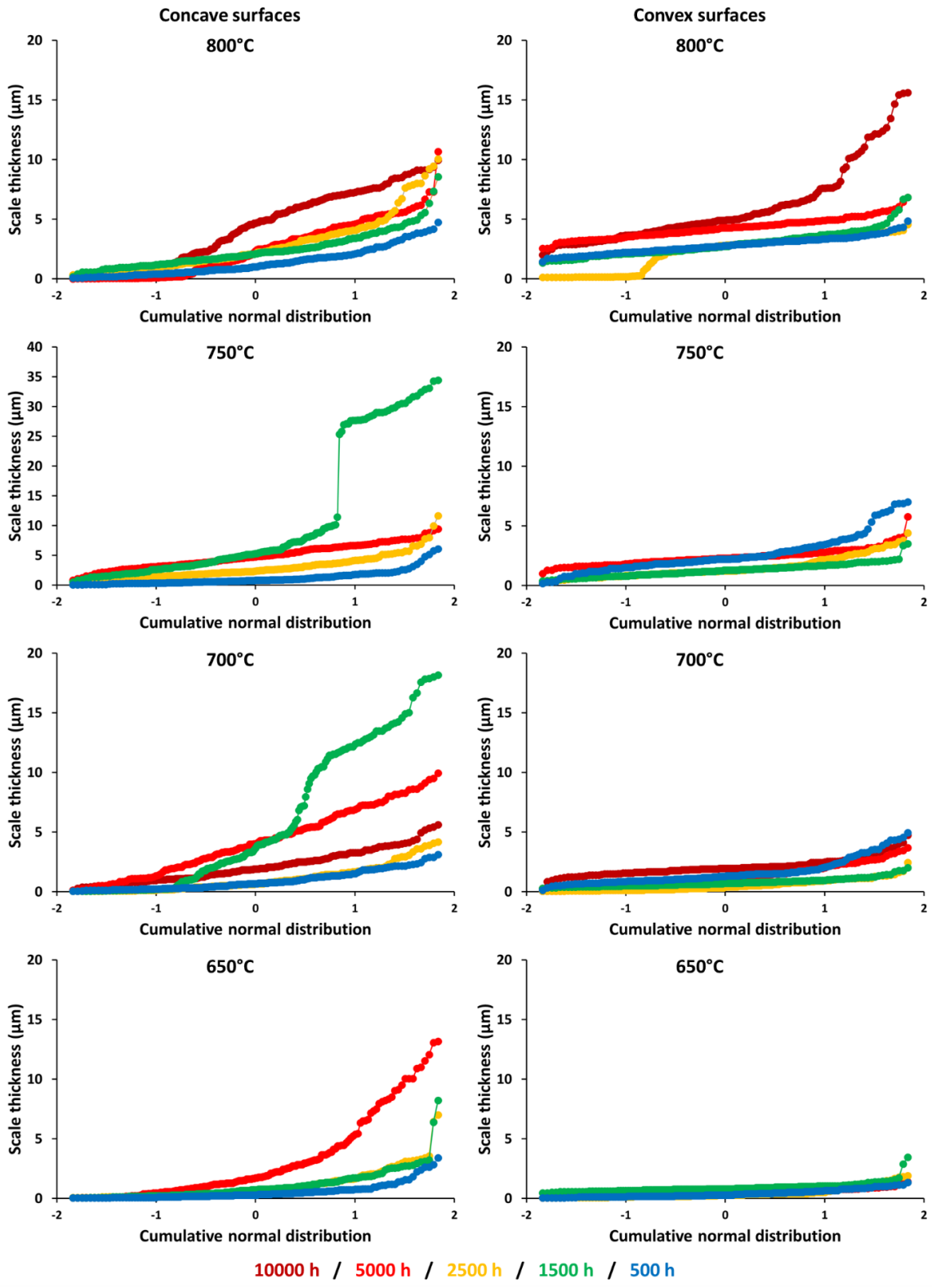

Figure 4-43: Cumulative normal distribution for the thickness of oxides formed on as-received concave surfaces and P1200 ground convex surfaces of Sanicro 25 after different exposure times at various temperatures.

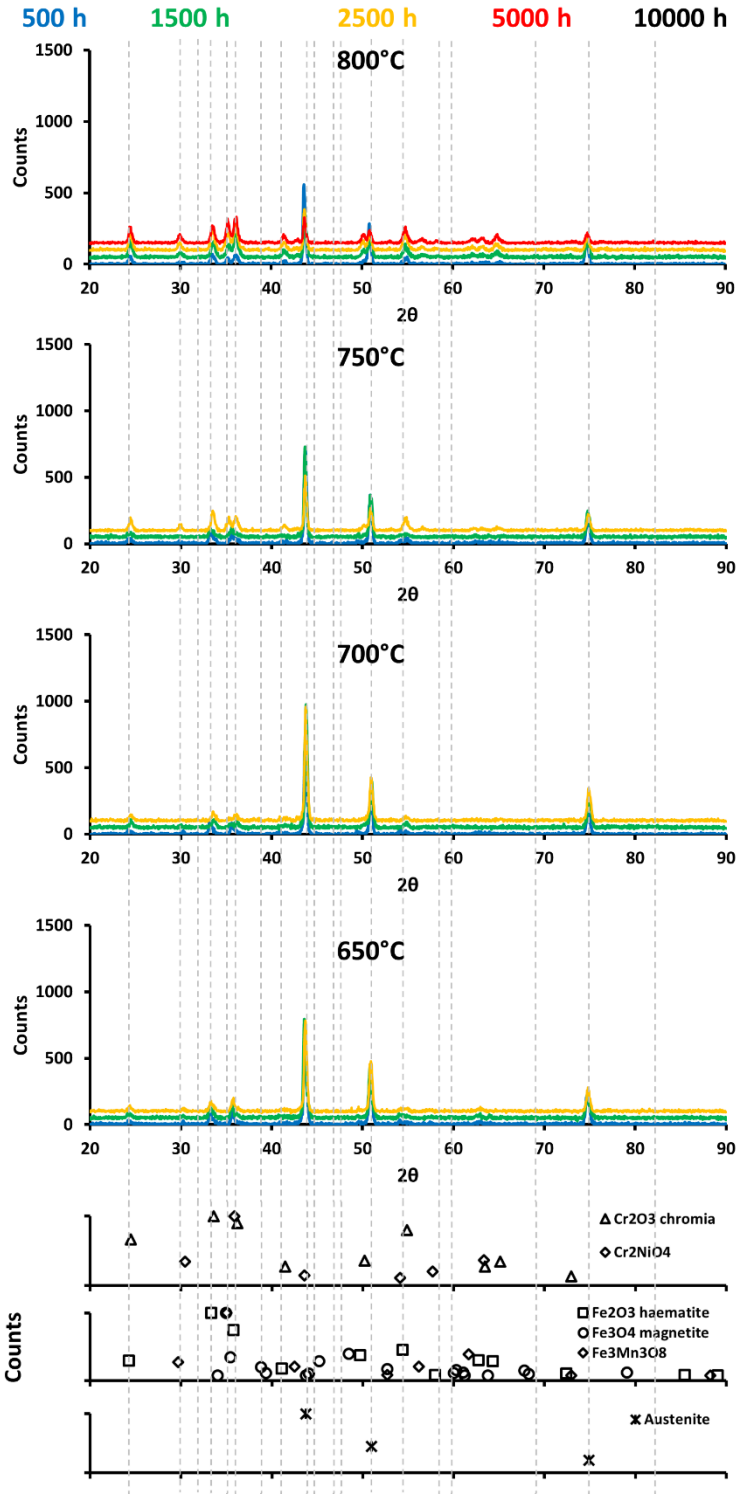

Figure 4-44: XRD spectra for Sanicro 25 with as-received surface finish after steam oxidation at different temperatures and exposure time.

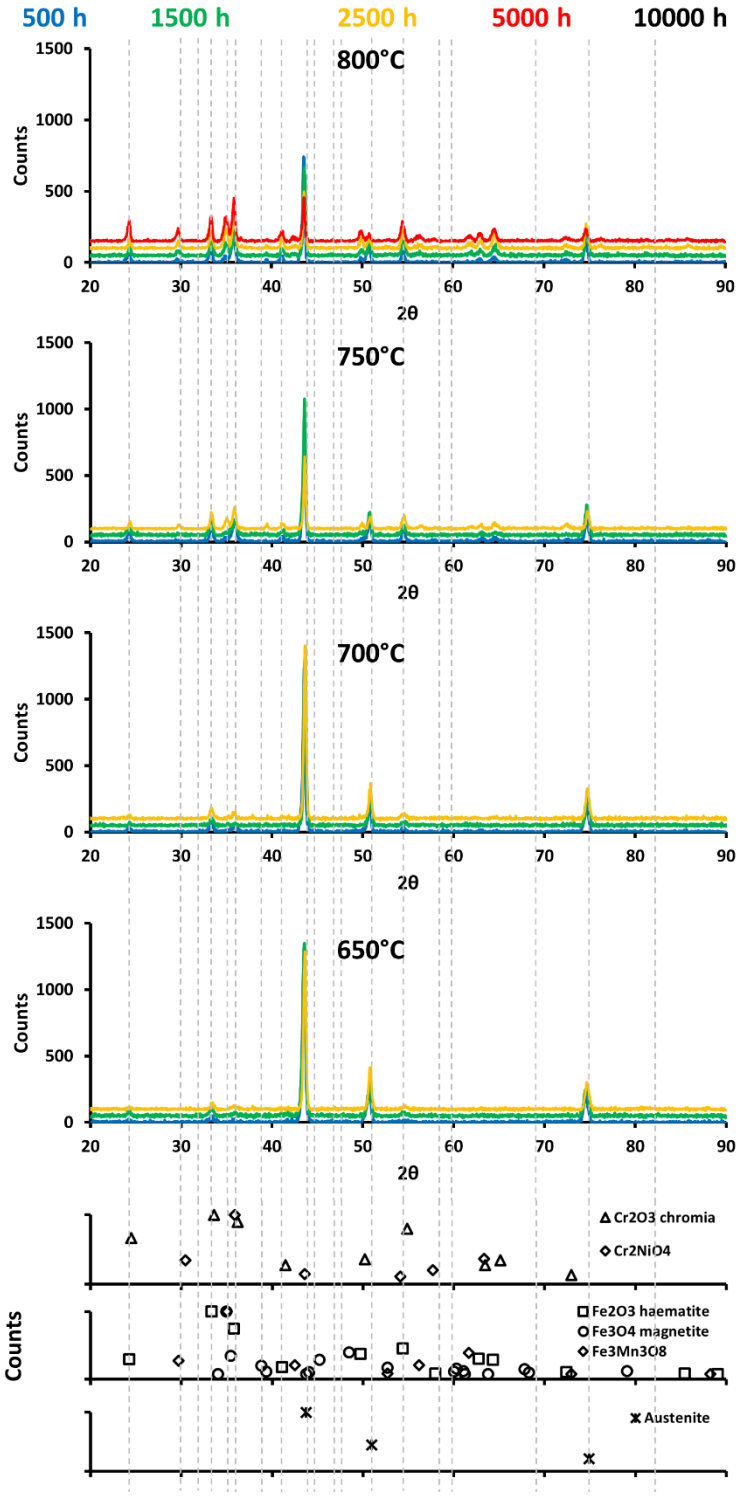

Figure 4-45: XRD spectra for Sanicro 25 with a P2500 ground surface finish after steam oxidation at different temperatures and exposure time.

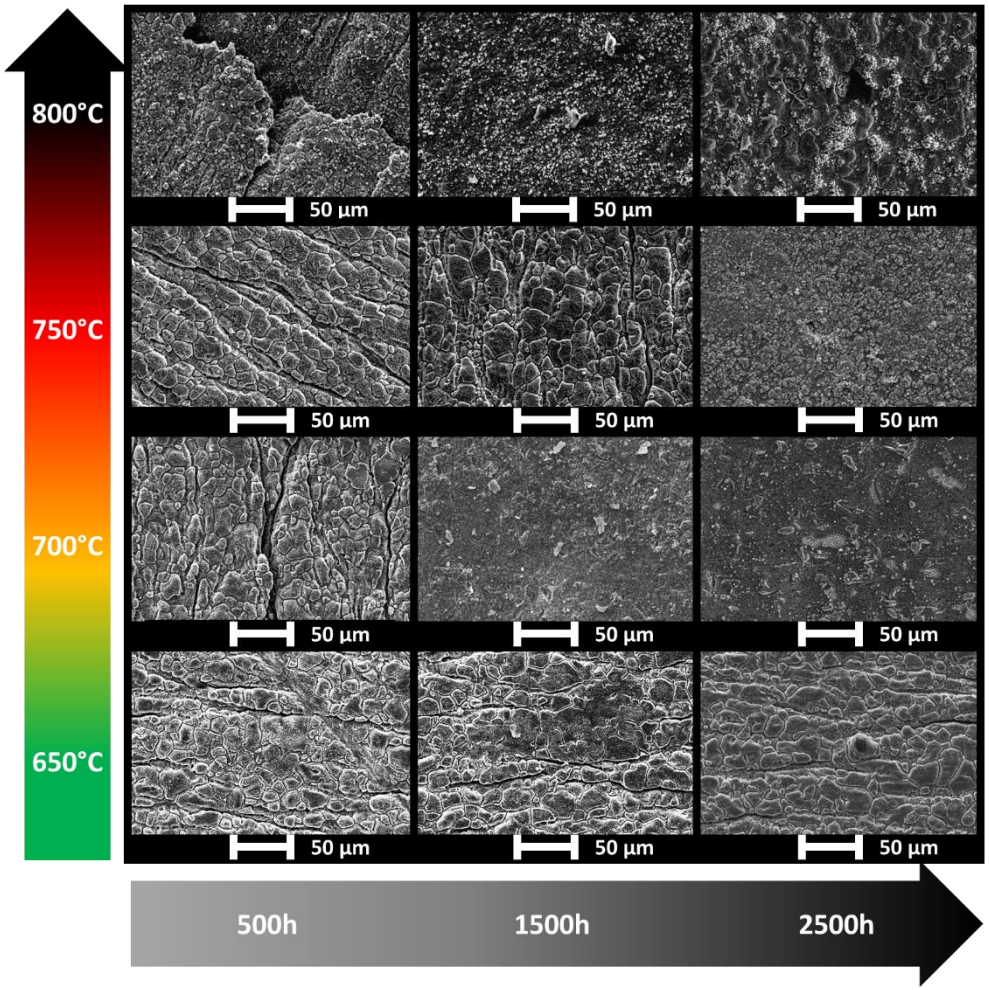

Figure 4-46: SEM images for Sanicro 25 with as-received surface finish after steam oxidation at different temperatures and exposure time.

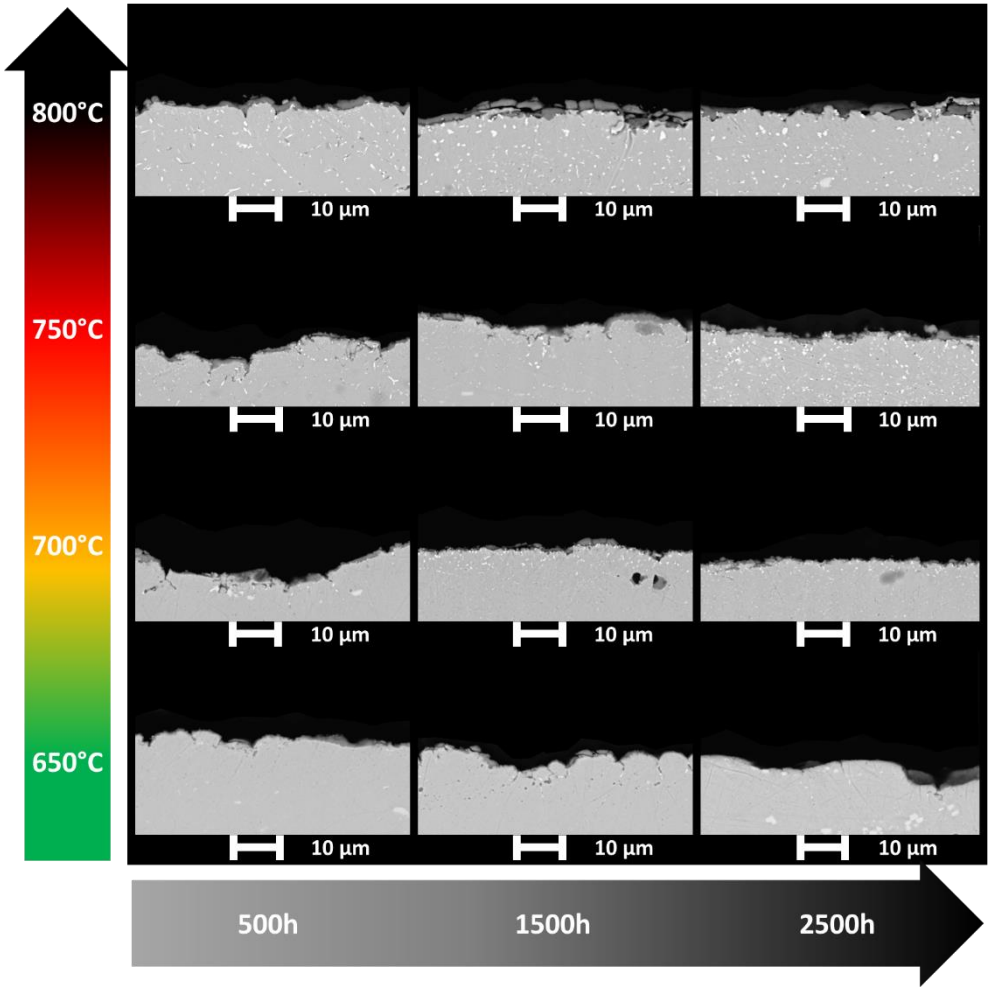

Figure 4-47: SEM images for cross-sections of Sanicro 25 with as-received surface finish after steam oxidation at different temperatures and exposure time.

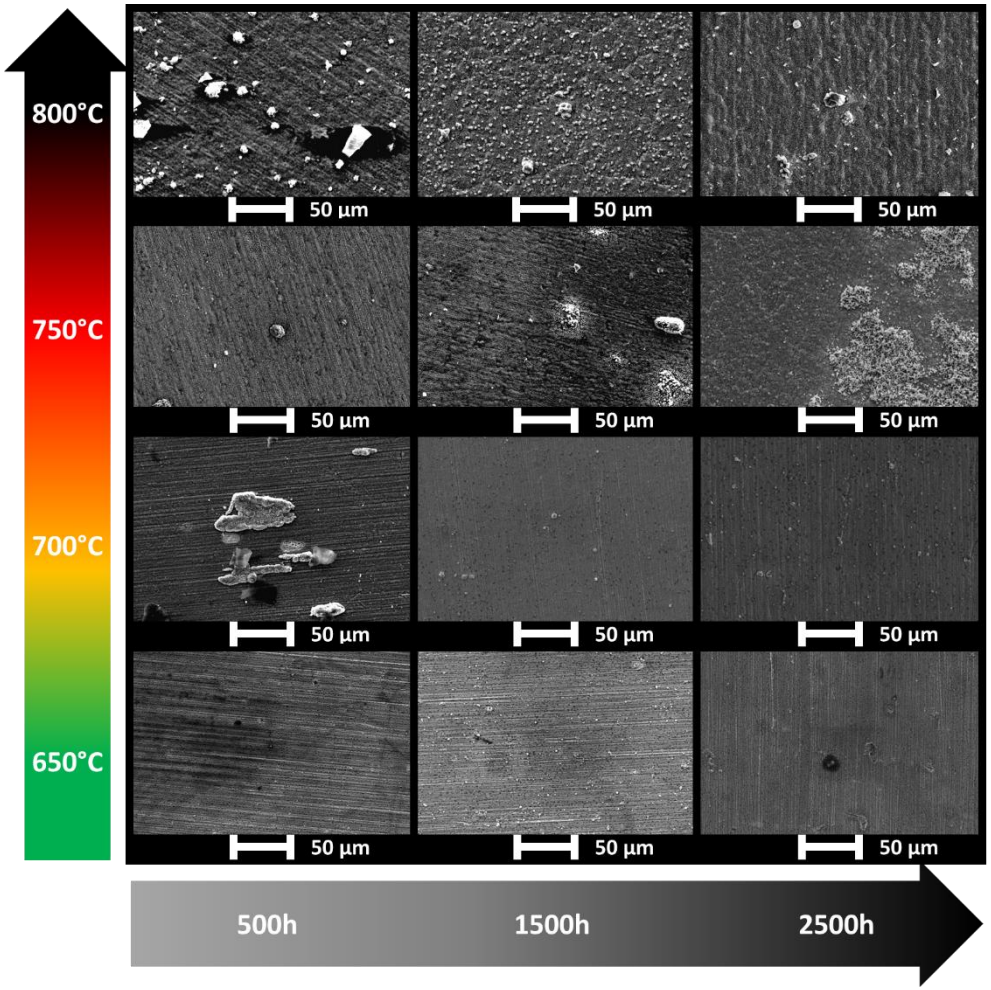

Figure 4-48: SEM images for Sanicro 25 with a P2500 ground surface finish after steam oxidation at different temperatures and exposure time.

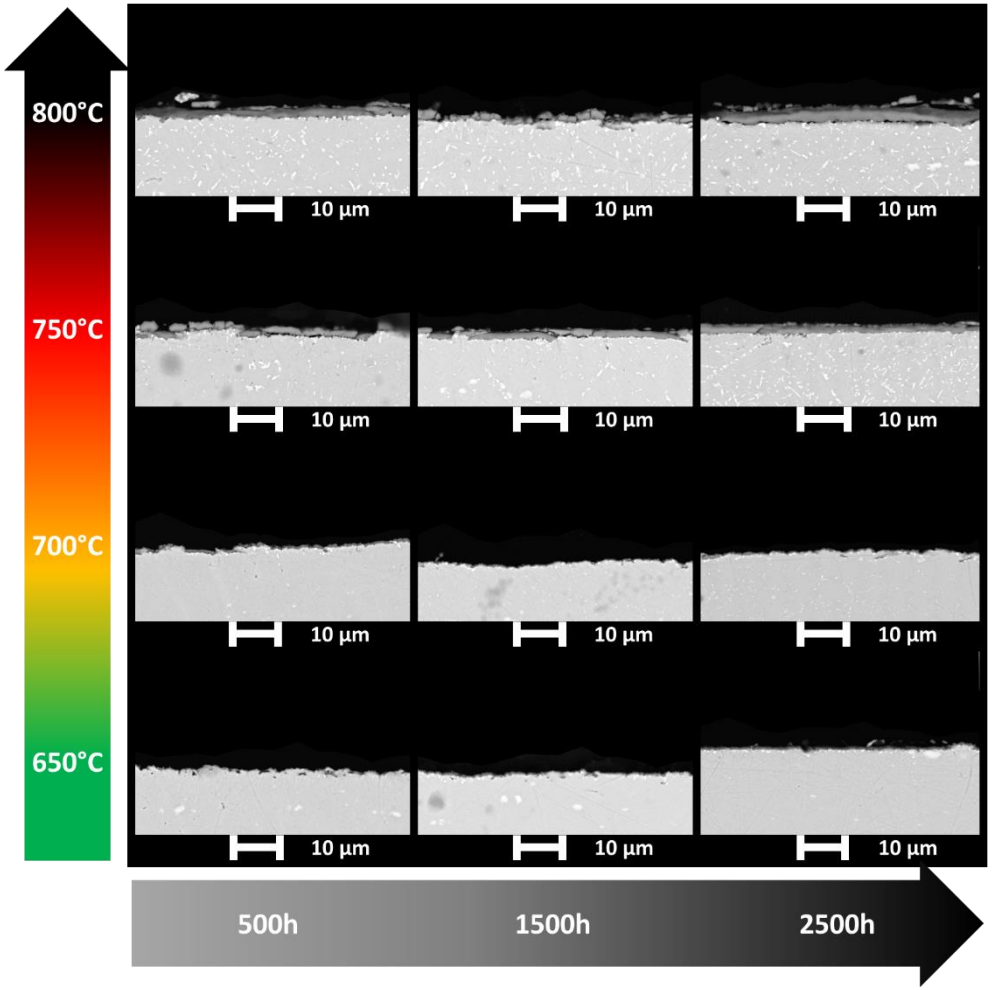

Figure 4-49: SEM images for cross-sections of Sanicro 25 with a P2500 ground surface finish after steam oxidation at different temperatures and exposure time.

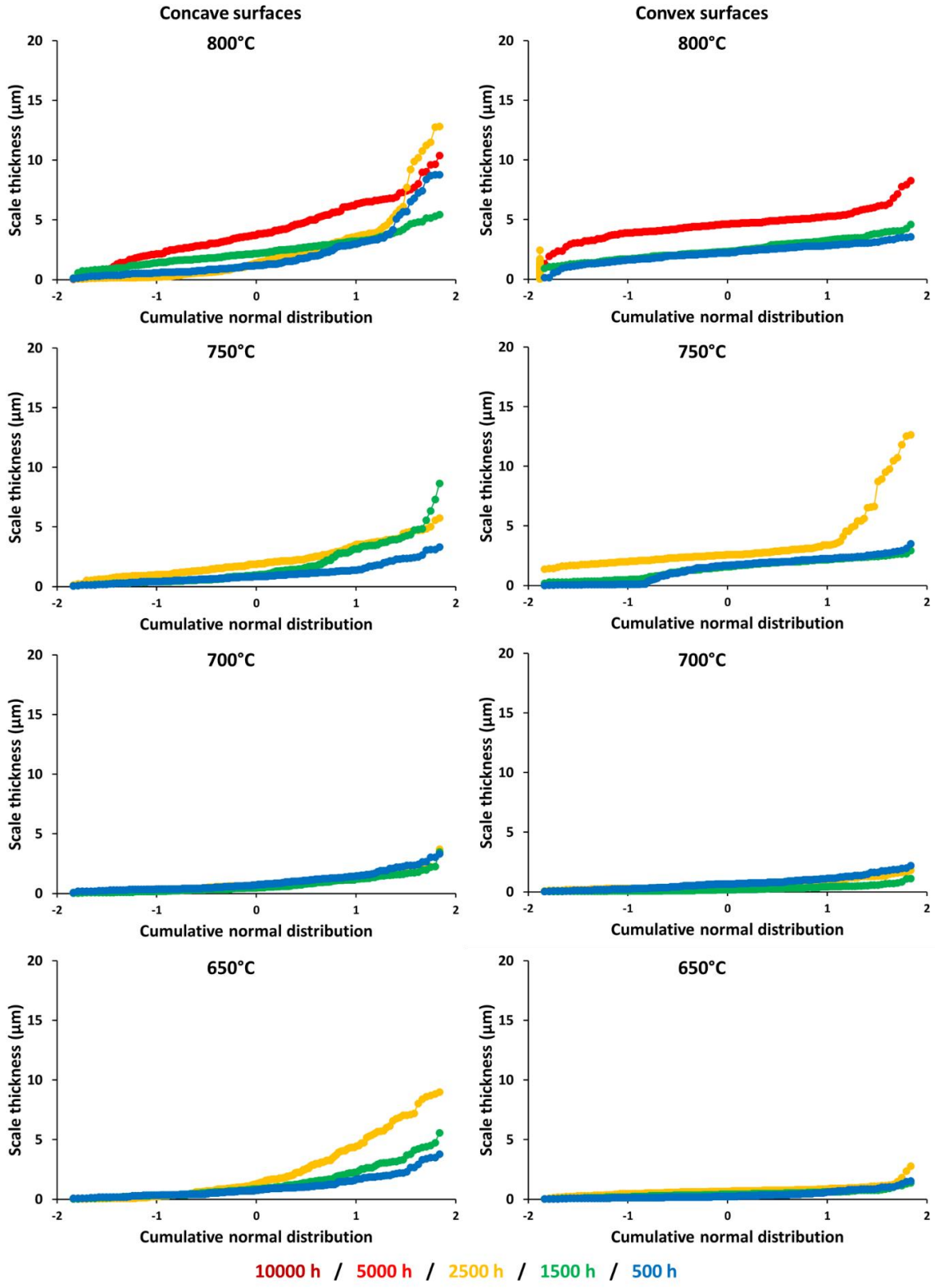

Figure 4-50: Cumulative normal distribution for the thickness of oxides formed on as-received concave surfaces and P2500 ground convex surfaces of Sanicro 25 after different exposure times at various temperatures.

XRD data (Figure 4-36) and SEM images associated with EDX (Figure 4-39 and Figure 4-40) show that a very thin chromia layer is formed on the P1200 ground surfaces of the material. Nevertheless a few iron-oxide nodules are visible after long exposure times as well as small areas were the chromia layer has exfoliated revealing the bare and unoxidized material underneath (Figure 4-41). The fact that the surfaces present at the exfoliated areas are not oxidized show that the exfoliation process is either due to the cool down process of the steam furnaces or to sample handling after the end of the sample exposure. Oxide thickness measurements on Figure 4-43 show an increase of the size of the oxide layer with increasing time and temperature.

For P2500 ground surfaces the mass data (Figure 4-34) is similar until 700°C but above this the oxidation is superior than for P1200 ground surfaces. In terms of oxide characterization, a thin chromia layer is formed at the surface of the samples with some iron-oxide nodules (Figure 4-42, Figure 4-45, Figure 4-48, and Figure 4-49) and the thickness of this layer (Figure 4-50) is of similar size than for P1200 ground surfaces.

The as-received surface finish is the type of surface which is the more affected by the steam oxidation process. Indeed, the mass change data (Figure 4-34) is much higher than for the other surface finishes even if only a thin chromia layer is observed on the surface of the material. The variations in the mass data may come from the de-correlation calculations to obtain the values for the as-received surfaces but it may also be caused by the nodular growth of iron-oxide nodules and their partial exfoliation. With increasing oxidation time and steam temperature, iron oxides are appearing on the surface of the material (Figure 4-35, Figure 4-37, Figure 4-38, Figure 4-44, Figure 4-46, and Figure 4-47). Oxide thickness data (Figure 4-43 and Figure 4-50) report a larger oxide layer on the as-received surfaces than on the other surface finishes studied. The different steps observed confirm the apparition of nodules and the partial exfoliation of the oxide layer.

4.2.1.3. Alloy 617

The net mass change presented in Figure 4-51 is the data for the longest exposed Alloy 617 samples (both P1200 and P2500 ground). For all temperatures, Alloy 617 samples exhibit a very low net mass change for both surface finishes tested. Although the mass change increases with increasing steam temperature and oxidation time, the values obtained could be considered low for high temperature steam oxidation. Some small steps in the mass change curves can be observed for some of the P1200 ground samples. This is usually representative of the oxide scale spallation, but in this case this is assumed to be an error due to the samples' manipulation during mass measuring.

This material shows a high oxidation resistance and thin and protective oxide scales are expected to be observed at the material's surface. It appears that surface finish does not significantly affect the steam oxidation process for this material. Further calculations regarding the kinetic parameters (see Section 4.3.1.2) confirm the previous statement.

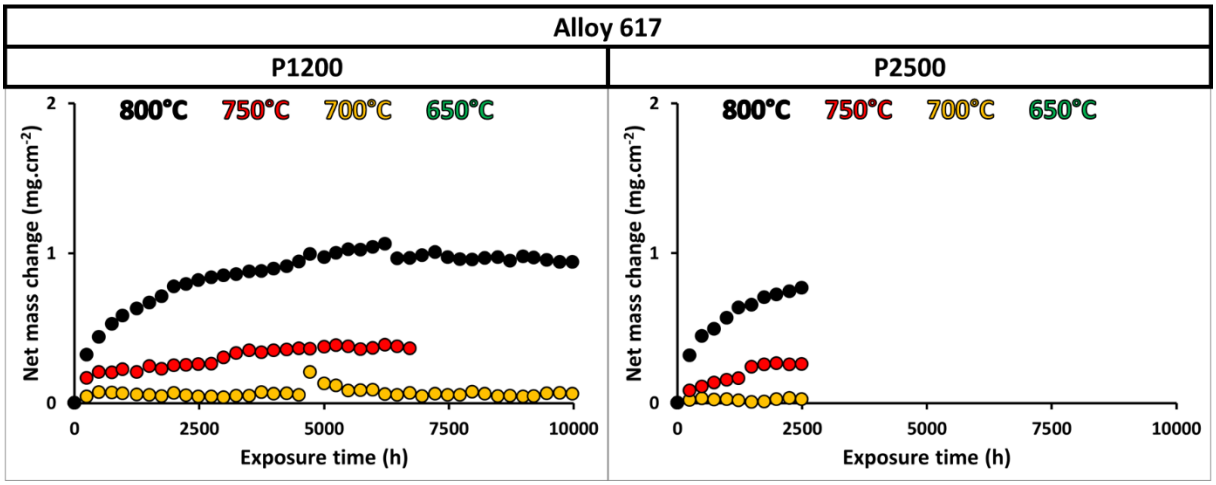

Figure 4-51: Net mass change data for Alloy 617 with P1200 groundand P2500 ground surface finish after steam oxidation at different temperatures and exposure time.

XRD spectra and SEM images of the oxidized surfaces for the P1200 ground samples are respectively presented in Figure 4-52 and Figure 4-53. Images of cross-sections for the oxidized P1200 ground surfaces are presented in Figure 4-54. Figure 4-55

shows the elemental mapping obtained from the EDX analysis of a cross-section and Figure 4-56 presents the thickness distributions for oxides formed on P1200 ground surfaces. For P2500 ground surfaces XRD spectra and SEM images are presented in Figure 4-57 and Figure 4-58. Figure 4-59 presents images of the cross sections for oxidized P2500 ground surfaces and the oxide thicknesses measured on these images are presented in Figure 4-60.

XRD data, for the P1200 ground surfaces, show peaks related to chromia and to the metal matrix of the original material. Thus it confirms the formation of a thin chromia layer at the surface of the different samples. Moreover, the height of the chromia peaks increase with increasing exposure time and steam temperature whereas the height of the metal matrix peak decrease. This shows that with increasing steam temperature and exposure time, there is the formation of a thicker chromia layer at the surface of the material. Oxide thickness measurements, presented later, will help confirm the previous statement. The same information can be deduced from the XRD data related to the P2500 ground surfaces. The XRD data for both surface finishes are close in every aspect (peak height and identity), thus no effect from surface finish can be observed here.

In terms of SEM images, P1200 ground (Figure 4-53) and P2500 ground (Figure 4-58) surfaces show the formation of a thin chromia layer (Figure 4-55) after oxidation in steam at every time and temperature tested. There does not seems to be differences caused by the different surface finishes applied to the material. Some small nodules can be observed at the material surface and have been identified as chromia as well. The preferential oxidation of the grain boundaries can been seen in multiple micrographs and the oxide formed at the grain boundaries' surface are identified as chromia. This observation confirm that chromium diffusion is enhanced at the grain boundaries.

Cross-sections were examined and the images taken (Figure 4-54 for P1200 ground surfaces and Figure 4-59 for P2500 ground surfaces) confirm the formation of a thin chromia layer for every samples tested (cf. Figure 4-55). These images show that the grain boundaries were oxidized and that inner oxides were formed alongside them. These external oxide formed is chromia whereas the internal oxides is alumina (Figure

4-55). This particular observation is in accordance with the fact that diffusion is enhanced along the grain boundaries. Thus images of the oxidized surfaces and of cross-sections show that the grain boundaries increase the outward diffusion of chromium and inward diffusion of oxygen.

The thickness of the oxide layers formed at the surface of the different samples tested was measured from the cross-section images and are presented in Figure 4-56 and in Figure 4-60 respectively for P1200 and P2500 ground surfaces. In accordance with what has been deduced from the XRD spectra, the thickness of the chromia layer increases with increasing steam temperature and exposure time. Similar thicknesses have been measured on P1200 and P2500 ground surfaces after steam oxidation which illustrates that surface working does not affect the steam oxidation process for Alloy 617. The shape of the different curves presented do not exhibit steps which indicates that spallation of the chromia layer has not occurred and validates the cause of the small variations observed in the mass change curves not being due to exfoliation.

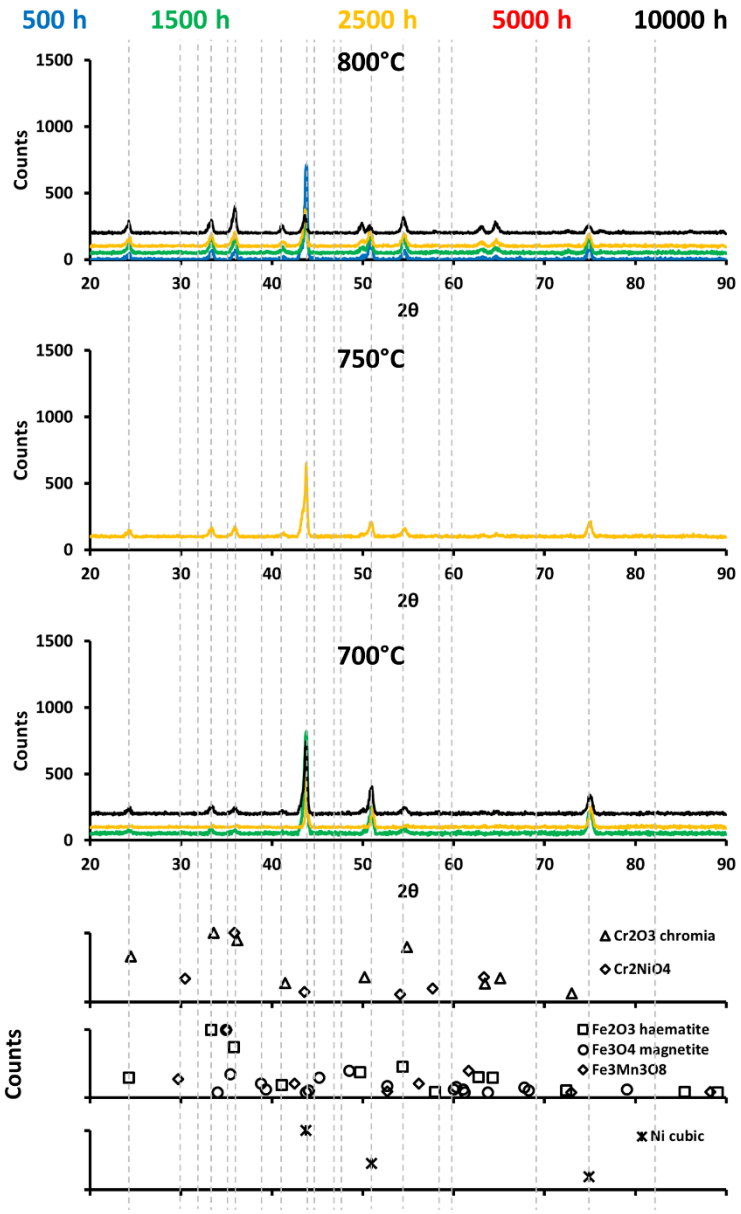

Figure 4-52: XRD spectra for Alloy 617 with a P1200 ground surface finish after steam oxidation at different temperatures and exposure time.

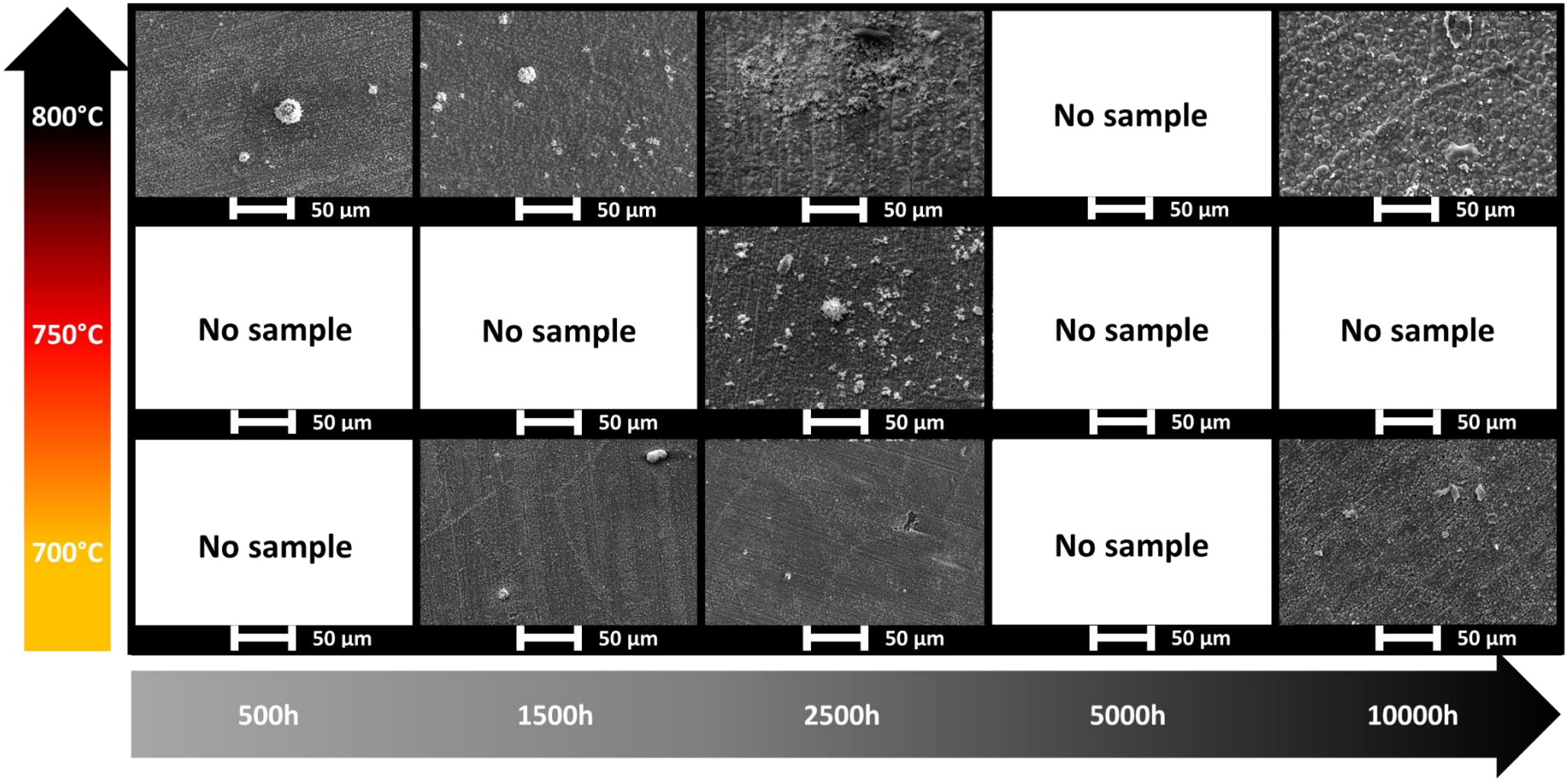

Figure 4-53: SEM images for Alloy 617 with a P1200 groundsurface finish after steam oxidation at different temperatures and exposure time.

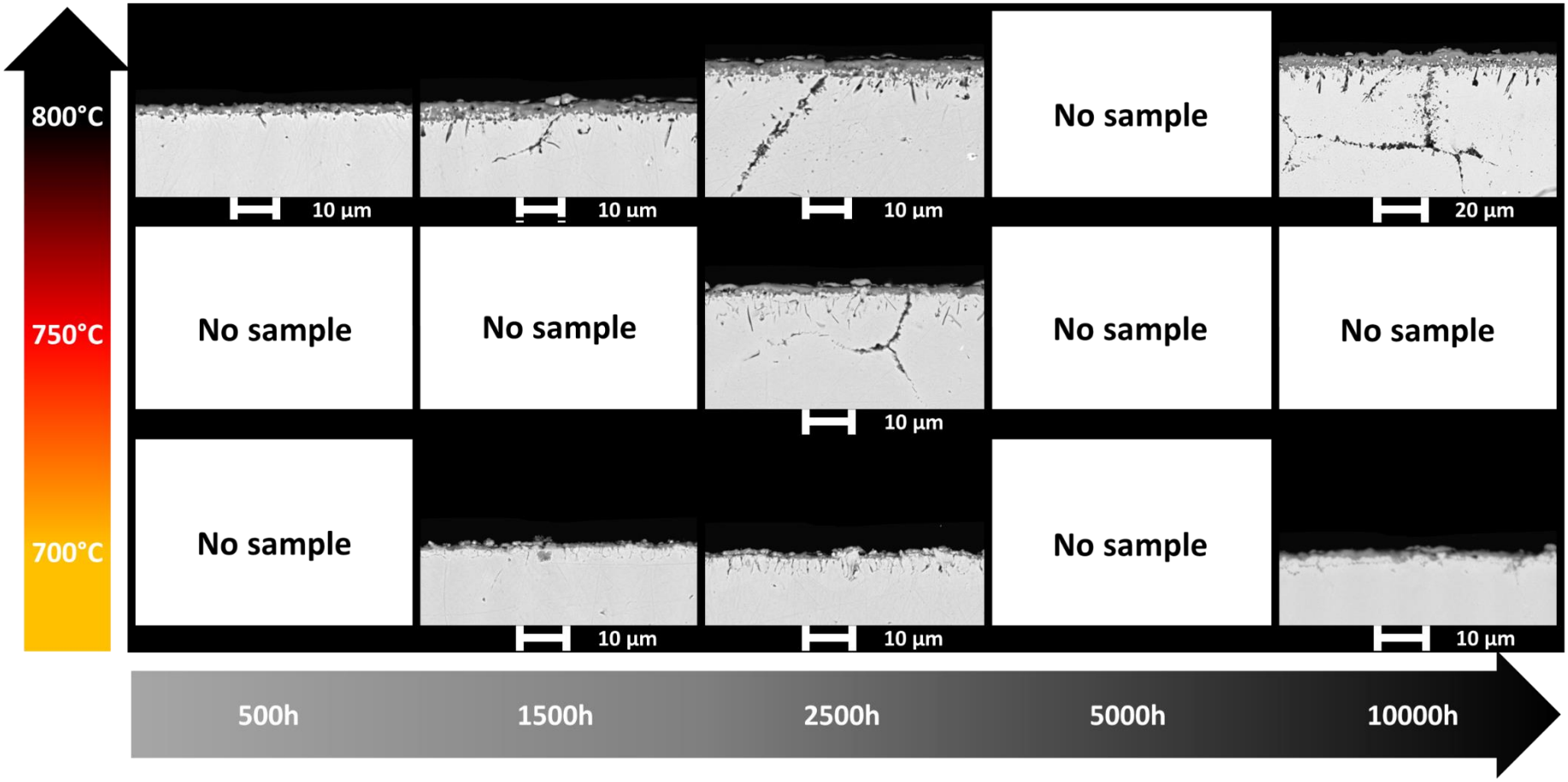

Figure 4-54: SEM images for cross-sections of Alloy 617 with a P1200 ground surface finish after steam oxidation at different temperatures and exposure time.

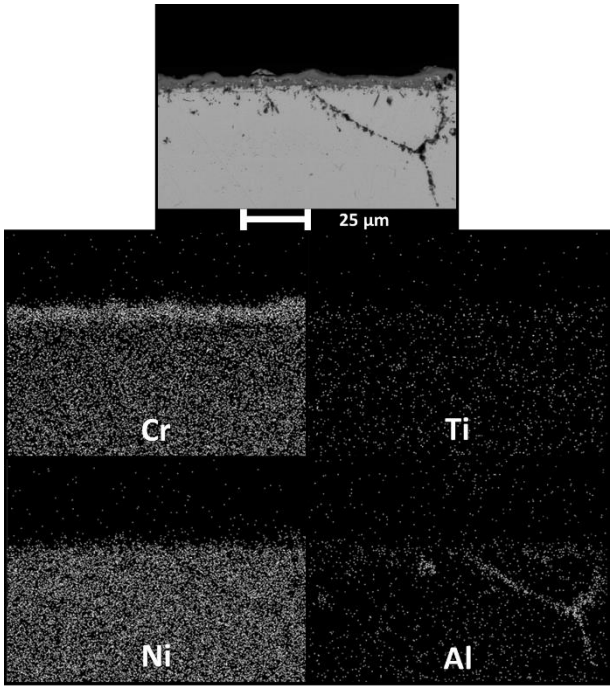

Figure 4-55: SEM image and elemental maps from EDX analysis for Alloy 617 with P1200 ground surface finish after steam oxidation at 800°C for 10,000 hours.

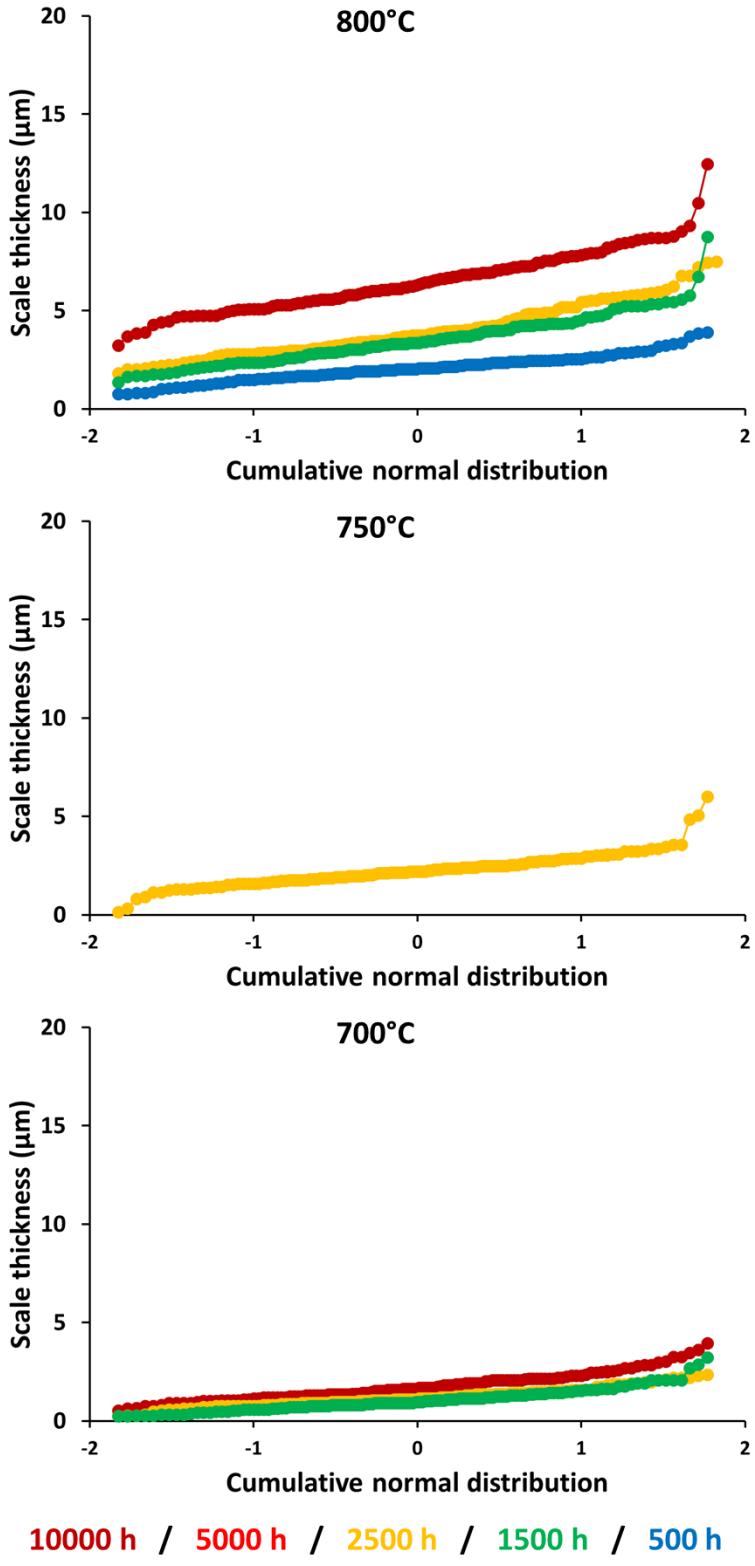

Figure 4-56: Cumulative normal distribution for the thickness of oxides formed on P1200 ground surfaces of Alloy 617 after different exposure times at various temperatures.

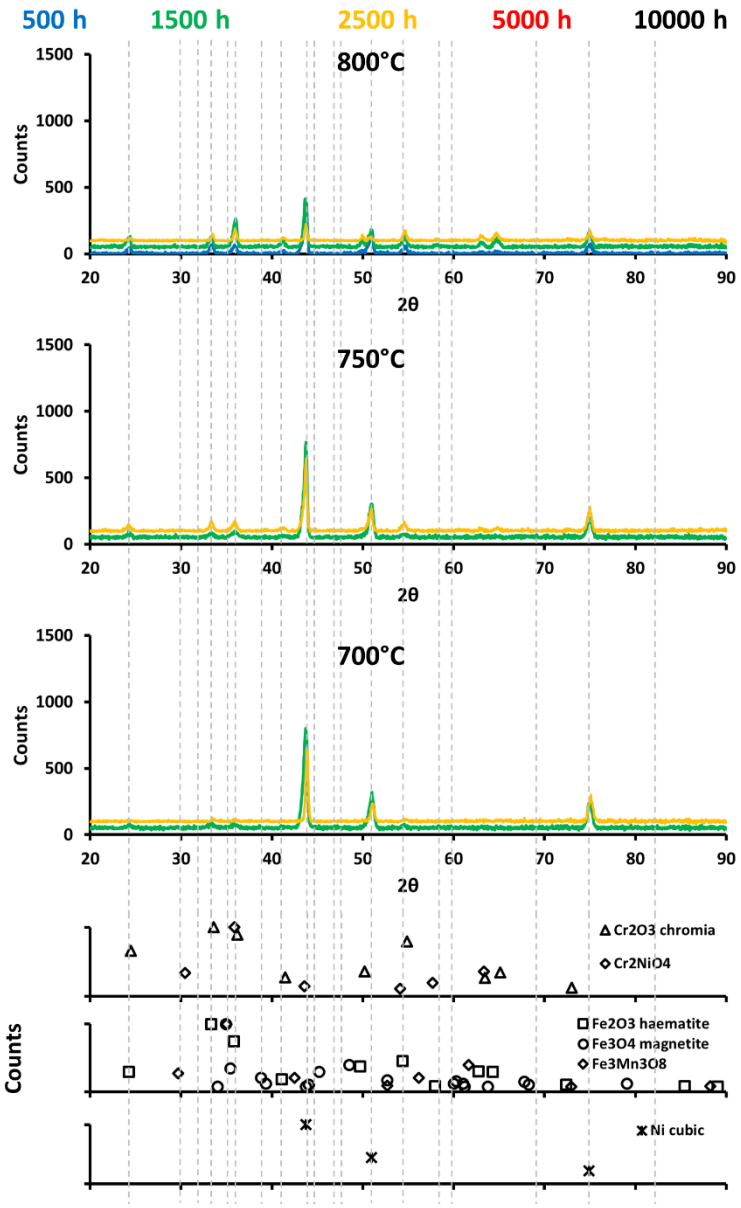

Figure 4-57: XRD spectra for Alloy 617 with a P2500 ground surface finish after steam oxidation at different temperatures and exposure time.

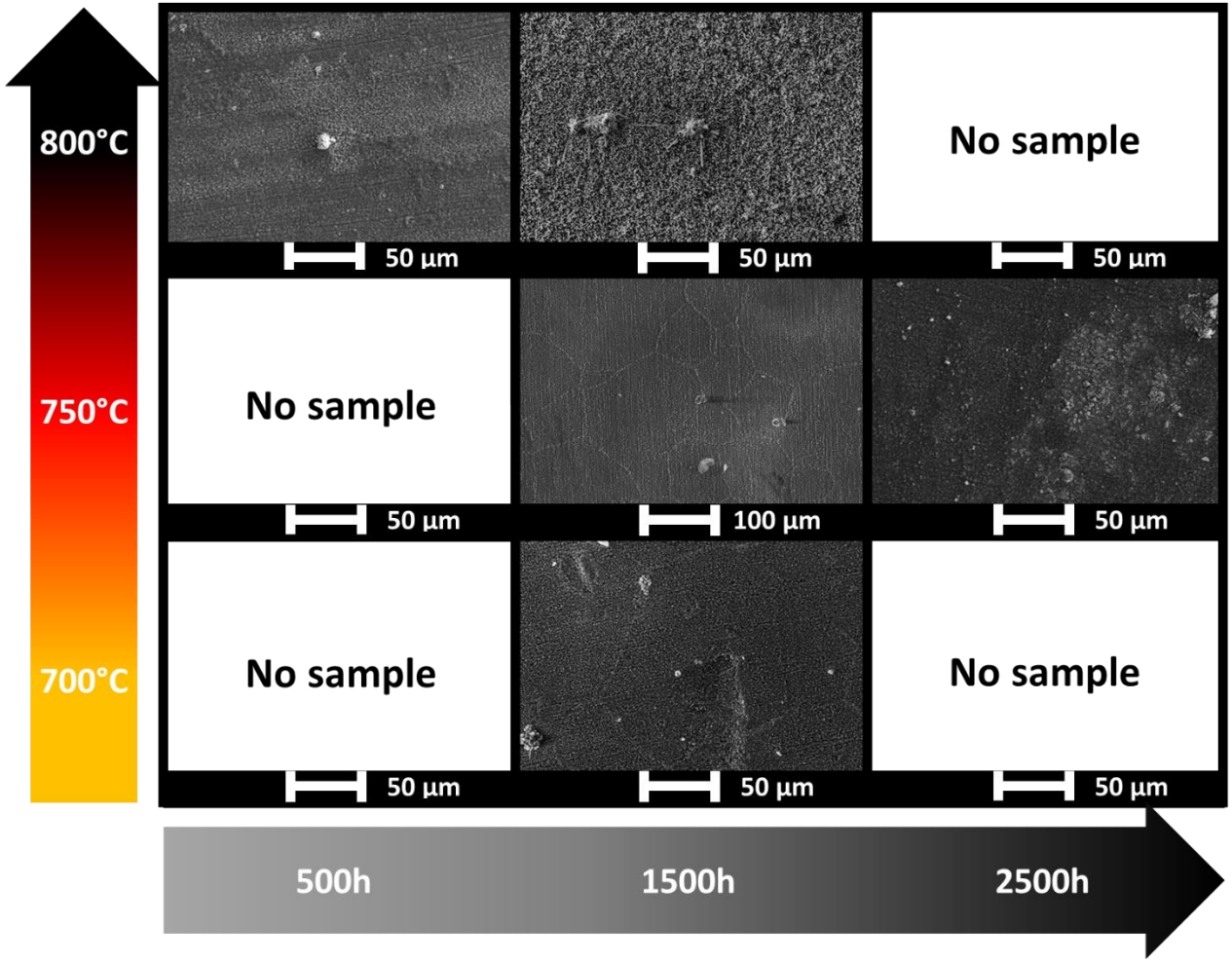

Figure 4-58: SEM images for Alloy 617 with a P2500 ground surface finish after steam oxidation at different temperatures and exposure time.

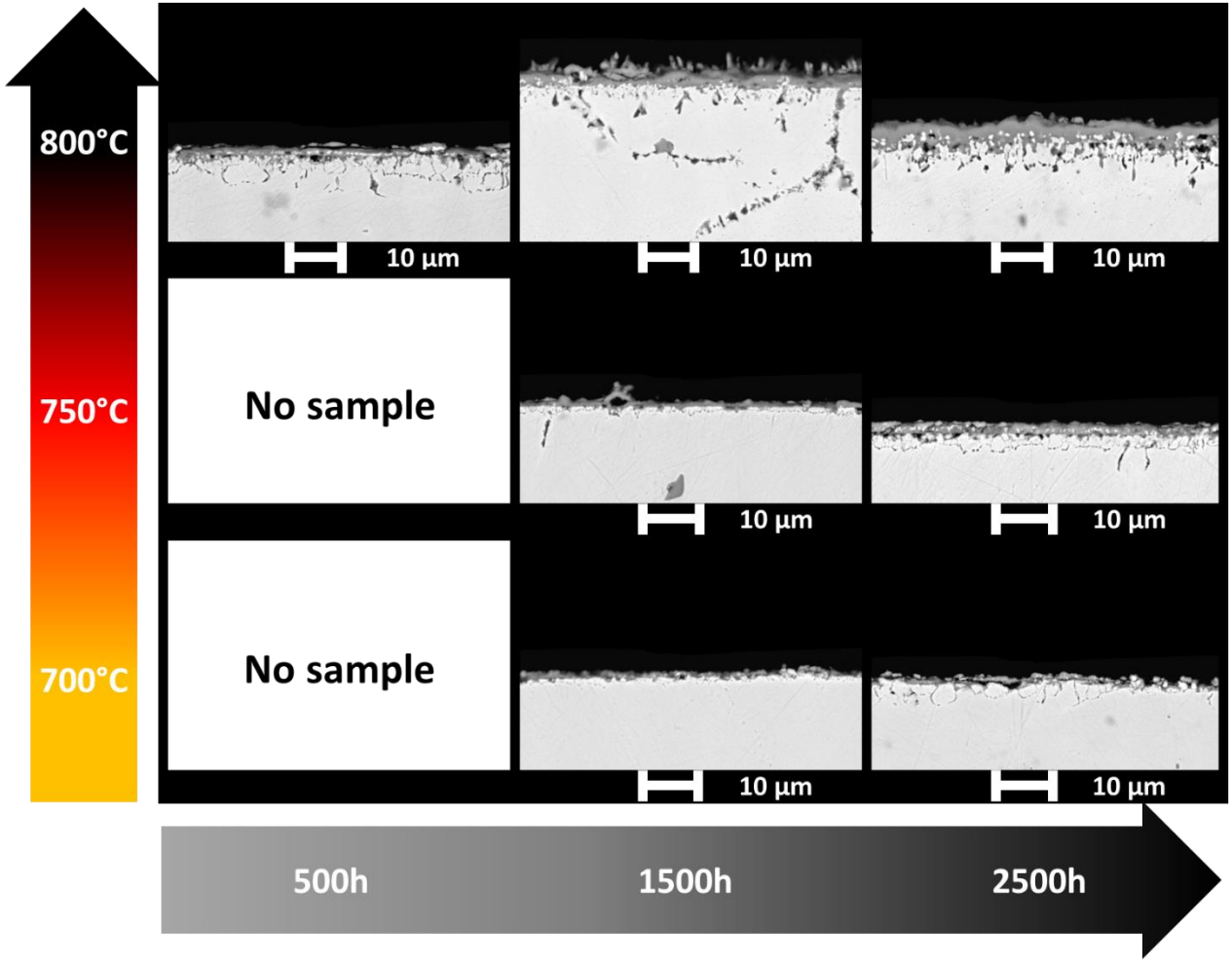

Figure 4-59: SEM images for cross-sections of Alloy 617 with a P2500 ground surface finish after steam oxidation at different temperatures and exposure time.

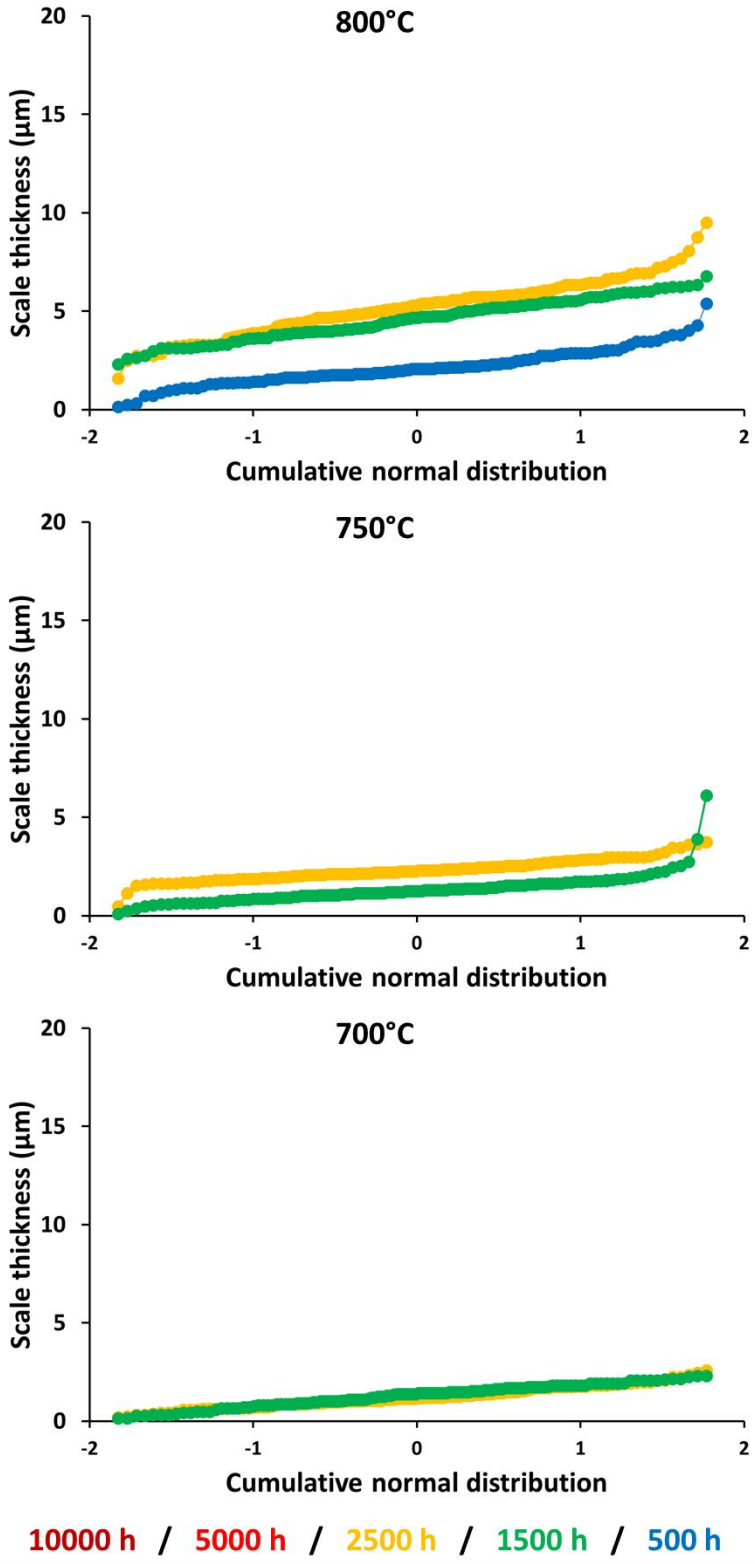

Figure 4-60: Cumulative normal distribution for the thickness of oxides formed on P2500 ground surfaces of Alloy 617 after different exposure times at various temperatures.

4.2.1.4. Alloy 263

For Alloy 263, the net mass change presented in Figure 4-61 reveals to be slightly higher than for Alloy 617. Nevertheless, the values obtained remain low and establish a high steam oxidation resistance for this material. Therefore, a thin and protective oxide layer is expected to be formed for the various samples. Spallation does not seem to occur and there is an increasing mass change with increasing steam temperature and exposure time.

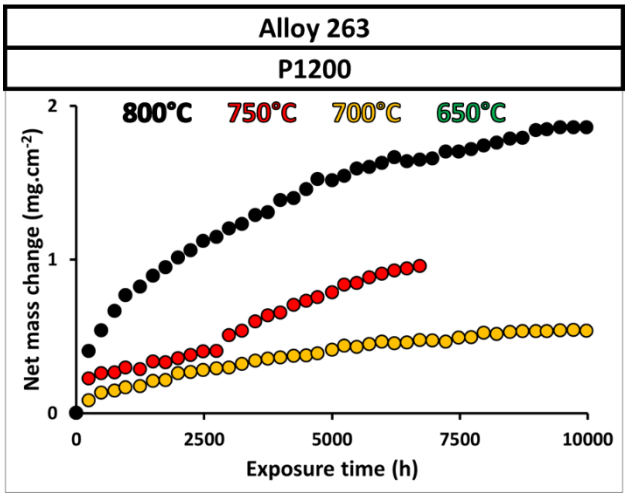

Figure 4-61: Net mass change data for Alloy 263 with P1200 ground surface finish after steam oxidation at different temperatures and exposure time.

Figure 4-62 presents the XRD spectra associated with the different exposed samples for Alloy 263. SEM images for oxidized surfaces and cross-sections of P1200 ground Alloy 263 are respectively presented in Figure 4-63 and Figure 4-64. The results from EDX analysis performed on a cross-section is presented in Figure 4-65, whereas Figure 4-66 presents the distributions of oxide thicknesses measured on the different samples.

Chromia is detected to be formed at the surface of the materials (Figure 4-62) and the original material can still be detected by XRD which means the chromia layer is thin. The peak related to the matrix of original material decreases with increasing steam

temperature and exposure time, thus the thickness of the chromia layer is expected to thicker with increasing steam temperature.

SEM images (Figure 4-63) illustrate the uniform formation of chromia at the surface of the different samples exposed (Figure 4-65). External oxidation of the grain boundaries can be observed as well as a few nodules. At 800°C and 10,000 hours, the oxides formed alongside the grain boundaries seem to start spreading at the surface of the material.

From the cross-section images (Figure 4-64) and thickness measurements (Figure 4-66) it can be observed that the oxide thickness increases with increasing steam temperature and exposure time. At 800°C the oxide thickness is twice that at 750°C (Figure 4-66). Internal oxide, composed of aluminium and titan (Figure 4-65), is formed along the grain boundaries and at 800°C the external growth of the oxide above the grain boundaries is confirmed to be larger.

Internal oxidation is observed to penetrate deeply into the material which may cause some weakness in real life exposure where the material is under strain.

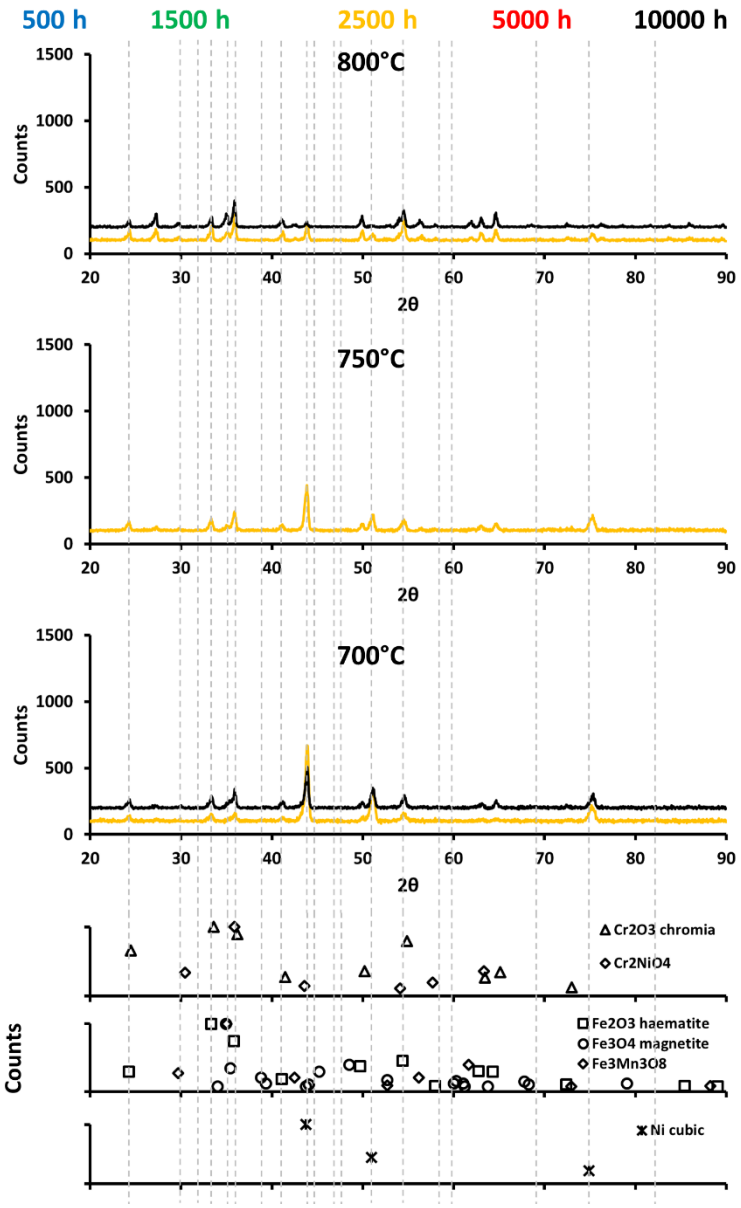

Figure 4-62: XRD spectra for Alloy 263 with a P1200 ground surface finish after steam oxidation at different temperatures and exposure time.

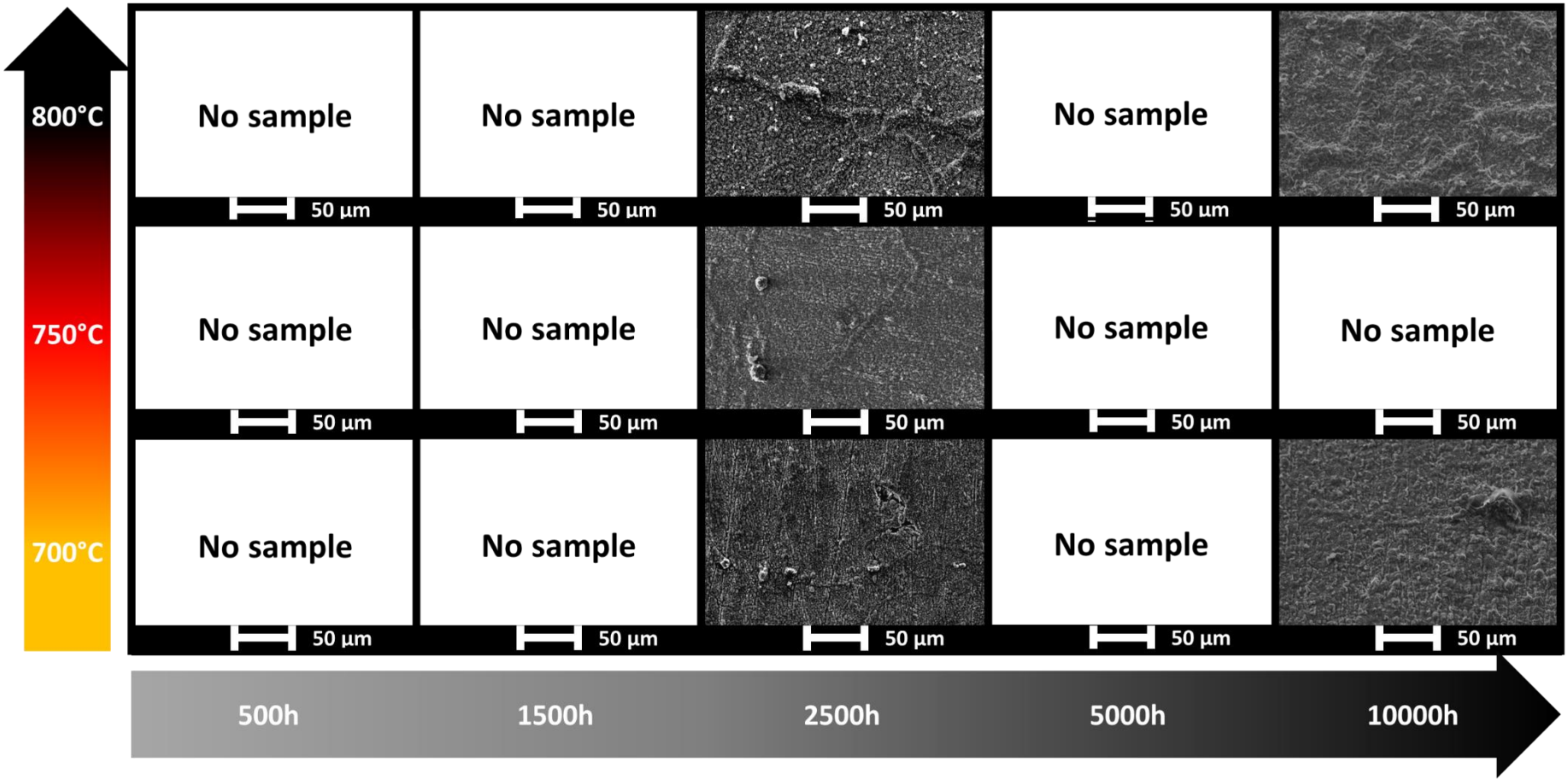

Figure 4-63: SEM images for Alloy 263 with a P1200 ground surface finish after steam oxidation at different temperatures and exposure time.

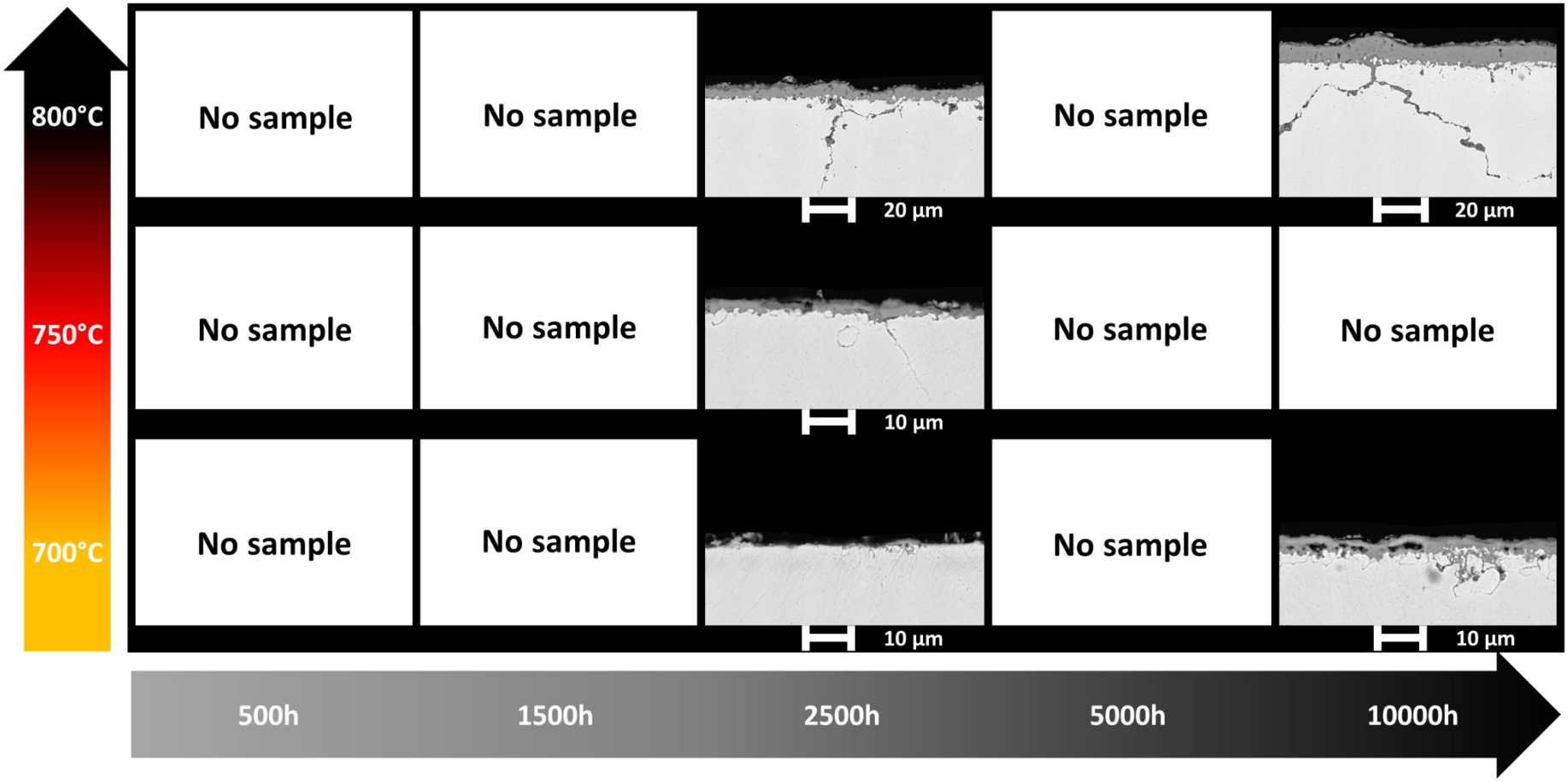

Figure 4-64: SEM images for cross-sections of Alloy 263 with a P1200 ground surface finish after steam oxidation at different temperatures and exposure time.

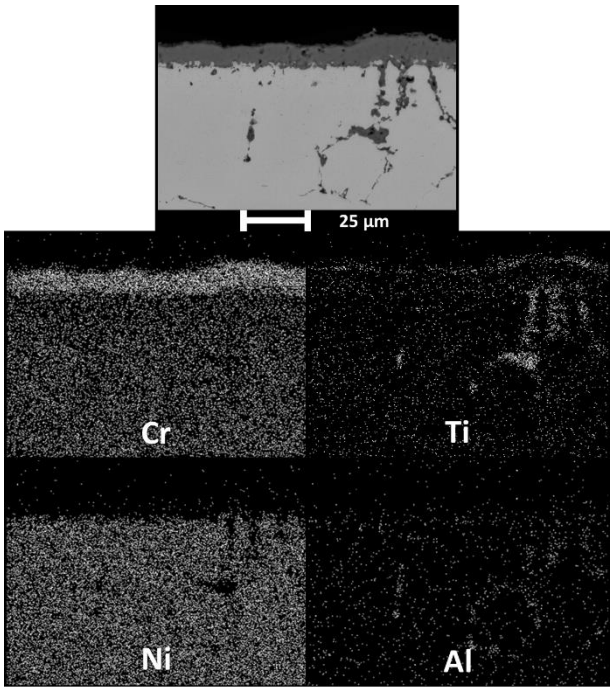

Figure 4-65: SEM image and elemental maps from EDX analysis for Alloy 263 with P1200 ground surface finish after steam oxidation at 800°C for 10,000 hours.

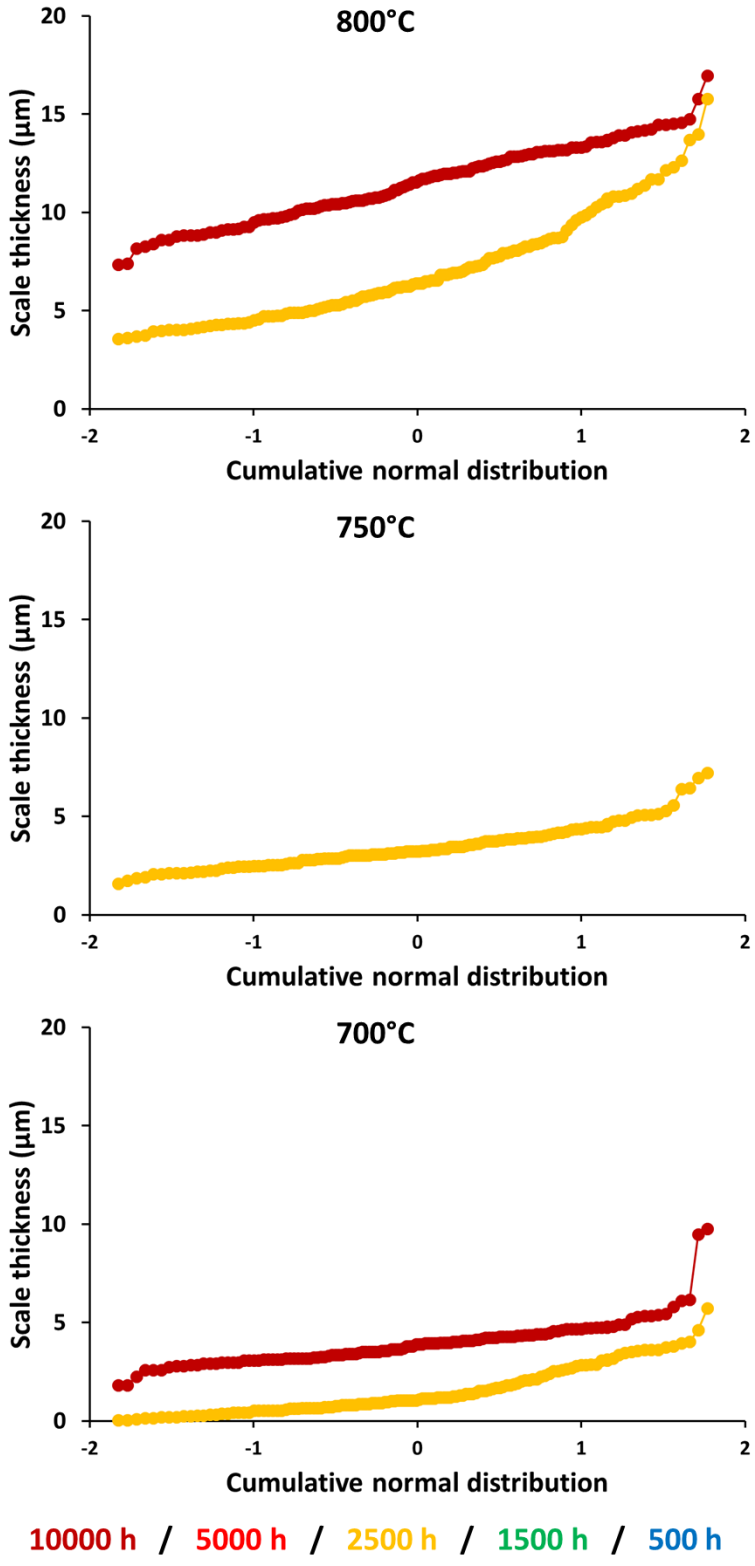

Figure 4-66: Cumulative normal distribution for the thickness of oxides formed on P1200 ground surfaces of Alloy 263 after different exposure times at various temperatures.

4.2.1.5. Alloy 740

Mass change data for P1200 ground Alloy 740 is presented in Figure 4-67. XRD spectra for the oxidized surfaces of this material are presented in Figure 4-68 whereas SEM images of the oxidized surfaces and cross-sections are respectively presented in Figure 4-69 and Figure 4-70. Figure 4-71 shows the results from the EDX analysis performed on a specific sample and Figure 4-72 presents the oxide thickness distributions.

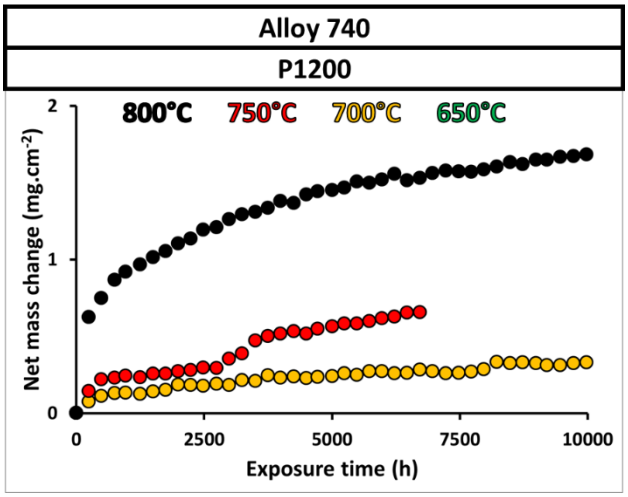

Figure 4-67: Net mass change data for Alloy 740 with P1200 ground surface finish after steam oxidation at different temperatures and exposure time.

Following the mass change during the steam oxidation of Alloy 740 represented in Figure 4-67, it can be seen that no spallation is observed but there is much larger mass gain at 800°C compared with the other temperatures. At 700 and 750°C, although mass gain is slightly larger at the highest temperature, the curves are very close to one another until 2500 hours where there seems to be a breakaway or an acceleration of the oxidation process at 750°C. Despite the large differences of mass gain observed at the different temperatures, the values remain small so the material possesses a good oxidation resistance and is expected to form a thin and protective layer at its surface.

XRD analyses (Figure 4-68) confirm the formation a chromia layer at the surface of the material which is a protective oxide (cf. Figure 4-71). Thicker chromia layers are expected with increasing steam temperature and exposure time.

In terms of surface imaging (Figure 4-69), small nodules can be seen at the surface of the different samples as well as external oxidation of grain boundaries. Marks from grinding are still present at 750°C but they are not visible at 800°C due to the increased oxidation kinetics happening at this temperature. Moreover, more chromia coverage seems to be present at 800°C and for 10,000 hours.

Cross-section images (Figure 4-70) and oxide thickness measurements (Figure 4-72) show the formation of a chromia monolayer which increases with increasing steam temperature and exposure time. No spallation could be detected on any of the images taken. The internal oxidation of grain boundaries is visible but remains low in comparison with the other nickel-based alloys. A few voids can be observed in the chromia layer at 800°C and after 10,000 hours. All thickness measurements show normal distributions.

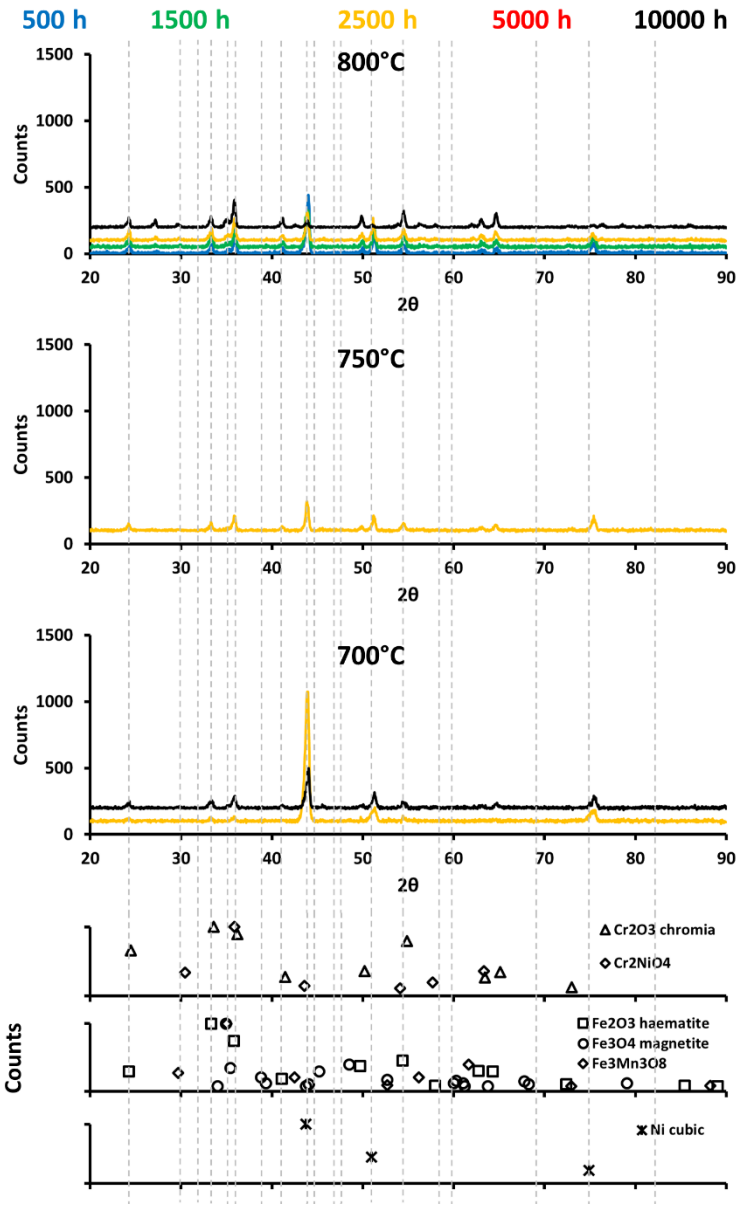

Figure 4-68: XRD spectra for Alloy 740 with a P1200 ground surface finish after steam oxidation at different temperatures and exposure time.

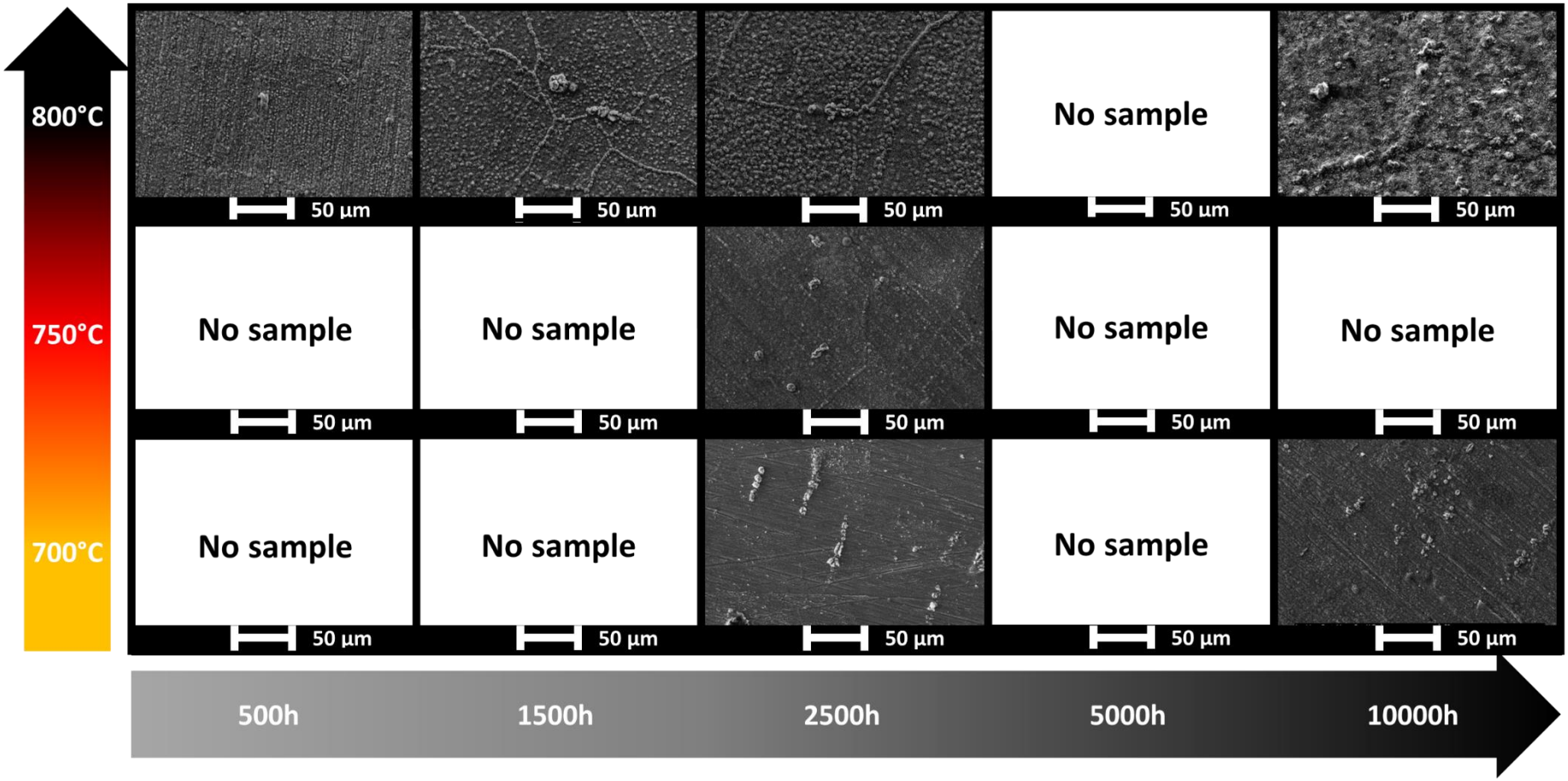

Figure 4-69: SEM images for Alloy 740 with a P1200 ground surface finish after steam oxidation at different temperatures and exposure time.

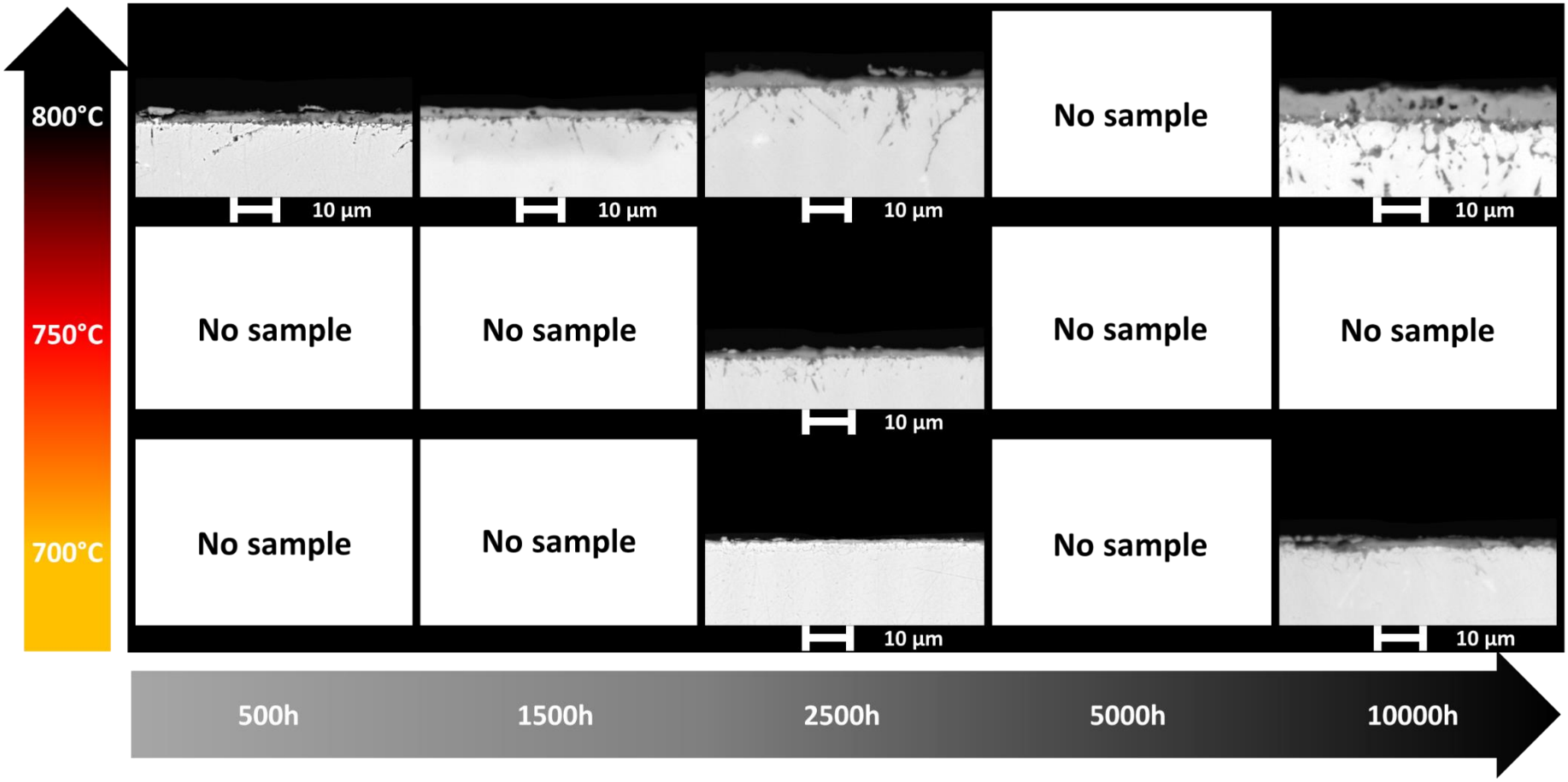

Figure 4-70: SEM images for cross-sections of Alloy 740 with a P1200 ground surface finish after steam oxidation at different temperatures and exposure time.

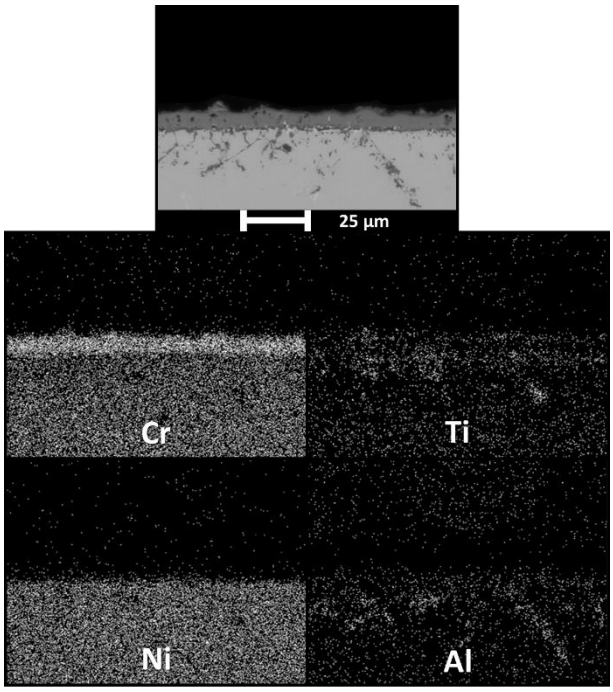

Figure 4-71: SEM image and elemental maps from EDX analysis for Alloy 740 with P1200 ground surface finish after steam oxidation at 800°C for 10,000 hours.

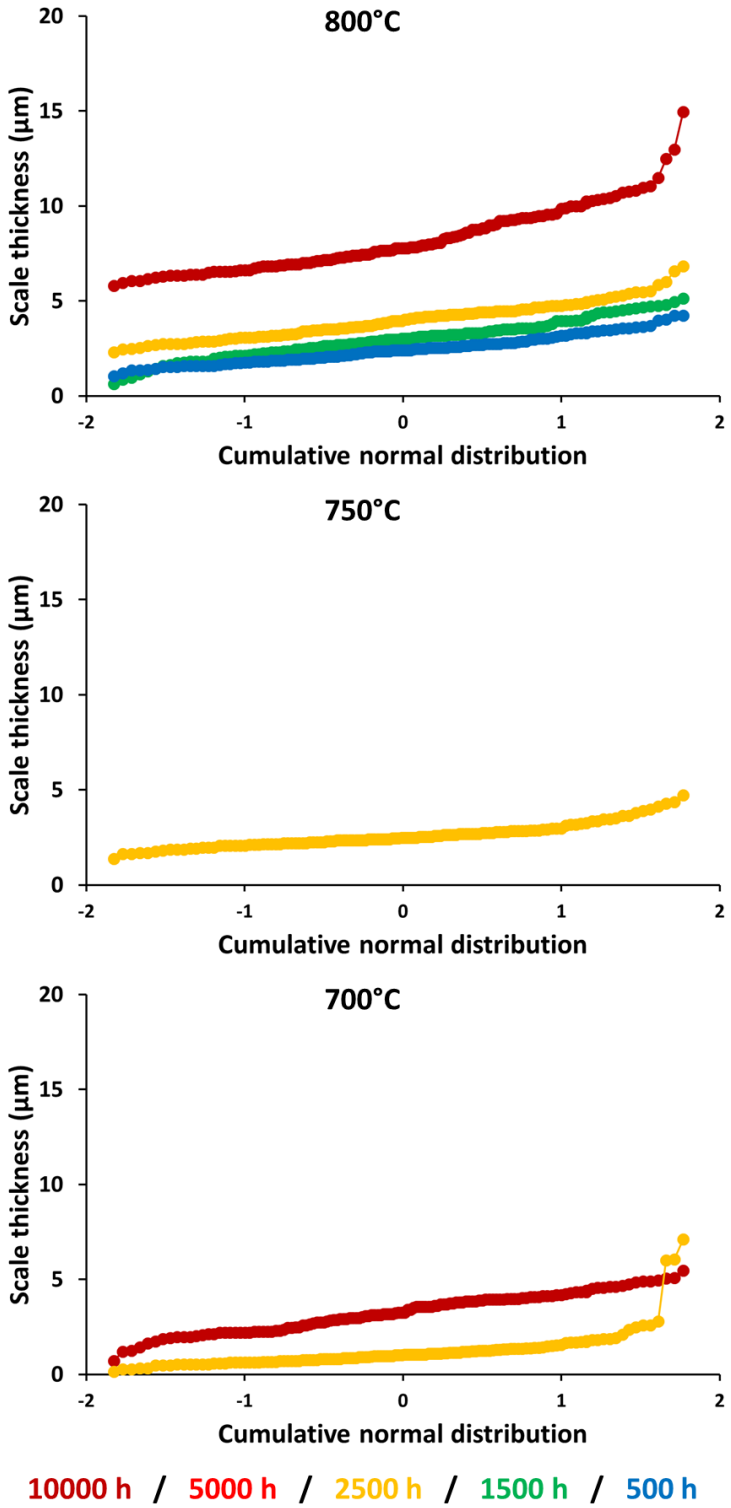

Figure 4-72: Cumulative normal distribution for the thickness of oxides formed on P1200 ground surfaces of Alloy 740 after different exposure times at various temperatures.

4.2.2. XRD and oxide thickness

It has been observed that there seems to be a link between the height of the XRD peak related to the iron matrix and the oxide thickness formed at the surface of exposed samples. It is supposed that the higher the iron matrix peaks, the thinner the oxide layer. Analyses have been done in order to affirm or refute this hypothesis. The height of different peaks of the XRD spectrum has thus been measured and correlations with the measured thickness of exposed samples have been looked at. Table 4-3 and Figure 4-73 show respectively the range of the different peaks in terms of angle of incidence and a typical example of a XRD spectrum showing the peaks that have been used to correlate their height to the actual oxide thickness developed on their surface.

Table 4-3: 2θ range of the different XRD peaks.

Peak number	Min angle	Max angle
1	22.52	25
2	30	32
3	32	34
4	35	37
5	40	42
6	43	45
7	49	50
8	50	52
9	53	55
10	56	58
11	62	63.52
12	63.56	64.56
13	74	76

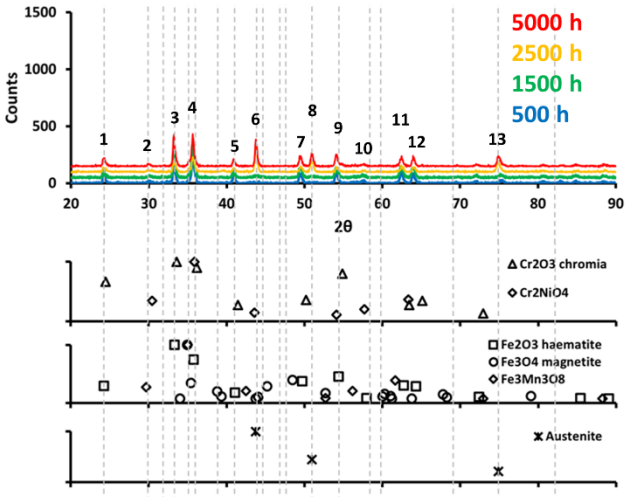

Figure 4-73: Peak identification on the XRD spectrum for as-received surfaces of TP347HFG oxidized at 650°C for different exposure times.

Each point represented in Figure 4-74 comes from a single sample for which the mean oxide thickness measure for the sample is plotted as a function of the number of counts related to the eighth peak measured on the sample's XRD

spectrum. The figure clearly indicates that the higher the eighth peak, the thinner the oxide layer formed. However, a few odd points can be observed and the scatter seems to be large for oxide thicknesses thicker than 15 µm. This figure uses the data obtained from every sample exposed during the project on which XRD analysis and oxide thickness measurements were performed.

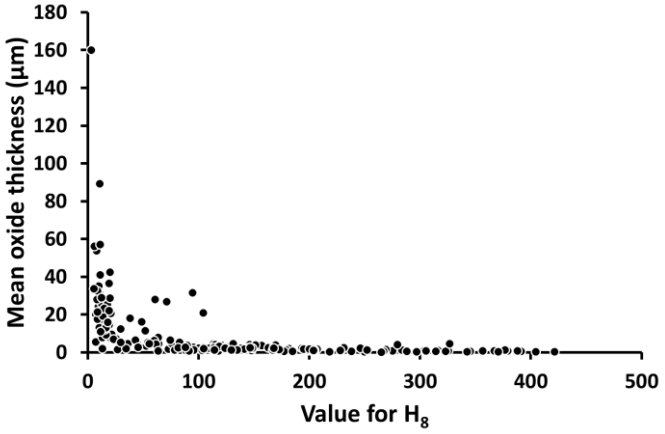

Figure 4-74: Thickness of oxide layer measured on individual samples plotted as a function of the number of counts for the eighth peak (H_8) of the sample's XRD spectrum.

Different mathematical transformations have been tried to link the peak height to the oxide thickness, and it appears that the best linear relationship has been found for peak number 8 and is:

$$\ln(x) = A\sqrt{H_8} + B \quad \textbf{(4-1)}$$

Where x is the mean oxide thickness $[\mu m]$, H_8 is the number of counts for the eighth peak of the XRD spectrum, and A and B are the linear fitting parameters.

Figure 4-75 (a) shows the correlation between the square root of the 8th peak height and the logarithm of the oxide thickness. This figure allows the determination of the fitting parameters A and B. With these parameters it is now possible to construct an equation linking the height of the 8th peak to the oxide thickness:

$$\mathrm{x} = \exp\left(-0.23\sqrt{H_8} + 3.57\right) \quad \textbf{(4-2)}$$

Equation (4-2) has been used to calculate the oxide thickness from the height of the 8th peak and Figure 4-75 (b) verifies the precision of the prediction.

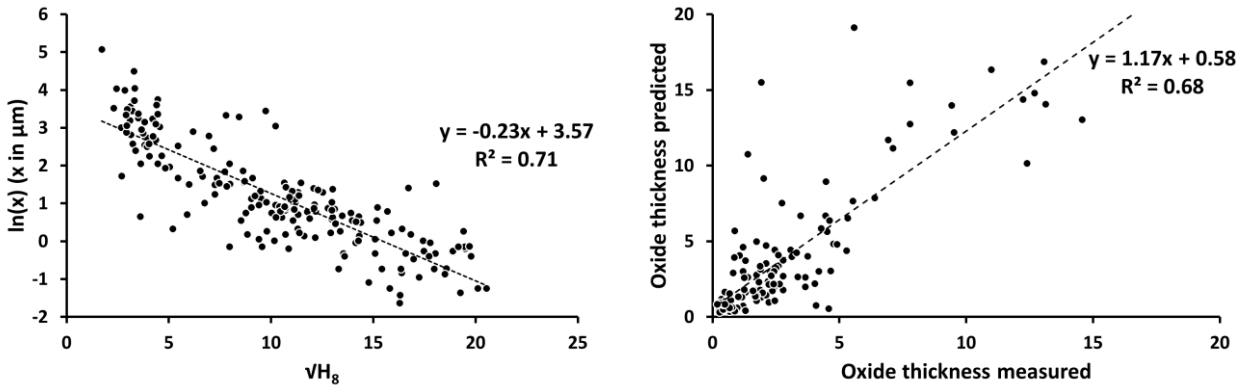

(a) (b)

Figure 4-75: (a) Linear correlation for Equation (4-1) and (b) verification of the accuracy of the thickness prediction model described by Equation (4-2).

Equation (4-2) allows a fair fitting parameter between the XRD data and the oxide thickness measured but it does not give very good prediction. Indeed, it appears that the thickness predictions show non-negligible errors due to the scatter of the data. Nevertheless, if extended work can be developed on linking data obtained from XRD spectra and oxide thickness measurements, it could allow linking more accurately the two sets of data. Such an tool, would be useful to quickly have an idea of the oxide thickness of some exposed samples without needing to perform cross-sections. This would also allow monitoring the oxide growth over time for a single sample by performing XRD analysis on its surface at the end of each cycle. This way, it would avoid the need to expose different samples to obtain oxide thickness data at different exposure times.

4.2.3. Nodule formation

Different nodules have been observed to form at the surface of the as-received surface of TP347HFG after 2500 hours of steam exposure at 600, 650, and 700°C. However, after 2500 hours at 750°C, the nodules have spread out and the whole as-received surface of the material was covered in a multi-layered oxide. To understand if the steam exposure temperature affects the nodules formation of the as-received surface, an analysis of the nodule dimensions formed has been performed. Figure 4-76 gathers the different images that have been used, in parallel with ImageJ software to measure the diameter of the nodules observed.

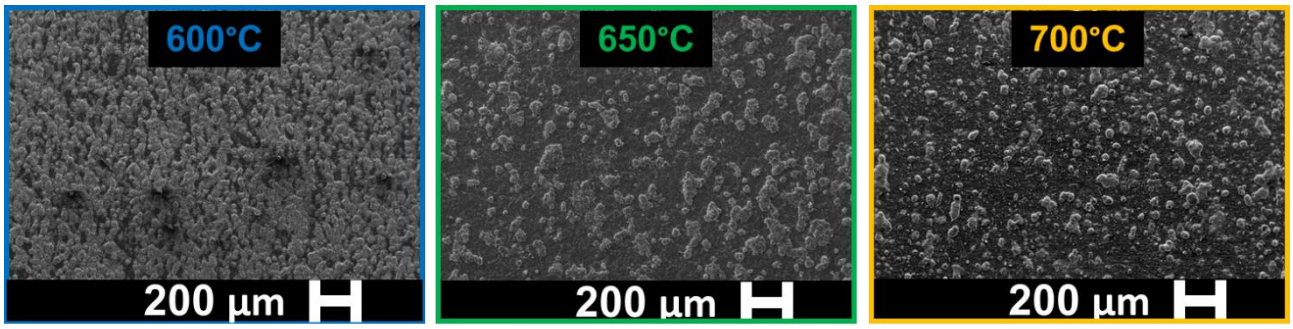

Figure 4-76: Oxide nodules formed at the as-received surface of TP347HFG after 2500 hours of steam exposure at 600, 650, and 700°C.

Figure 4-77 (a) and (b) show respectively the distribution and the probability plot of the nodule diameters measured. There is no notable difference in the nodule dimensions observed, thus it is reasonable to say that between 600 and 700°C the steam temperature does not affect the size of the nodules formed on the as-received surface of TP347HFG. This result was not expected, and this would mean that the size of the nodules depend on the oxidation time.

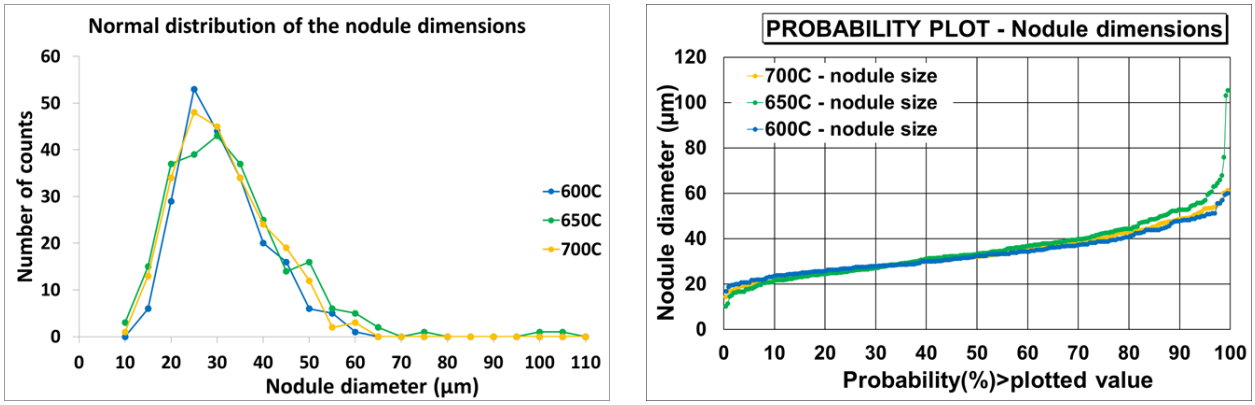

(a) (b)

Figure 4-77: (a) distribution and probability plot of the nodule diameter formed on the as-received surface of TP347HFG after 2500 hours steam exposure at 600, 650, and 700°C.

4.2.4. Oxide spallation

During the steam exposure tests, exfoliation was observed on the different samples, as show in Figure 4-78 where large oxide flakes, of the size of the top surface of the samples, are seen to spall. Such oxide flakes have only been observed for TP347HFG samples and always come from the top side surfaces of the exposed samples. The fact that the steam was flowing parallel to this top side surface may be the reason why spallation was observed over the entire surface. The exfoliated oxide flakes have been recovered from the crucibles in which the samples were exposed. SEM imaging was used to characterize the morphology of the different surfaces of the exfoliated flakes. The observation of the exfoliated oxide flakes might provide some useful information to explain the exfoliation mechanism.

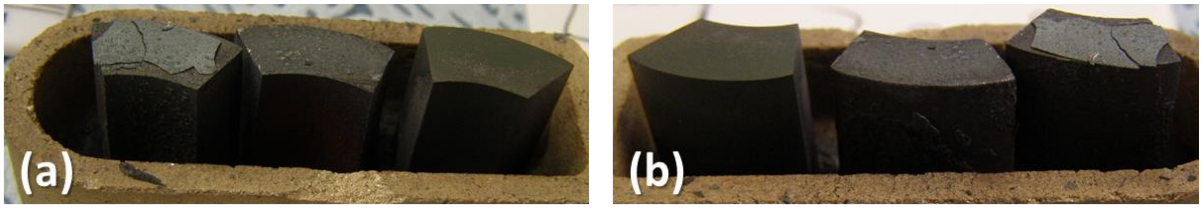

Figure 4-78: Photos of oxidized TP347HFG samples after 500 hours of steam exposure at 800°C.

It is supposed that the exfoliation process has occurred between the outer and inner oxide layer formed on TP347HFG. On the original steam-side interface of oxide flakes gathered from tests at 700 and 750°C, oxide crystals of different shapes can be observed (Figure 4-79 (a) and (b)). This oxide has been identified as magnetite. In addition, needles or plates of oxide can be observed and these are characteristic of Fe_2O_3 formation [82]. On the other side of the flake (i.e., side which was in contact with the oxide remaining attached to the material's surface) different zones can be visualized (Figure 4-79 (e) and (f)):

- Smooth areas: that could be due to rapid fracture processes from the propagation of cracks driven by thermal contraction [23] causing stress during cool down. This could be considered for a potentially strong interface just prior to the exfoliation process.

- Porous/more crystalline areas: These zones are representative of the porosity in the Fe-rich part of the oxide scale. These could be considered as potentially weak interfaces prior to the exfoliation process as these gaps within the oxide scale reduce the contact area between the upper and lower oxide layers. The oxide grains seem to possess sharper edges which could be due to brittle fractures as a result of stress build up in the scales. Large cavities can also be observed in some cases (Figure 4-79 (e)).

Observation of the edges of the exfoliated oxide flakes (Figure 4-79 (c) and (d)) have shown that the grains located towards the metal/oxide side of the flake are columnar (4-10 µm long) and large (2.5-5 µm in width). However, at the

steam/oxide interface, the oxide grains are a lot smaller in size (<1 µm). The observation of large columnar magnetite grains present in the oxide scales with smaller magnetite grains on top of it is consistent with the literature [23] where a double layer of magnetite has been reported.

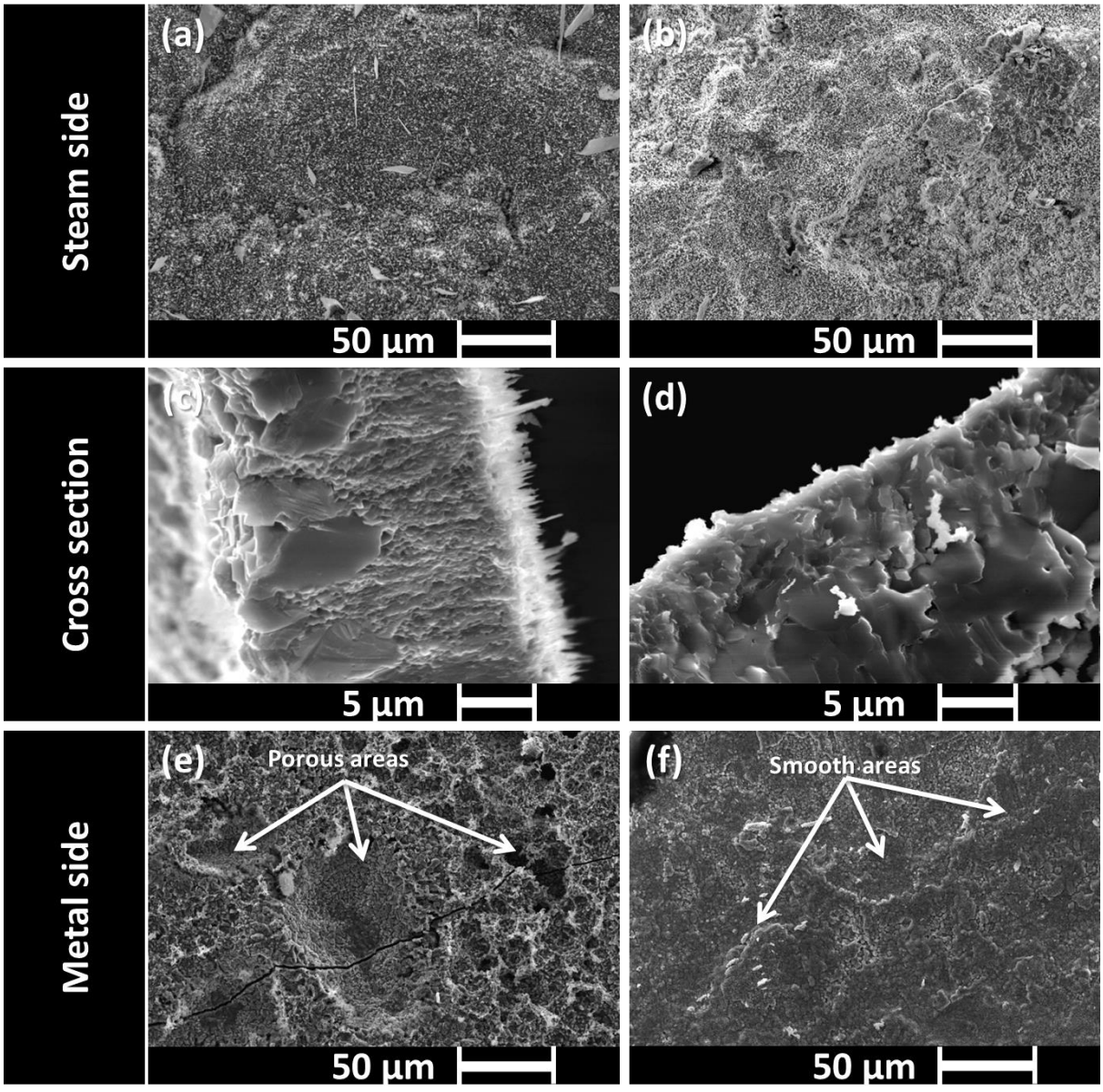

Figure 4-79: SEM imaging of exfoliated oxide flakes: original steam side at (a) 700°C and (b) 750°C; image of the side of a flake at (c) 700°C and (d) 750°C; side of the flake which was in contact with the remaining oxide at the material's surface at (e) 700°C and (f) 750°C.

Observations of exfoliated oxide flakes from samples exposed at 800°C are shown in Figure 4-80 and Figure 4-81. These show that there are occasionally large growing magnetite grains, between 80 and 160 µm long, on P1200 ground surfaces exposed to steam at 800°C after 500 and 1500 hours respectively. Lyta et al. [51] reported that, for austenitic steels such as TP347HFG, surface magnetite grain sizes could became larger with increasing oxidation time.

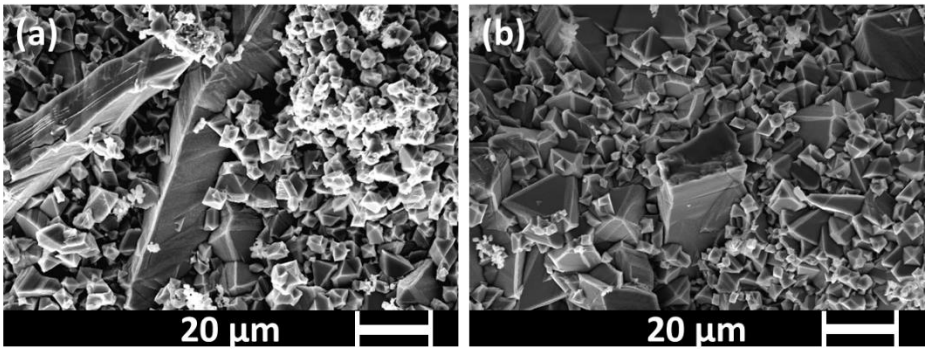

Figure 4-80: Two example SEM secondary electron images of the steam side of an exfoliated oxide flake at 800°C after 500 hours of steam exposure.

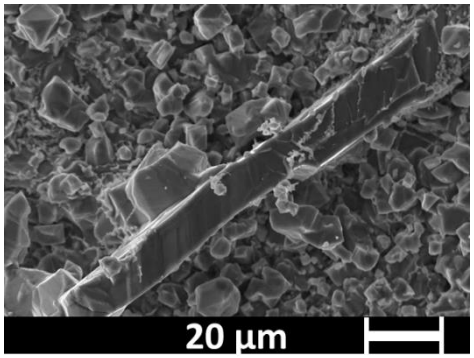

Figure 4-81: SEM image of the steam side of an exfoliated oxide flake at 800°C after 1500 hours of steam exposure.

Figure 4-82 shows examples of large Fe-rich oxide grains formed during 1500 hours of steam exposure at 800°C. It was observed that smaller oxide grains were present between the large crystals of magnetite.

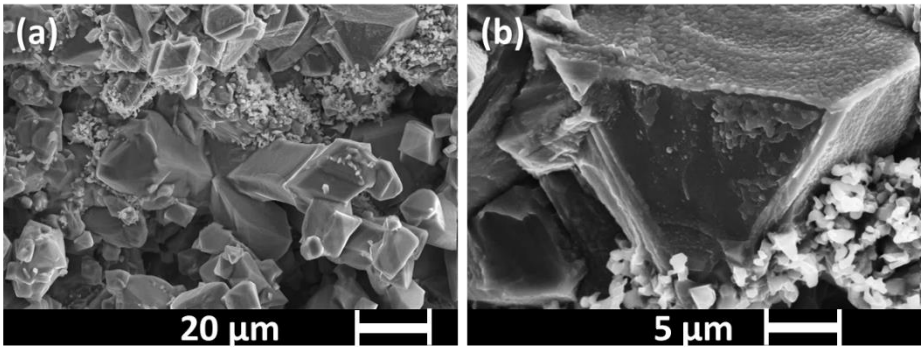

Figure 4-82: Two example SEM secondary electron images of the steam side of an exfoliated oxide flake at 800°C after 1500 hours of steam exposure.

The reasons for the formation of such large grains and for the mechanisms associated with their growth could not be determined with the experimental tests from which these spalled oxides come from. However, since these long magnetite grains were not observed on oxide flakes exfoliated from tests at 700 and 750°C, it would appear that they are characteristic of steam oxidation processes occurring at higher temperatures (such as 800°C).

4.2.5. Discussions

The large amount of results obtained from the laboratory tests at atmospheric pressures have helped drawing some interesting conclusions regarding the effect of composition, temperature and surface finish upon the steam oxidation process.

Austenitic steel TP347HFG, possessing low chromium and nickel content compared to Sanicro 25, experiences very detrimental oxidation when exposed to steam at a temperature above 700°C. This is symbolised by a large mass loss, starting at 2750 hours for the exposition at 700°C and at temperatures of 750 and 800°C, mass loss starts as early as 500 hours and 250 hours. Due to the low oxidation resistance of this material, different finishes have been applied to the surface of the material to try to increase its oxidation resistance. Indeed, increasing the number of defects and the level of compressive stresses at a

surface increases the chromium diffusion so that a protective chromia can be formed. The different surface finishes tested were either left as-received, P1200 ground, P2500 ground, machined or shot-peened. For surface finishes with only weak compressive stresses, a chromia layer is observed to be initially formed at the surface of the material at the various temperatures before failing. Failure happens earlier with increasing steam temperature. Having a P1200 or P2500 ground surface delays the failure of the protective layer compared with a surface left as-received. Breakaway oxidation is first characterized by the apparition of iron-oxide nodules. The nodules appear on top of grains from the bulk material and are multi-layered with an inner and outer oxide. The outer part of the nodules are composed of iron oxides, mainly magnetite with few traces of haematite, whereas the inner part gathers chromium-rich oxides. These chromium-rich oxides, $(FeNiCr)_3O_4$, formed in the bulk of the material's grains, are delimited by a thin chromia layer formed at the grain boundary location. This observation is coherent and is proof that the grain boundaries are preferential and faster diffusion paths for chromium and oxygen compared with diffusion in grain bulks. With increasing oxidation time, the nodules spread out at the surface of the material until the entire surface is covered with a multi-layered oxide. The internal oxide layer gather the oxidized grains of the original material. The grain boundaries of the original material have been replaced by chromia and the grain bulk by chromium-rich oxide.

The growth of the inner oxide associated with the nodule formation is observed (Figure 4-83) to follow the following steps:

1. Formation of an internal oxidation zone in the bulk of a grain located underneath the previously oxidized areas. The front of the internal oxidation zone penetrates the material's grain until it reaches its grain boundaries.
2. The grain boundary oxidizes and forms a thin chromia layer.
3. Transformation of the chromia layer into $(FeCr)_3O_4$ and oxidation of the grain's bulk with the formation of $(FeNiCr)_3O_4$. The nickel is then concentrated at the centre of the oxidized grains.

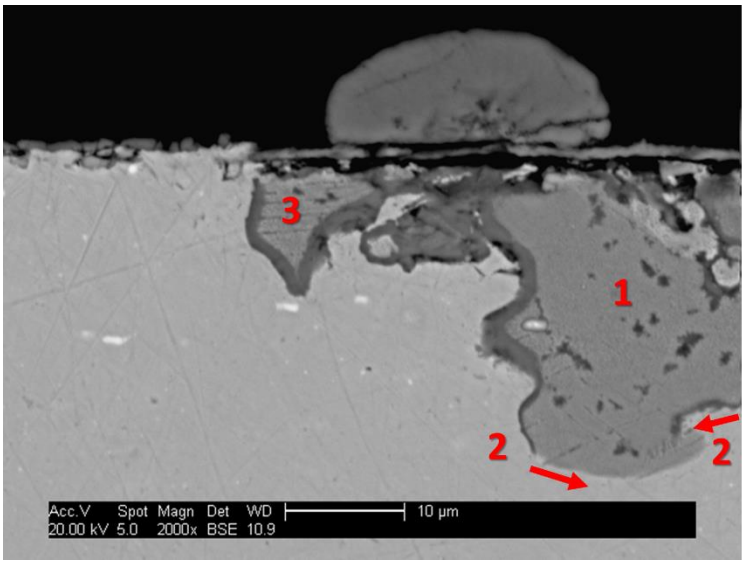

Figure 4-83: SEM image of a nodule formed on TP347HFG showing the different steps for internal oxidation.

This procedure describing the growth of the internal oxide is similar to what was described by Jianmin et al. [28,52]. However, since the exposure tests have lasted for a longer time, $(FeNi)_3O_4$ was observed in the outer layer. Actually, this oxide is present between the inner layer and the magnetite formed.

The apparition of a multi-layered oxide is one of the reason why spallation occurs. The amount of oxide loss measured on Figure 4-12 strongly suggest mass loss dependence as a function of the steam temperature on TP347HFG. Exfoliated areas are visible on multiple SEM images and some oxide flakes have been recovered and analysed. The observation of spalled oxide flakes lead to the understanding that the interface were spallation occurs is composed of weak and strong areas. The weak areas arose from the presence of internal porosity. This porosity is formed due to the mismatch of crystalline lattice between the different oxides. Strong areas are represented by smooth areas formed by the rapid failure of the interface from where the oxide flake exfoliates. Failure is triggered by rapid change in temperature during the cooling down of the steam furnaces at the end

of each cycle. Since the different oxide formed possess different coefficient of thermal expansion, stresses build up inside the multi-layered oxide leading to the apparition of cracks which propagate and cause spallation.

Surface finishes with strong compressive stresses such as after machining and shot-peening, drastically increase the oxidation resistance of the material. Indeed, in terms of oxide thickness measured, only a thin oxide layers have been measured, even after 10,000 hours of steam exposure at 800°C (Figure 4-32). The thickness measured is similar to the results obtained for Sanicro 25 and nickel-based alloys. The two different shot-peened techniques used for sample preparation were not known but it seems the SANYO shop-peening leads to better oxidation resistance than the PISCO shot-peening. The machining technique for sample preparation also provide a large increase in the steam oxidation resistance of the material.

Machining the samples' surfaces thus increases the oxidation resistance of the materials because it contributes to the formation of dislocations near the surface of the material. These dislocations enhance the diffusion of chromium towards the surface of the material at the early stages of the oxidation process which allow the formation of a protective chromium-rich layer [12,23,44]. The higher the compressive stresses brought to the surface, the higher the oxidation resistance of the material.

As a remark from TP347HFG sample analyses, it seems that the samples prepared by a previous student, labelled to possess an as-received concave surface and P1200 ground convex surface, and exposed between 650 and 750°C for 500, 1500 and 2500 hours actually possess a machined surface finish on the convex. This would explain why only a chromia layer is detected on their surfaces (Figure 4-18).

For Sanicro 25, the mass change values obtained with the different surface finishes tests only show very little mass gain and does not seems affected by spallation. The values obtained are similar to what has been recorded for nickel-based alloys ($<2 mg.cm^{-2}$). This is quite impressive for an iron-based alloy to

demonstrate such a high oxidation resistance. In terms of oxide composition and morphology, all samples exposed have formed a very protective chromia layer. A few iron-oxide nodules have been observed on some samples but their number is very low. Some areas where the chromia layer has exfoliated have also been pointed out. The effect of surface finish on this sample was not crucial, indeed the results in terms of mass change, oxide composition and morphology, and oxide thickness are similar with the different surface finishes tested. It even seems that P1200 and P2500 ground surfaces are the ones that exhibit nodule formation and chromia spallation, whereas on as-received surfaces only thin chromia layer is present.

The various nickel-based alloys exposed to high temperature steam all exhibit low mass gain (<2mg.cm^{-2}) and no exfoliation. In terms of oxide morphology, only thin chromia layers are formed. Preferential oxidation above the grain boundaries is observed. This is due to an enhancement of the chromium and oxygen diffusion along grain boundaries. For the alloy 617, from which P1200 and P2500 ground samples have been prepared and exposed, it results that no clear effect from surface finish could be observed. This result proves that for this material, there is no need to increase the chromium outward diffusion in the early stage of the oxidation process.

As an attempt to interpret the different standard normal distribution plots obtained and to quantify and give significance to the different parts of the curves, different distributions could be used. The normal distribution is the most common continuous distribution that one can encounter to study an entire population. If the population studied follows a normal law, then its standard normal distribution plot should be a straight line. Another distribution, the Gumbel distribution, also called double exponential distribution, can be used in material sciences to evaluate extreme data.

Table 4-4: Different functions associated with the Normal and Type-I Gumbel distributions. μ and σ represent respectively the mean and the standard deviation of the different distributions [83].

	Normal distribution	Type-I Gumbel distribution
Probability density function $f(x)$	$f(x) = \frac{1}{\sigma\sqrt{2\pi}} \exp\left(-\frac{(x-\mu)^2}{2\sigma^2}\right)$	$f(x) = \frac{1}{\sigma} \exp\left[-\frac{x-\mu}{\sigma}\right] * \exp\left[\exp\left(-\frac{x-\mu}{\sigma}\right)\right]$
Cumulative distribution function $F(x)$	$F(x) = \frac{1}{2}\left[1 + \mathrm{erf}\left(\frac{x-\mu}{\sigma\sqrt{2}}\right)\right]$	$F(x) = \exp\left[-\exp\left\{-\frac{x-\mu}{\sigma}\right\}\right]$
Link between x and $F(x)$	$\sqrt{2}\,\mathrm{erf}^{-1}(2F(x)-1) = \frac{x-\mu}{\sigma}$	$\ln\left(\ln\left(\frac{1}{F(x)}\right)\right) = \frac{\mu - x}{\sigma}$

The cumulative distribution function $F(x)$ is obtained by ordering the measured data in increasing value and then calculation the ratio of their ranking position over the number of values in total plus 1. Eg. N points are ordered $x_1 < x_2 < \cdots < x_1 < \cdots < x_N$ and the cumulative probability of each point is calculated as $F(x_i) = \frac{i}{N+1}$.

Once $F(x)$ has been calculated $Y(x)$ can be plotted as a function of x and then a linear regression allows to evaluate the values of μ and σ for the different distributions.

After the measuring of the oxide scale thickness of an exposed sample, the cumulative standard normal distribution of the values is plotted, as shown in Figure 4-84. Typically the curve obtained is not linear but can be separated three different linear sections: low, medium and high values. The data points from the three different sections are then isolated and plotted under an appropriate distribution allowing the best description of the reduced data sets:

- Low values are best described by the normal distribution
- Medium values are best described by the normal distribution
- High values are best described by the Gumbell distribution.

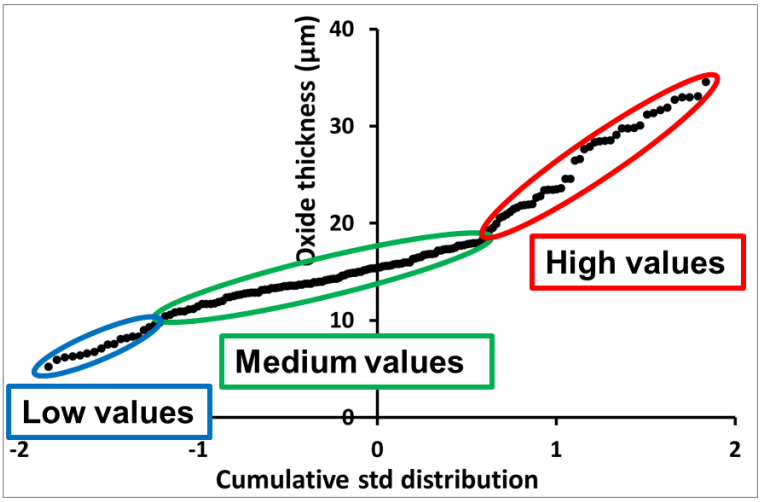

Figure 4-84: Cumulative standard normal distribution plot for the oxide scale thickness measured on the as-recevied surface of TP347HFG after 500 hours of steam exposure at 750°C.

In order to give some significance to the different data sets extracted from the original thickness data, some hypothesis have been made and can be justified. The different hypothesis are:

- Low values: they represent either the thickness of the protective oxide formed at short exposure time before it breaks down or the remaining oxide thickness a locations where exfoliation has occurred.
- Medium values: they represent the average oxide growth mechanism after the breaking down of the protective oxide layer and before exfoliation occurs.
- High values: they represent the nodular growth mechanism of the oxide and gives information about the maximum thickness value of the oxide layer before exfoliation occurs.

One thing has to be kept in mind when analysing the reduced data sets is that data points represented in the low values data set can come from areas where exfoliation has occurred and therefore these points should have appeared in the high value data set if exfoliation did not occur. This transfer of data due to the exfoliation process can be the reason why, for some case, the medium part of the curve possesses a larger slope at high exposure time.

Another remark can be made regarding the cumulative standard normal distribution plot. In the case of Figure 4-85, it is possible to observe that the lower values part of the curve does not exhibit a linear behaviour. Instead different steps can be seen. These steps may be representative of different stages of oxide regrowth at location where exfoliation could have occurred at different time.

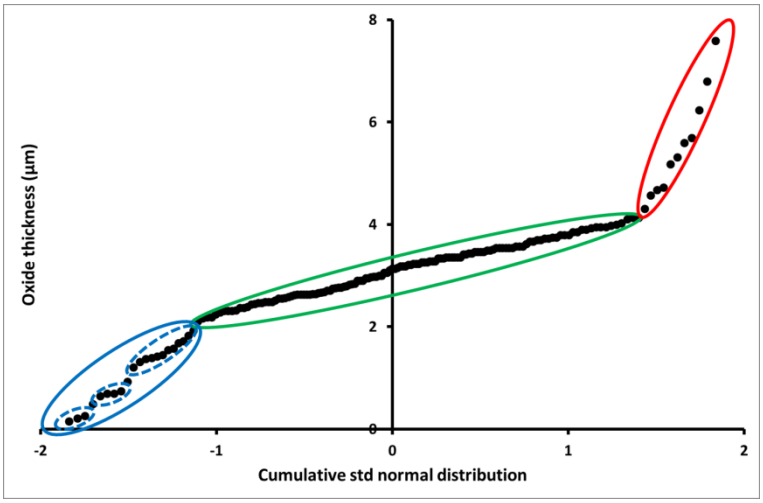

Figure 4-85: Cumulative standard normal distribution plot for the oxide scale thickness measured on the P1200 ground surface of TP347HFG after 2500 hours of steam exposure at 750°C.

4.3. Steam oxidation kinetics and modelling

In this Section, steam oxidation kinetics regarding the mass change and the oxide thickness growth for different materials are presented. This contributes to quantify

the differences in oxide formation as a function of the alloy and surface finish applied.

4.3.1. Mass change kinetics

The mass change data obtained is used to calculate the kinetic parameters for the different materials and different surface finishes. The kinetic parameters of interest are the activation energy and the standard rate constant. In order to obtain comparable values in terms of oxidation rates, the same order of reaction has to be chosen. It has been decided to use an order of reaction of 2 so the determined oxidation rates are parabolic.

The mass change equation for a parabolic rate is written

$$\Delta m^2 = k_p t + c \quad \textbf{(4-3)}$$

Where Δm is the mass change per unit of area [$mg.cm^{-2}$], k_p is the parabolic rate [$(mg.cm^{-2})^2.h^{-1}$], c is a constant in [$mg.cm^{-2}$] and t is time [h].

The effect of temperature on the oxidation rate is described by the Arrhenius equation. The following equation presents the Arrhenius law for parabolic rates:

$$k_p = k_0 \exp\left(-\frac{Q}{RT}\right) \quad \textbf{(4-4)}$$

Where Q is the activation energy of the oxidation reaction [$J.mol^{-1}$], R is the gas constant [$J.mol^{-1}.K^{-1}$], T is the absolute temperature [K], and k_0 is the standard rate constant [$(mg.cm^{-2})^2.h^{-1}$].

The determination of the oxidation parameters k_0 and Q is possible by using Arrhenius plots which represents $\ln(k)$ as a function of $\frac{1}{T}$. Since the logarithmic transformation of Equation (4-4) is Equation (4-5), a linear fitting of the

experimental data contributes to the determination of the activation energy Q and of the standard rate constant k_0.

$$\ln(k_p) = \ln(k_0) - \left(\frac{Q}{R} * \frac{1}{T}\right) \quad \textbf{(4-5)}$$

Arrhenius plots presenting the oxidation rates obtained by fitting the mass change data using Equation (4-3) were used. These plots have been used to determine the activation energy Q and the standard rate constant k_0. These plots are also useful to compare the oxidation kinetics of different materials and different surface finishes.

However, when spallation takes place, the oxidation rates can no longer be properly calculated from a fitting process of the global data set. To counter this problematic raised by the spallation process, the parabolic rates have been calculated for each positive mass change data point individually, using Equation (4-6) and represented in Arrhenius plots adapter to include the time parameter:

$$k_p = \frac{\Delta m^2}{t} \quad \textbf{(4-6)}$$

Where Δm is the mass change per unit of area [$mg.cm^{-2}$], k_p is the parabolic rate [$(mg.cm^{-2})^2.h^{-1}$], and t is time [h].

The idea with using these plots with the time dimension is to observe the evolution of the oxidation rate as a function of the exposure time. Indeed, in the literature multiple works report the oxidation rate that they have observed at a different given times, so this solution might help understand and mitigate the differences observed between the different values reported.

The combined used of both Arrhenius plots presented later, help visualize the difference between the oxidation rates calculated by fitting the mass change data set and those calculated individually for each data point. As a mean to set reference points regarding the oxidation resistance of the materials from which the oxidation rates are calculated, linear fittings of oxidation rates found in the literature for the oxidation of pure chromium [70] and for the oxidation of pure iron

[84–88] are represented in the different graphs. These values have been selected from different works encountered during the literature review. If the calculated points are close to the reference points for pure chromia formation, then the material possesses a high oxidation resistance and the oxide formed must be chromia. Similarly, when the calculated points are close to the reference points for the oxidation of pure iron, the material possesses a low oxidation resistance and iron oxides are formed. Materials with oxidation rates located in between the two sets of reference points can be considered to possess an intermediate oxidation resistance.

4.3.1.1. Austenitic steels

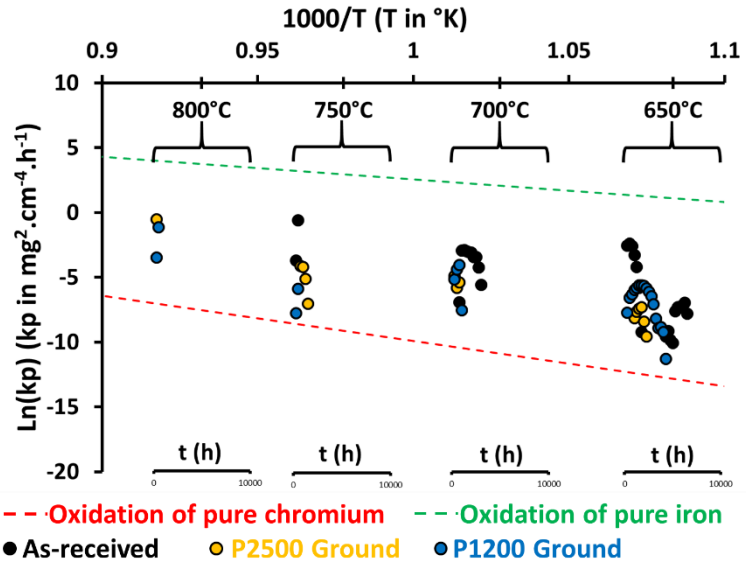

Figure 4-86: Adapted Arrhenius plot for mass change parabolic rates calculated for TP347HFG.

Figure 4-86 shows the oxidation rate calculated for the different surfaces finishes of TP347HFG as a function of both time and exposure time. Only positive mass change data was plotted. Since mass change calculated at 800°C for the as-

received surface of the material is negative since the first cycle, there is no value represented at this temperature.

The calculated oxidation rates are in between the two reference lines. This is consistent with what has been visualised on the cross-sections of the different samples exposed where multi-layered oxides are formed with inner chromium-rich oxide and outer iron oxides. Moreover, since this particular material experiences exfoliation, the loss of oxide mass interfere with the calculation of the parabolic oxidation rates which is represented by a decrease of the calculated rates for mass change data. Nevertheless, the oxidation rates increase with increasing steam temperature.

Comparing the different surface finishes, it appears that grinding and polishing the surface lead to a visible reduction of the oxidation rates calculated which means it increases the oxidation resistance of the materials compared to the as-received surface finish.

Figure 4-87 represents the Arrhenius plots of the parabolic oxidation rates calculated by fitting the mass change data during the cycles of the oxidation tests before spallation starts. The calculation of the kinetic parameters was performed by a fitting procedure. As-received surfaces possess higher values of oxidation rates compared with P1200 and P2500 ground surfaces. However, the activation energy calculations give some results difficult to explain. Indeed, for the different surface finishes, the activation energy calculated is higher for the surfaces showing the higher oxidation resistance.

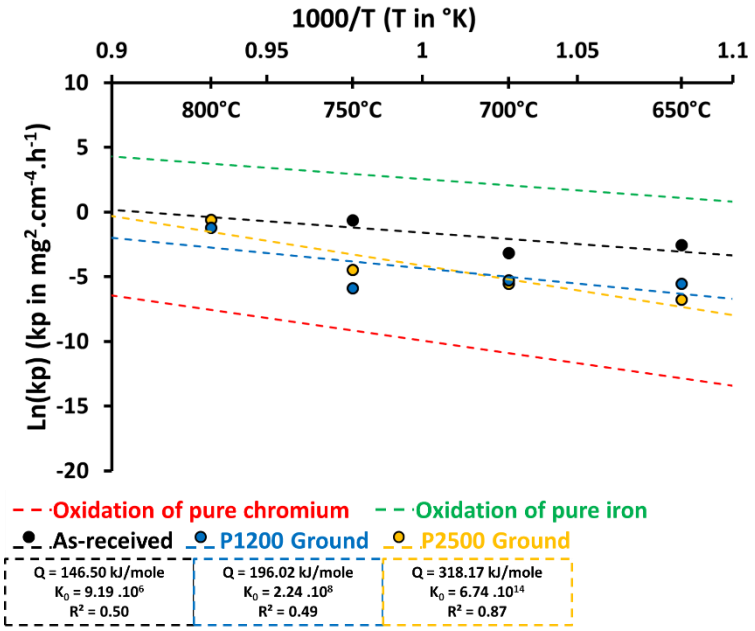

Figure 4-87: Arrhenius plot for parabolic mass change oxidation rate, before spallation occurs, calculated for TP347HFG.

Figure 4-88 shows the linear mass change oxidation rate calculated from fitting the mass change data when spallation and oxide growth happen simultaneously. The values obtained for the different surface finishes of TP347HFG are all close to one another. This means the simultaneous oxide growth and spallation processes are not affected by surface preparation.

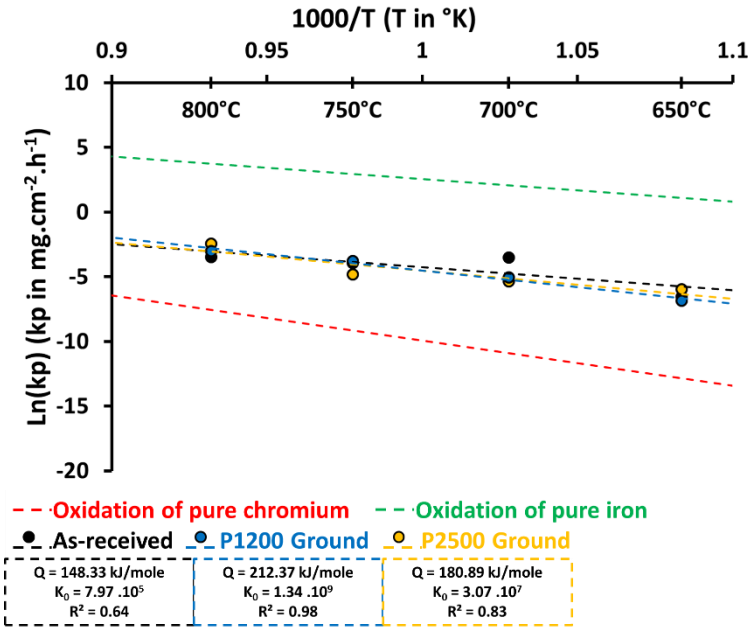

Figure 4-88: Arrhenius plot for linear mass change oxidation rate during spallation calculated for TP347HFG.

For austenitic steel Sanicro 25, the parabolic oxidation rates calculated are much lower than those for TP347HFG. The values presented in Figure 4-89 are close to the reference line for the oxidation of pure chromium. This means the material possess a high oxidation resistance and mostly forms chromia oxide at its surface. This is consistent with the surface analyses performed on oxidized surfaces of Sanicro 25 and presented in Section 4.2.1.2. Even though exfoliation was observed only in small amount on the SEM images, the mass change data remains representative of a material experiencing only oxide growth.

A large scatter can be seen at 750 and 650°C for as-received surfaces. This is due to the de-correlation procedure used to calculated mass change for the as-received surfaces. In general, P1200 and P2500 ground surfaces exhibit higher steam oxidation resistance than surfaces left as-received. The parabolic rates calculated for P1200 and P2500 ground surfaces decrease with increasing oxidation time. It is believed that since Sanicro 25 is a chromia forming alloy, the thicker the chromia layer, the more protective the material. This would mean that the material sees its oxidation resistance increase with increasing oxidation time. For surfaces left as-received, the values calculated at 800°C remain stable with

increasing oxidation time. Moreover, at 700°C, the parabolic rate first decrease and then stabilize at a higher level. This behaviour for the as-received surface at 700°C may arise from the early formation of protective chromia layer which increases the protectiveness of the material with increasing oxidation time until a sudden growth of oxide is detected and becomes steady. This sudden increase of oxidation rate can be due to the breakaway of the chromia layer but no iron oxides are detected on the surface of the sample. At 800°C, the growth of the chromia layer does not decrease with increasing oxidation time but is constant. Thus it can be inferred that grinding and polishing are beneficial to the oxidation of Sanicro 25 due to their ability to promote the formation of a chromia layer increasing the oxidation resistance of the material over time.

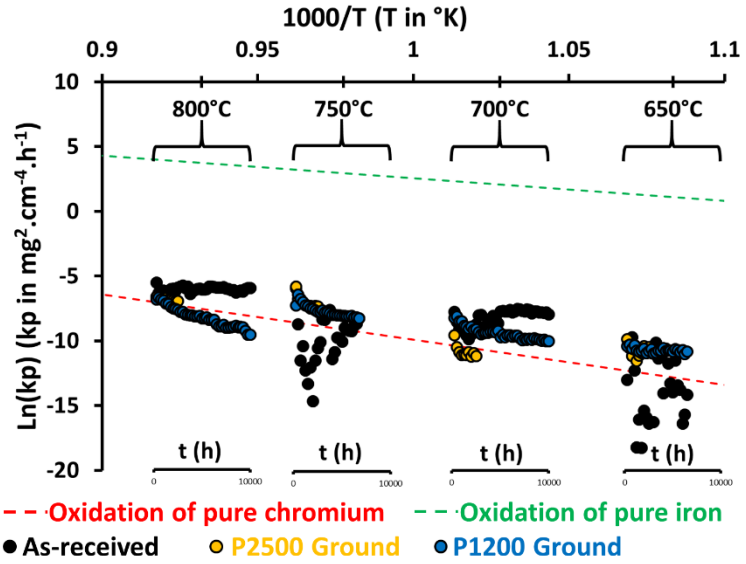

Figure 4-89: Adapted Arrhenius plot for mass change parabolic rates calculated for Sanicro 25.

Figure 4-90 represents the parabolic rates calculated from fitting the mass change data for the different surfaces of Sanicro 25. The values for the different surfaces are close to each other, unlike what was observed in Figure 4-89. However, the activation energy calculated decrease with the presence of surface working. This means the effect of temperature is less significant for P1200 ground

surfaces compared to P2500 ground surfaces and even less significant than for surfaces left as-received.

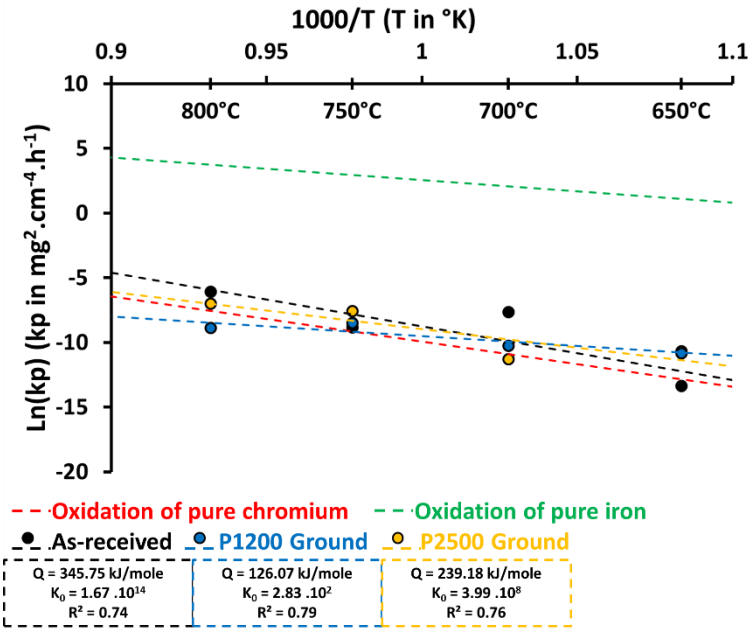

Figure 4-90: Arrhenius plot for parabolic mass change oxidation rate calculated for Sanicro 25.

4.3.1.2. Nickel-based alloys

For the different nickel-based alloys studied, the parabolic oxidation rates are represented in Figure 4-91. Similarly than for Sanicro 25, the values calculated for the Alloy 617, Alloy 263 and Alloy 740 are close to the reference line for the oxidation of pure chromium. Hence, the different nickel-based alloys possess a high steam oxidation resistance. On the adapted Arrhenius plots, Figure 4-91, it can be seen that the oxidation rate decreases with increasing exposure time for all the materials and all the temperatures tested. The reason for this trend would be the outward diffusion of chromium cations decreases with and increasing chromia layer thickness. This explanation is coherent with the protective properties of the chromia layer. In terms of mass change, the lower oxidation rates are obtained for Alloy 617 and then Alloy 263 and Alloy 740 show similar

values. The effect of surface finish has only been investigated for Alloy 617 however, Figure 4-92 show that parabolic rates are not affected by the surface finish.

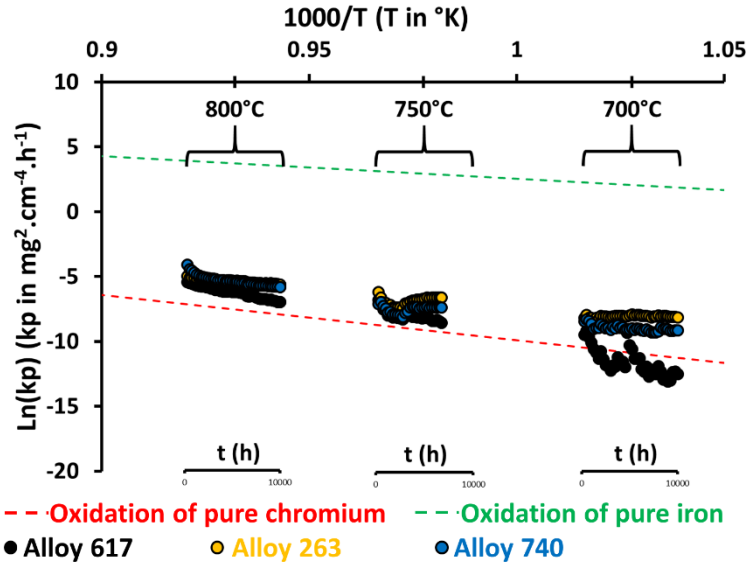

Figure 4-91: Adapted Arrhenius plot for mass change parabolic oxidation rates calculated for nickel-based alloys with P1200 ground surface finish.

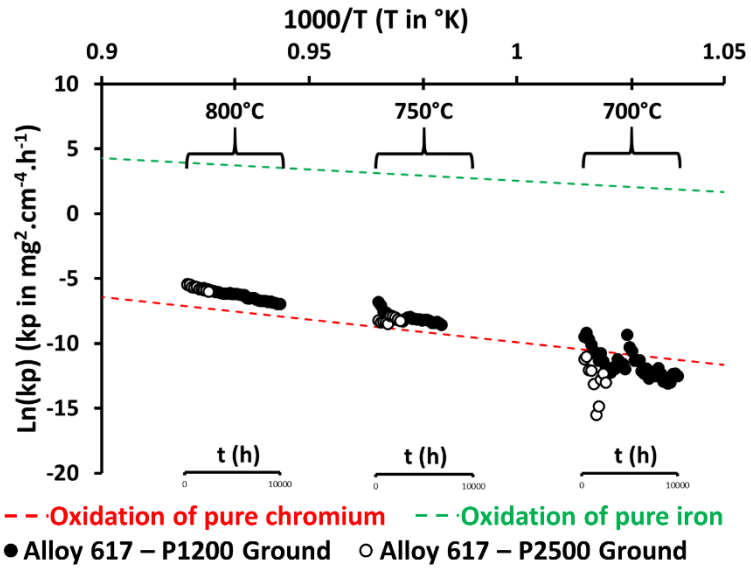

Figure 4-92: Adapted Arrhenius plot for mass change parabolic oxidation rates calculated for nickel-based alloy 617 with P1200 and P2500 ground ground surface finishes.

Figure 4-93 shows the parabolic rates calculated from fitting the mass change data for the different nickel-based alloys. Alloy 263 is seen to possess the higher oxidation rates, followed by Alloy 740 and then Alloy 617 with both P1200 and P2500 ground surfaces. The activation energies calculated do not follow the order described earlier. The very low oxidation rates calculated at 700°C for Alloy 617 result in a steep slope for the linear fitting which has lead to the calculation of a very high activation energy for the material even though it is the one that shows the best oxidation resistance.

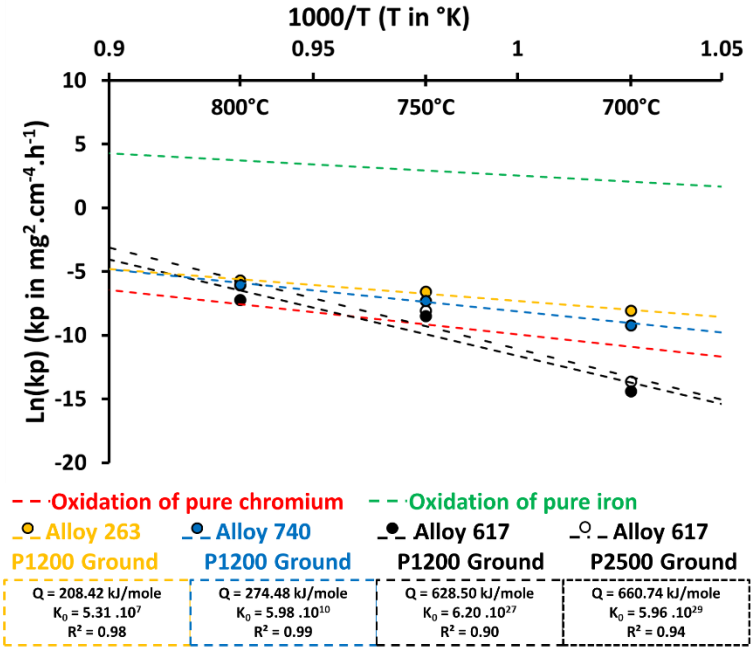

Figure 4-93: Arrhenius plot for mass change parabolic oxidation rates calculated for nickel-based alloys with P1200 and P2500 ground surface finishes and determination of the kinetics parameters.

4.3.2. Mass change modelling

A method for modelling mass change has been developed using the mass change data gathered from the experimental results. The model proposed here can be used for cyclic modelling and takes into consideration spallation. The

different kinetic parameters used for the modelling have been determined via the fitting of the experimental data obtained for the different samples exposed for 10,000 hours. Spallation is taken into account in the model through a spalling parameter which determines the proportion of the mass of oxide formed that spalls. The determination of this parameter was been done manually. The model developed is based on the transformation of the net mass change data obtained into the mass of oxide formed. Indeed as described in Equation (4-7), the mass change data measured during the experiments corresponds to the mass of oxygen absorbed minus the mass of oxide spalled. To calculate the mass of oxide formed, it is necessary to calculate the mass of oxygen absorbed and the mass of metal transformed (Equation (4-8)). The mass of metal transformed can be written as a fraction of the mass of the oxide formed (Equation (4-10)) and the mass of oxide spalled is assumed to be a fixed fraction of the mass of the oxide formed (Equation (4-11)). Eventually, Equation (4-12) links directly the net mass change measured to the mass of oxide formed.

$$\Delta m_{measured} = \Delta m_{oxygen\ absorbed} - \Delta m_{oxide\ spalled} \quad \textbf{(4-7)}$$

$$\Delta m_{oxide\ formed} = \Delta m_{oxygen\ absorbed} + \Delta m_{metal\ transformed} \quad \textbf{(4-8)}$$

$$\Delta m_{oxygen\ absorbed} = \Delta m_{oxide\ formed} - \Delta m_{metal\ transformed} \quad \textbf{(4-9)}$$

$$\Delta m_{metal\ transformed} = A\ \Delta m_{oxide\ formed} \quad \textbf{(4-10)}$$

A is a constant and represents the theoretical ratio of the molar mass of metal transformed over the molar mass of oxide formed. A values for chromia and magnetite formation have respectively been calculated to be 0.68 and 0.72. For austenitic steels that form multi-layered oxides, with outer iron-oxides and inner chromium-rich oxides, the parameter A was chosen to be 0.7.

$$\Delta m_{oxide\ spalled} = F\ \Delta m_{oxide\ formed} \quad \textbf{(4-11)}$$

F represents the proportion of oxide exfoliating. Hence $0 \leq F \leq 1$.

$$\Delta m_{measured} = (1 - A - F)\Delta m_{oxide\ formed} \quad \textbf{(4-12)}$$

For the previous equations $\Delta m_{measured}$ stands for the mass change density measured during the exposure experiments, $\Delta m_{oxygen\ absorbed}$ is the mass density of oxygen absorbed, $\Delta m_{oxide\ spalled}$ is the mass density of oxide spalled and $\Delta m_{metal\ transformed}$ is the mass density of metal transformed into oxide. All those mass densities are in $mg.cm^{-2}$.

The different materials studied do not possess the same behaviour when exposed to high temperature steam, indeed some experience spallation and some other do not. Two different equation have thus been developed to differentiate the two cases that can be encountered but they are both based on the same mathematical basis. The first part of the model considers the early stage of the oxidation process when spallation is not occurring (F=0). At this stage the mass change is considered parabolic. The second stage concerns the mass change after the material starts experiencing spallation. Long after the time when spallation starts occurring, the net mass change data follows a linear trend and it seems the materials are in a kind of established regime. Then the rates for oxide formation and oxide spallation can be assumed to be equilibrated. It can thus be considered that oxide formation follows a linear trend and that a proportion of the mass of oxide formed spalls.

There could be a debate whereas the early stages of the oxidation process is important for the materials experiencing exfoliation such as TP347HFG. Indeed the pre-breakaway could be very short and for industrial uses where the material is required to last for 100,000 hours the material would be in the spalling stage for most of his lifetime. In consequence, for materials experiencing exfoliation, the linear part of the model could be the most interesting one for an industrial point of view.

Table 4-5 presents the two parts of the modelling equation, the first one describing the oxide quantification before spallation occurs and the second being the oxide quantification when the material experience spallation.

Table 4-5: Presentation of the equations used for the two parts of the model, i.e. before and during spallation.

Case before spallation (F=0)	Case during spallation (F≠0)
$\Delta m_{oxide} = \frac{\Delta m_{measured}}{(1-A)}$ **(4-13)**	$\Delta m_{oxide} = -\frac{\Delta m_{measured}}{(1-A-F)}$ **(4-15)**
$\Delta m_{oxide} = \left(k_p t + C_p\right)^{\frac{1}{2}}$ **(4-14)**	$\Delta m_{oxide} = (k_l t + C_l)$ **(4-16)**
	$\Delta m_{measured} = \Delta m_{oxide}(1-A-F)$ **(4-17)**

After gathering the two parts of the equation, the quantification of the mass change experienced by the oxidizing material can be described with the following equation:

$$\Delta m_{measured} = (1-A)\left(k_p t + C_p\right)^{\frac{1}{2}} + \left(\frac{1}{2}[1+\tanh(t-t_t)]\right)(1-A-F)\,(k_l(t - t_t) + C_l) \quad \textbf{(4-18)}$$

The term $\left(\frac{1}{2}[1+\tanh(t-t_t)]\right)$ is used in the equation so that before the transition time (t_t) the linear part of the equation is null. For highly resistant materials, the transition time is outside the time interval studied so the second part of the equation is always null (this is the case for Sanicro 25 and the different nickel-based alloys studied).

The different rates C_p and C_l used in Equation (4-18) where linked with temperature using Arrhenius Equation (4-4) and the different kinetic parameters

determined previously in Section 4.3.1. However, the constants C_p and C_l used in Equation (4-18) proved not to be linked with temperature, and were then chosen to be null. As a result, the modelling equation developed were quite simple.

For TP347HFG, which is the only material studied experiencing spallation, a correlation between the transition time and the temperature has been developed. The transition times, at which the oxidation kinetics switch from a parabolic rate to a linear rate, have been determined using the mass change data presented in Figure 4-12 and were plotted in Figure 4-94 as a function of steam temperature independently of the surface finish applied to the different samples. The points show a direct linear correlation between transition time and steam temperature. As a consequence, for all surface finishes of TP347HFG, the transition time is considered dependant on steam temperature following Equation (4-19):

$$t_t = (8675 - 9.67 * T) \quad \textbf{(4-19)}$$

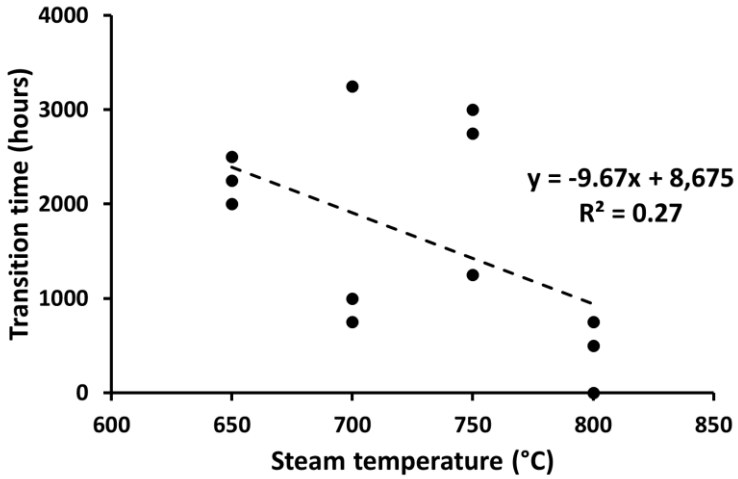

Figure 4-94: Linear correlation between transition times and steam temperature for all surfaces of TP347HFG studied.

4.3.2.1. Austenitic steels

Mass change modelling equations for the different surfaces of TP347HFG are presented bellow. Equations (4-20), (4-21) and (4-22) describe the mass change evolution for as-received, P1200 and P2500 ground surfaces respectively.

Mass change modelling equation for as-received surfaces of TP347HFG:

$$\Delta m = (0.3)\left(9.19\ 10^{+6}\exp\left(-\frac{146.50}{RT}\right)t\right)^{\frac{1}{2}} - \left(\frac{1}{2}[1+\tanh(t-t_t)]\right)(7.97\ 10^{+5}\exp\left(-\frac{148.33}{RT}\right)(t-t_t)) \quad \textbf{(4-20)}$$

Mass change modelling equation for P1200 ground surfaces of TP347HFG:

$$\Delta m = (0.3)\left(2.24\ 10^{+8}\exp\left(-\frac{196.02}{RT}\right)t\right)^{\frac{1}{2}} - \left(\frac{1}{2}[1+\tanh(t-t_t)]\right)(1.34\ 10^{+9}\exp\left(-\frac{212.37}{RT}\right)(t-t_t)) \quad \textbf{(4-21)}$$

Mass change modelling equation for P2500 ground surfaces of TP347HFG:

$$\Delta m = (0.3)\left(6.74\ 10^{+14}\exp\left(-\frac{318.17}{RT}\right)t\right)^{\frac{1}{2}} - \left(\frac{1}{2}[1+\tanh(t-t_t)]\right)(3.07\ 10^{+7}\exp\left(-\frac{180.89}{RT}\right)(t-t_t)) \quad \textbf{(4-22)}$$

Modelling results for TP347HFG are presented in Figure 4-95 for as-received surfaces, Figure 4-96 for P2500 ground surfaces and Figure 4-97 for P1200 ground surfaces. In general the model allows a fair prediction of the mass change during the early and late stages of the oxidation process. The biggest differences have been observed around the transition time when the spallation process starts occurring.

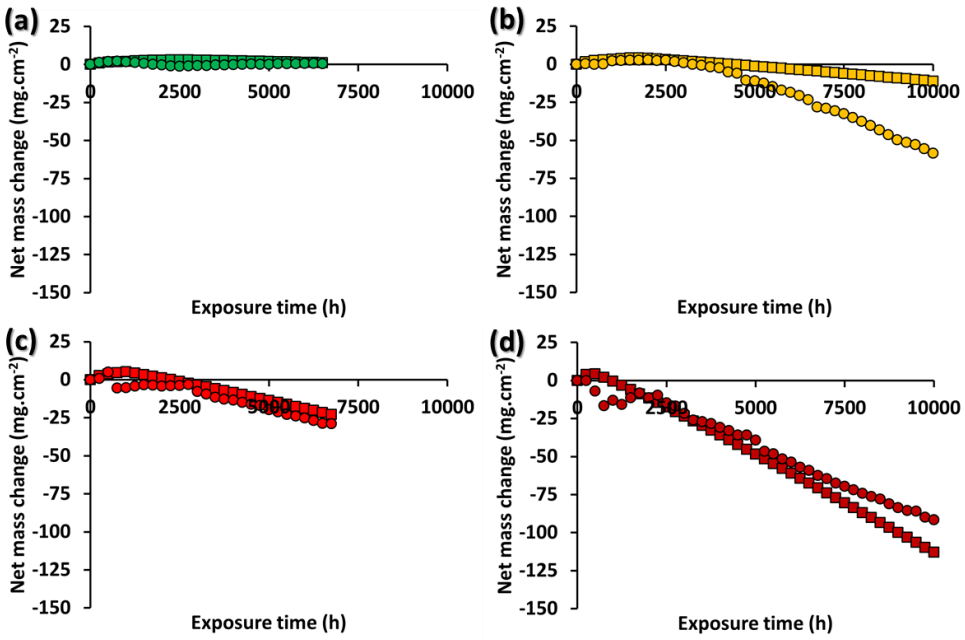

Figure 4-95: Comparison between experimental mass change data (○) and calculated data (□) for as-received surfaces of TP347HFG at (a) 650, (b) 700, (c) 750, and (d) 800°C.

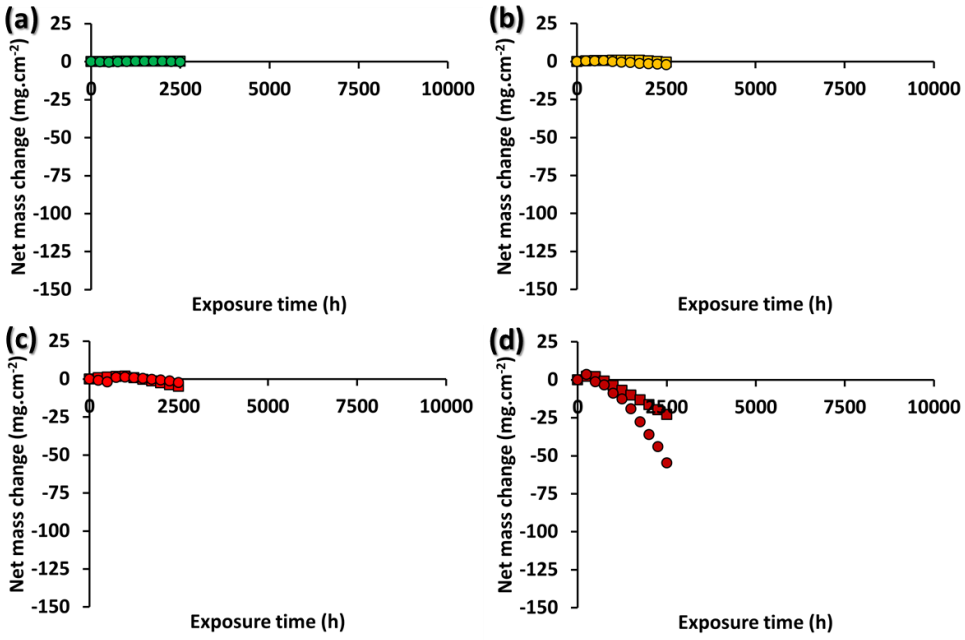

Figure 4-96: Comparison between experimental mass change data (○) and calculated data (□) for P2500 ground surfaces of TP347HFG at (a) 650, (b) 700, (c) 750, and (d) 800°C.

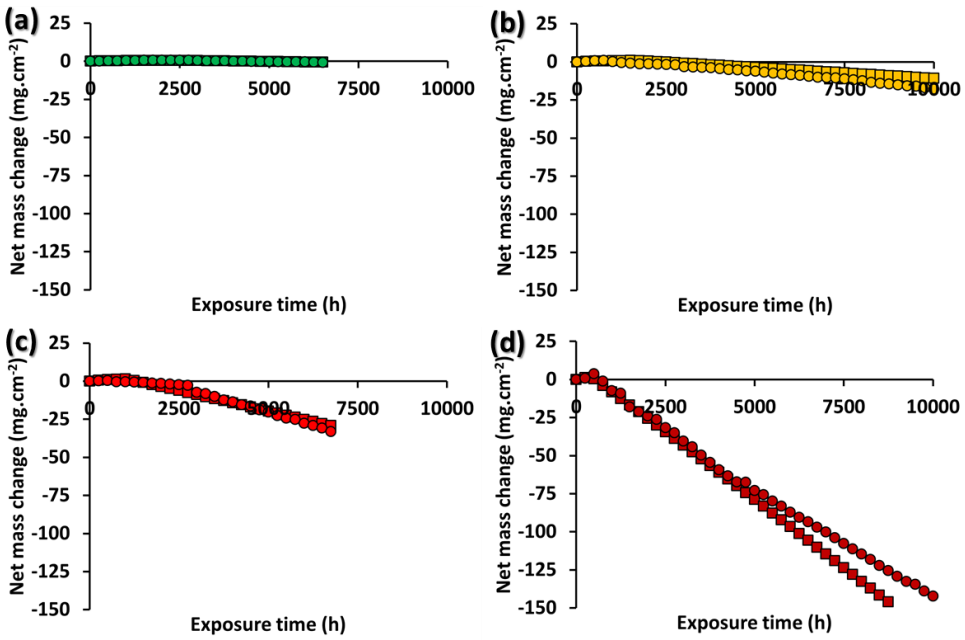

Figure 4-97: Comparison between experimental mass change data (○) and calculated data (□) for P1200 ground surfaces of TP347HFG at (a) 650, (b) 700, (c) 750, and (d) 800°C.

Figure 4-98 shows the degree of correlation between experimental and predicted mass change values for the different surfaces of TP347HFG. For all surface finishes, the overall correlation factor is reasonably good (between 0.74 and 0.99). However, when looking in detail at the predictions of the different temperatures, the correlation between experimental and predicted values can be very low. This observation is mainly true for as-received and P2500 ground surfaces from which the mass change data is obtained after a de-correlation process. For the P1200 ground surfaces data, the predictions at all temperatures show very high correlation (> 0.96) with experimental data. This is a very promising result and the model used for predicting mass change for P1200 ground surfaces would be useful for any industrial who would like to make some long time predictions for steam oxidation of TP347HFG.

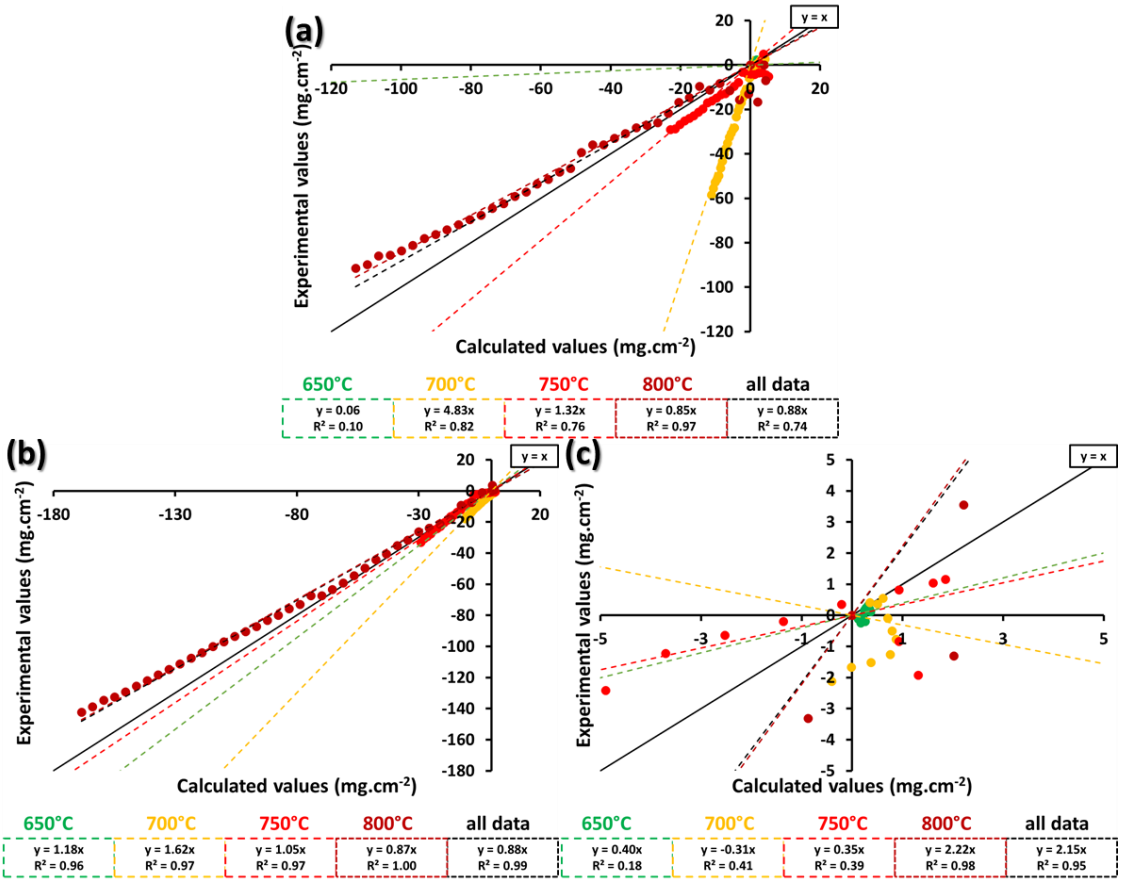

Figure 4-98: Comparative plots with correlation factor calculation between experimental and calculated mass data for TP347HFG with (a) as-received, (b) P1200 ground and (c) P2500 ground surface finish.

For Sanicro 25, mass change for P1200 ground surfaces was predicted using Equation (4-23) and was plotted and compared with experimental data in Figure 4-99. Similarly, Equation (4-24) predicted mass change for P2500 ground surfaces which is presented in Figure 4-100 and for as-received surfaces Figure 4-101 presents the mass change calculated using Equation (4-25).

Mass change modelling equation for P1200 ground surfaces of Sanicro 25:

$$\Delta m = (0.32)\left(2.83\ 10^{+2}\exp\left(-\frac{126.07}{RT}\right)t\right)^{\frac{1}{2}} \quad \textbf{(4-23)}$$

Mass change modelling equation for P2500 ground surfaces of Sanicro 25:

$$\Delta m = (0.32)\left(3.99\ 10^{+8}\exp\left(-\frac{239.18}{RT}\right)t\right)^{\frac{1}{2}} \quad \textbf{(4-24)}$$

Mass change modelling equation for as-received surfaces of Sanicro 25:

$$\Delta m = (0.32)\left(1.67\ 10^{+14}\exp\left(-\frac{345.10}{RT}\right)t\right)^{\frac{1}{2}} \quad \textbf{(4-25)}$$

For the different surfaces, the models fit the experimental data well at the various temperatures tested except for 750°C. It seems that the Arrhenius equation linking the oxidation rate and the temperature does not work well in this case. Moreover, for P1200 ground surfaces (Figure 4-99) at 700 and 800°C, the mass change data curves become horizontal after 1000 hours of exposure. Due to this shape, the model deviates from the experimental data. Good prediction has been made for P2500 ground surfaces as well, except, again, at 750°C. However, since the experimental data for as-received surfaces is very odd, there is no way to tell if the model is performant. The odd points obtained for surfaces left as-received are due to the de-correlation calculation used to determine the mass change values.

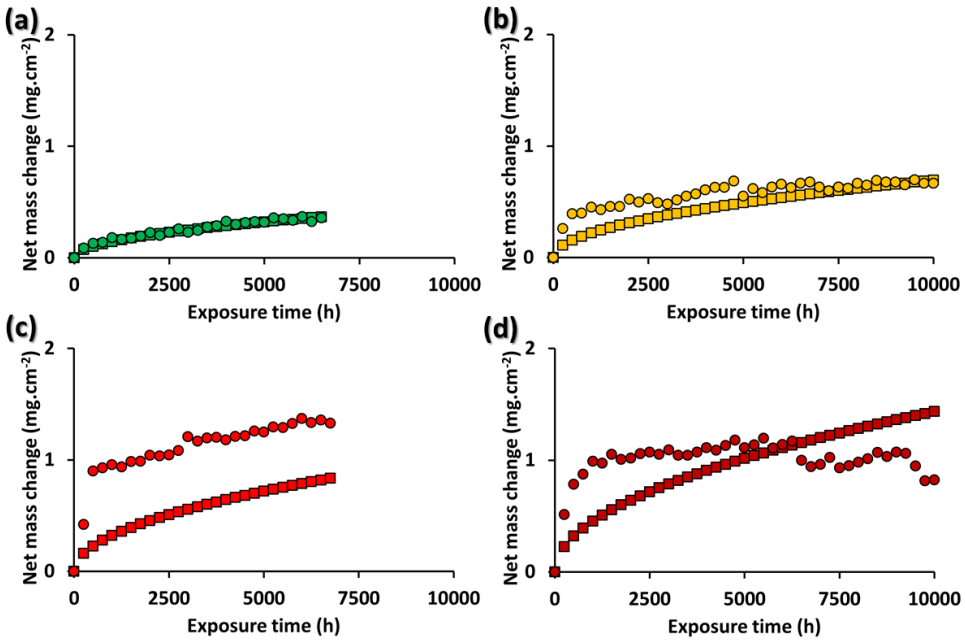

Figure 4-99: Comparison between experimental mass change data (○) and calculated data (□) for P1200 ground surfaces of Sanicro 25 at (a) 650, (b) 700, (c) 750, and (d) 800°C.

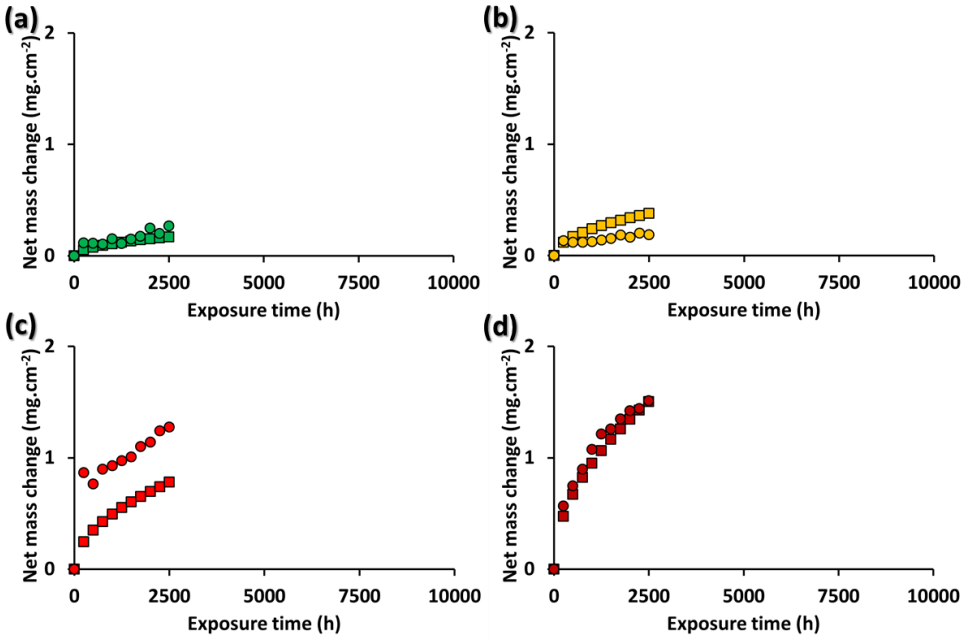

Figure 4-100: Comparison between experimental mass change data (○) and calculated data (□) for P2500 ground surfaces of Sanicro 25 at (a) 650, (b) 700, (c) 750, and (d) 800°C.

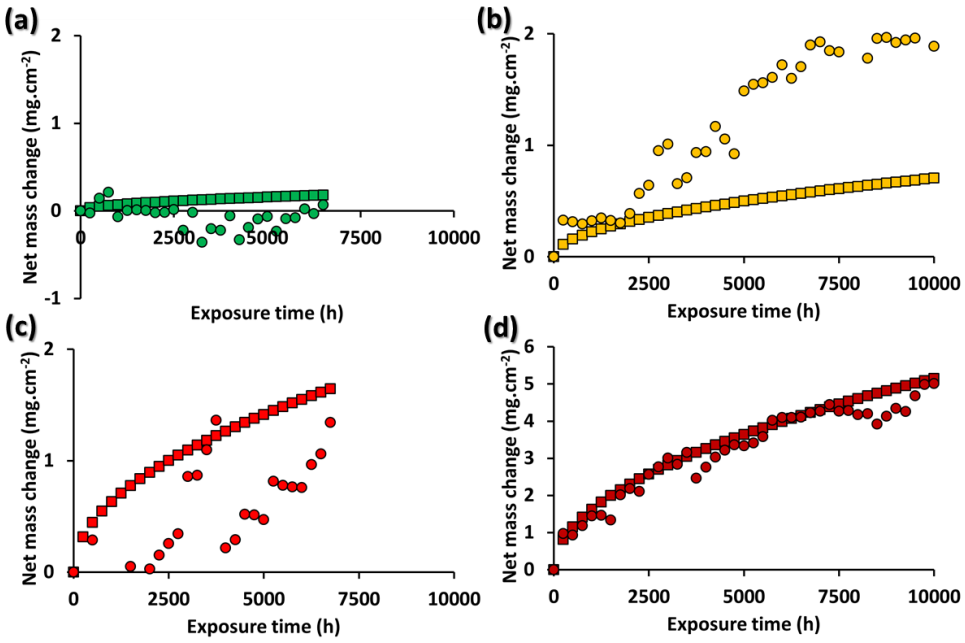

Figure 4-101: Comparison between experimental mass change data (○) and calculated data (□) for as-received surfaces of Sanicro 25 at (a) 650, (b) 700, (c) 750, and (d) 800°C.

Figure 4-102 presents the correlation between experimental and predicted mass change for the different surfaces of Sanicro 25. The correlation factors for the overall data sets and for each temperatures are presented as well. The correlation factors obtained for P1200 ground surfaces are not satisfying. Better correlations are obtained for as-received and P2500 ground surfaces. This was not expected in regards with the way data from as-received and P2500 ground surfaces are calculated.

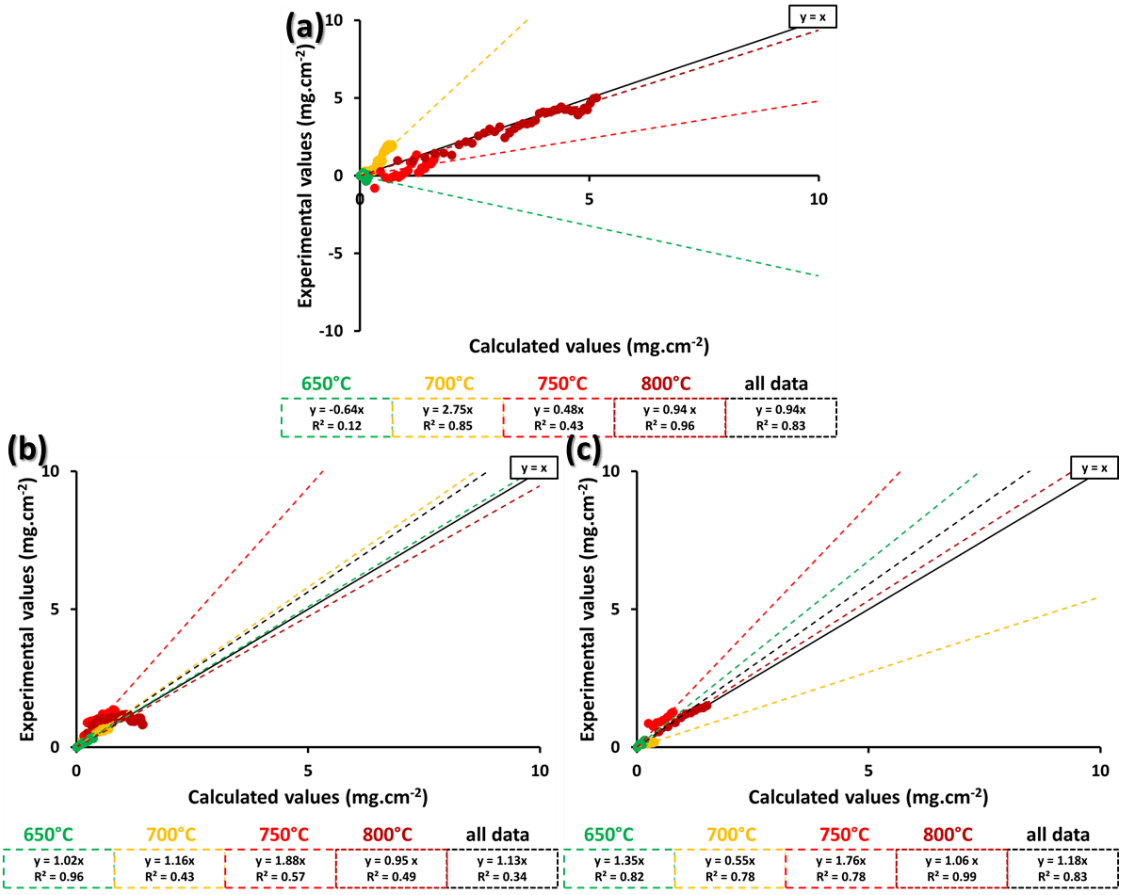

Figure 4-102: Comparative plots with correlation factor calculation between experimental and calculated mass data for Sanicro 25 with (a) as-received, (b) P1200 ground and (c) P2500 ground surface finish.

4.3.2.2. Nickel-based alloys

The different mass modelling equations describing the oxidation process for P1200 and P2500 ground Alloy 617, P1200 ground Alloy 263 and P1200 ground Alloy 740 are presented in this Section.

Mass change modelling equation for P1200 ground surfaces of Alloy 617:

$$\Delta m = (0.32)\left(6.20\ 10^{+27}\exp\left(-\frac{628.51}{RT}\right)t\right)^{\frac{1}{2}} \quad \textbf{(4-26)}$$

Mass change modelling equation for P2500 ground surfaces of Alloy 617:

$$\Delta m = (0.32)\left(5.96\ 10^{+29}\exp\left(-\frac{660.74}{RT}\right)t\right)^{\frac{1}{2}} \quad \textbf{(4-27)}$$

Mass change modelling equation for P1200 ground surfaces of Alloy 263:

$$\Delta m = (0.32)\left(5.31\ 10^{+7}\exp\left(-\frac{208.42}{RT}\right)t\right)^{\frac{1}{2}} \quad \textbf{(4-28)}$$

Mass change modelling equation for P1200 ground surfaces of Alloy 740:

$$\Delta m = (0.32)\left(5.98\ 10^{+10}\exp\left(-\frac{274.48}{RT}\right)t\right)^{\frac{1}{2}} \quad \textbf{(4-29)}$$

Fitting experimental data with the models' predictions for P1200 and P2500 ground Alloy 617, P1200 ground Alloy 263 and Alloy 740 are respectively represented in Figure 4-103, Figure 4-104, Figure 4-105, and Figure 4-106. The predicted values for P1200 and P2500 ground Alloy 617 show some large variations with the experimental data.

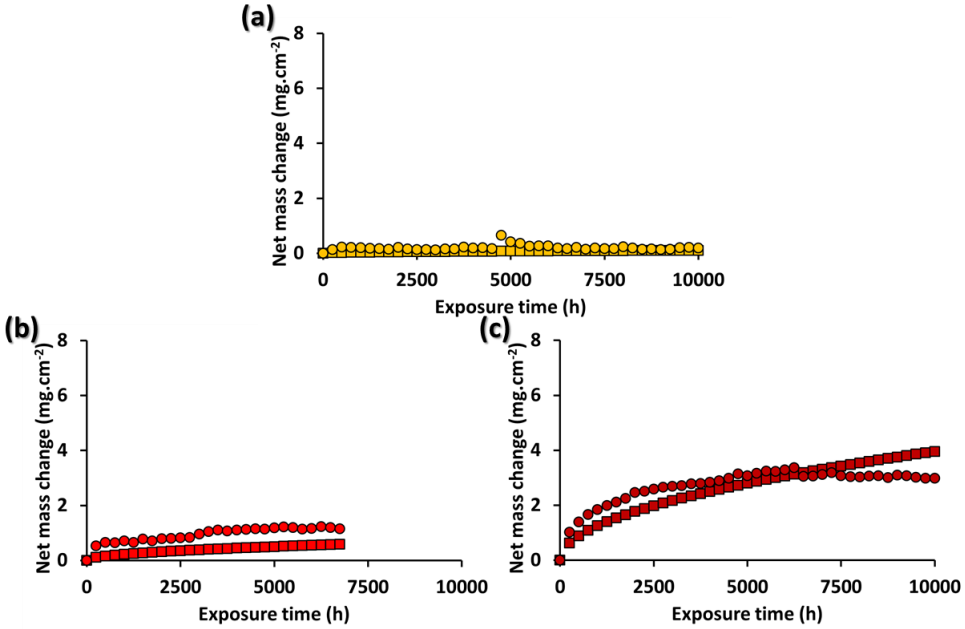

Figure 4-103: Comparison between experimental mass change data (○) and calculated data (□) for P1200 ground surfaces of Alloy 617 at (a) 700, (b) 750, (c) 800°C.

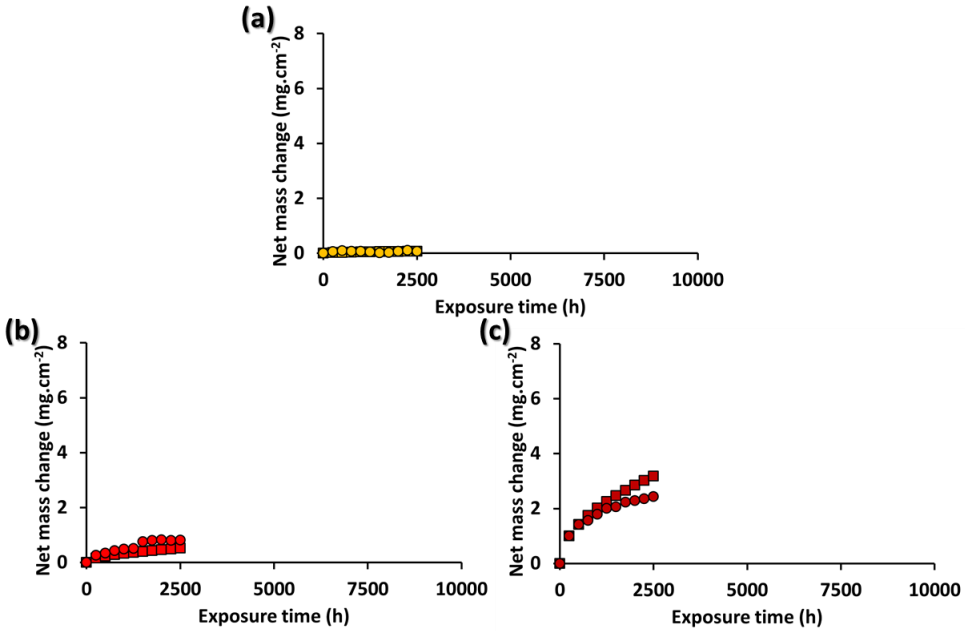

Figure 4-104: Comparison between experimental mass change data (○) and calculated data (□) for P2500 ground surfaces of Alloy 617 at (a) 700, (b) 750, (c) 800°C.

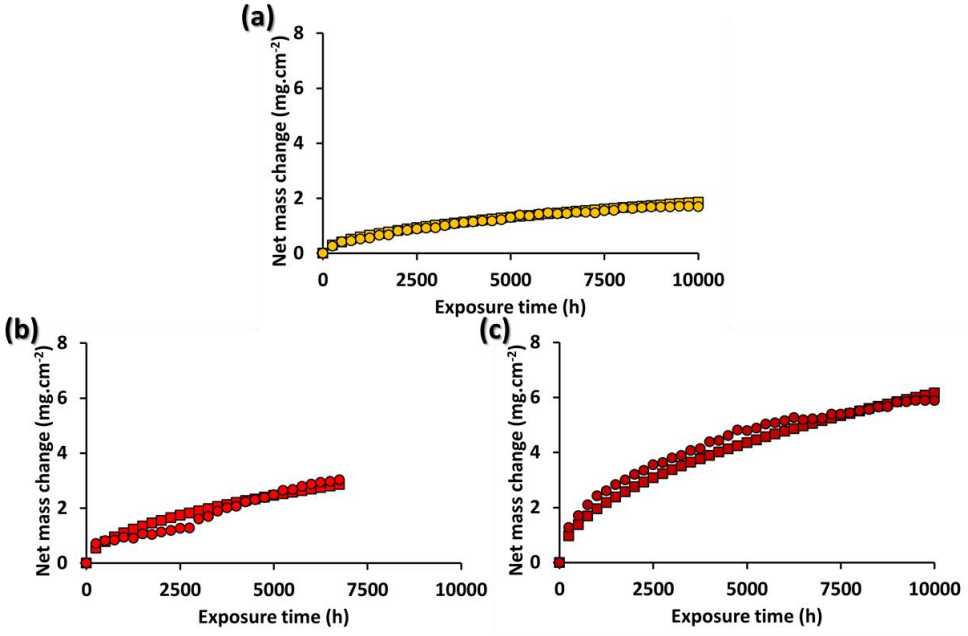

Figure 4-105: Comparison between experimental mass change data (○) and calculated data (□) for P1200 ground surfaces of Alloy 263 at (a) 700, (b) 750, (c) 800°C.

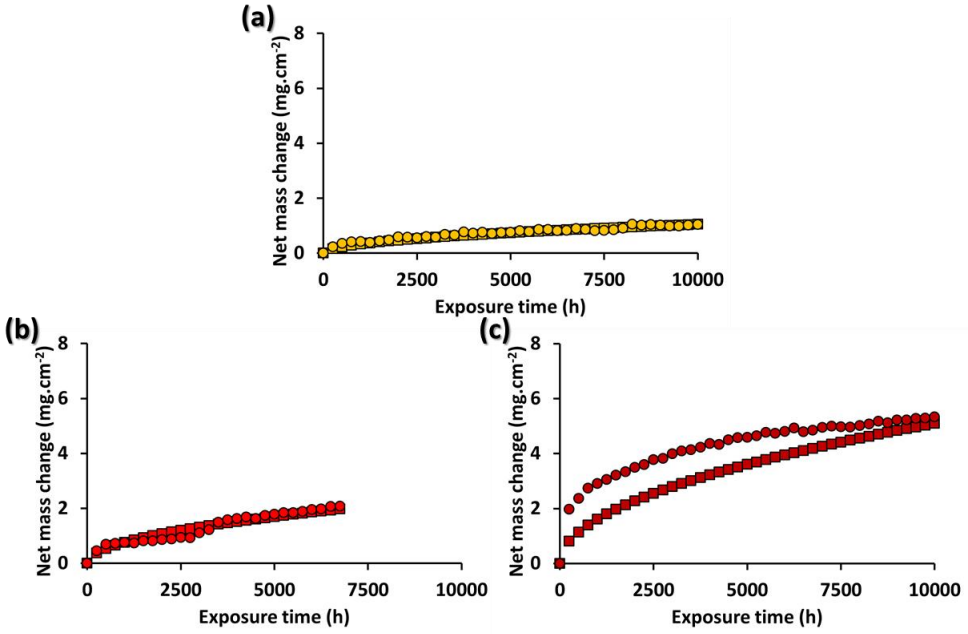

Figure 4-106: Comparison between experimental mass change data (○) and calculated data (□) for P1200 ground surfaces of Alloy 740 at (a) 700, (b) 750, (c) 800°C.

Figure 4-107 confirms the low correlation factors for mass prediction for P1200 ground Alloy 617 at 700 and 800°C as well as for P2500 ground Alloy 617 at 700°C. However, the fitting parameters for the entire data set for each prediction are above 0.87 which means the model developed could still prove useful for mass change predictions of the different nickel-based alloys tested.

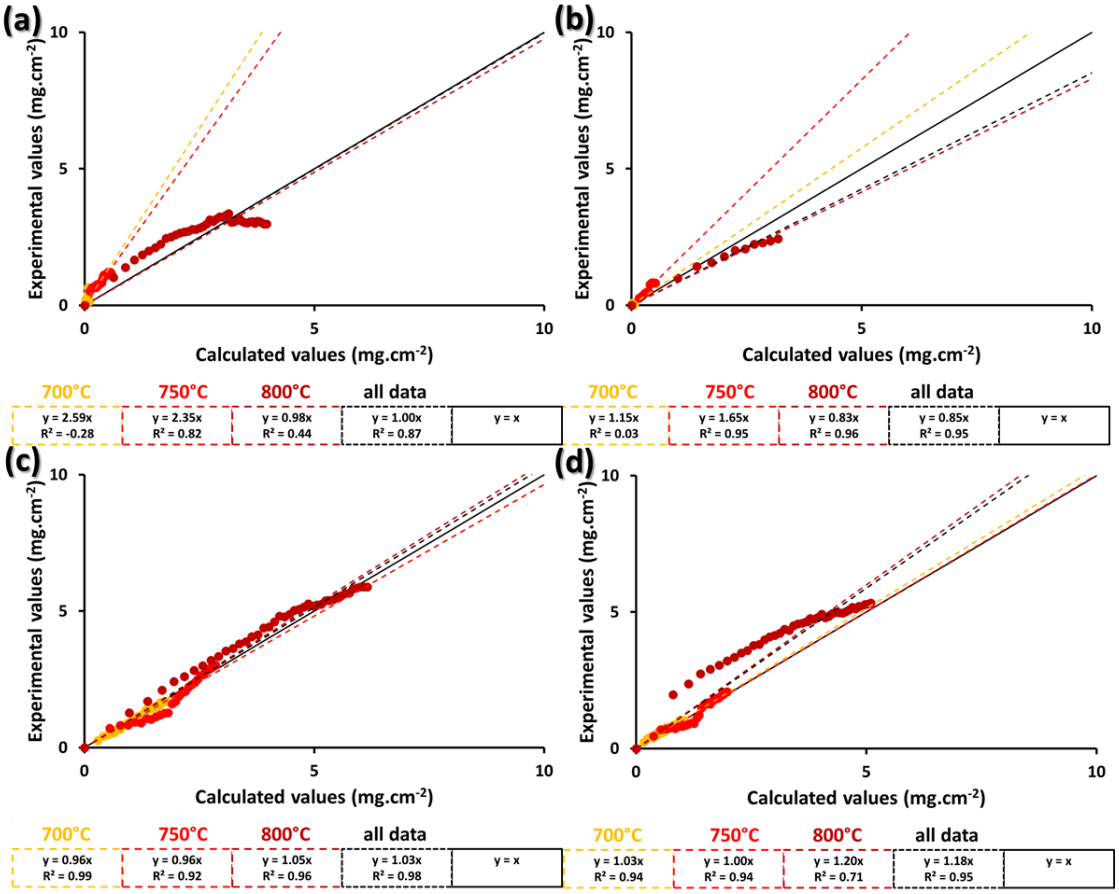

Figure 4-107: Comparison between the mass change experimental data and the values calculated from the modelling equation for (a) P1200 ground and (b) P2500 ground surfaces of Alloy 617, (c) P1200 ground surfaces of Alloy 263, (d) and P1200 ground surfaces of Alloy 740.

4.3.3. Discussions of the mass change evaluation

During the mass change modelling, calculating the kinetic parameters for the different materials has revealed to be challenging. Indeed, when plotting the parabolic oxidation rates for the different samples, it can be observed that the values obtained are not independent from the exposure time. For TP347HFG which experience spallation, the parabolic rates calculated quickly decrease when spallation starts occurring. For the highly resistive materials studied, such as Sanicro 25 and the different nickel-based alloys, the adapted Arrhenius plots associated with the different samples show that the oxidation rate decreases with increasing oxidation time. The hypothesis set to explain this is that the oxidation resistance of the materials at this temperature are very high therefore the oxidation rate is very low and further decreases with the formation of the protective chromium oxide. Montgomery et al. [89] pointed out that parabolic rate constants are generally calculated to be higher for short term tests than for long term. In this study it was pointed out that this observation was one of the reason why it was difficult to compare different results obtained at different times. Yi et al. [90] observed the effect of pre-aging a material on the steam oxidation process. It appears that the oxidation rate calculated from the pre-aged material decreased with increasing pre-aging time. Therefore, it could be assumed that each exposure cycle act as a pre-aging cycle which eventually lead to the slow decrease of the calculated oxidation rates with increasing exposure time.

The problem with having a time dependant oxidation rate is that there is no good answer about which value should be taken for the modelling work: the higher value, the lower, the average or the value obtained from the fitting of the mass change data set. It was decided to use the value obtained from fitting the mass change dataset for the highly resistive materials. For TP347HFG, subject to spallation, two different oxidation rates were determined: a parabolic oxidation rate describing the early mass gain for the samples and a linear oxidation rate describing the part of the mass change curve showing mass loss.

From the oxidation rates of the different materials at the different temperatures studied, kinetic parameters were determined to develop mass change equations describing the oxidation process for the various surface finishes for the different materials studied. The equations developed are simple mass change equations with the different parabolic and linear constants set to zero. Monceau et al. [91] explained that the use of the classic parabolic rate equation with a null constant value results in assuming that the oxidation mechanism is purely controlled by diffusion. This is why for some of the modelled mass change curves there is an offset difference with the experimental data set.

The mass change equations developed revealed to give adequate mass change predictions when considering the overall dataset. However, it appears that when refining to the mass change data for a specific temperature, the predictions made do not always provide good results.

4.3.4. Oxide growth kinetics

Using oxide thickness distributions obtained for the different samples exposed, the oxidation kinetics in terms of oxide growth have been studied. The oxide thickness values at 90% of the cumulative probability plots have been used.to calculate the parabolic rates and later the kinetics parameters. These kinetics parameters have been used in oxide growth models describing the evolution of oxide thickness for the different materials and surface finishes studied. In regards to the earlier work performed with mass change data, the oxide growth was supposed parabolic.

The oxide growth equation for a parabolic rate is written

$$x^2 = k_p t + c_p \quad \textbf{(4-30)}$$

Where x is the oxide thickness measured [μm], k_p is the parabolic rate [$\mu m^2 . h^{-1}$], c_p is a rate constant in [μm] and t is time [h].

The effect of temperature on the oxide growth rate is described by the Arrhenius equation. The following equation presents the Arrhenius law for parabolic rates:

$$k_p = k_0 \exp\left(-\frac{Q}{RT}\right) \quad \textbf{(4-31)}$$

Where Q is the activation energy of the oxidation reaction [$J.mol^{-1}$], R is the gas constant [$J.mol^{-1}.K^{-1}$], T is the absolute temperature [K], and k_0 is the standard rate constant [$\mu m^2.h^{-1}$].

Similarly to what was explained in Section 4.3.1, adapted and regular Arrhenius plots have been used to respectively observe the effect of exposure time on the parabolic rates calculated and deduce the values of the kinetic parameters (activation energy and standard rate constant) for oxide growth. Arrhenius plots present oxidation rates calculated by fitting the experimental data with Equation (4-30) whereas adapted Arrhenius plots represent the oxidation rates calculated individually for each oxide thickness data point using Equation (4-33)

$$k_p = \frac{\Delta x^2}{t} \quad \textbf{(4-32)}$$

Where Δx is the oxide thickness at 90% of the cumulative probalibity plot [μm], k_p is the parabolic rate [$(mg.cm^{-2})^2.h^{-1}$], and t is time [h].

Reference lines have been drawn on the difference Arrhenius plots using data found in the literature regarding the oxidation of pure chromium [69,92] and pure iron [93].

4.3.4.1. Austenitic steels

For austenitic steel TP347HFG, Figure 4-108 shows all the parabolic rates calculated from the different samples exposed. Large variability of the parabolic rates calculated can be observed. The highest values obtained are for as-received, P1200 and P2500 ground surface finishes. They are located in between

the two reference lines for the oxidation of pure iron and pure chromium. These points are then related to the measurements of thick multi-layered oxide thickness which has not experienced large spallation. The lowest values are located around the reference line for the oxidation of pure chromium. These data points come from the measurement of oxide layer that have experienced spallation and from which the outer iron-oxide layer has spalled and only the iron-rich oxide layer remains. These low values are calculated for the machined and shot-peened surface finishes mainly but also for some samples with P1200 ground, P2500 ground or as-received surface finishes.

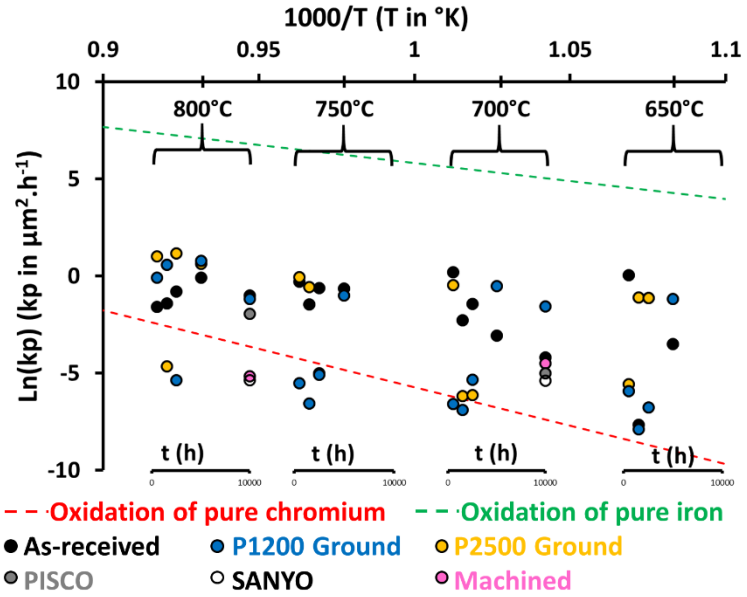

Figure 4-108: Adapted Arrhenius plot for oxide growth parabolic rates calculated for TP347HFG's samples prepared with various surface finishes.

Figure 4-109 shows the parabolic rates calculated from fitting the oxide thickness data and also present the kinetic parameters for the different surfaces of TP347HFG. For shot-peened (PISCO and SANYO) and machined surface finishes, only two points were available to perform the calculation of the kinetic parameters. This is why the values obtained for machined and the SANYO shot-

peened surfaces are so odd. Indeed the Arrhenius curve is almost flat, meaning the temperature would have no influence of the steam oxidation of those surfaces.

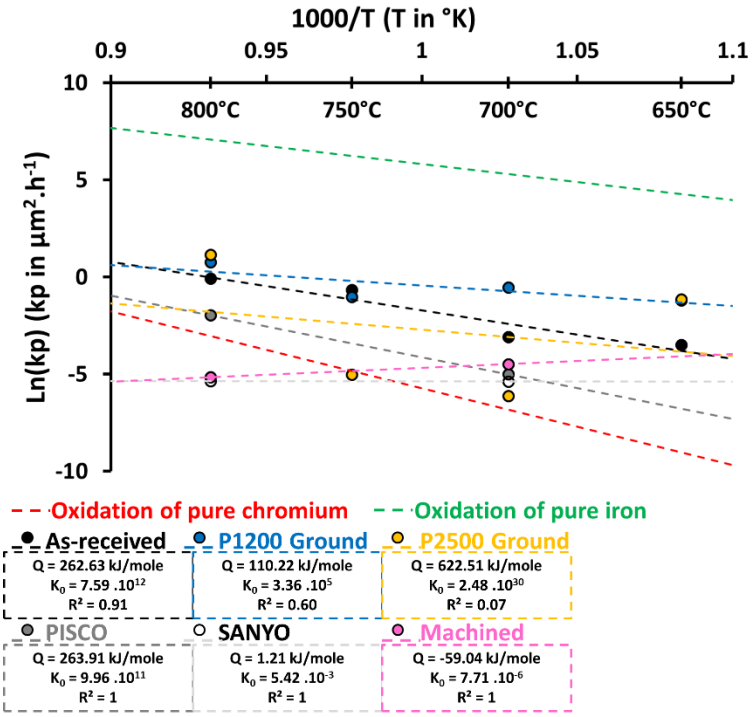

Figure 4-109: Arrhenius plot for oxide growth parabolic rates for TP347HFG's samples prepared with various surface finishes and determination of the kinetics parameters.

Figure 4-110 represents the activation energy calculated for the different surface finishes applied on TP347HFG as a function of the residual stresses applied by the surface finishes of interest. Even if no clear link was calculated between the activation energy calculated and the stresses applied by the different surfaces finishes, due to the large scatter of the data obtained, it seems that with increasing compressive stresses applied at a material's surface there is an exponential decrease of the activation energy. This means that with increasing compressive stresses, the steam oxidation of a surface is less impacted by an

increase of temperature. However, it has been pointed out earlier that the very low and negative activation energies values calculated for the SANYO shot-peened and the machined surfaces could be considered as odd points. As a consequence, even if there seems to be an exponential correlation between the activation energy and the surfaces' residual stresses, this observation has to be backed up with more experimental data that could eventually confirm this hypothesis.

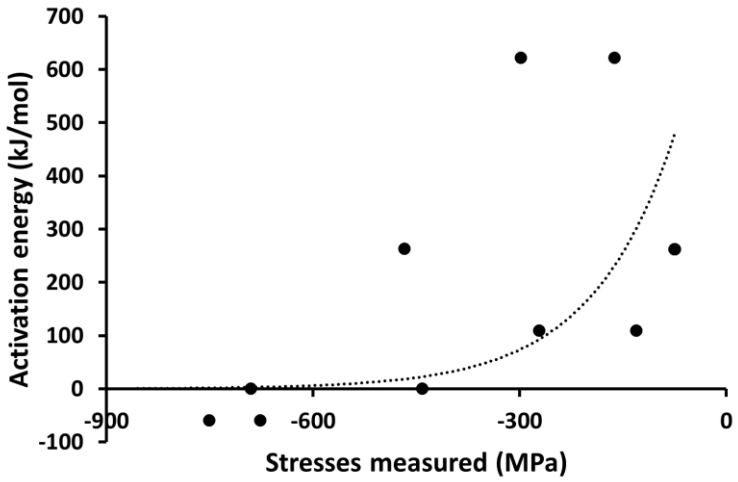

Figure 4-110: Representation of the activation energy calculated for various TP347HFG's samples as a function of the residual stress measured on the surfaces oxidized after 10,000 hours steam oxidation at 700 and 800°C.

Figure 4-111 presents the adapted Arrhenius plot for the different surfaces of Sanicro 25. The values obtained are scattered but it can be agreed that all the parabolic rates calculated are located around the reference line for the oxidation of pure chromium. This is coherent with the results obtained about the composition of the oxide layers formed on Sanicro 25, which were presenting the formation of chromia oxide only.

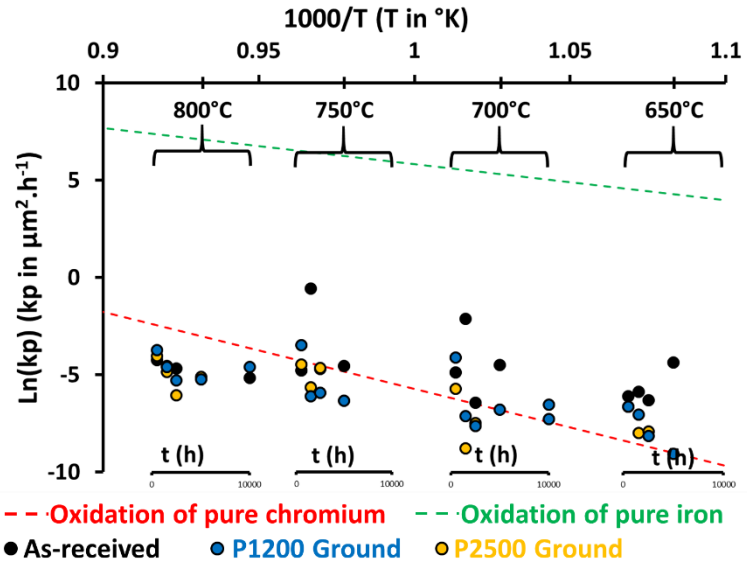

Figure 4-111: Adapted Arrhenius plot for oxide growth parabolic rates calculated for Sanicro 25's samples prepared with various surface finishes.

Figure 4-112 present the kinetic parameters calculated from parabolic rates issued from the fitting of the different datasets. P1200 and P2500 ground surfaces show an increasing oxidation rate with increasing temperature, which is what can be expected, however, for surfaces left as-received, the parabolic rates calculated are observed to decrease with increasing temperature. It is difficult to find an explanation for such a trend. Indeed the material does not experience spallation, which could explain such a low value.

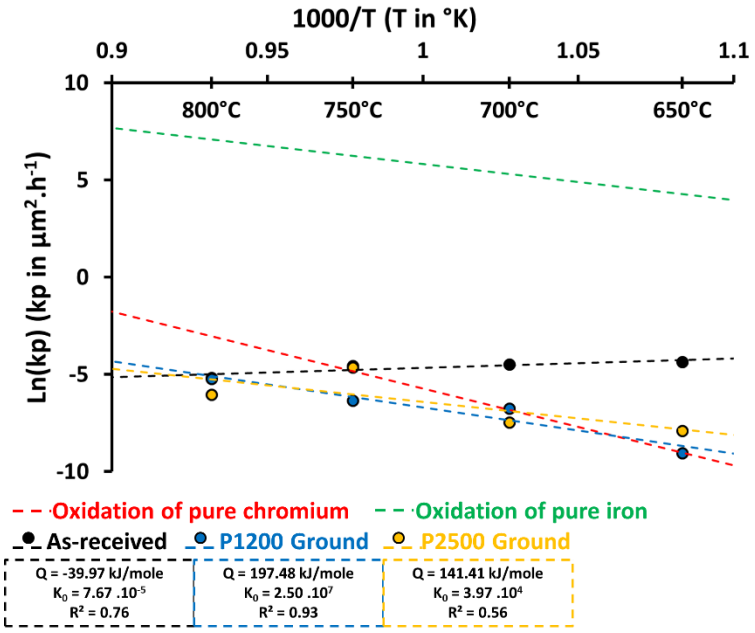

Figure 4-112: Arrhenius plot for oxide growth parabolic rates for Sanicro 25's samples prepared with various surface finishes and determination of the kinetics parameters.

4.3.4.2. Nickel-based alloy

Figure 4-113 show the adapted Arrhenius plot for P1200 ground surfaces of Alloy 263, Alloy 617 and Alloy 740. The values obtained are the same order of magnitude than the reference line for the oxidation of pure chromium. Moreover, the parabolic rates calculated decrease with increasing exposure time. Which is similar to the evolution of the oxidation rate for mass change calculated in Section 4.3.1.2. Alloy 617 and Alloy 740 show slightly lower parabolic oxide growth rates than Alloy 263.

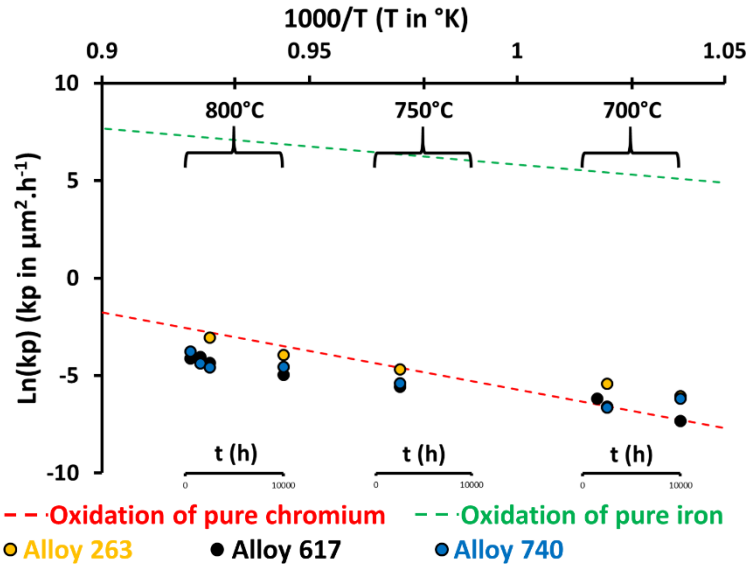

Figure 4-113: Adapted Arrhenius plot for oxide growth parabolic oxidation rates calculated for nickel-based alloys with P1200 ground surface finish and determination of the kinetics parameters.

Figure 4-114 compares the parabolic oxidation rates for oxide growth calculated on P1200 and P2500 ground surfaces of Alloy 617. The values calculated for both surface finishes are very similar which confirms that applying a surface finish inducing low compressive stresses at the surface of nickel-based oxides does not influence its steam oxidation resistance.

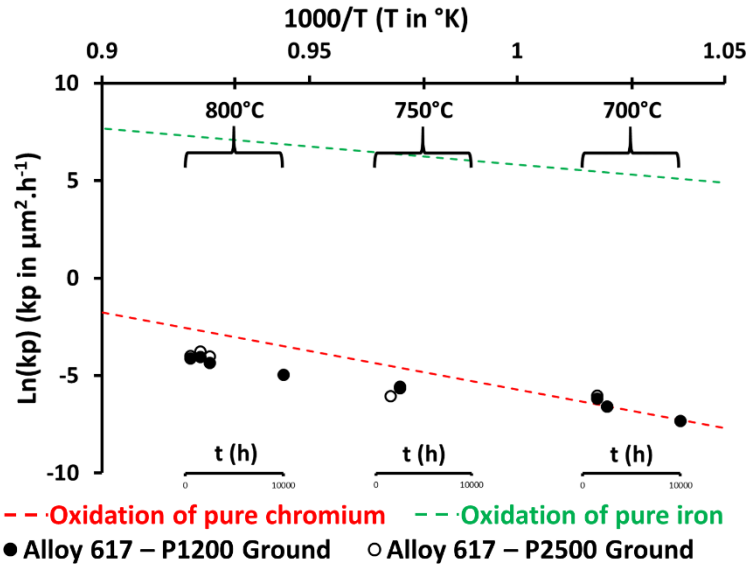

Figure 4-114: Adapted Arrhenius plot for oxide growth parabolic oxidation rates calculated for nickel-based alloy 617 with P1200 and P2500 ground surface finishes and determination of the kinetics parameters.

Figure 4-115 presents the Arrhenius plots for the parabolic oxide growth rate calculated for the different materials after 2500 hours of steam exposure. The kinetic parameters for nickel-based alloys have not been calculated from fitting the all oxide thickness dataset due to the lack of points at 750°C. This choice has been made to keep consistency between the calculations made at the different temperatures. As observed with the adapted Arrhenius plot in Figure 4-113, Alloy 263 exhibits the highest oxidation rates compared to Alloy 617 and Alloy 740.

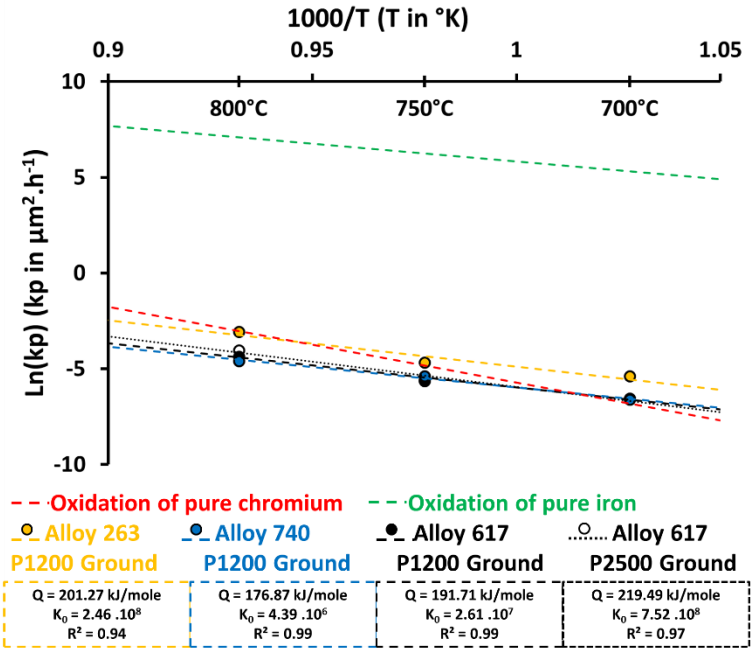

Figure 4-115: Arrhenius plot for oxide growth parabolic oxidation rates calculated for nickel-based alloys with P1200 and P2500 ground surface finishes and determination of the kinetics parameters.

4.3.5. Oxide growth modelling

For the modelling of the oxide growth in terms of thickness, a simple equation has been used:

$$\Delta x = \left(k_p t\right)^{\frac{1}{2}} \quad \textbf{(4-33)}$$

Where x is the oxide thickness measured [μm], k_p is the parabolic rate [$\mu m^2.h^{-1}$], and t is time [h]. The parabolic rate k_p is determined using the different kinetic parameters calculated in Section 4.3.4 implemented in the Arrhenius Equation (4-31). The parabolic constant presented in Equation (4-30) was chosen to be null due to its inability to linked with time and temperature.

The effect of spallation for predicting the oxide growth could not be implemented. Indeed, the oxide thickness dataset of the different samples is very restrained. More data from intermediate times is required to implement spallation effect.

4.3.5.1. Austenitic steels

Oxide growth models for the P1200, P2500 ground and as-received surfaces of TP347HFG have been developed (Equations (4-34), (4-35), and (4-36)), and the predicted values were compared to experimental values in Figure 4-116, Figure 4-117, and Figure 4-118 respectively.

Oxide growth modelling equation for P1200 ground surfaces of TP347HFG:

$$\Delta x = \left(3.36\ 10^{+5} \exp\left(-\frac{110.22}{RT}\right) t\right)^{\frac{1}{2}} \quad \textbf{(4-34)}$$

Oxide growth modelling equation for P2500 ground surfaces of TP347HFG:

$$\Delta x = \left(2.48\ 10^{+30} \exp\left(-\frac{622.51}{RT}\right) t\right)^{\frac{1}{2}} \quad \textbf{(4-35)}$$

Oxide growth modelling equation for as-received surfaces of TP347HFG:

$$\Delta x = \left(7.59\ 10^{+12} \exp\left(-\frac{262.63}{RT}\right) t\right)^{\frac{1}{2}} \quad \textbf{(4-36)}$$

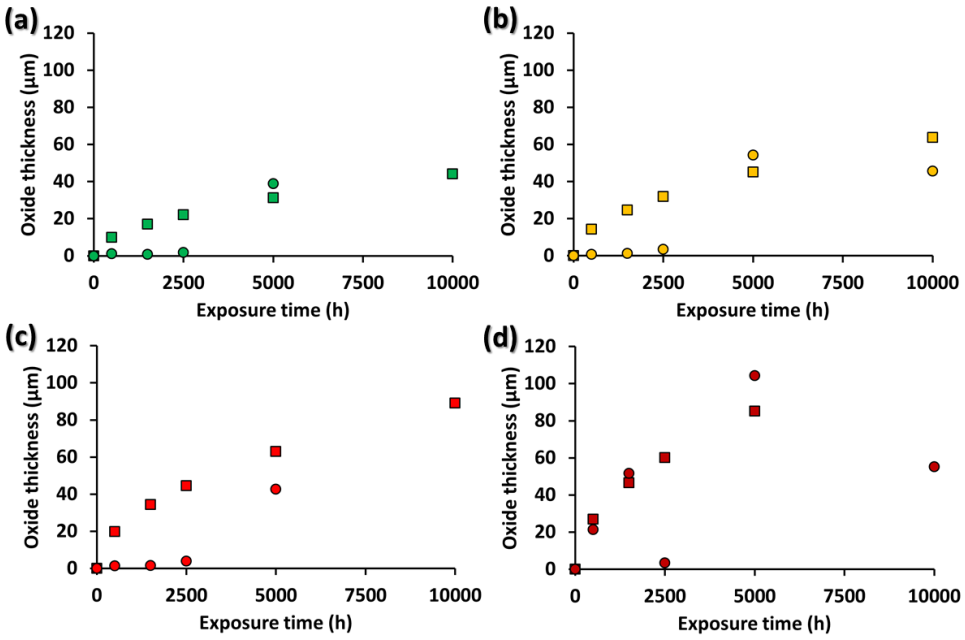

Figure 4-116: Comparison between experimental oxide thickness data (○) and calculated data (□) for P1200 ground surfaces of TP347HFG at (a) 650, (b) 700, (c) 750, and (d) 800°C.

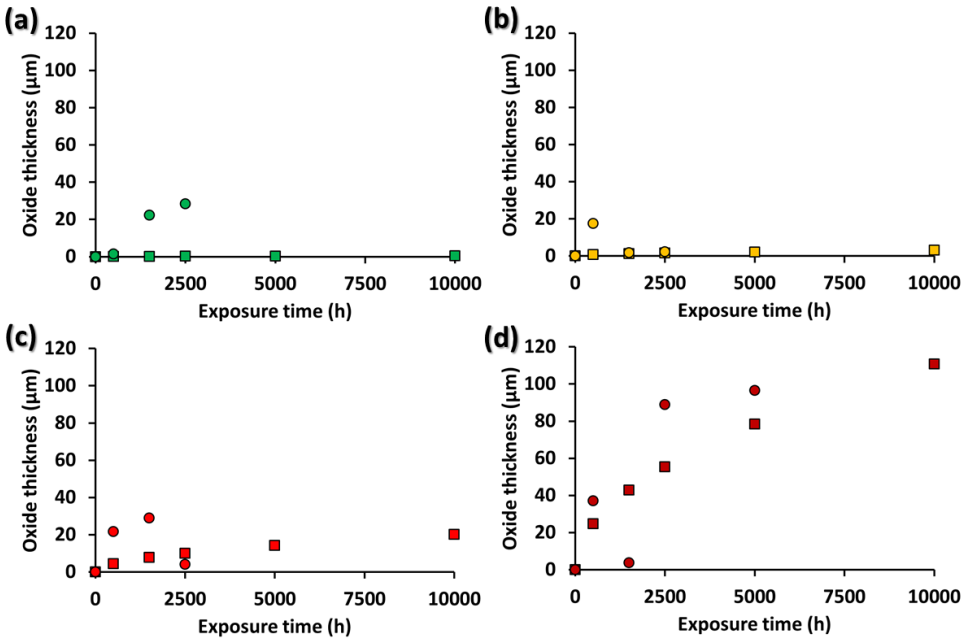

Figure 4-117: Comparison between experimental oxide thickness data (○) and calculated data (□) for P2500 ground surfaces of TP347HFG at (a) 650, (b) 700, (c) 750, and (d) 800°C.

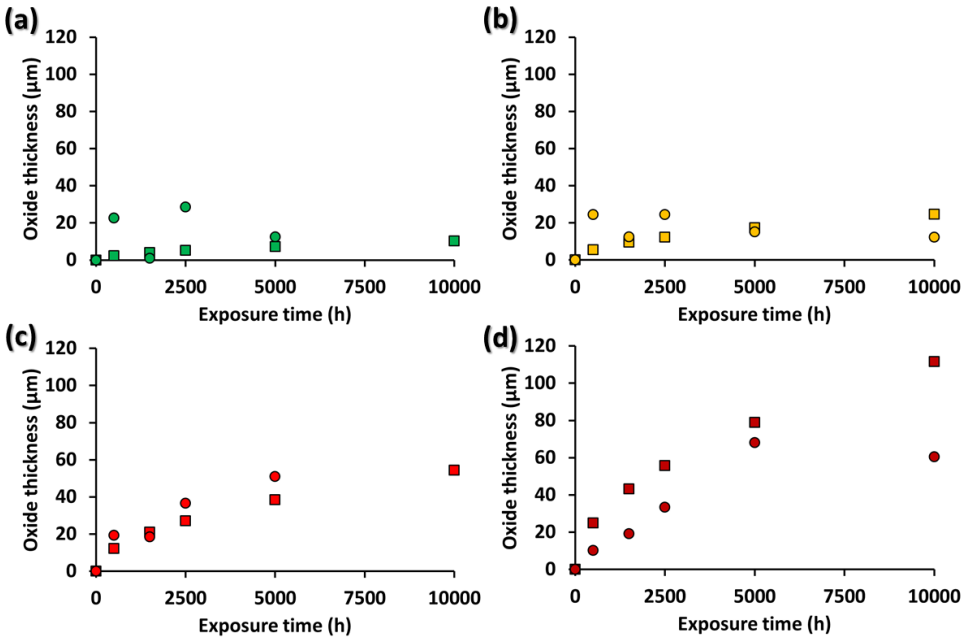

Figure 4-118: Comparison between experimental oxide thickness data (○) and calculated data (□) for as-received surfaces of TP347HFG at (a) 650, (b) 700, (c) 750, and (d) 800°C.

The oxide growth modelling for P1200 ground surfaces of TP347HFG, which results were presented in Figure 4-116 shows a good fitting of the oxide thickness measured after 2500 hours but bad results for the early points between 650 and 750°C. It was explained in Section 4.2.1.1 that the different samples exposed at 650, 700 and 750°C for 500, 1500 and 2500 hours, and labelled with their concave surface as-received and all their other surfaces P1200 ground, were actually prepared by a former MSC student at Cranfield University. After gathering oxide thickness data for these samples it appears that the convex surfaces, on which oxide thickness measurements of P1200 ground surfaces was performed, were actually machined and not ground. However, it was shown in Section 4.3.2.1 that machined surfaces possess a much higher oxidation resistance the P1200 ground surfaces. As a result, it can now be expected that the early points between 650 and 750°C exhibit lower oxide growth compared to the model developed. Moreover some data points far from the calculated values

have also been observed. These points that can seem odd come from the fact that spallation directly affects the oxide thickness measurements for the different samples. It was observed previously during the mass change modelling Section that spallation plays a critical and major role in the oxidation process of TP347HFG. In consequence, Figure 4-119 (b) report low degree of correlation between the calculated and experimental data for P1200 ground surfaces.

For P2500 ground surfaces, Figure 4-117 shows that the calculated values fits a part of the experimental dataset but not all of it. Again, the fact that spallation occurs brings a lot of scattering of the experimental data which makes it difficult to fit the entire dataset. Indeed, the correlation factor between the experimental and calculated oxide thickness values presented in Figure 4-119 (c) is very low.

Similarly, oxide growth modelling for the as-received surface does not allow a perfect prediction of the experimental data acquired (Figure 4-118). Figure 4-119 (a) also presents a low correlation factor between the model and the experimental data. Spallation is definitely one reason for the low correlation observed.

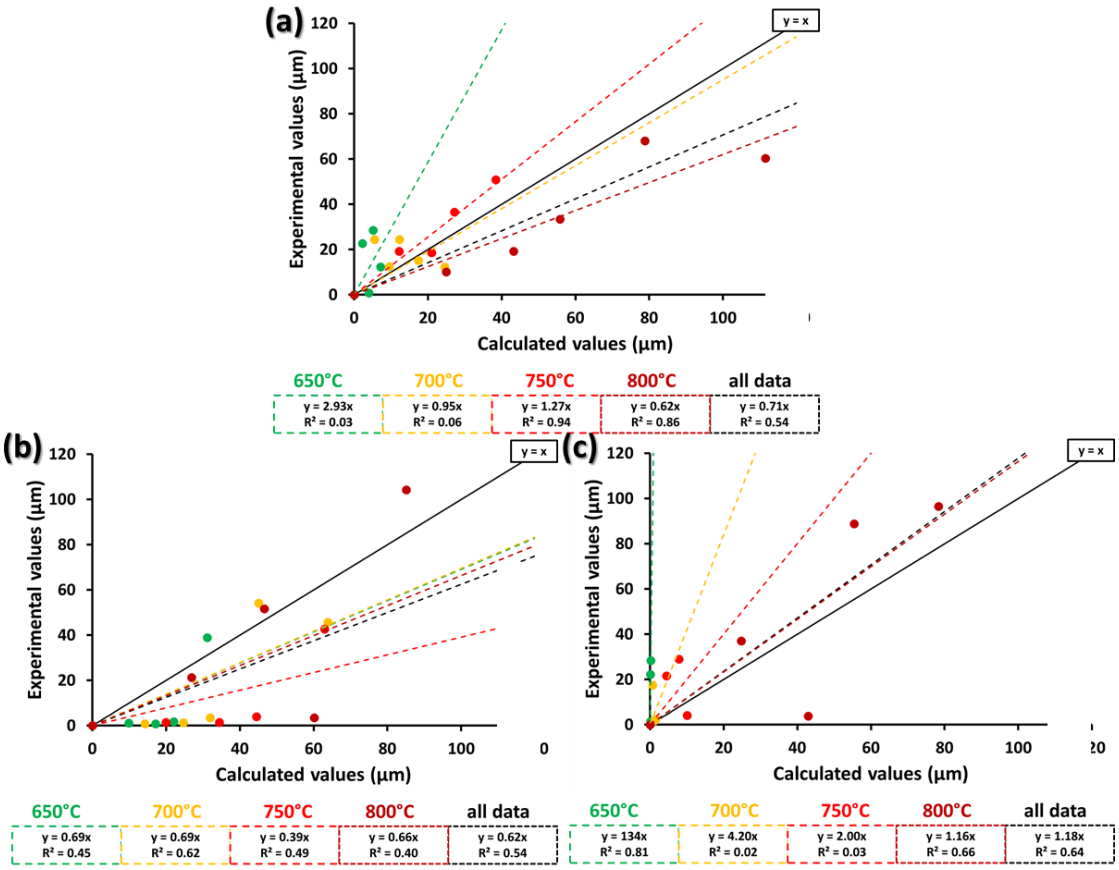

Figure 4-119: Comparative plots with correlation factor calculation between experimental and calculated oxide thicknesses for TP347HFG with (a) as-received, (b) P1200 ground and (c) P2500 ground surface finish.

For Sanicro 25, Equations (4-37), (4-38), and (4-39) present how oxide thickness modelling was performed for P1200, P2500 ground, and as-received surfaces.

Oxide growth modelling equation for P1200 ground surfaces of Sanicro 25:

$$\Delta x = \left(2.50\ 10^{+7} \exp\left(-\frac{197.48}{RT}\right) t\right)^{\frac{1}{2}} \quad \textbf{(4-37)}$$

Oxide growth modelling equation for P2500 ground surfaces of Sanicro 25:

$$\Delta x = \left(3.97\ 10^{+4} \exp\left(-\frac{141.41}{RT}\right) t\right)^{\frac{1}{2}} \quad \textbf{(4-38)}$$

Oxide growth modelling equation for as-received surfaces of Sanicro 25:

$$\Delta x = \left(7.67\ 10^{+5} \exp\left(-\frac{-39.97}{RT}\right) t\right)^{\frac{1}{2}} \quad \textbf{(4-39)}$$

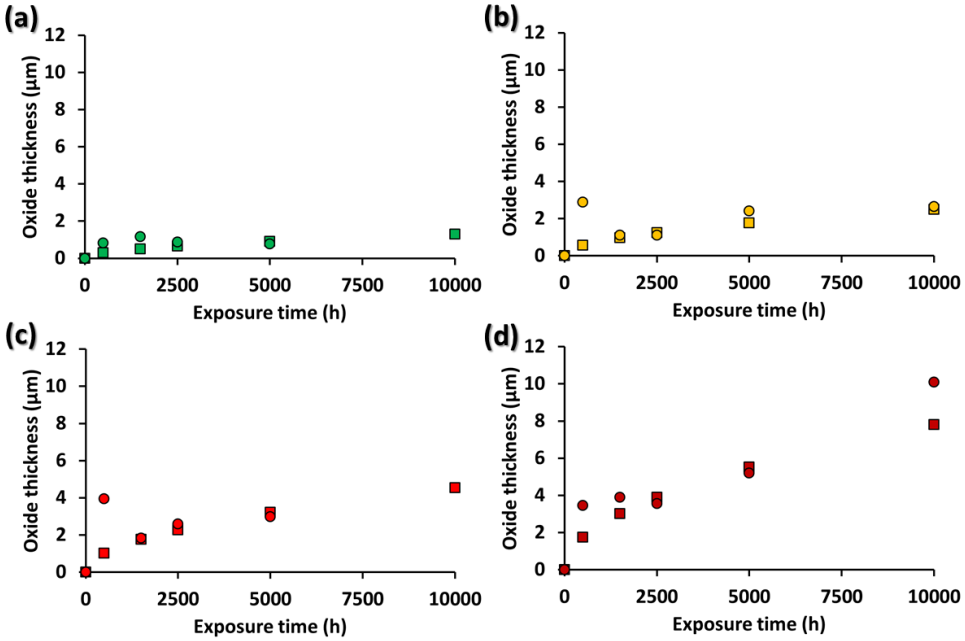

Figure 4-120: Comparison between experimental oxide thickness data (○) and calculated data (□) for P1200 ground surfaces of Sanicro 25 at (a) 650, (b) 700, (c) 750, and (d) 800°C.

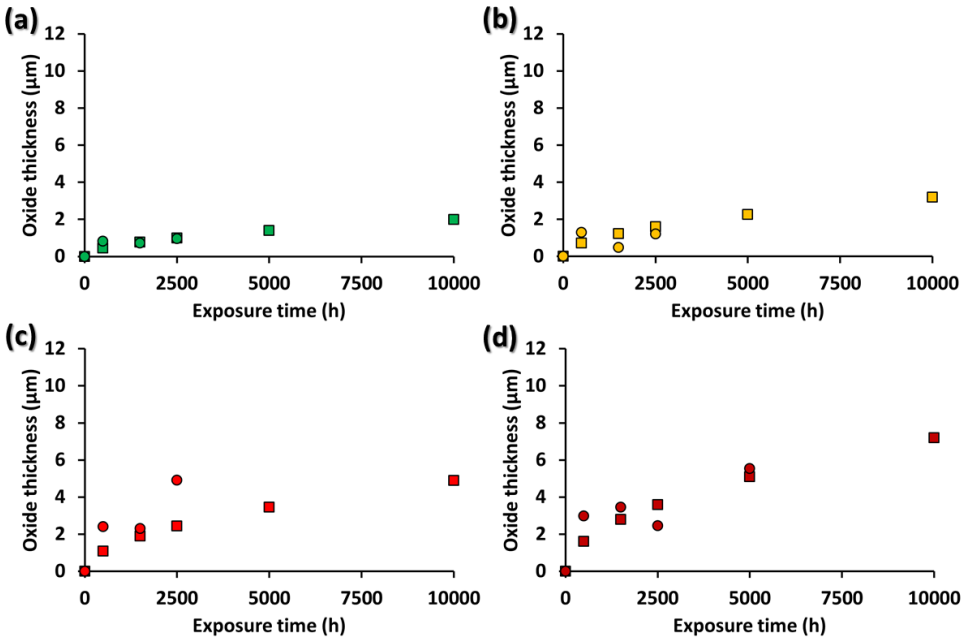

Figure 4-121: Comparison between experimental oxide thickness data (○) and calculated data (□) for P2500 ground surfaces of Sanicro 25 at (a) 650, (b) 700, (c) 750, and (d) 800°C.

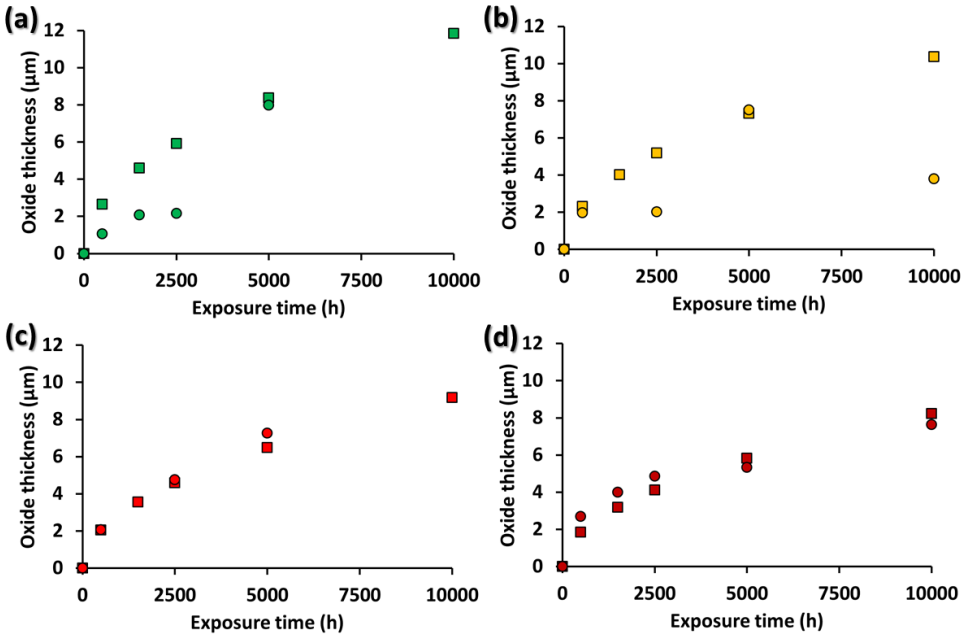

Figure 4-122: Comparison between experimental oxide thickness data (○) and calculated data (□) for as-received surfaces of Sanicro 25 at (a) 650, (b) 700, (c) 750, and (d) 800°C.

Figure 4-120, Figure 4-121, and Figure 4-122 compare the experimental and calculated oxide thickness values for P1200, P2500 ground, and as-received surfaces of Sanicro 25. For the various surface finishes, steam temperatures and exposure times, the models developed seem to give reasonably good fitting the experimental dataset obtained. However, some experimental values remain far from the values calculated using the modelling equations. Figure 4-123 presents the correlation factors for the different temperatures and surfaces finishes. The correlations between the experimental and calculated oxide thicknesses are not satisfactory in many case which is due to the high differences between some of the experimental data points and the calculated values. Even though Sanicro 25 is not subject to severe spallation of the oxide scales formed on its different surfaces, it has to be kept in mind that each data point obtained comes from a different sample which increase greatly the scattering of the dataset obtained.

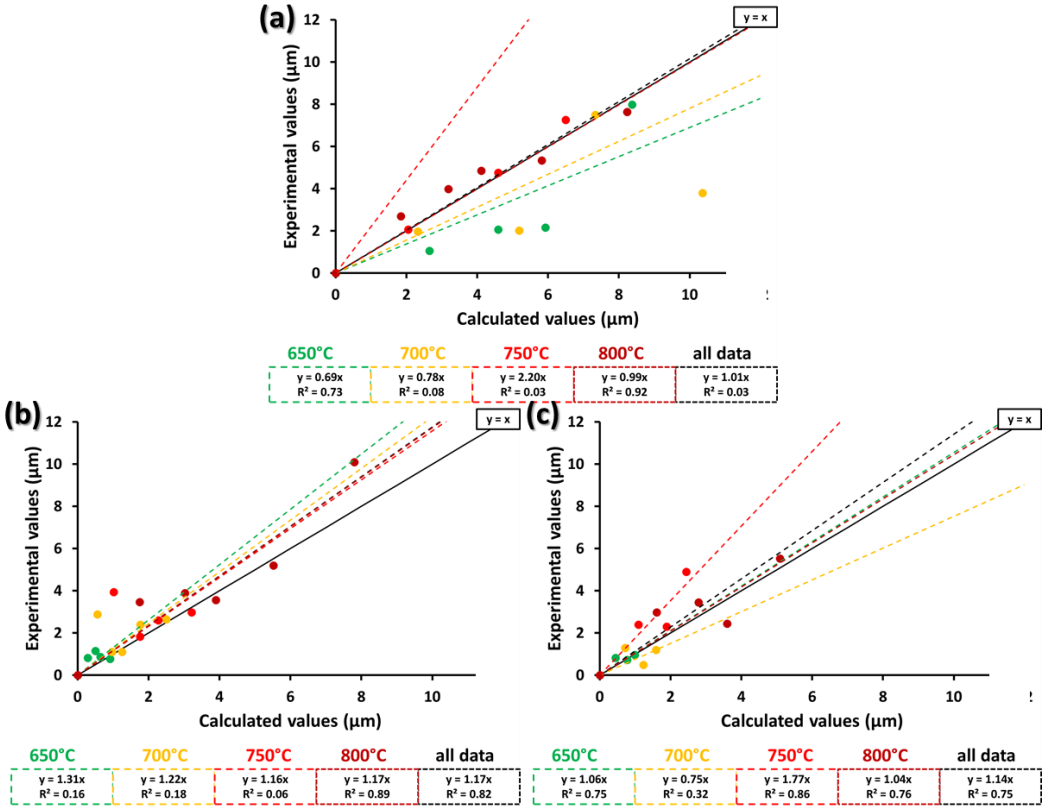

Figure 4-123: Comparative plots with correlation factor calculation between experimental and calculated oxide thicknesses for Sanicro 25 with (a) as-received, (b) P1200 ground and (c) P2500 ground surface finish.

4.3.5.2. Nickel-based alloy

Oxide growth for P1200 ground Alloy 617 was modelled using Equation (4-40) and the calculated values are presented in Figure 4-124 along with the experimental data to allow comparison. Experimental and calculated data are observed to be very similar at all temperatures tested. Moreover, Figure 4-125 confirms the effectiveness for the model for the prediction of the oxide thickness on P1200 ground Alloy 617.

Oxide growth modelling equation for P1200 ground surfaces of Alloy 617:

$$\Delta x = \left(2.61\ 10^{+7} \exp\left(-\frac{191.74}{RT}\right) t\right)^{\frac{1}{2}} \quad \textbf{(4-40)}$$

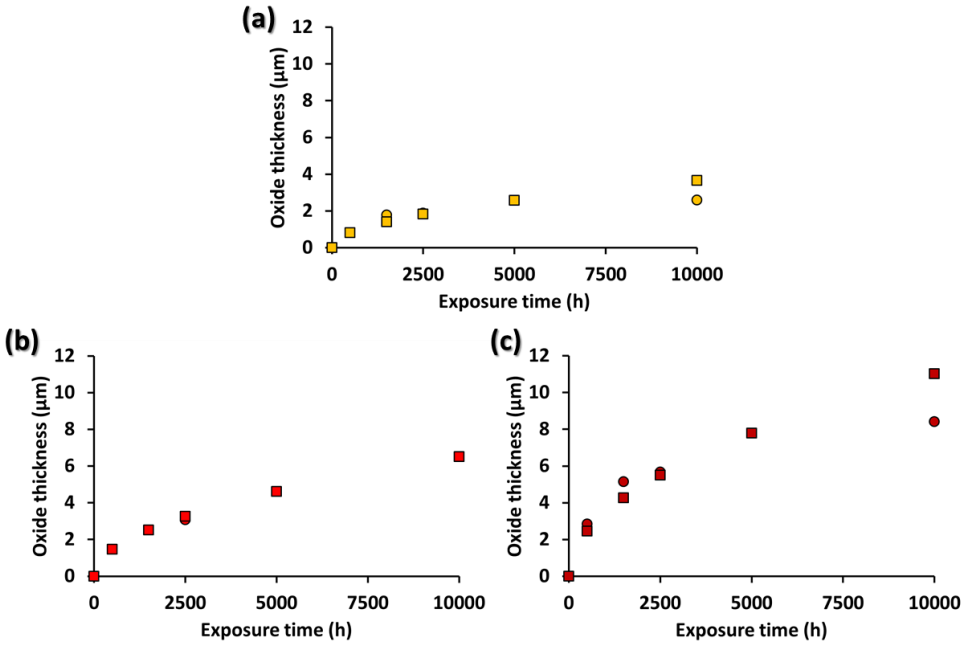

Figure 4-124: Comparison between experimental oxide thickness data (○) and calculated data (□) for P1200 ground surfaces of Alloy 617 at (a) 650, (b) 700, and (c) 750°C.

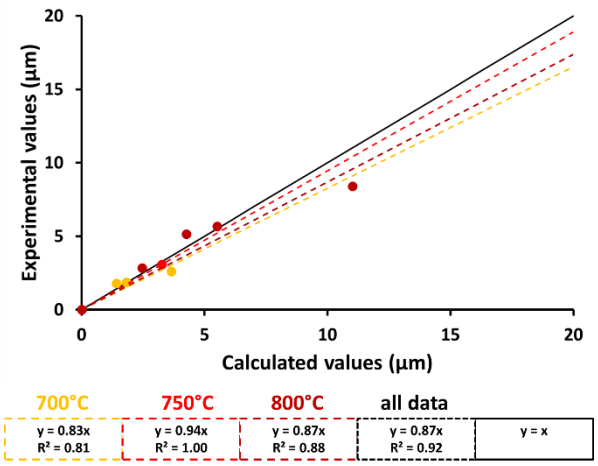

Figure 4-125: Comparison between the oxide thickness experimental data and the values calculated from the modelling equation for P1200 ground surfaces of Alloy 617.

For P2500 ground surfaces of Alloy 617, the modelling equation (Equation (4-41)) allows very good prediction of the oxide thickness as Figure 4-126 and Figure 4-127 present.

Oxide growth modelling equation for P2500 ground surfaces of Alloy 617:

$$\Delta x = \left(7.52\ 10^{+8} \exp\left(-\frac{219.49}{RT}\right) t\right)^{\frac{1}{2}} \quad \textbf{(4-41)}$$

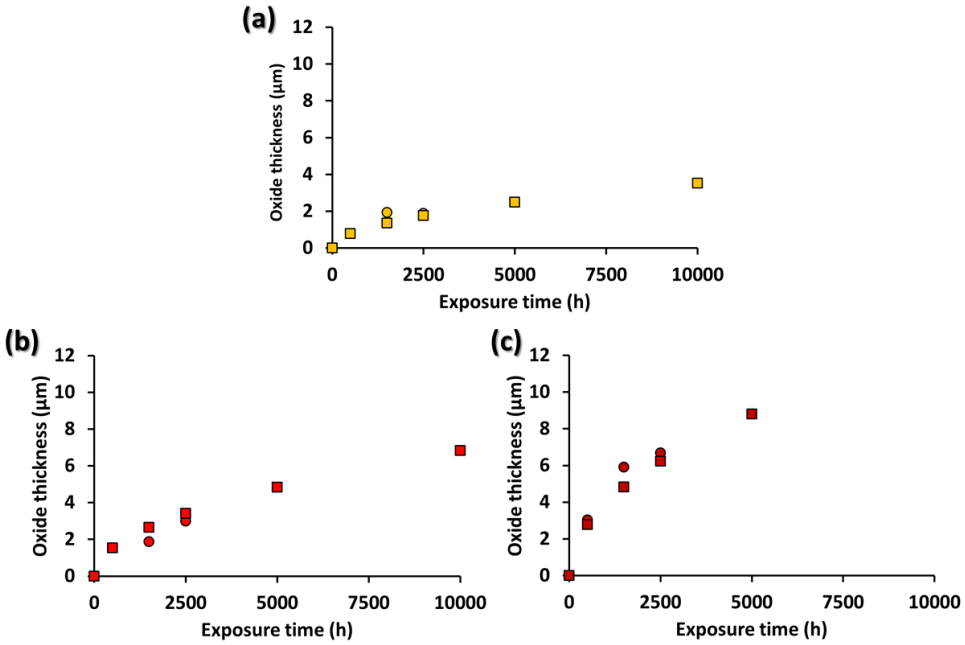

Figure 4-126: Comparison between experimental oxide thickness data (○) and calculated data (□) for P2500 ground surfaces of Alloy 617 at (a) 650, (b) 700, and (c) 750°C.

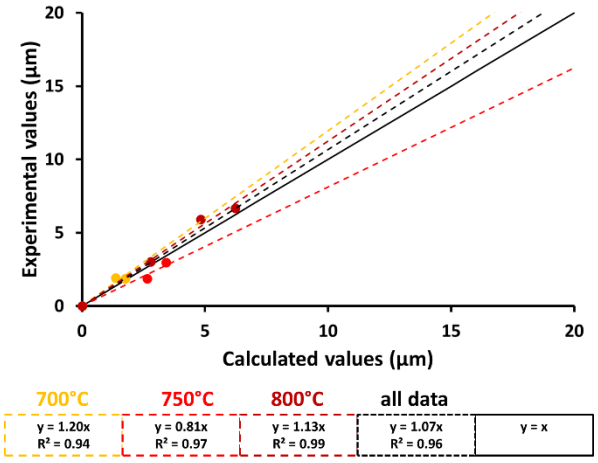

Figure 4-127: Comparison between the oxide thickness experimental data and the values calculated from the modelling equation for P2500 ground surfaces of Alloy 617.

Equation (4-42) was used to predict the thickness of the oxide layer developed on P1200 ground surfaces of Alloy 263. As Figure 4-128 and Figure 4-129 both show very good correlation between the calculated and experimental values for oxide thickness, it could thus be affirmed that the model developed is performant.

Oxide growth modelling equation for P1200 ground surfaces of Alloy 263:

$$\Delta x = \left(2.46\ 10^{+8} \exp\left(-\frac{201.27}{RT}\right) t\right)^{\frac{1}{2}} \quad \textbf{(4-42)}$$

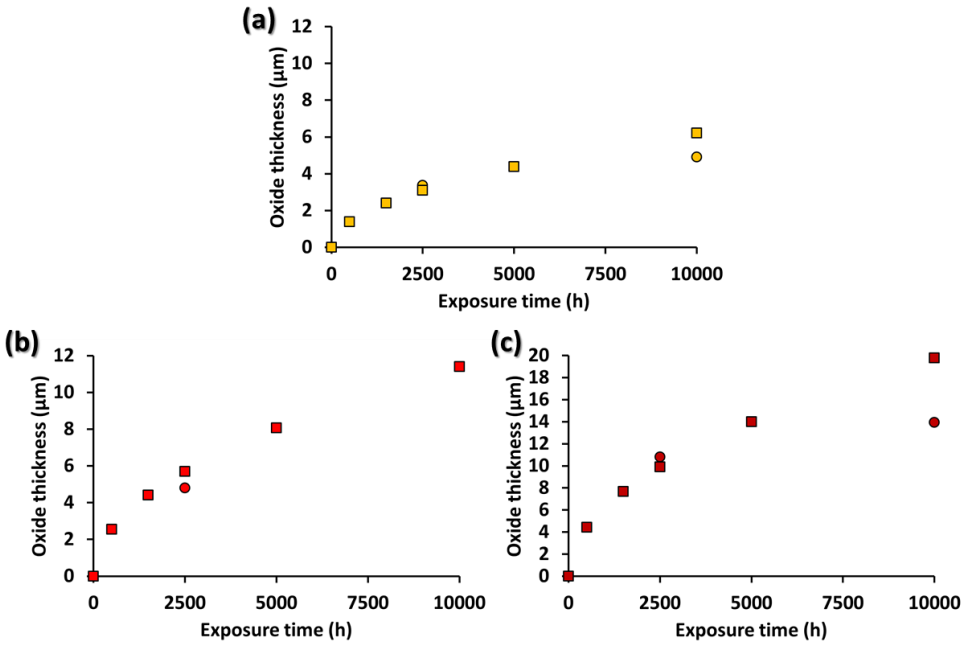

Figure 4-128: Comparison between experimental oxide thickness data (○) and calculated data (□) for P1200 ground surfaces of Alloy 263 at (a) 650, (b) 700, and (c) 750°C.

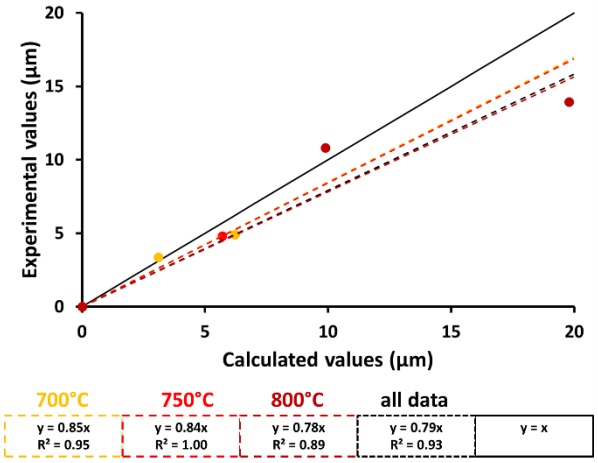

Figure 4-129: Comparison between the oxide thickness experimental data and the values calculated from the modelling equation for P1200 ground surfaces of Alloy 263.

For P1200 ground surfaces of Alloy 740, Equation (4-43) was developed and gives satisfaction in predicting the thickness of the oxide layers grown on their surface, as is confirm in Figure 4-130 and Figure 4-131.

Oxide growth modelling equation for P1200 ground surfaces of Alloy 740:

$$\Delta x = \left(4.39\ 10^{+6} \exp\left(-\frac{176.87}{RT}\right) t\right)^{\frac{1}{2}} \quad \textbf{(4-43)}$$

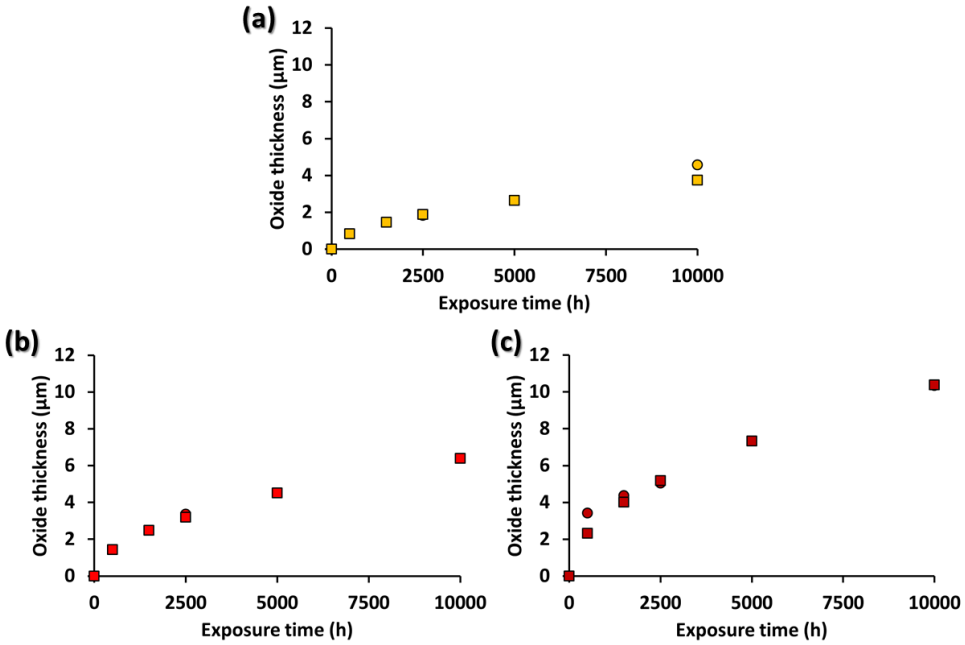

Figure 4-130: Comparison between experimental oxide thickness data (○) and calculated data (□) for P1200 ground surfaces of Alloy 740 at (a) 650, (b) 700, and (c) 750°C.

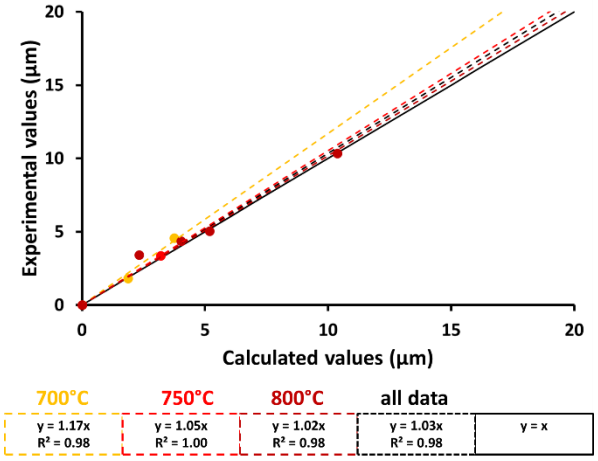

Figure 4-131: Comparison between the oxide thickness experimental data and the values calculated from the modelling equation for P1200 ground surfaces of Alloy 740.

4.3.6. Discussions of the oxide thickness evaluation

For the different materials and surface finishes studied, oxide thickness evaluation and modelling have proven to be challenging but have allowed gathering precious information.

Firstly, in terms of oxide thickness evaluation, having adapted Arrhenius plots for the parabolic oxide growth rates brings important information. Indeed, unlike with mass change data, oxide thickness is always a positive value, so the entire oxide thickness dataset can be represented using this type of graphic.

For materials affected by spallation, such as TP347HFG, the parabolic rates calculated show large variations with increasing oxidation time. As described in [16,55], oxide spallation and regrowth happen simultaneously, which is why there is no trend of oxide thickness variation over time. Considering the highest parabolic rate values obtained, it can be observed that they are represented between the reference lines for oxidation of pure chromium and pure iron. These points represent measurements on surfaces which have not experienced spallation recently before the end of their exposure test, which is consistent with the results obtained in the cross-section images, presented in Section 4.2.1.1, showing the formation of a multi-layered oxide composed of iron oxides formed on top of an inner chromium-rich layer. The lowest values presented in the adapted Arrhenius plots refer to oxide layers having experienced exfoliation shortly before the exposure test end. Therefore, since spallation mostly happens between the inner and outer layers, only the inner layer composed of chromium-rich oxides remains at the surface of the material (also observed on cross-section images in Section 4.2.1.1). The fact that these lowest values are all located around the reference line for the oxidation of pure chromium is consistent with the fact that only chromium-rich oxide remains on the surfaces where these low parabolic rates are calculated.

For the materials studied which are not affected by spallation, such as Sanicro 25, Alloy 617, Alloy 263 and Alloy 740, it can be observed that the parabolic rates calculated for oxide growth are close to the reference line for the oxidation of pure chromium and that the values decrease with increasing oxidation time. Several explanations can be given for this observation:

- The decrease can be due to the fact that the steam oxidation reaction does not strictly follow a parabolic rate.
- The decrease is due to an increase of protectiveness cause by the growth of the chromia layer present on the surfaces of the samples exposed.

Theoretically, when the protectiveness of a surface increases due to the formation of protective oxides, then the steam oxidation of the material follows a logarithmic rate [9,27]. For these materials, logarithmic rates have been tried and result in lower correlation when calculating the kinetic parameters (activation energy and standard rate constant).

When comparing the effect of the different surface finishes applied, it has been observed that the parabolic rate decrease with the increasing amount of compressive stresses applied to the surfaces. Compared with surfaces left as-received, surface finishes with low compressive stresses, such as P1200 and P2500 ground surfaces, possess a slightly higher oxidation resistance at the early stages of the steam oxidation process which postpones the transition time to breakaway oxidation. However on TP347HFG, when the outer layer starts to grow, surface finish does not play any protective role. For highly resistant materials (Sanicro 25 and the various nickel-based alloys), even if the chromium diffusion is enhanced at the early stages of the oxidation process to promote the formation of a better chromia layer, the protectiveness of this layer causes the reduction in the oxidation rate. Therefore, with increasing oxidation time there would be a catching up of oxidation rate from samples with lower chromium diffusion at the early stages of the steam oxidation process. For high compressive stresses surface finishes (machining and shot-peening), it has been observed that for TP347HFG, the oxidation resistance of the material is significantly

increased. These surface finishes are so effective that their parabolic rates, calculated at high temperature (800°C), are of the same order of magnitude than for oxidation of pure chromia. However, at 700°C, the oxidation rate remains higher than the oxidation of pure chromium despite the enhanced chromium diffusion brought by cold working. This unexpected behaviour has been previously reported for ferritic steels [43] which show increased steam oxidation resistance with increasing steam temperature. The given explanation for this observation was that both the outward iron diffusion through the oxide scales, leading to breakaway oxidation, and the chromium diffusion to the surface of the material, leading to the formation of the protective chromia layer, possess temperature ranges where one process is dominant over the other. Thus at 800°C, the chromia layer formation process dominates the outward diffusion of iron, but at 700°C, it appears that the chromium diffusion is not significantly enhanced to protect the material.

Regarding the oxide growth modelling work, the precision of the predictive equations developed greatly depends on the material studied. The models have only been developed for as-received, P1200 and P2500 ground surface finishes as there remains a lack of data points to build up models for machined and shot-peened surfaces.

For the different surfaces of TP347HFG, which all form a multi-layered oxide, the models developed do not show a good fitting of the experimental data. As discussed earlier, spallation occurs on TP347HFG's surfaces which complicates the modelling work. Moreover, it has also been pointed out that some of the surfaces that have been labelled as P1200 ground were in reality machined. Therefore some experimental data have to be removed from the dataset to calculate the different models. Nevertheless, the equations developed still fit some of the experimental data. To be able to develop more precise oxide growth models taking into account spallation, more data at intermediate times would be needed.

For the highly resistant Sanicro 25, and nickel-based alloys Alloy 617, Alloy 263 and Alloy 740, the oxide growth modelling gave satisfaction. Indeed, no spallation was observed on these materials which brings more coherence to the experimental data. These models could be used by any industrial who wish to predict oxide growth for these materials.

4.4. Study of the effect of pressure

The study of the effect of pressure was performed by comparing samples exposed to high or atmospheric pressure steam at 650°C for 1000 hours. Mass change, oxide morphology and composition as well as oxide thickness were investigated. In service exposed samples were also observed to point out what the differences between laboratory and in service exposure tests could be.

4.4.1. Laboratory exposure experiments

Three different materials have been used to perform the laboratory exposure experiments: ferritic steel T 92 and austenitic steels TP347HFG and Sanicro 25. T 92 samples had a cut-on-reel geometry with P1200 ground surfaces. The two austenitic steels were cut from tubes and had different surface finishes on their various surfaces. The concave surfaces of the samples were left as-received whereas the other surfaces (flat and convex surfaces) were ground.

Samples of austenitic steels TP347HFG and Sanicro 25 with P1200 ground and as-received surfaces as well as P1200 ground ferritic steel T 92 have been exposed to steam either at 36 bars in a high temperature and high pressure steam loop associated with an autoclave or at atmospheric pressure in an isothermal furnace at 650°C for 1000 hours. Although the atmospheric pressure test used oxidation cycles of 250 hours compared to the continuous test with the

pressurize autoclave, comparison of the mass change results obtained from both experimental setups enables observation of the specific effects of pressure on high temperature steam oxidation.

The net mass change for the different samples is given in Figure 4-132. At atmospheric pressure P1200 ground T 92 shows a high mass change, following a parabolic trend. From the mass change data it can be inferred that spallation does not occur. At 36 bars the mass change is measured to be higher than at atmospheric pressure which is a first evidence of the oxidation enhancement due to an increase of pressure. For TP347HFG, the mass change of the sample exposed at atmospheric pressure seems to fluctuate. This is due to the growth and exfoliation of the oxides formed; nevertheless the mass change stays positive during the 1000 hour test. However for the test at 36 bars only mass loss has been recorded. This could result from a thicker oxide growth than at atmospheric pressure which then mostly exfoliated during cool-down from the single thermal cycle (but exfoliated oxides could not be recovered for examination). The exfoliation process is expected to take place during the cooling down of furnaces used for high temperature steam exposure tests due to the relative changes in coefficient of thermal expansion. The mass change data for both atmospheric and 36 bar Sanicro 25 samples shows that the steam oxidation process at 36 bars has led to an enhanced mass of adherent oxides compared to the test at atmospheric pressure.

For the austenitic steels studied, the mass change data does not allow a determination whether the as-received surface, the P1200 ground surface, or both are undergoing an accelerated oxidation rate at the higher pressure as a single sample has both surface finishes. Due to its higher chromium and nickel content, Sanicro 25 shows a higher oxidation resistance than TP347HFG. Furthermore, the exfoliation taking place on TP347HFG complicates any mass change data analysis; a well-known limitation of mass change techniques and one of the many reasons for examining cross-sections through samples. However, the two austenitic steel both show a higher oxidation resistance than T 92.

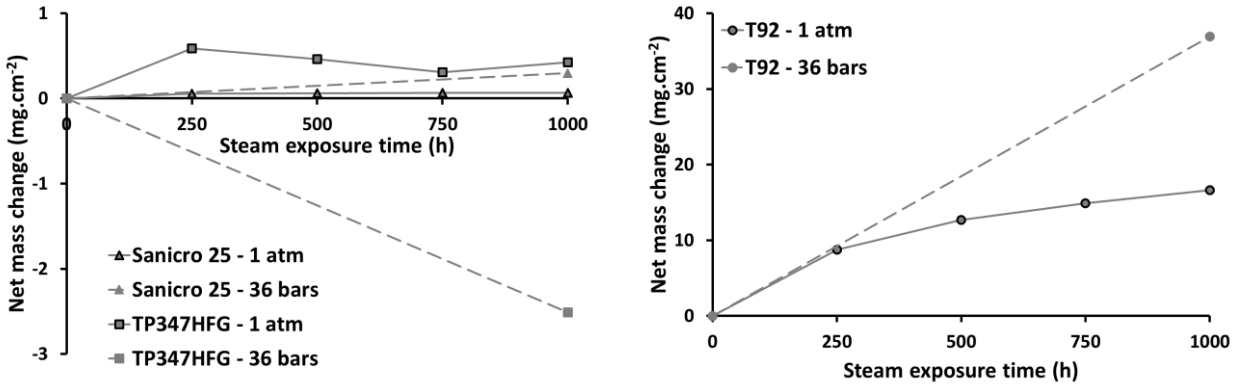

(a) (b)

Figure 4-132: Net mass change per unit of area for the (a) TP347HFG and Sanicro 25 samples, and the (b) T 92 samples exposed at 650°C for 1000 hours in the 36 bar autoclave and the atmospheric pressure furnace.

To characterize the oxide morphology, composition and phases of the oxides formed at the surface of the different exposed samples, SEM associated with EDX as well as XRD have been used. XRD spectra for the different materials are presented in Figure 4-133 for (a) as-received and (b) P1200 ground surfaces. SEM images are presented in Figure 4-134 for as-received surfaces and in Figure 4-135 for P1200 ground surfaces. EDX results for oxidized surfaces are presented in Figure 4-136, Figure 4-137, Figure 4-138, and Figure 4-139. Cross-sections images for as-received and P1200 ground surfaces are respectively presented in Figure 4-140 and Figure 4-141. Results from EDX analyses of cross-sections are shown in Figure 4-142, Figure 4-143, Figure 4-144, Figure 4-145.

For P1200 ground ferritic steel T 92, XRD spectrum at 1 atmosphere shows peaks related to the formation of haematite Fe_2O_3 at the sample's surface. The observation of the oxide formed using SEM and its composition analysis (Figure 4-142) confirms the formation of haematite. In terms of oxide morphology, the sample is mostly covered with a smooth oxide layer with the presence of whiskers all over it. Interestingly, the features of a broken oxide sphere is also visible at the surface of the sample, which is also composed of iron oxide. This can be the result from the formation of an iron-oxide layer at the steam interface which has

experienced stresses leading to the elevation of this layer under the shape of a sphere until a part of it breaks down. This show that at 650°C and 1 atmosphere spallation occurs on P1200 ground surfaces of T 92 (Figure 4-135). The mass change data for this sample does not confirm that spallation occurs even though mass change was monitored during the oxidation process. The loss of mass from the spallation of these oxide spheres is thus non significant in comparison with the mass gained by the sample.

At 36 bars, the XRD spectrum shows peaks related to the iron-rich oxide $Fe_3Mn_3O_8$. No other species were detected to be formed at the surface of the sample. SEM imaging, presented in Figure 4-135 and EDX analysis performed on the cross-section of the material (Figure 4-143) confirm the composition of the $Fe_3Mn_3O_8$ oxide formed and allow observing the specific shape of the oxide which looks like small pyramids. The entire sample's surface is covered with this oxide.

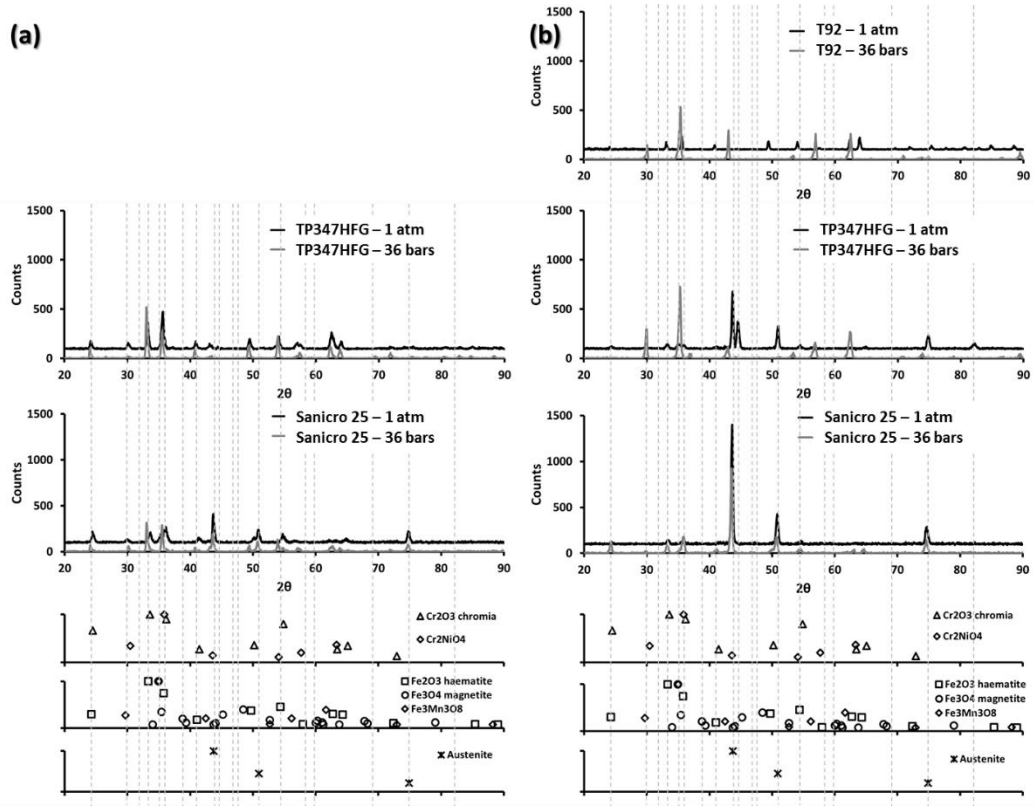

Figure 4-133: XRD spectra of (a) as-received and (b) P1200 ground surfaces of the different materials tested after 1000 hour steam exposure at 650°C and 1 atmosphere or 36 bars.

XRD spectra for as-received surfaces of TP347HFG show that the XRD peaks related to the underlying sample's austenite matrix are not visible. This suggests the formation of a relatively thick oxide on its surface. The peaks related to the iron-rich oxides have greater intensity for samples exposed to steam at 36 bars rather than atmospheric pressure, which is consistent with a thicker oxide layer forming with increasing pressure on the as-received surface of TP347HFG. Microscopic images (Figure 4-134) and EDX analyses of the surfaces (Figure 4-136) and cross-sections (Figure 4-144) confirm the formation of a multi-layered oxide scale with an outer layer of iron-rich oxides (magnetite and haematite) which is seen to have exfoliated in some areas revealing an inner Fe-Cr oxide layer underneath (as confirmed by Figure 4-136).

The P1200 ground surfaces of TP347HFG show the austenite matrix peaks on their XRD spectra as well as peaks that can correspond to either iron-rich or chromium-rich oxides. Microscopic images (Figure 4-135) and analyses (Figure 4-137 and Figure 4-145) confirmed that iron-rich oxide nodules have developed on the surface of a chromium-rich oxide layer. It seems that, on the P1200 ground surfaces at both pressures, chromium-rich oxides have been formed. However, at atmospheric pressure large iron-rich nodules develop sporadically (Figure 4-135), whereas at higher pressure the surface is more homogeneously covered by iron-rich oxides of lesser thickness.

The as-received surfaces of Sanicro 25 show XRD peaks related to the austenite matrix as well as for chromium-rich oxides (confirmed by SEM/EDX analyses (Figure 4-138)). The chromium-rich oxide XRD peaks have greater relative intensity on the surface exposed to steam at 36 bars rather than at atmospheric pressure, which means a thicker chromium-rich oxide layer should be observed.

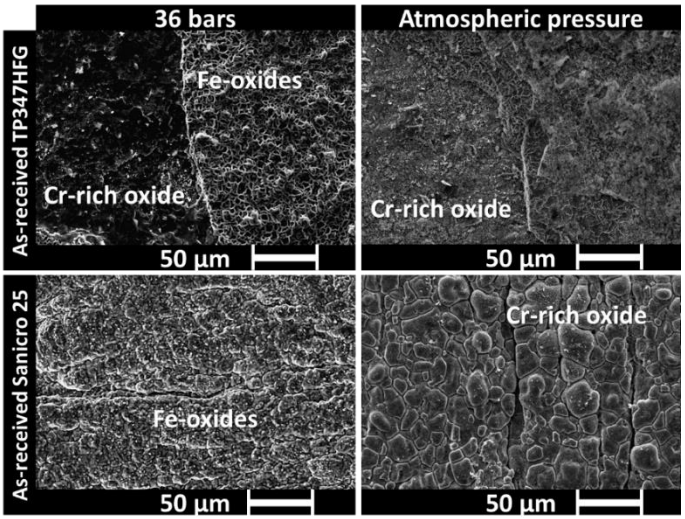

Figure 4-134: SEM imaging of oxidized surfaces of the various as-received surfaces of the materials exposed for 1000 hours at 650°C at 1 atmosphere or 36 bars.

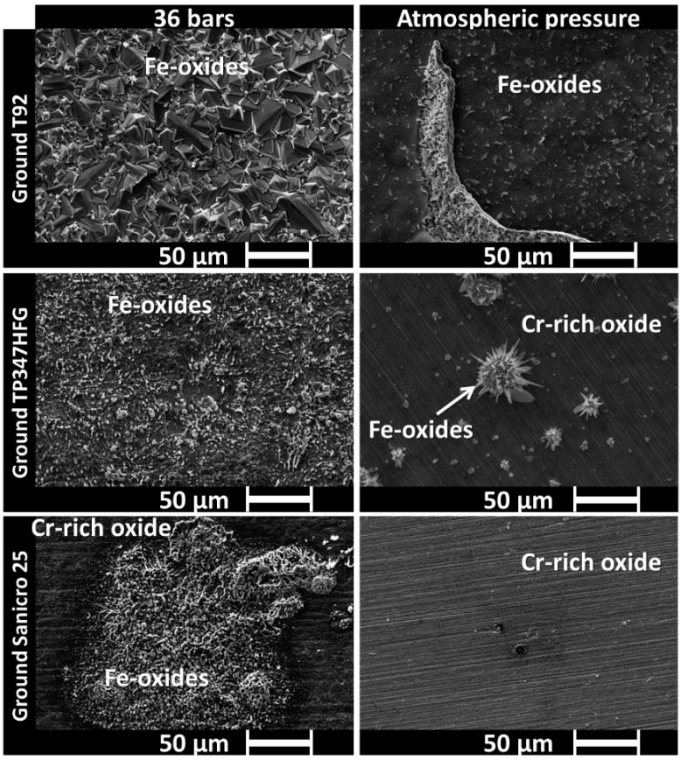

Figure 4-135: SEM imaging of oxidized surfaces of the various P1200 ground surfaces of the materials exposed for 1000 hours at 650°C at 1 atmosphere or 36 bars.

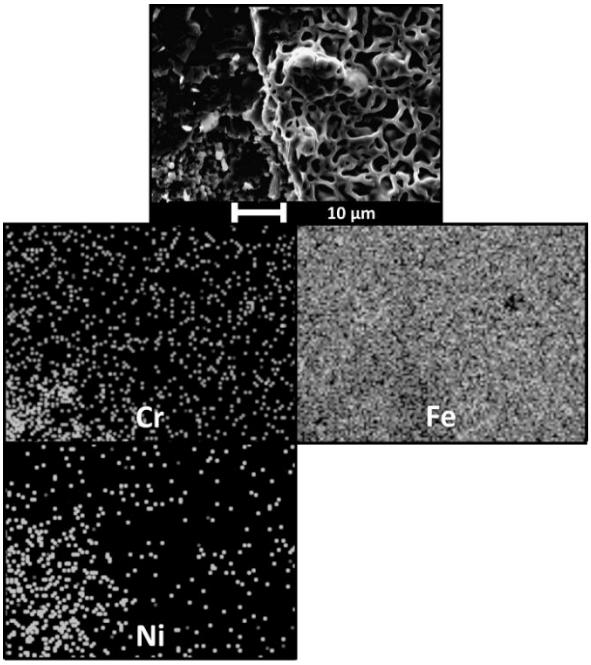

Figure 4-136: SEM image and elemental maps from EDX analysis for the oxidized as-received surface of TP347HFG after steam exposure at 36 bars and 650°C for 1000 hours.

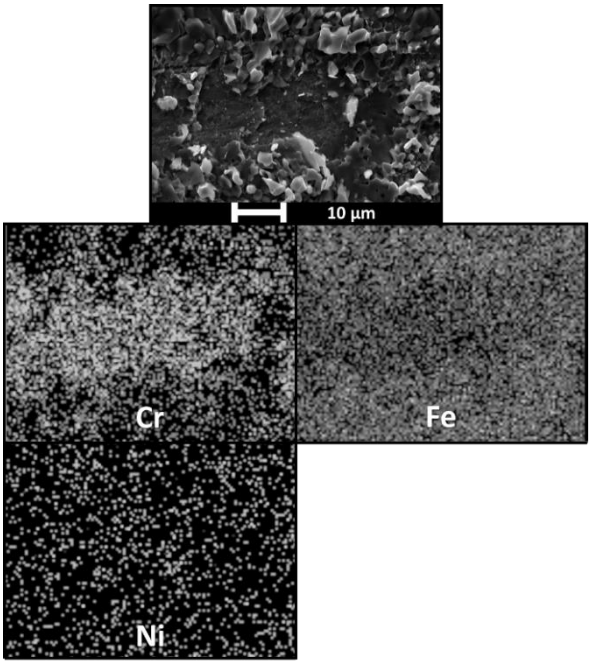

Figure 4-137: SEM image and elemental maps from EDX analysis for the oxidized ground surface of TP347HFG after steam exposure at 36 bars and 650°C for 1000 hours.

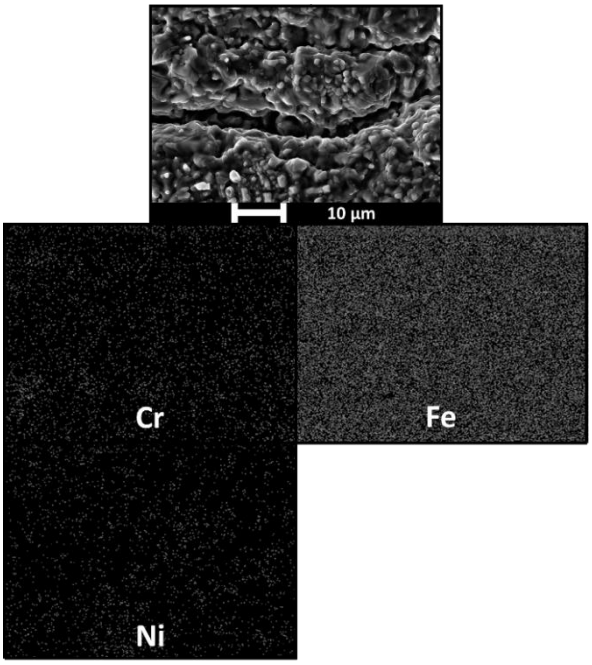

Figure 4-138: SEM image and elemental maps from EDX analysis for the oxidized as-received surface of Sanicro 25 after steam exposure at 36 bars and 650°C for 1000 hours.

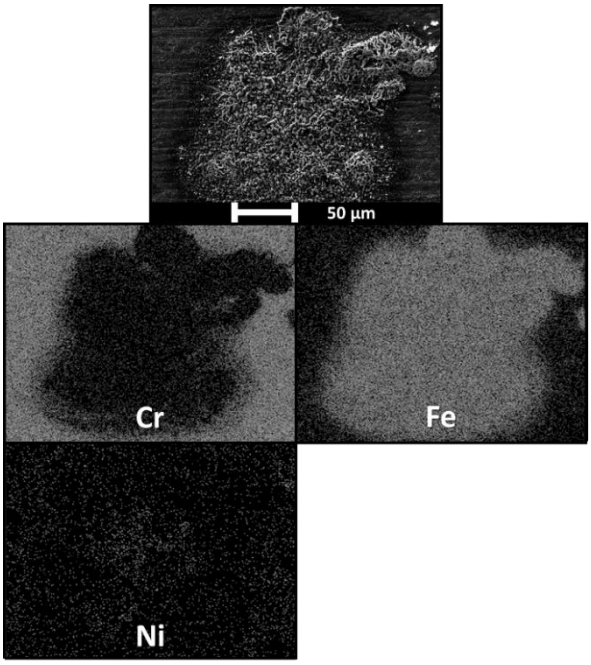

Figure 4-139: SEM image and elemental maps from EDX analysis for the oxidized ground surface of Sanicro 25 after steam exposure at 36 bars and 650°C for 1000 hours.

The P1200 ground surfaces of Sanicro 25 from both exposure pressures show high intensity XRD peaks for the austenite matrix which means that a thin oxide layer has been formed. The SEM/EDX data (Figure 4-139) shows that, at atmospheric pressure, only a thin chromium-rich layer is observed whereas at 36 bars some iron-rich oxides have started to break through the chromium-rich layer.

Cross-sections of the samples were examined to determine oxide thicknesses. The oxide layers formed on the different surfaces are shown in Figure 4-140 for as-received surfaces and in Figure 4-141 for P1200 ground surfaces. Due to the very thin oxides formed on the Sanicro 25 P1200 ground surfaces, only the oxide thicknesses from as-received surfaces have been measured. For TP347HFG, measurements were also made only for as-received surfaces. These data and oxide thickness measurements for the oxide layer formed on P1200 ground T 92 are shown in Figure 4-146. Figure 4-146 plots cumulative normal probability related to scale thickness for the different samples (exposed to either 1 or 36 bar pressure and with either an as-received or P1200 ground surface). To obtain this data, multiple measurements of the oxide thicknesses were recorded and then ordered from smallest to greatest recorded oxide thickness. In such a plot of oxide variation, the central data point is the median oxide thickness, while the standard deviation from this median value is obtained from the slope of the data.

Cross-section images of oxidized P1200 ground surfaces of T 92 show that at both pressures tested, a large multi-layered oxide is formed at the samples' surface. For both samples, iron oxides are composing the outer oxide layer and Fe-Cr spinel oxide forms the inner oxide layer (Figure 4-142 and Figure 4-143). An internal oxidation zone is also visible at the metal / oxide interface. At atmospheric pressure, more porosity is present inside the iron-oxide layer than at high pressure. The visualisation of increased porosity in the sample exposed at atmospheric pressure can be due to the fact that the exposure was performed following 250 hours cycles. Using cycles to perform the steam exposure tests induced more stresses into the oxide layer, due to the multiple temperature change and the difference in CTE between the different oxide layers, resulting in the formation of higher porosity. The broken oxide layers formed at the surface

of the sample exposed at atmospheric pressure are also visible on the cross-section images. In terms of oxide thickness, it is clear that at high pressure the sample forms a thicker oxide layer than at atmospheric pressure, as later presented in Figure 4-146.

For TP347HFG, the as-received surfaces exhibit a multi-layered oxide with a chromium-rich oxide at the inner oxide/metal interface. The inner oxide layer is composed of an Fe-Ni-Cr oxide and iron oxides form the outer layer (Figure 4-144). A higher nickel concentration has been observed in the centre of the inner oxide layer. The oxide layers formed possess similar compositions at both pressures but, the thicknesses are different; the higher pressure steam exposure leads to the formation of a thicker oxide layer than the atmospheric pressure test samples. This thickness variation is shown in Figure 4-146.

The P1200 ground surfaces of TP347HFG have been observed to form very different oxides layers at 36 bars and at atmospheric pressure after 1000 hours exposure. A multi-layered oxide is formed at high pressure (Figure 4-145) whereas atmospheric pressure exposure only results in a thin chromium-rich layer with some nodules scattered on the surface. The 36 bar, multi-layered oxide consists of a large and complex inner oxide layer, identical to that described earlier, but with a thin iron-rich outer oxide layer. It has been reported in other tests[10,23] that in multi-layered oxides the inner and outer layers grow at the same rate when exfoliation does not occur, hence the relatively thin outer oxide layer observed here strongly suggests that the large exfoliation recorded in the mass change data comes from the exfoliation of the outer layer formed on this surface. The nodules formed at atmospheric pressure are composed of iron-rich oxides in their outer parts and Fe-Ni-Cr oxides in their inner parts. The multi-layered composition of the nodules is the same as that of the multi-layered oxide formed on the as-received surfaces where the breakaway oxidation has occurred (Figure 4-144). This is consistent with the fact that breakaway oxidation results from nodular growth spreading across the surfaces of the austenitic steels oxidised in steam [23].

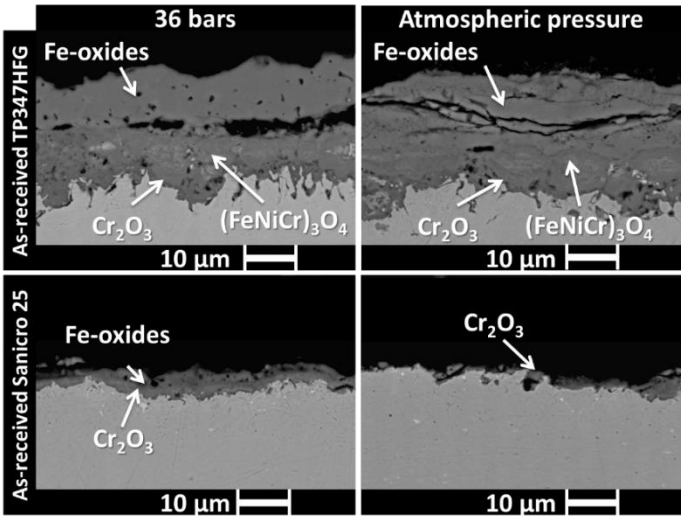

Figure 4-140: SEM imaging of cross-sections associated with various as-received surfaces of the materials exposed for 1000 hours at 650°C at 1 atmosphere or 36 bars.

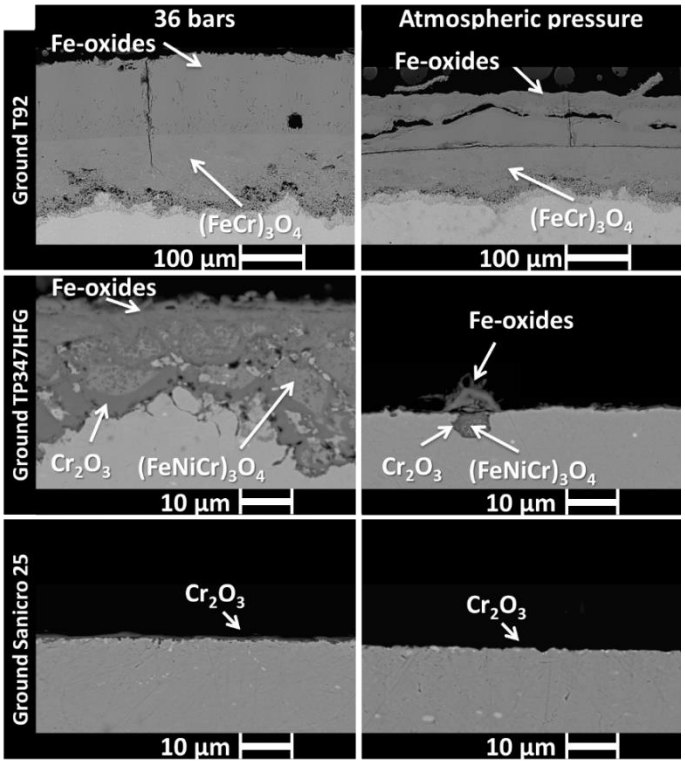

Figure 4-141: SEM imaging of cross-sections associated with various P1200 ground surfaces of the materials exposed for 1000 hours at 650°C at 1 atmosphere or 36 bars.

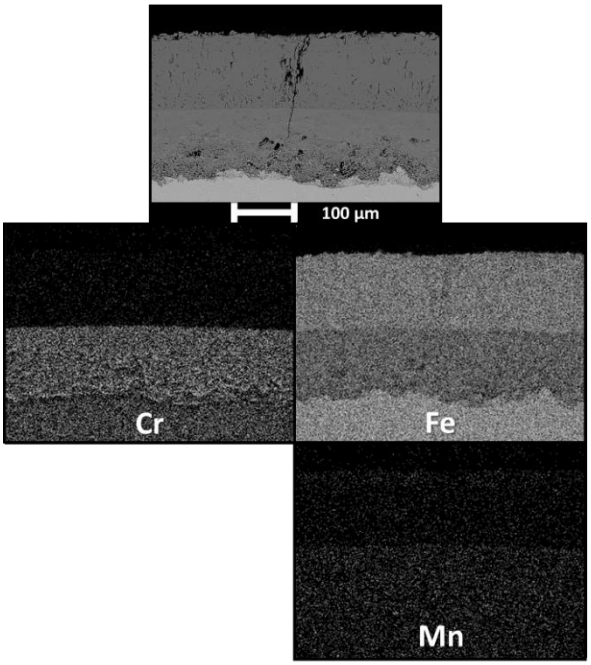

Figure 4-142: SEM image and elemental maps from EDX analysis for the cross-section of P1200 ground T 92 after steam exposure at 1 atmosphere and 650°C for 1000 hours.

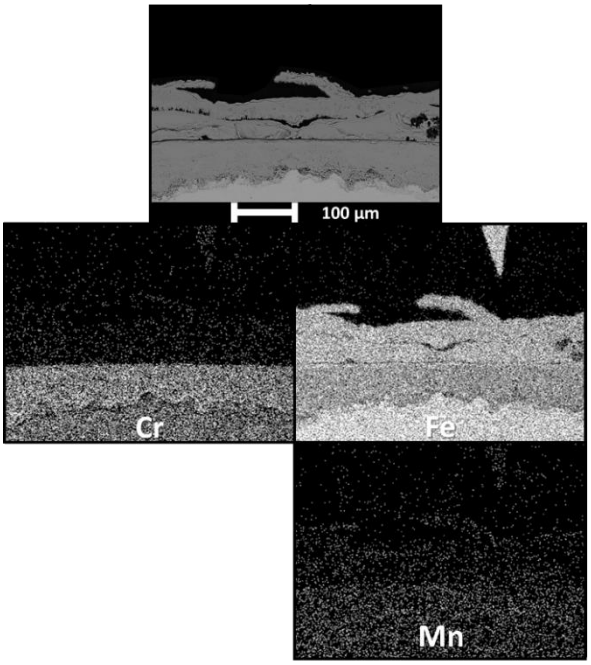

Figure 4-143: SEM image and elemental maps from EDX analysis for the cross-section of P1200 ground T 92 after steam exposure at 36 bars and 650°C for 1000 hours.

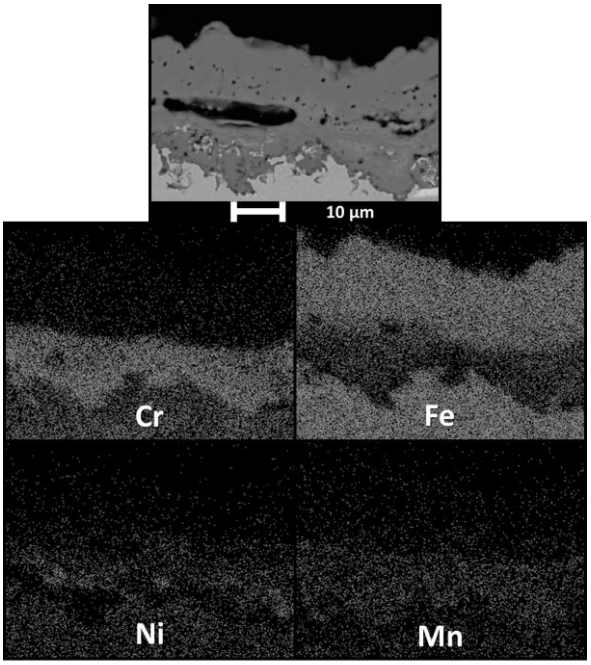

Figure 4-144: SEM image and elemental maps from EDX analysis for the cross-section of as-received TP347HFG after steam exposure at 36 bars and 650°C for 1000 hours.

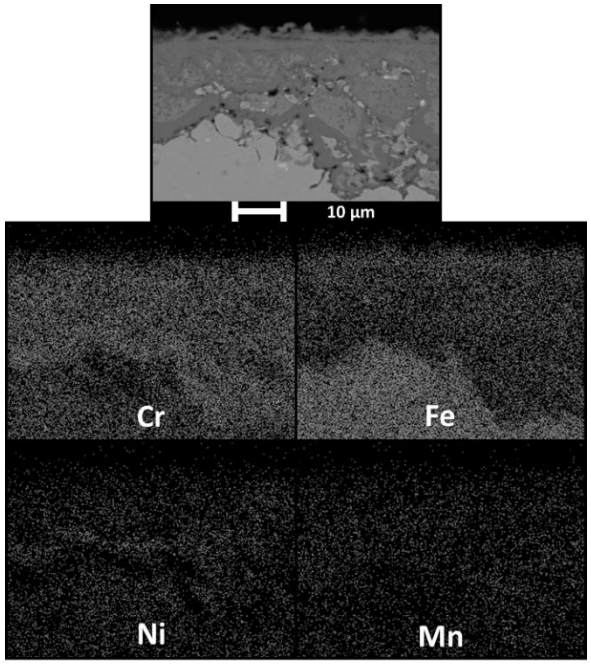

Figure 4-145: SEM image and elemental maps from EDX analysis for the cross-section of P1200 ground TP347HFG after steam exposure at 36 bars and 650°C for 1000 hours.

Sanicro 25 samples show the formation of thin chromium-rich oxide layers on their as-received surfaces (Figure 4-138). Figure 4-146 shows that the oxide thicknesses are slightly higher at high pressure than those formed on the sample exposed at one atmosphere, and Figure 4-140 shows that they are developing a more complex structure. For the P1200 ground surfaces, thin layers are observed at 36 bars whereas at 1 atmosphere the chromia layer is so thin it has not been resolved with the SEM.

Oxide thicknesses were measured on P1200 ground surfaces of T 92 and only for the as-received surfaces for both austenitic steels as this was the only type of tested surface finish that formed resolvable oxide layers on both samples in both conditions, thus allowing comparison. T 92 and TP347HFG samples show roughly normal distributions of oxide thicknesses, as the cumulative normal probabilities produce roughly consistent gradients (Figure 4-146). The deviations from normal distribution observed on the extremity of each samples' dataset may be characteristic of partial oxide exfoliation, which has previously been supposed to occur on the as-received surfaces of TP347HFG during the steam oxidation process and on T 92 at atmospheric pressure. However, the Sanicro 25 datasets in Figure 4-146 show transitions between two types of oxide behaviour: some areas are still protected by chromium-rich oxides whereas on other areas more rapid oxidation is starting to occur. It appears 1000 hours is too soon to get a comparison between stable long term oxide layer growth rates for this material.

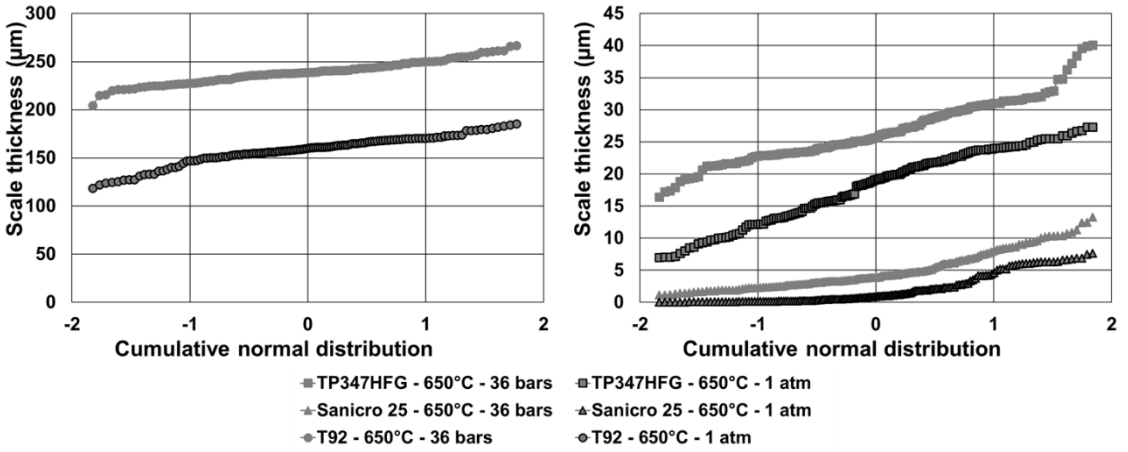

Figure 4-146: Cumulative normal distribution associated with the P1200 ground surfaces of the materials exposed for 1000 hours at 650°C at 1 atmosphere or 36 bars.

Some studies [8,23] report that, an increase of pressure increase the steam oxidation rate by modifying the oxygen diffusion in the oxide layers. The following equation has been developed and described the link between the oxidation kinetics and the steam pressure [8].

$$k_p \propto P^{\left(\frac{2}{3}\right)\left(\frac{b}{2a(\alpha+1)}\right)} \quad (4\text{-}44)$$

Where k_p is the parabolic oxidation rate $[(mg.cm^{-2})^2.h^{-1}]$, P is the pressure $[bars]$, a and b are respectively the metal and oxygen stoichiometry of a M_aO_b oxide and α is the effective charge of the metal vacancy in the oxide of interest M_aO_b.

Theoretically, increasing the pressure from the atmospheric pressure (1 bar) to 36 bars should result in an increase in the parabolic rate by a factor depending on the nature of the oxide formed: 1.57 for chromia and between 1.70 and 1.49 for magnetite (in magnetite iron ions' effective charge are either 2 or 3). Table 4-6 gathers the mean oxide thickness measured on the surfaces for the different materials at the two pressures tested. Using Equation (4-44) the ratio $\frac{k_{p36}}{k_{patm}}$ calculated for T 92 is 2.22, 1.80 for TP347HFG, and 19.34 for Sanicro 25.

Table 4-6: Median oxide thickness measured on as-received surfaces of TP347HFG and Sanicro 25, and on P ground surfaces of T 92 exposed at atmospheric and high pressure.

		Median value of oxide thickness (µm)	Parabolic rate k_p (µm².h^{-1})	Ratio $\frac{k_{p36}}{k_{patm}}$
T 92 Ground	36 bars	238.85	5.70 .10^{1}	2.22
	1 bar	160.38	2.57 .10^{1}	
TP347HFG as-received	36 bars	25.65	6.58 .10^{-1}	1.80
	1 bar	19.14	3.66 .10^{-1}	
Sanicro 25 as-received	36 bars	3.87	1.50 .10^{-2}	19.34
	1 bar	0.88	7.74 .10^{-4}	

The $\frac{k_{p36}}{k_{patm}}$ ratio values obtained for T 92 and TP347HFG are slightly higher than what was predicted with the theoretical calculations, but for Sanicro 25 the difference is more important. The small differences between the theoretical values and those calculated from the experimental data may be explained by the fact that the actual inner and outer oxide scales measured on the exposed samples are not composed of either pure chromia or pure magnetite. Moreover, whereas the high pressure test was performed continuously, the atmospheric steam exposure test was conducted cyclically with heating and cooling of the samples every 250 hours to record the mass change of the samples exposed in the steam furnaces. These cycles cause an increasing exfoliation process resulting in a decrease of the oxide scale measured at atmospheric pressure and thus increasing the ratio $\frac{k_{p36}}{k_{patm}}$. The large difference obtained with Sanicro 25 is

explained by the difference in oxidation behaviour between the two samples compared. Indeed, the sample at atmospheric pressure is still in a protective stage where its surface is still largely covered with thin protective chromia while at high pressure iron oxides are starting to grow.

Nevertheless, it appears that the increase of the oxygen partial pressure is linked with the thicknesses of the oxides grown in the steam, as suggested in Wagner's model (Equation (4-44)) [8]. The results obtained in this study contrast with what Jianmin et al. [52] reported. The difference between these results can be explained by the differences in the experimental parameters.

4.4.2. In service exposed materials

Superheater and reheater tubes exposed to high temperature steam under service conditions were obtained from industrial partners and have been observed. Their observation enabled pointing out differences between the results obtained from in service and laboratory exposure tests. These samples observed come from the outlet of the final superheater (180 bars) and reheater (40 bars) tubes of a coal power-plant and are either composed of ferritic steel T91 or austenitic steel HR3C. Even though the materials are different from the ones used for laboratory tests, general observations regarding the oxide layer composition and the variations of oxidation kinetics caused by an increase of pressure can be useful. Details regarding the in service exposure conditions were not fully provided. The only available information was that the exposure lasted for 123,000 hours with a temperature around 580°C.

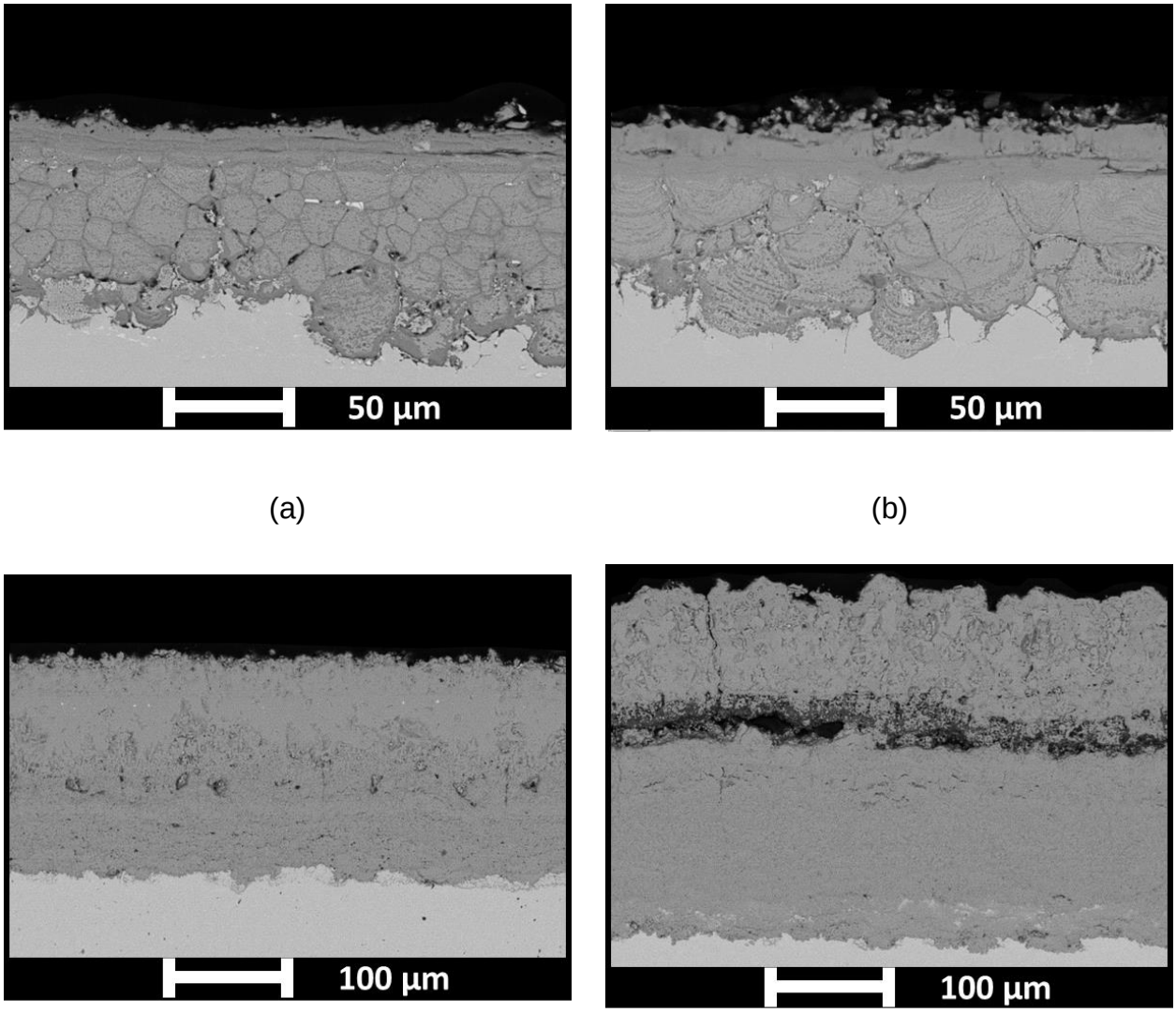

Figure 4-147: SEM images of the oxide scale formed at the surface of (a) HR3C and (c) T91 superheater tubes (180 bars) and (b) HR3C and (d) T91 reheater tubes (40 bars) after in service steam oxidation for 123,000 hours at ≈580°C.

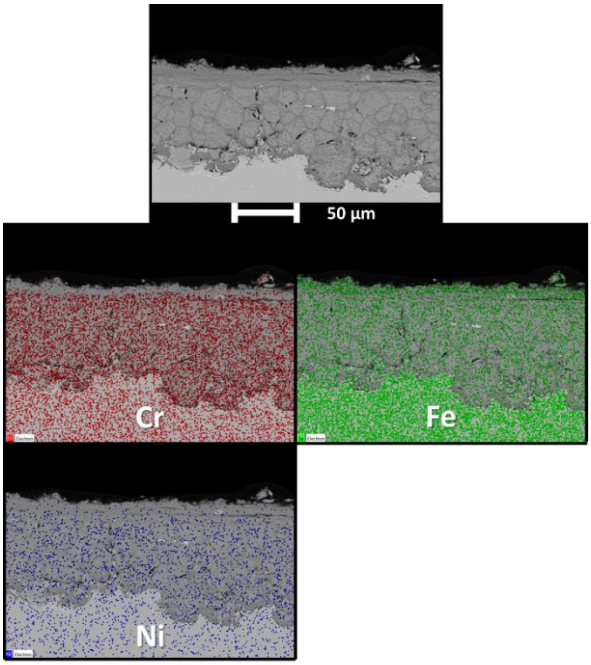

Figure 4-148: SEM image and elemental maps from EDX analysis for the HR3C superheater tube after in service steam oxidation at 180 bars and ≈580°C for 123,000 hours.

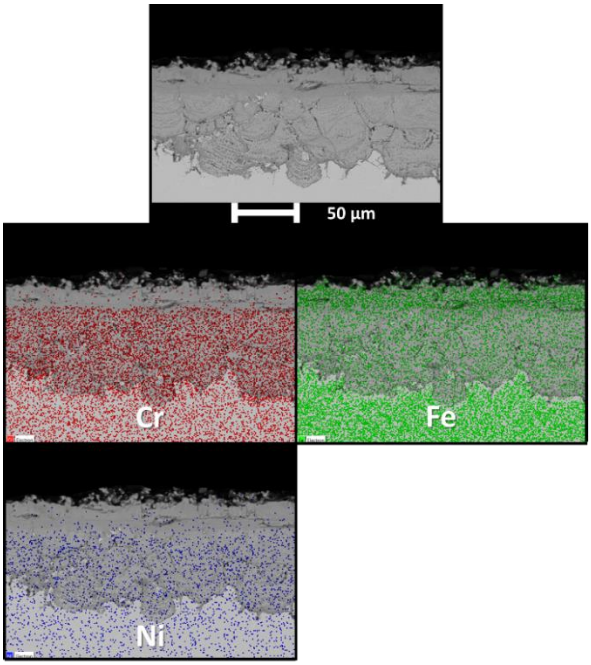

Figure 4-149: SEM image and elemental maps from EDX analysis for the HR3C reheater tube after in service steam oxidation at 40 bars and ≈580°C for 123,000 hours.

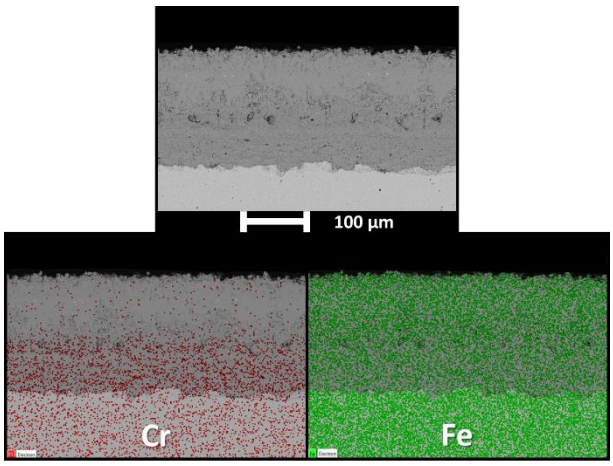

Figure 4-150: SEM image and elemental maps from EDX analysis for the T91 superheater tube after in service steam oxidation at 180 bars and ≈580°C for 123,000 hours.

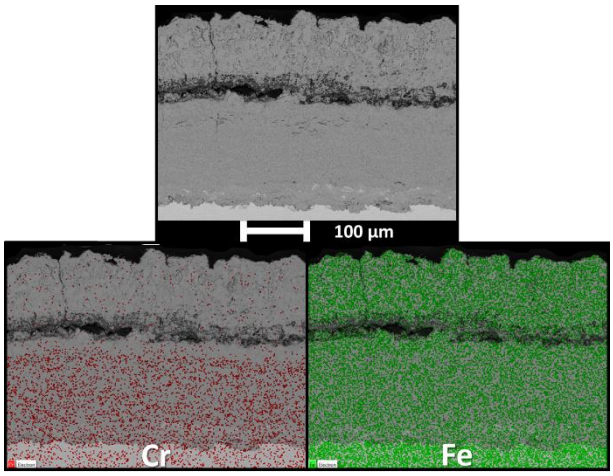

Figure 4-151: SEM image and elemental maps from EDX analysis for the T91 reheater tube after in service steam oxidation at 40 bars and ≈580°C for 123,000 hours.

Figure 4-147 shows the oxide layers formed on different superheater and reheater tubes. The elemental maps obtained from the EDX analyses performed

on the different samples are presented in Figure 4-148, Figure 4-149, Figure 4-150, and Figure 4-151. On HR3C tubes (a) and (b), a large inner Cr-rich scale can be observed with an outer Fe-rich oxide layer on top of it (Figure 4-148 and Figure 4-149). The inner scale is composed of Fe-Ni-Cr oxide and nickel is observed to be concentrated in the middle of the oxidized metal grains, which are surrounded by chromia located at the former grain boundaries. A chromia layer can also be observed at the interface between the inner oxide and the metal. Internal oxidation can be observed for the metal grains being oxidized at the interface between the inner oxide and the metal. At the outermost part of the inner oxide layer, an intermediate oxide under the outer Fe-rich layer, it is possible to observe a Fe-Cr oxide layer with no nickel inside of it (Figure 4-148 and Figure 4-149). This layer may be the reminiscence of the initially growing protective chromia layer which has then transformed into Fe-Cr oxide.

T91 tubes (c) and (d) exhibit a double oxide layer with an iron only oxide layer formed on top of a spinel Fe-Cr oxide layer (Figure 4-150). A high amount of voids/porosity are present at the interface between these two layers. For the reheater tube (Figure 4-147 (d) and Figure 4-151), a crack parallel to the surface can be observed in the outer layer and is present all along the oxide layer which indicate that spallation could be happening.

The different probability plots presented in Figure 4-152 show the dimensions of the different oxide layers formed on in service exposed superheaters and reheaters. The median value of the oxide thicknesses measured are specified in the different graphs. The different cumulative normal distributions obtained demonstrate straight-line shapes meaning that the oxide thickness follows a normal distribution. However, for ferritic steel T91 at 40 bars, there is a step in the oxide thickness distribution curves which result from the measurement of oxide thickness where partial spallation of the oxide layer has happened. Spallation was expected to happen as large cracks were observed on the SEM images in Figure 4-147 (d).

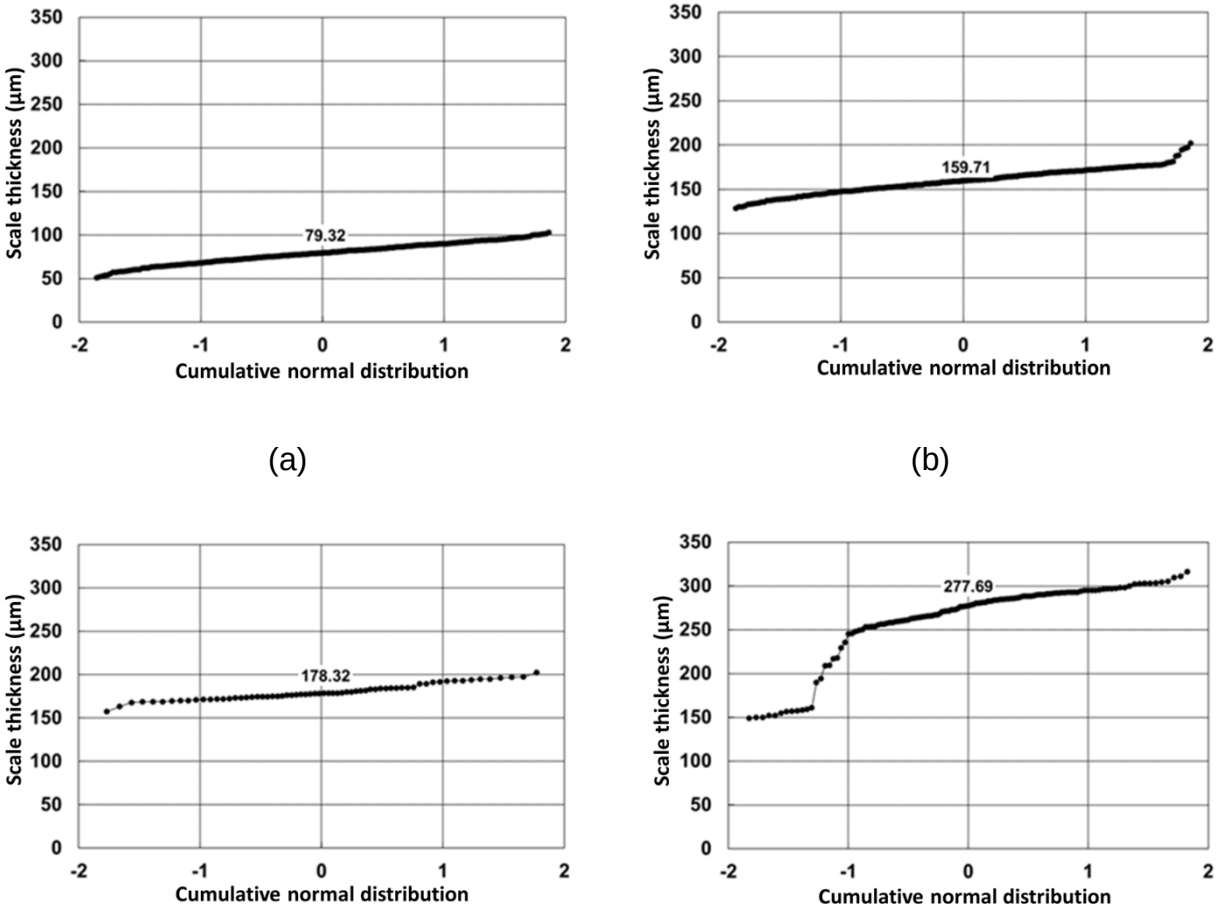

Figure 4-152: Standard normal probability plot of the thickness of the different oxide layers observed at the surface of (a) HR3C and (c) T91 superheater tubes (180 bar) and (b) HR3C and (d) T91 reheater tubes (40 bar) after 123,000 hours at ≈580°C.

Table 4-7 presents the values for the median oxide thickness measured for the different samples and compares the parabolic oxidation associated to oxide growth for both materials.

Table 4-7: Median oxide thickness measured for different oxide layers observed at the surface of HR3C and T91 superheater tubes (180 bar) and reheater tubes (40 bar) after 123,000 hours at ≈580°C.

		Median value of oxide thickness (µm)	Parabolic rate k_p (µm².h^{-1})	Ratio $\frac{k_{p180}}{k_{p40}}$
T91	180 bars	79.32	5.70 .10^{-2}	0.25
	40 bars	159.71	2.57 .10^{-1}	
HR3C	180 bars	178.32	6.58 .10^{-1}	0.41
	40 bars	277.69	3.66 .10^{-1}	

Using Equation (4-44) and assuming magnetite formation for both alloys, it was expected that an 140 bars increase would lead to an increase of the parabolic rate by a factor between 2.08 and 1.73. However, it appears that for in service materials, an increase of steam pressure results in the formation of a thinner oxide layer.

4.4.3. Discussions about the effect of pressure

As was introduced in the literature review, the effect of pressure on the steam oxidation process was difficult to assess. The results from laboratory steam exposure tests and in service exposed materials presented in this Section present the same variety of results as what could have been read in the literature and confirm the ambiguous effect of pressure [23].

The laboratory experiments demonstrated that an increase of pressure lead to an increase in oxidation rate and that pressure and oxidation rate can be linked using a simple factor. For the different materials exposed to 650°C steam for 1000 hours at either atmospheric pressure or 36 bars, a pressure increase has always been accompanied by an increase of the degree of oxidation. Indeed, for the various samples, not only the oxide thickness of the samples exposed at 36 bars was higher than at atmospheric pressure, but the morphology and composition of the oxides was different. In terms of linking the pressure and the oxidation rate using Wagner's model [8], some differences have been noticed but what was calculated from the experimental results remains close to what the theory states. However, as pointed out earlier, to compare oxidation rates for two samples of the same material exposed at different pressures, the two samples need to be in the same stage of the oxidation process where the same oxidation mechanisms happen. These results are coherent with some of the studies made by other researchers [8,23,94].

Observations for in service exposed materials show completely different results from the laboratory exposure tests. It appears that with higher pressure, the oxidation rate decreases significantly. This was also reported by Jianmin et al. [28,52] after having performed in service exposure tests on TP347HFG. The differences in the results obtained can be due to a large number of differences in terms of experimental parameters. Indeed, the in service exposure was performed at a much lower temperature (≈580°C instead of 650°C), the pressures were also very different (1 atm and 36 bars compared to 40 and 180 bars). The other differences that can be pointed out are: higher steam flow, presence of heat flux and mechanical stresses for in service tests. Spallation happening for the in service exposed materials could not have been tracked using mass change monitoring. The loss of oxide may also be a reason for the lower oxidation rates calculated for materials exposed at higher pressure. Nevertheless, results from in service exposed materials show that an increase of pressure can be beneficial for the increase of the steam oxidation resistance of heat exchanger tube materials.

In the literature review, it was pointed out that more voids and cavities were observed at high pressures [10,23,35,73]. It is also possible to observe that for the cross-section images of the materials exposed, there seems to be an increasing number of voids and cavities near the interface between the inner oxide and the metal. However, this observation could not be quantified. For the laboratory test performed at atmospheric pressure, the fact that the exposure was performed following 250 hours cycles has to be kept in mind. Indeed, the cyclic exposure of the different materials favours the propagation of cracks which can affect the number of voids and cavities observed.

4.5. Study of diffusion in oxide scales

4.5.1. Background

The use of isotopes in the study of high temperature oxidation has been reported in various studies and has allowed the interpretation of interesting mechanisms. The complementary use of $^{16}O_2$ and $H_2{}^{18}O$ on pure chromium has revealed that the oxygen transfer kinetics are significantly larger from H_2O than O_2 during high temperature oxidation process [95]. The importance of the role of H_2O during the high temperature oxidation of ferritic steel P91 has also been demonstrated by Ehlers et al. [25]. It has been shown that with a gas mixture composed of $^{16}O_2$, $H_2{}^{18}O$, and N_2, oxides formed from the reaction with $H_2{}^{18}O$ were found predominantly in the outer scale. The oxygen coming from $^{16}O_2$ was present in the inner oxide scale in greater amounts and present at the same quantity as oxygen from steam in the outer scale before breakaway oxidation occurred. These two studies [25,95] support the fact that high temperature oxidation is enhanced by the presence of water vapour and explain why the presence of steam in the gas mixture leads to more aggressive oxidation process than under environments containing oxygen molecules as the only oxygen source.

Chevalier et al. [59] used isotope doped steam in a steam-only atmosphere to study the oxygen penetration during the oxidation on pure nickel. Isotope doped water, used in the second part of a two steps experiment, allowed the calculation the bulk and grain boundary diffusion coefficients of oxygen. While trying to observe if it was metal or oxygen species transport that was responsible for oxide growth, they were able to demonstrate that the growth of the inner oxide scale was due to inward oxygen transport through short circuit diffusion paths. It appears that the inner oxide layer grows by forming fine grains due to inward diffusion of oxygen and the growth of the outer oxide scale is controlled by outward diffusion of cations forming columnar grains [59].

Brittle fractures of austenitic materials due to hydrogen embrittlement were reported [50]. It was pointed out that as the same time as oxygen coming from steam dissociation oxidized the exposed material, a portion of the hydrogen produced was absorbed by the material [46]. Hydrogen permeability in austenitic steels was observed to be limited by diffusion [96], hence the presence of oxide scale at the surface of a material lead to the decrease of the hydrogen permeation into the material [96,97].

4.5.2. Aim of the study

The use of isotope doped steam to increase the understanding of high temperature steam oxidation mechanisms has thus proved to be extremely relevant. For this reason it has been chosen to study oxygen and hydrogen diffusion in the oxide layers using steam doped with oxygen and hydrogen isotopes. Calculating the diffusion parameters for the different species of interest, using the Arrhenius equation for diffusion (2-35), were possible using samples exposed to isotope doped steam at different temperatures.

4.5.3. Methodology

Samples exposed in the high temperature and atmospheric steam furnaces were used for this study. While keeping the samples at the same temperature at which they had been previously exposed, the samples were then exposed for 100 hours to the isotope doped steam (81.8 $\%_w$ $H_2{}^{16}O$ – 9.1 $\%_w$ $H_2{}^{18}O$ – 9.1 $\%_w$ $D_2{}^{16}O$). A selection of these samples were then analysed with a focused ion beam equipped with secondary ion mass spectrometry (FIB-SIMS). FIB-SIMS maps obtained should bring some information regarding the location of the new oxides formed and new hydrogen atoms absorbed, distinguished by the presence of the isotopes.

Two TP347HFG samples exposed respectively at 650 and 700°C for 1500 hours have been selected for FIB-SIMS analysis. The sample preparation for FIB-SIMS analyses consisted of making cross-sections of the samples and polishing them as described in the post-exposure preparation Section (Section 3.4). However, an extra 5-minute polishing step with colloidal silica was applied. Moreover, since the resin used as standard when making cross-sections is not conductive, the bottom of the cross-section was cut as well to ensure electronic conductivity (Figure 4-153).

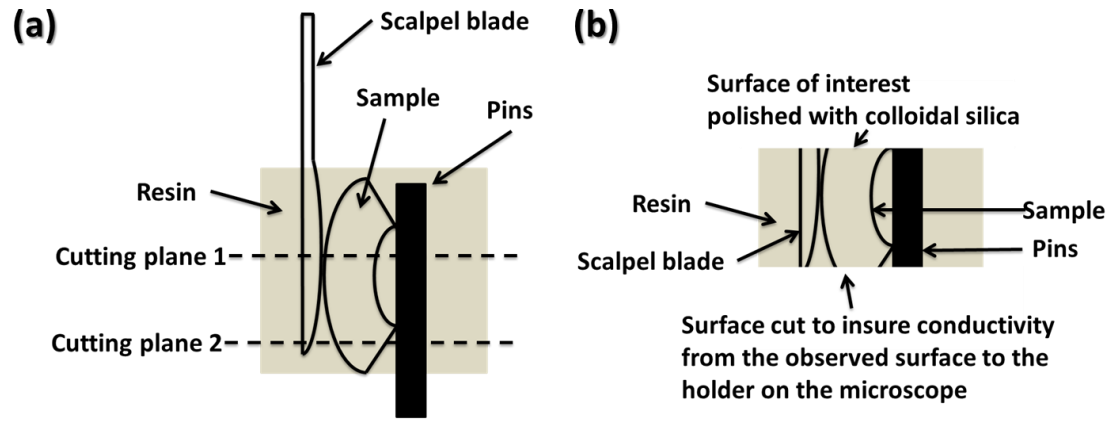

Figure 4-153: Schematics for sample mounting and cross-section preparation for FIB-SIMS analyses.

The analyses were performed on the as-received surfaces of the samples. The areas analysed were divided in a 250*250 pixel matrixes and their dimensions depends on the magnification at which the analysis was performed. The SEM images presented hereafter have received a 52° tilt correction. The principle for the FIB-SIMS analysis is to shoot a focused ion beam at the surface of interest to mill a small trench in the surface and then analyse the mass of secondary ions escaping to identify the species constituting the analysed region.

Due to the use of oxygen and hydrogen isotopes, the different species to be tracked were $^{16}O^{2-}$ (mass 16), $^{18}O^{2-}$ (mass 18), H^{+} (mass 1), D^{+} (mass 2), $^{16}OH^{-}$ (mass 17), $^{18}OH^{-}$ (mass 19), $^{16}OD^{-}$ (mass 18), $^{18}OD^{-}$ (mass 20). These different anions were tracked because the interest of the study was to understand hydrogen and oxygen diffusion. When analysing the results obtained, $^{18}O^{2-}$ and $^{16}OD^{-}$ possess the same atomic mass, therefore, there is no way to differentiate the two species with the FIB-SIMS results.

4.5.4. FIB-SIMS results

As-received surfaces of TP347HFG exposed at 650 and 700°C for 1500 hours have been observed and the results obtained are presented in Figure 4-154 and Figure 4-155. The two samples exhibit thick multi-layered oxide scales with external iron oxides (Fe_3O_4) and internal chromium-rich oxides ($(Fe,Cr,Ni)_3O_4$ + Cr_2O_3). Cracks and cavities can be observed at the interface between the inner and outer oxide scales.

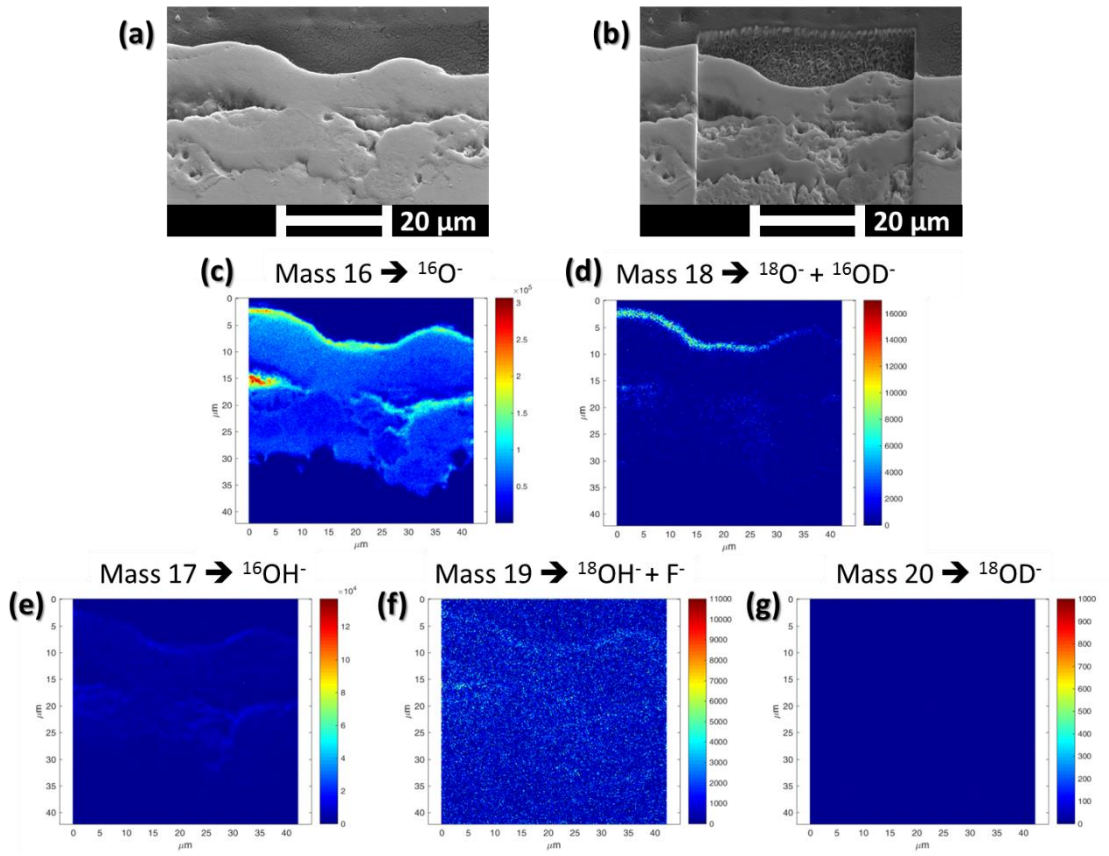

Figure 4-154: FIB-SIMS analysis for TP347HFG exposed at atmospheric pressure at 650°C for 1500 hours. (a) cross-section image of the studied area before FIB-SIMS analysis, (b) cross-section image of the studied area after FIB-SIMS analysis, (c) FIB-SIMS mapping for atomic mass 16, (d) FIB-SIMS mapping for atomic mass 18, (e) FIB-SIMS mapping for atomic mass 17, (f) FIB-SIMS mapping for atomic mass 19, (g) FIB-SIMS mapping for atomic mass 20.

Figure 4-154 shows the analysis performed on an area where a multi-layered oxide was formed. High levels of oxygen are observed over the entire oxide layer and enhanced levels of oxygen are present at the interface oxide / resin and also in between the inner and outer oxide layer where some cavities are present. For the atomic mass 18, small amounts of the related species have been detected inside the oxide layers, however around the cavities and at the oxide / resin interface, the species' concentration is higher due to the enhanced FIB milling at this location. Hydroxides (atomic mass 17) are also detected in the oxide layer, however, no hydroxide composed of deuterium and the oxygen isotope was

detected (atomic mass 20). Species with the atomic mass 19 have been detected all over the studied area, even where the resin is the only matter present. This observation is due to the presence of F^- which possess the same atomic mass as $^{18}OH^-$ and, due to its high electronegativity, F^- presence, however small is always detected. Hence the results obtained concerning $^{18}OH^-$ have to be considered carefully.

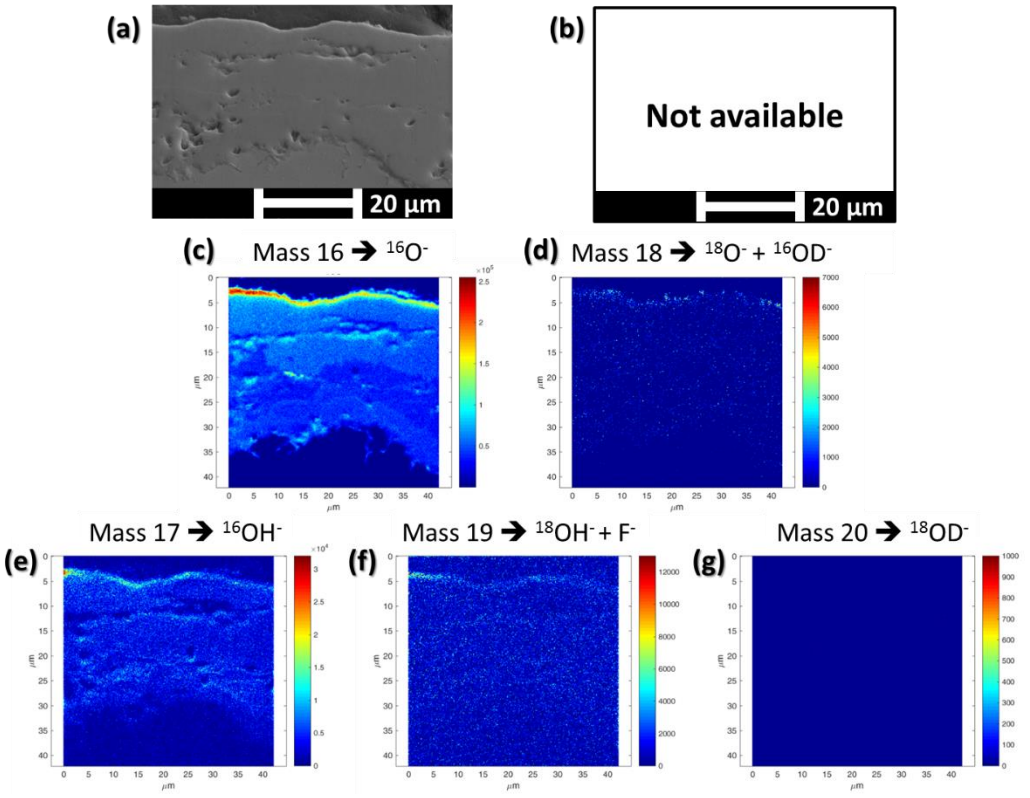

Figure 4-155: FIB-SIMS analysis for TP347HFG exposed at atmospheric pressure at 700°C for 1500 hours. (a) cross-section image of the studied area before FIB-SIMS analysis, (b) cross-section image of the studied area after FIB-SIMS analysis, (c) FIB-SIMS mapping for atomic mass 16, (d) FIB-SIMS mapping for atomic mass 18, (e) FIB-SIMS mapping for atomic mass 17, (f) FIB-SIMS mapping for atomic mass 19, (g) FIB-SIMS mapping for atomic mass 20.

In Figure 4-155, oxygen-16 and hydroxide (with a atomic mass of 17) are also present over the entire the oxide layer as in Figure 4-154. The oxygen-18 isotope is present only in reduced quantities in the oxide layer. Fluoride also creates noise for the atomic mass 19 components and no $^{18}OD^-$ was detected over the surface analysed. Similarly with Figure 4-154, enhanced concentrations of the different species are present at the oxide / resin interface and around the cavities in the multi-layered oxide.

In Figure 4-154 (b) it can be seen that a certain amount of the solid present in the analysed area has been removed from the sample's surface during the FIB-SIMS process. This matter removal was not homogeneous over the entire area analysed. Indeed, depending on the composition of the matter present, the milling rate of the focused ion beam is different. This difference in milling rate as a function of the oxide composition has to be kept in mind to mitigate what has been observed. It seems that the matter removal is quicker from the metal matrix and from iron oxides than from chromium-rich areas. This is one reason why the oxygen concentration is slightly higher in the iron oxide areas compared to areas with chromium-rich oxides. Whereas in reality, in terms of composition, chromium-rich oxides ($(Fe,Cr,Ni)_3O_4$) show the same atomic concentration of oxygen than iron oxides (Fe_3O_4).

At the interface of the oxide / resin, the ion beam mills through the surface of the softer resin material and starts analysing the volume originally located beneath the sample's surface. Thus, at this interface, the shape of the oxide layer interacts with the FIB-SIMS analysis. This is the reason why an enhanced concentration of all the species observed is detected at this location.

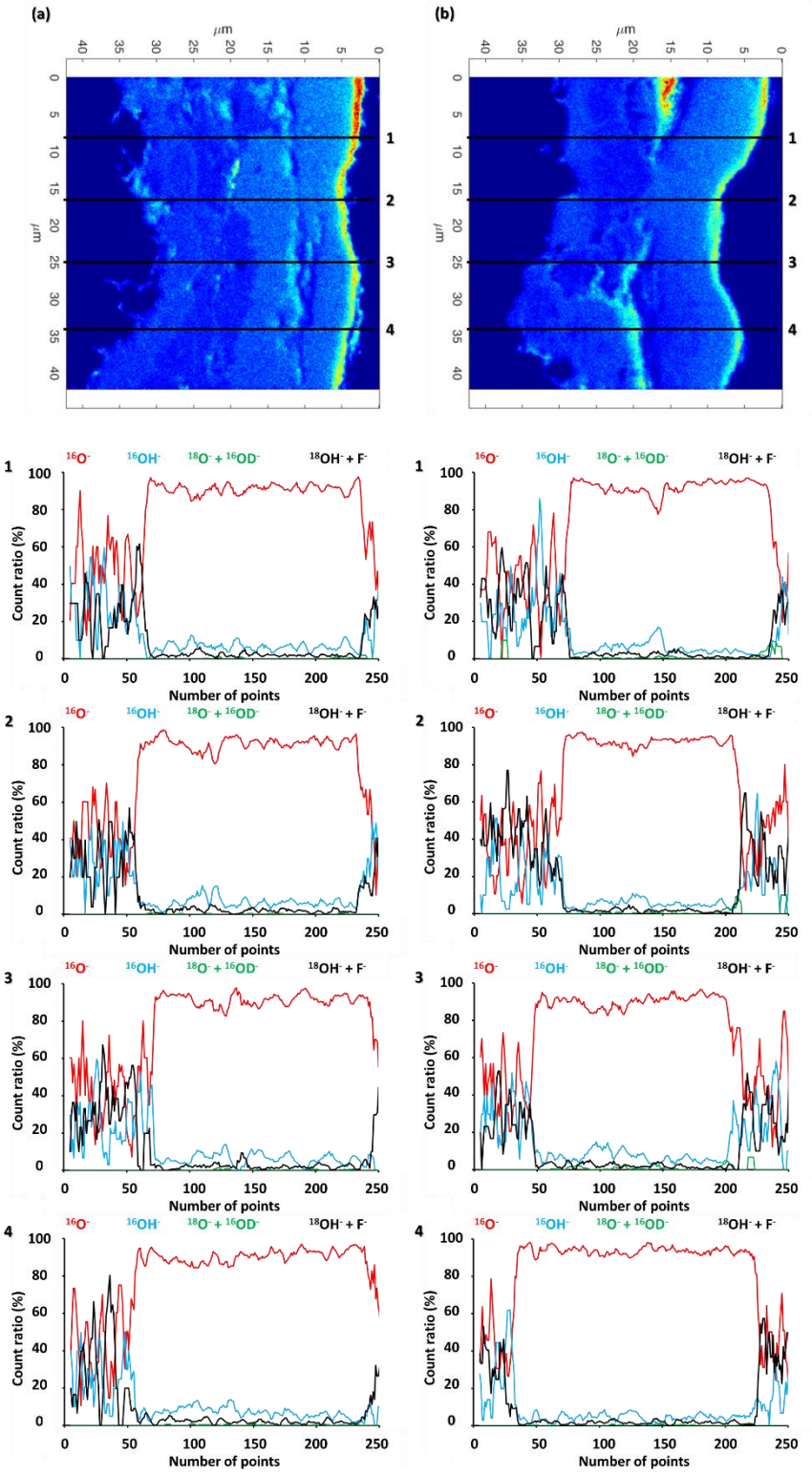

Figure 4-156: FIB-SIMS maps for atomic mass 16 associated with TP347HFG exposed at atmospheric pressure at (a) 700°C and (b) 650°C for 1500 hours. Scan lines taken for different locations (1-4) of the analysed area.

To get rid of any underlying surface shape effect and differences in milling velocities, ratios $\frac{SIMS\ count\ for\ the\ specie\ of\ interest}{total\ number\ of\ SIMS\ counts}$ for the different species have been calculated. Figure 4-156 presents multiple plots of the ratios calculated along various lines for both samples previously presented. The lines are built by taking the average of five consecutive points to smooth the datasets obtained. Despite averaging the datasets, the scan lines still exhibit local variations.

For all scan lines plotted in Figure 4-156, non-isotopic oxygen (^{16}O) is observed to be the main anion present in the oxide layers. Indeed it represents between 80 and 100% of the total anions present in the oxide layers. This was expected since the samples have been exposed for 1500 hours to regular steam before the isotope doped steam exposure. The other anions (atomic masses 17 and 19, respectively representing $^{16}OH^-$ and $^{18}OH^- + F^-$), are detected in the oxide scales and represent between 0 and 20% of the anions. However, only between 1 and 2% of the anions are oxygen isotope $^{18}O^{2-}$.

The small values obtained for $^{18}O^{2-}$, do not give any clear indication of where the oxide are formed during the isotope doped steam exposure. Therefore, from the tests done it is not possible to calculate the diffusion coefficient for oxygen and hydrogen diffusion into the oxide layers formed on the two samples analysed. Moreover, from Figure 4-154 (d), it would seem that the oxygen isotope is present in the inner-oxide layer which would mean the newly formed oxides are located at the interface between the metal and the inner oxide. However, this observation could not be backed up by the scan lines of Figure 4-156.

Since atomic mass 19 gather both $^{18}OH^-$ and F^- and that only a small percentage of oxygen-18 isotope was detected, it can be deduced that the line scan obtained for atomic mass 19 actually comes from the presence of fluoride and therefore are just noise.

The presence of hydroxide in the oxide layers is interesting because it supports the transport mechanism of iron as an hydroxide volatile specie towards the surface of the oxide layer [23–25]. Indeed, the presence of OH^- either comes

either from the presence of $Fe(OH)_2$ or $Ni(OH)_2$, or from the fact that hydroxide is only absorbed in the oxide layer.

4.5.5. Discussions about the study of diffusion

The understanding of oxygen and hydrogen diffusion through the oxide layers was a main objective of this project. The PhD thesis written by Lukaszewicz [79] relates the use of isotope doped steam to study the oxygen diffusion in oxide layers during a steam oxidation process at 700°C. However, in Lukaszewicz's study, the samples exposed to isotope doped steam were analysed using FIB-SIMS directly at the surface of the samples exposed by milling a crater through the oxide layers with an ion beam (Figure 4-157 (a)). During the milling process the mass of the secondary ions released were measured making it possible to plot a curve showing the concentration of the species of interest through the depth of the oxide layers (Figure 4-157 (b)).

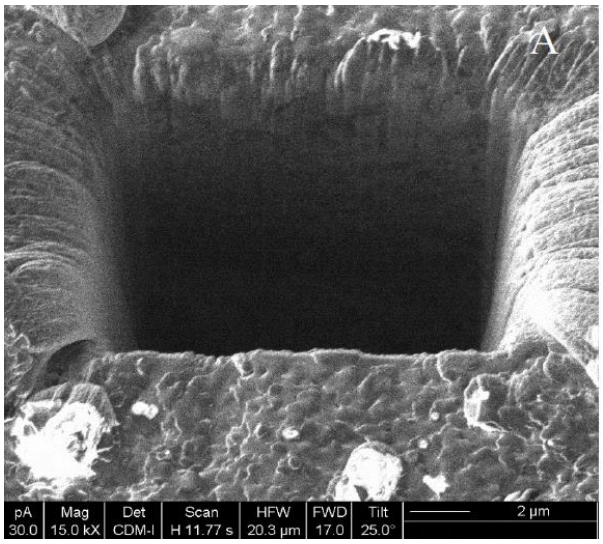

(a)

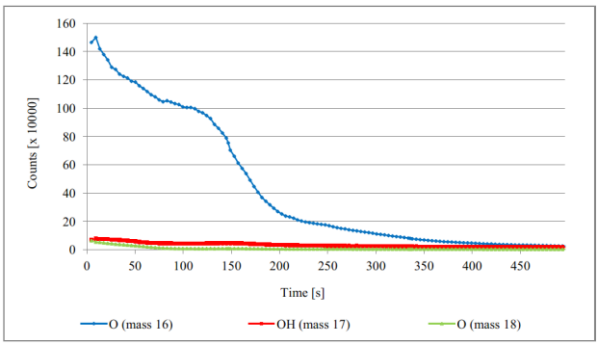

(b)

Figure 4-157: (a) Example of the crater resulting from focused ion beam milling obtained by Lukaszewicz [19] **and (b) example of the result associated with the crater milling.**

Even though the mapping of the different masses over a surface may allow a better visualisation of the location of the different species, the milling technique used by Lukaszewicz [19] obtained more useful curves for calculating the diffusion coefficient of the isotope species.

For this study, isotope exposure tests have been performed for 100 hours at the different temperatures studied during this project (650, 700, 750, 800°C) with only a volume of 250 ml of isotope doped water which was reused each time. A loss of isotope doped water was noticed during the isotope exposure, which interfered with the experiments by possibly changing the exposure parameters in terms of gas composition.

However, even though using isotope doped steam has not allowed the determination of the oxygen and hydrogen diffusion coefficients in the oxide layers, it has nevertheless showed that a non negligible amount of the anions located in the oxide layers are hydrogen and/or hydroxides (between 0 and 20%). Therefore, hydrogen was observed to have penetrated the oxide layers in large quantity.

5. General discussion

5.1. Introduction

The different steam exposure tests performed during this project have increased the understanding of long term high temperature steam oxidation. As presented in the preceding Sections, the effects of materials composition, temperature, exposure time, surface finish, and pressure have been investigated. Results have been obtained in terms of mass change, oxide morphology, oxide composition and phase, as well as oxide scale dimensions allowing the increasing understanding of steam oxidation process.

The exposures were performed in pure steam furnaces at 650, 700, 750 and 800°C and either at atmospheric or 36 bars. The total exposure times, varied between 500 and 10,000 hours, separated in 250 hours steam exposure cycles. The lack of long term laboratory exposure tests has previously been pointed out by the scientific community [23,34]. The 10,000 hours tests performed in this project have addressed this and the resultant data were of interest to understand the long term effects of the steam oxidation processes.

5.2. Materials and surface finishes

The different materials tested have proven to be very different in regard to steam oxidation. The austenitic steel TP347HFG, containing 18.4%$_w$ Cr and 11.5%$_w$ Ni, showed a much more detrimental reaction to high temperature steam than Sanicro 25, which is an austenitic steel containing 22.5%$_w$ Cr and 25%$_w$ Ni. The other materials studied were nickel-based Alloy 617, Alloy 263 and Alloy 740, which all possess much higher oxidation resistances. Their high oxidation

resistance, is an additional reason why tests have been performed for up to 10,000 hours.

As-received surfaces of TP347HFG formed multi-layered oxides and this complex oxide scale experienced spallation. This oxide layer consisted of iron oxides on top of chromium-rich oxides, and exfoliation was mainly observed for the outer iron oxide layer. Spallation was such that after about 1500 hours at the different temperature tested, the samples exposed showed a loss of mass. Despite this loss of mass, oxide layers were still present on the surfaces of the exposed samples when examined by SEM/EDX and XRD. When the multi-layered oxide was examined closely, it was observed that inner part of the oxide followed a pattern similar to that observed by Jianmin et al. [28,52]. This was that the internal propagation of the inner chromium-rich oxide started with the formation of an internal oxidation zone in the bulk of a metal's grain which grew until reaching the grain boundary where the oxidation front stopped. Then, potentially due to enhanced oxygen and chromium diffusion along the grain boundaries, chromia formed at the grain boundaries. Finally, a chromium-rich oxide $(FeCrNi)_3O_4$ replaced the internal oxidation zone. The chromia layer formed along the grain boundary, protected the material against further oxidation until the oxygen diffuses through it and start forming a new internal oxidation zone in the next grain's bulk.

Different surface finishes have been applied on the surfaces of TP347HFG samples to investigate its effect on the oxidation resistance of the material. In addition to its original as-received surface, TP347HFG was exposed with P1200 ground, P2500 ground, machined and shot-peened (SANYO and PISCO) surfaces. Residual stress measurements for the different surface finishes applied on TP347HFG allowed their classification in two different groups:

- Surface finishes applying low compressive stresses on the surface, as those measured on as-received, P1200 ground, and P2500 ground surfaces.

- Surface finishes applying high compressive stresses on the surface, as those measured on machined, and SANYO and PISCO shot-peened surfaces.

It was observed that using surface finishes with low compressive stresses increased the oxidation resistance of TP347HFG during the early stages of the oxidation process by helping with the early formation of a protective chromia layer at the surface of the material (Section 4.2.1.1). However, after the appearance of the multi-layered oxide scale, this cold working did not play a further role in the steam oxidation process.

For machined and the different shot-peened surfaces, even after 10,000 hours of steam exposure test at 800°C, only a thin chromium-rich layer was observed on the surfaces of TP347HFG. This is a very interesting result which proves that by only preparing the surface of the material, it is possible to significantly increase its oxidation resistance. As a results, in terms of the thickness of the oxide layers developed, these highly resistant surfaces react similarly to the oxidation behaviour of the Sanicro 25 and the nickel-based alloys studied. However, it has to be kept in mind that the temperature of interest for TP347HFG is below 650°C due to its creep resistance [23,34], as shown in Figure 5-1.

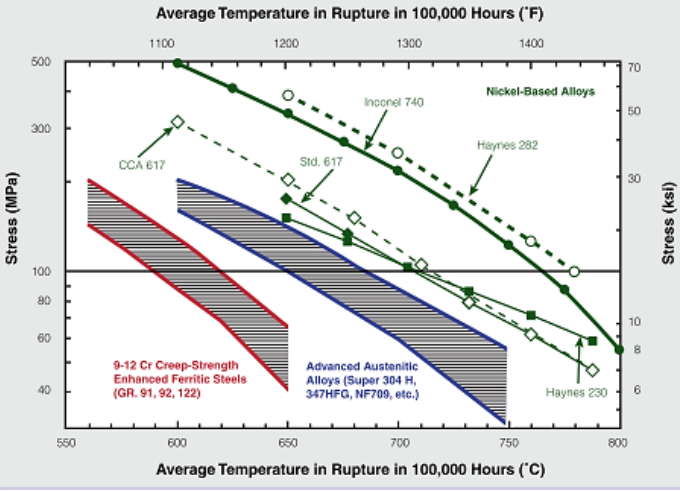

Figure 5-1: Representation of the temperature limitations for 100,000 hour-creep rupture as a function of the level of applied stress for different materials (100 MPa is a typical stress level of interest for superheater materials) [34]**.**

The austenitic steel Sanicro 25 has shown low steam oxidation rates due to its high chromium and nickel content. Therefore, protective chromia layers were formed on the surfaces of the material (Section 4.2.1.2). In terms of both mass change and oxide thickness measurements, the values obtained are of the same order of magnitude as the nickel-based alloys studied. However, even if the oxidation resistance of the material is very high, it may not be used for very high pressure tubes due to the drop off in creep properties with increasing temperature [23,34]., as pointed out in Figure 5-2. The study of as-received, P1200 and P2500 ground surfaces of Sanicro 25 showed that no clear effect of the surfaces finishes applied has been observed during the steam oxidation exposures (Sections 4.2.1.2, 4.3.1.1, and 4.3.4.1). The different surface finishes all showed the formation of a thin chromia layers which were still protecting the material even after exposure to steam at 800°C for 10,000 hours. The 22.5%$_w$ chromium content for this material is sufficient for the formation of protective chromia layers without the need for any enhancement of chromium diffusion from cold working.

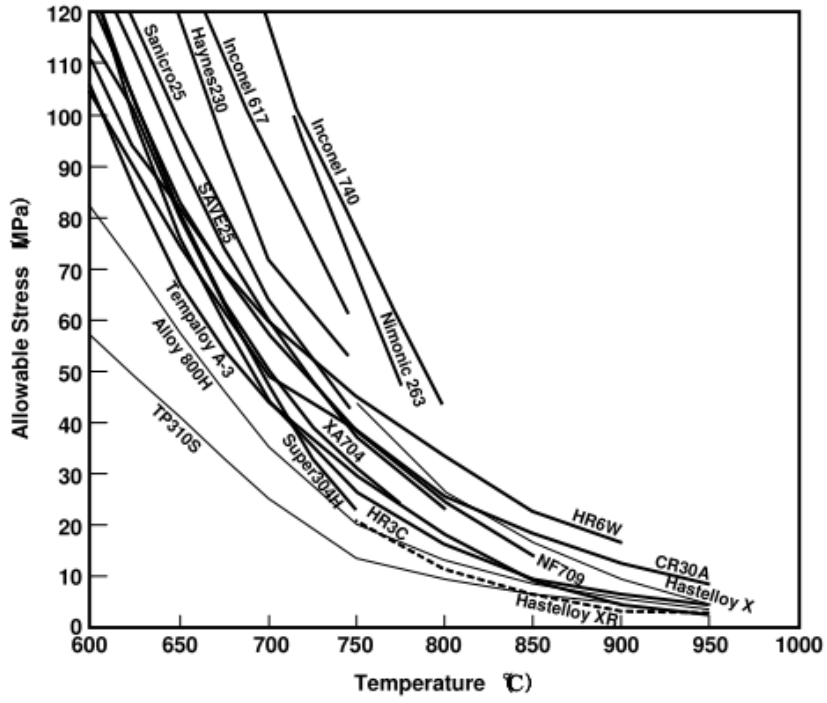

Figure 5-2: Maximum allowable stresses for superheater alloys for 100,000 hour creep rupture [98]**.**

The different nickel-based alloys exposed to high temperature steam have exhibited very high oxidation resistance. In concertation with their good creep properties at high temperature (Figure 5-1 and Figure 5-2), this make them the most interesting materials for use in the highest pressure and temperature parts of the superheaters. The P1200 ground surfaces of Alloy 617, Alloy 263 and Alloy 740 all formed thin chromia layers. In terms of oxide thickness, the oxidation rates calculated for Alloy 263 have revealed to be twice the values for Alloys 617 and Alloy 740. P2500 ground surfaces were also studied for Alloy 617, but no differences were fund compared with the P1200 ground surface of the same material in terms of its oxidation behaviour.

5.3. Steam oxidation kinetics and modelling

In terms of mass change kinetics calculations, Arrhenius plots have been used to determine the parabolic rates for the different surfaces of the studied materials. It was observed that the parabolic rates calculated were dependant on the steam exposure time. This was also observed by Montgomery et al. [89] and others [91].They explained that this could be due to the parabolic rate calculations using a parabolic constant set to null as explained in Section 4.3.3. Arrhenius plots have allowed the calculation of activation energies and standard rate constants which have later been used in equation modelling the mass change for the different surfaces of the various materials studied. The mass change models developed (Section 4.3.2) take into consideration spallation with the addition of the linear term describing mass loss. The models allow the prediction of mass change for the different samples.

Oxide thickness distributions were measured for samples and, for the each sample, the thickness value at 90% of the cumulative normal distribution was used for oxide thickness kinetics analysis and modelling. Arrhenius plots representing the parabolic rates for oxide thickness growth were used to calculate

the oxide growth kinetic parameters (activation energy and the standard rate constant). Thus, modelling of oxide growth for the different materials' surfaces was possible. The models obtained (Section 4.3.5) allowed good predictions of the experimental data for the highly resistant materials (Sanicro 25, Alloy 617, Alloy 263 and Alloy 740). However for TP347HFG, the spallation process affecting the steam oxidation of the material caused very variable oxide thickness data as a function of the oxidation time. Thus, the modelling of the oxide growth for this particular material proved to be difficult and less accurate ($0.5 < R^2 < 0.7$) than for the other materials ($0.9 < R^2$).

Unlike the mass change data, which is acquired every 250 hours for each sample, obtaining the oxide thickness data required destructive analysis of one sample for every data point; consequently many samples are needed to gather data for a range of exposure temperatures and times. Moreover, repeatability measurements are difficult to obtain. Therefore, for the analyse of oxide thickness, the number of data point to work with is significantly lower and less regular than for the mass change analysis, which do not allow spallation to be included in the oxide thickness prediction model. A link between XRD and oxide thickness has been observed in Section 4.2.2 and should be more developed to enable oxide growth monitoring for a single sample without the need to perform cross-sections.

6. Conclusions

The study of steam oxidation of a range of candidate superheater and reheater materials presented in this report was performed by exposing austenitic steels and nickel-based alloys to pure steam between 650 and 800°C and for up to 10,000 hours. Pure steam was used to exclude potential issues resulting from the use of gas carriers such as argon. These laboratory exposure tests lead to the acquisition of data from higher temperatures and after longer exposure times than what was previously used for the study of steam oxidation. The new data obtained increased the understanding of the high temperature steam oxidation process.

First, the effect of the different surface finishes studied has been visualized using SEM/EDX and XRD. Then, the nature and the morphology of the oxides formed on surfaces with different surface finishes have been characterized. Mass change and oxide thickness data have allowed the calculation of kinetic parameters associated with steam oxidation. The modelling of the mass change and oxide thickness has also been developed.

Moreover, the effect of an increase of pressure on the steam oxidation rate for various materials has been evaluated from laboratory exposure tests and in service exposed materials.

Finally, tests with isotope doped steam have also been performed to oxygen and hydrogen permeation in the oxide scales.

6.1. Austenitic steel TP347HFG

The steam oxidation process is dependant of the steam temperature and exposure time. For as-received, P1200 and P2500 ground surfaces of TP347HFG it has been observed that:

- At the different temperatures tested, initially mass gains were observed resulting from oxide formation. However, these were followed by steady mass losses due to the spallation process.
- The time when oxide spallation started occurring decreases with increasing temperature. In terms of mass change data.
- During the early stage of the steam oxidation process, a thin and protective chromia layer has been observed at the surface of TP347HFG. The protectiveness of this chromia layer was superior on P1200 ground surfaces of the material compared to P2500 ground and as-received surfaces.
- The failure of the chromia layer is characterized by the appearance of nodules piercing through this protective layer. These nodules are composed of outer iron oxides and inner chromium-rich oxides.
- The nodule size did not depend on the steam temperature but rather on the oxidation time.
- The spread of nodules with increasing oxidation time eventually leads to the formation of multi-layered oxide scales on the surface of the material. These complex scales consist of inner chromium-rich layer and outer iron-oxide (magnetite) layer. The inner oxide, growing towards the bulk of the material, is composed of $(FeCrNi)_3O_4$ at the centre of the oxidized metal's grains surrounded by chromia layers formed alongside the original material's grain boundaries.
- Oxide thickness data was gathered for all the samples exposed, including additional surfaces such as machined and shot-peened surfaces.

- For as-received, P1200 and P2500 ground surfaces, large variations of the oxide thickness data has been noticed due to the partial spallation of the multi-layered oxides. It has been observed that the iron-oxide layer was affected by exfoliation due to the weakening of the interface between the inner and outer parts of the multi-layered oxide scales.
- For machined and shot-peened surfaces for TP347HFG, only thin chromia oxide layers have been identified and measured.
- For TP347HFG, surface finishes applying high compressive surface stresses (>400MPa) allow the drastic improvement of the oxidation resistance of the material, resulting in 6 times thinner oxide scales than for surfaces with compressive stresses inferior to 300MPa.

- Kinetic parameters for mass change and oxide thickness related to the different surfaces of TP347HFG have been determined using Arrhenius plots. These parameters have been used in simple models describing the evolution of mass change and oxide thickness.
  - Due to the larger number of mass change data (every 250 hours), the equations predicting mass change evolution include the spallation effect and allow a good prediction of the mass change for as-received, P1200 and P2500 ground surfaces for TP347HFG.
  - Oxide thickness equations describing oxide growth for the different surface finishes on TP347HFG have shown large differences with the experimental data. The lack of data points is one of the reason for the difficulty to develop a precise model taking into account exfoliation.

6.2. Austenitic steel Sanicro 25

As-received, P1200 and P2500 ground surfaces of Sanicro 25 have been exposed to high temperature steam oxidation. Deeper knowledge and understanding of the high temperature steam oxidation process have been obtained for this material:

- Mass change for the different samples increase with increasing steam temperature and exposure time. The low mass change values obtained are a consequence of the high oxidation resistance of the material.
- Thin chromia layers are mainly formed on the different surface finishes of the material. A few nodules are visible on the samples exposed at the highest temperatures and for the longest exposure times.
- No specific effect of surface finish was observed due to high chromium content of the material.
- With only 4%$_w$ more chromium that TP347HFG, Sanicro 25 only developed chromia layers which were nearly ten times thinner oxide scales than TP347HFG.
- Mass change and oxide thickness modelling equations have been developed and give satisfaction regarding the prediction of the experimental data.

6.3. Nickel-based Alloys

P1200 ground samples of Alloy 263, Alloy 617 and Alloy 740, as well as P2500 ground Alloy 617, exposed to high temperature steam have increased the understanding of the steam oxidation process for these materials. The new knowledge were:

- The three nickel-based alloys with P1200 ground surfaces showed very high steam oxidation resistance over the range of temperatures and

exposure times used during this project. However, Alloy 263 shows two times higher oxidation rates in terms of oxide thickness compared with Alloy 617 and Alloy 740.

- Experimental values obtained for mass change and oxide thickness increase with increasing steam temperature and exposure time.
- Thin and protective chromia layers form at the surface of the three materials. Internal oxidation and precipitate formation have also been observed.
- For Alloy 617, no specific effect of surface finish has been assessed due to the high chromium content of the material.
- The mass change and oxide growth models developed give satisfaction regarding their predicting capabilities ($0.85 < R^2$ for the various models).

6.4. Effect of surfaces finish

Different surface finishes have been used for the five materials studied.

- Surface finishes that result in low compressive stresses in the surfaces of the materials, such as P1200 and P2500 ground surface finishes, have been used.
    - It appeared that for the austenitic steel TP347HFG, which contains lower chromium and nickel contents than the other alloys in this study, P1200 and P2500 ground surfaces allowed the early formation of a better protective chromia layer than the as-received surfaces. It is believed that this is a result of enhancing the chromium diffusion towards the surface of the material. However, when the chromia layer breaks down, no further effect of the surface finish was observed.
    - For the more highly oxidation resistant materials (Sanicro 25, Alloy 263, Alloy 617 and Alloy 740), surface finishes were not found to

have affected the steam oxidation process. These materials possessed higher chromium contents that allowed the rapid formation and maintenance of protective chromia layers.

- Machining and shot-peening were applied to TP347HFGand caused high compressive stresses in the surfaces which is associated with an increase number of dislocations. Thus, chromium diffusion is enhanced which enables the formation of a protective chromia layer that has been observed to be protective even after 10,000 hours at 800°C. As a result, machining and shot-peening the surface of TP347HFG allowed this lower chromium and nickel containing steel to resist to high temperature steam oxidation as well as Sanicro 25 and nickel-based alloys for the duration of these exposures.

6.5. Effect of pressure

Laboratory experiments have been performed at 1 atmosphere and 36 bars, for 1000 hours with a steam temperature of 650°C, to observed the specific effect of pressure over the steam oxidation process. Ferritic steel T 92 and austenitic steels TP347HFG and Sanicro 25 have been used for these laboratory experiments. The conclusions from this comparison are:

- For T 92 and TP347HFG, an increase of pressure has been observed to significantly increase the steam oxidation of the materials. In terms of oxide thickness, the factors associated with the increase of the parabolic oxidation rate have been calculated to be 2.22 and 1.80 respectively, and are consistent with the thermodynamics of steam oxidation.
- For Sanicro 25, increasing the pressure increases the effects of the steam oxidation process. However, it has been difficult to quantify the increase in oxidation rate caused by the increase of pressure because the two samples compared did not show similar oxidation mechanisms.

Service exposed materials (T91 and HR3C) have also been observed after 123,000 hours of steam exposure at 580°C and either 40 or 180 bars. However, in contrast to the results obtained with the laboratory experiments, the increase of pressure from 40 to 180 bars was accompanied with a lower oxidation rate for the oxidized materials.

6.6. Study of oxygen and hydrogen diffusion in oxide scales

Isotope steam exposure tests, with oxygen (^{18}O) and hydrogen ($^{2}H = D$) isotopes used for part of the exposures, have been performed to increase the understanding of the oxygen and hydrogen diffusion in the oxide scales. These tests have been performed at different temperatures to observed the temperature effect on diffusion and permeation processes.

It appears that the results obtained did not help in regards to the determination of the diffusion coefficient for the anionic species of interest. However, it was observed that hydrogen and/or hydroxides were distributed throughout the oxide layers and composed up to 20% of the anionic species present in the oxide scales.

7. Recommendations for future work

Suggested actions to improve and complete the results presented in this thesis are:

- Place every sample in individual crucibles and measure the mass of spalled oxide at each cycle. This method would help create a more accurate spallation model in terms of mass change. In parallel the total mass gain of the crucible containing the sample should be measured to calculate the total mass gain of the samples, which takes into account the mass of spalled oxide.
- Perform long term tests at intermediate temperatures that have not been tested to validate the models developed and to complete the set of data.
- In response to a remark and observation that have been made in Section 4.2.4 (saying that increased exfoliation seems to occur on surfaces parallel to the steam flow), it would be interesting to observed the surfaces that were parallel to the steam flow during the exposure tests. Indeed, since the interest were mainly on the concave and convex surfaces, the other surfaces have not been analysed. Another possibility would be to orientate the concave and convex surfaces of the samples parallel to the steam flow.
- Different solutions for fitting the samples into the steam furnaces should be tried. Indeed, the surface on which the samples are in contact with the crucible seems to show less oxidation that the other surfaces. However, since this study focussed on the observation of concave and convex surfaces, this has not been addressed. Maybe by suspending the samples in the furnaces, more homogeneous oxidation will be observed.
- Develop a model linking the XRD spectra to the oxide thickness. This was partially investigated in this thesis. However, if a more robust correlation can be developed, there is no doubt this would be helpful for following the

oxide thickness evolution as a function of exposure time for a single sample.

- During the steam exposure tests the furnaces have been loaded with more samples than the one which have been presented in this thesis. However, due to the limited amount of time for the completion of the study, not all materials have been presented. Super 304 and HR3C samples have been oxidized and already partially analysed but it would be useful the analyses of these materials are continued.
- Longer exposure times could be done for nickel-based alloys and austenitic steels with the higher chromium and nickel content.
- The oxide growth models developed in this thesis should be implemented into a heat transfer model describing the temperature distribution in the heat exchanger materials taking into account oxide growth, and exfoliation at the steam side of the tube.
- Study the heat flux effect on the steam oxidation process. Some materials exposed in a steam rig in Cranfield University were available but there was not enough time to perform deep analyses of the samples obtained. Moreover, there was a serious lack of experimental data (temperature, exposure time) regarding the tests performed.

REFERENCES

1. Presidency of European Council. Conclusion of the Brussels European Council 8/9 March 2007 Presidency conclusions. 2007.

2. Department of Energy and Climate Change. UK Energy in brief 2015. 2015.

3. Department for Business Energy & Industrial Strategy. UK Energy in brief 2018. 2018.

4. International Energy Agency. Energy and Climate Change. World Energy Outlook Special Report. 2015.

5. European Commission. LIFE and Climate change mitigation. 2015. Available at: DOI:10.2779/59738

6. Oakey J. Power plant life management and performance improvement. Oakey JE (ed.) Woodhead; 2011.

7. Rogalev N., Golodnitskiy A. A Survey of State-of-the-Art Development of Coal-Fired Steam Turbine Power Plant Based on Advanced Ultrasupercritical Steam Technology. Contemporary Engineering Sciences. 2014; 7(34): 1807–1825. Available at: http://dx.doi.org/10.12988/ces.2014.410191

8. Holcomb GR. High Pressure Steam Oxidation of Alloys for Advanced Ultra-Supercritical Conditions. Oxidation of Metals. 2014; 82: 271–295. Available at: DOI:10.1007/s11085-014-9491-6

9. Khanna A. Introduction to High Temperature Oxidation and Corrosion. ASM International; 2002.

10. Viswanathan R., Sarver J., Tanzosh JM. Boiler Materials for Ultra-Supercritical Coal Power Plants — Steamside Oxidation. Journal of Materials Engineering and Performance. 2006; 15(June): 255–274. Available at: DOI:10.1361/105994906X108756

11. Fry AT., Brown LJ., Banks JP. The Effect of Heat Flux on the Steam Oxidation Kinetics and Scale Morphology of Low Alloy Materials. 6th Internaltional Conference on Advances in Materials Technology for Fossil Power Plants. 2011. : 171–184.

12. Tuurna S., Olli SY., Auerkari P., Zabetta EC., Vänskä K. Influence of Temperature and Surface Treatment on Steamside Oxidation. 10th Liege Conference on Materials for Advanced Power Engineering. Liege; 2014.

13. Haruyama A., Kutsumi H., Kuroda S., Abe F. Effect of shot peening and pre-oxidation treatment in air on steam oxidation resistance of Mod . 9Cr-1Mo steel Effect of shot peening and pre-oxidation treatment in air on steam oxidation resistance of Mod . 9Cr-1Mo steel. Proccedings of the 4th International Conference on Advances in Materials Technology for Fossil Power Plants. 2005. : 412–419.

14. Elliott. Standard Handbook of Powerplant Engineering. McGraw-Hill Professional (ed.) 1997.

15. Simms NJ., Kilgallon PJ., Oakey JE. Degradation of heat exchanger materials under biomass co-firing conditions. Materials at High Temperatures. 2007; 24(4): 333–342.

16. Yeo WH., Fry AT., Purbolaksono J., Ramesh S., Inayat-Hussain JI., Liew HL., Hamdi M. Oxide scale growth and presumed exfoliation in a 700°C or higher steam condition: A simulation study for future operations of ultra-supercritical power plants. The Journal of Supercritical Fluids. Elsevier B.V.; 2014; 92: 215–222. Available at: DOI:10.1016/j.supflu.2014.06.002

17. Incropera FP., DeWitt DP., Bergman TL., Lavine AS. Fundamentals of Heat and Mass Transfer. Incropera FP (ed.) John Wiley & Sons; 2007. Available at: DOI:10.1016/j.applthermaleng.2011.03.022

18. Lienhard JH. Heat Transfer. Journal of Heat Transfer. 2010; 82(1): 198. Available at: DOI:10.1115/1.3246887

19. Lukaszewicz M. Steam oxidation of advanced high temperature resistant alloys for ultra-supercritical applications. PhD thesis Cranfield University. Cranfield University; 2012. Available at: DOI:10.1017/CBO9781107415324.004

20. Gleeson B. Oxidations of metals: Editorial. Oxidation of Metals. 2009; 71(1–2): 1–3.

21. Syed A. Fireside corrosion study of superheater materials in advanced power plants. Cranfield University; 2011.

22. Birks N., Meier GH., Pettit FS. Introduction to the High-Temperature Oxidation of Metals. second edi. Crambridge Univeristy Press (ed.) 2009.

23. Dooley RB. Program on Technology Innovation : Oxide Growth and Exfoliation on Alloys Exposed to Steam. EPRI final report. 2007; 1013666.

24. Wright IG., Pint BA. An Assessment of the High-Temperature Oxidation Behavior of Fe-Cr Steels in Water Vapor and Steam. NACE International. 2002. : 1–15.

25. Ehlers J., Young DJ., Smaardijk EJ., Tyagi a. K., Penkalla HJ., Singheiser L., Quadakkers WJ. Enhanced oxidation of the 9%Cr steel P91 in water vapour containing environments. Corrosion Science. 2006; 48(11): 3428–3454. Available at: DOI:10.1016/j.corsci.2006.02.002

26. Cambridge U of. The Ellingham diagram. Available at: https://www.doitpoms.ac.uk/tlplib/ellingham_diagrams/ellingham.php (Accessed: 26 June 2018)

27. Schutze M. Corrosion and Environmental Degradation. Wiley-VCH; 2000.

28. Jianmin J., Montgomery M., Larsen OH., Jensen SA. Investigation on steam oxidation behaviour of TP347HFG Part 1: Exposure at 256 bar. Materials and Corrosion. 2005; 56(7): 459–467. Available at: DOI:10.1002/maco.200403856

29. Bischoff J., Motta AT. Oxidation behavior of ferritic – martensitic and ODS steels in supercritical water. Journal of nuclear materials. Elsevier B.V.; 2012; 424(1–3): 261–276. Available at: DOI:10.1016/j.jnucmat.2012.03.009

30. Young DJ., Zurek J., Singheiser L., Quadakkers WJ. Temperature dependence of oxide scale formation on high-Cr ferritic steels in Ar-H2-H2O. Corrosion Science. Elsevier Ltd; 2011; 53(6): 2131–2141. Available at: DOI:10.1016/j.corsci.2011.02.031

31. Smyth DM. The Defect Chemistry of Metal Oxides. Oxford University Press; 2000.

32. Glicksman ME. Diffusion in Solids: field theory, solid-state principles, and applications. Wiley-Blackwell; 2000.

33. Wagner C. The formation of thin oxide films on metals. Corrosion Science. 1973; 13: 23–52.

34. Viswanathan R., Henry JF., Tanzosh J., Stanko G., Shingledecker J., Vitalis B., Purgert R. U . S . Program on Materials Technology for Ultra-Supercritical Coal Power Plants. 2005; 14(June): 281–292. Available at: DOI:10.1361/10599490524039

35. Fry A., Osgerby S., Wright M. Oxidation of Alloys in Steam Environments – a Review. NPL Report MATC (A). 2002; 90(September): 1–39.

36. Was GS., Ampornrat P., Gupta G., Teysseyre S., West EA., Allen TR., Sridharan K., Tan L., Chen Y., Ren X., Pister C. Corrosion and stress corrosion cracking in supercritical water. Journal of Nuclear Materials. 2007; 371(1–3): 176–201. Available at: DOI:10.1016/j.jnucmat.2007.05.017

37. Ennis PJ., Quadakkers WJ. Mechanisms of steam oxidation in high strength martensitic steels. International Journal of Pressure Vessels and Piping. 2007; 84: 75–81. Available at: DOI:10.1016/j.ijpvp.2006.09.007

38. Zhong X., Wu X., Han E-H. The characteristic of oxide scales on T91 tube after long-term service in an ultra-supercritical coal power plant. The Journal of Supercritical Fluids. Elsevier B.V.; 2012; 72: 68–77. Available at: DOI:10.1016/j.supflu.2012.08.015

39. Chen Y., Sridharan K., Allen T. Corrosion behavior of ferritic–martensitic steel T91 in supercritical water. Corrosion Science. 2006; 48(9): 2843–2854. Available at: DOI:10.1016/j.corsci.2005.08.021

40. Osgerby S., Fry T. Simulating Steam Oxidation of High Temperature Plant Under Laboratory Conditions : Practice and Interpretation of Data. Materials Research. 2004; 7(1): 141–145.

41. Ennis PJ., Quadakkers WJ. Implications of steam oxidation for the service life of high-strength martensitic steel components in high-temperature plant. International Journal of Pressure Vessels and Piping. 2007; 84: 82–87. Available at: DOI:10.1016/j.ijpvp.2006.09.008

42. Muhich CL., Aston VJ., Trottier RM., Weimer AW., Musgrave CB. First-Principles Analysis of Cation Diffusion in Mixed Metal Ferrite Spinels. Chemistry of materials. 2016; 28: 214–226. Available at: DOI:10.1021/acs.chemmater.5b03911

43. Zurek J., Wessel E., Niewolak L., Schmitz F., Kern TU., Singheiser L., Quadakkers WJ. Anomalous temperature dependence of oxidation kinetics during steam oxidation of ferritic steels in the temperature range 550-650°C. Corrosion Science. 2004; 46(9): 2301–2317. Available at: DOI:10.1016/j.corsci.2004.01.010

44. Grabke HJ., Strauss S., Pippel E., Woltersdorf J. Effects of Grain Size , Cold Working , and Surface Finish on the Metal-Dusting Resistance of Steels. Oxidation of Metals. 1998; 50(314): 241–254.

45. Trindade VB., Krupp U., Wagenhuber PEG., Christ HJ. Oxidation mechanisms of Cr-containing steels and Ni-base alloys at high-

temperatures - Part I: The different role of alloy grain boundaries. Materials and Corrosion. 2005; 56(11): 785–790. Available at: DOI:10.1002/maco.200503879

46. Mu N., Jung K., Yanar NM., Pettit FS., Holcomb GR., Howard BH., Meier GH. The effects of water vapor and hydrogen on the high-temperature oxidation of alloys. Oxidation of Metals. 2013; 79(1): 461–472. Available at: DOI:10.1007/s11085-012-9349-8

47. Abe H., Hong SM., Watanabe Y. Oxidation behavior of austenitic stainless steels as fuel cladding candidate materials for SCWR in superheated steam. Nuclear Engineering and Design. Elsevier B.V.; 2014; 280: 652–660. Available at: DOI:10.1016/j.nucengdes.2014.08.020

48. Liang Z., Zhao Q., Singh PM., Wang Y., Li Y., Wang Y. Field studies of steam oxidation behavior of austenitic heat-resistant steel 10Cr18Ni9Cu3NbN. Engineering Failure Analysis. Elsevier Ltd; 2015; 53: 132–137. Available at: DOI:10.1016/j.engfailanal.2015.02.019

49. Jonsson T., Karlsson S., Hooshyar H., Sattari M., Liske J., Svensson J., Johansson L. Oxidation After Breakdown of the Chromium-Rich Scale on Stainless Steels at High Temperature : Internal Oxidation. Oxidation of Metals. Springer US; 2016; 85(5): 509–536. Available at: DOI:10.1007/s11085-016-9610-7

50. Lo KH., Shek CH., Lai JKL. Recent developments in stainless steels. Materials science and engineering R. 2009; 65: 39–104. Available at: DOI:10.1016/j.mser.2009.03.001

51. Lyta., Ueda M., Kawamura K., Takeyama M., Maruyama T. Microstructure Development of Oxide Scale during Steam Oxidation of the Fe-20Cr-30Ni-2Nb (at%) Austenitic Steel at 1073 K. Materials Transactions. 2013; 54(12): 2276–2284.

52. Jianmin J., Montgomery M., Larsen OH., Jensen SA. Investigation on

steam oxidation behaviour of TP347HFG Part 2: Exposure at 91 bar. Materials and Corrosion. 2005; 56(7): 459–467. Available at: DOI:10.1002/maco.200403856

53. Zurek J., Yang S-M., Lin D-Y., Hüttel T., Singheiser L., Quadakkers WJ. Microstructural stability and oxidation behavior of Sanicro 25 during long-term steam exposure in the temperature range 600-750 °C. Materials and Corrosion. 2015; 66(4): 315–327. Available at: DOI:10.1002/maco.201407901

54. Whittle D., Wood G., Evans D., Scully D. Concentration profiles in the underlying alloy during the oxidation of iron-chromium alloys. Acta Metallurgica. 1967; 15(11): 1747–1755. Available at: DOI:10.1016/0001-6160(67)90066-1

55. Sabau AS., Wright IG., Shingledecker JP. Oxide Scale Exfoliation and Regrowth in TP347H Superheater Tubes. Materials and Corrosion. 2012; 63(10): 896–908. Available at: DOI:10.1002/maco.201206640

56. Essuman E., Meier GH., Zurek J., Hänsel M., Norby T., Singheiser L., Quadakkers WJ. Protective and non-protective scale formation of NiCr alloys in water vapour containing high- and low- pO2 gases. 2008; 50: 1753–1760. Available at: DOI:10.1016/j.corsci.2008.03.001

57. Gorman DM., Higginson RL., Du H., Mccolvin G., Fry AT., Thomson RC. Microstructural Analysis of IN617 and IN625 Oxidised in the Presence of Steam for use in Ultra-Supercritical. 2013; : 553–566. Available at: DOI:10.1007/s11085-012-9342-2

58. Unocic KA., Shingledecker JP., Tortorelli PF. Microstructural Changes in Inconel 740 After Long-Term Aging in the Presence and Absence of Stress. The Minerals, Metals & Materials Society. 2014; 66(12): 2535–2542. Available at: DOI:10.1007/s11837-014-1208-4

59. Chevalier S., Desserrey F., Larpin JP. Oxygen Transport during the High

Temperature Oxidation of Pure Nickel. Oxidation of Metals. 2005; 64(3–4): 219–234. Available at: DOI:10.1007/s11085-005-6560-x

60. Akhiani H., Nezakat M., Penttilä S., Szpunar J. The oxidation resistance of thermo-mechanically processed Incoloy 800HT in supercritical water. The Journal of Supercritical Fluids. Elsevier B.V.; 2015; 101: 150–160. Available at: DOI:10.1016/j.supflu.2015.03.019

61. Di Schino A., Kenny JM. Effects of the grain size on the corrosion behavior of refined AISI 304 austenitic stainless steels. Journal of materials science letters. 2002; 21: 1631–1634.

62. Ren X., Sridharan K., Allen TR. Effect of Shot Peening on the Oxidation of Ferritic-Martensitic Steels in Supercritical Water. Corrosion 2008. 2008; (08425): 1–12.

63. Zengwu Y., Min F., Xuegang W., Xingeng L. Effect of Shot Peening on the Oxidation Resistance of TP304H and HR3C Steels in Water Vapor. Oxidation of Metals. 2012; 77: 17–26. Available at: DOI:10.1007/s11085-011-9270-6

64. Tan L., Ren X., Sridharan K., Allen TR. Effect of shot-peening on the oxidation of alloy 800H exposed to supercritical water and cyclic oxidation. Corrosion Science. 2008; 50: 2040–2046. Available at: DOI:10.1016/j.corsci.2008.04.008

65. Xingeng L., Jiawen H. Effect of shot blasting on oxidation behavior of TP304H steel at 610-770°C in water vapor. Materials Letters. 2006; 60(3): 339–344. Available at: DOI:10.1016/j.matlet.2005.08.046

66. Tossey BM. Steam Oxidation Resistance of Shot Peened Austenitic Stainless Steel Superheater Tubes. 2011.

67. Berger M-C., Gregory J. Residual stress relaxation in shot peened Timetal 21s. Materials Science and Engineering: A. 1999; 263: 200–204. Available at: DOI:10.1016/S0921-5093(98)01165-4

68. Belyakov a., Miura H., Sakai T. Dynamic recrystallization under warm deformation of a 304 type austenitic stainless steel. Materials Science and Engineering: A. 1998; 255(1–2): 139–147. Available at: DOI:10.1016/S0921-5093(98)00784-9

69. Cruchley S., Taylor MP., Ding R., Evans HE., Child DJ., Hardy MC. Comparison of Chromia Growth Kinetics in a Ni-based Superalloy , with and without Shot-peening. Corrosion Science. Elsevier Ltd.; 2015; 100: 242–252. Available at: DOI:10.1016/j.corsci.2015.07.033

70. Cruchley S., Evans HE., Taylor MP., Hardy MC., Stekovic S. Chromia layer growth on a Ni-based superalloy : Sub-parabolic kinetics and the role of titanium. Corrosion Science. Elsevier Ltd; 2013; 75: 58–66. Available at: DOI:10.1016/j.corsci.2013.05.016

71. Wright IG., Sabau AS., Dooley RB. Development of strain in oxides grown in steam tubes. 7th International Symposium on High Temperature Corrosion and Protection of Materials. Les Embiez; 2008. : 387–395.

72. Holcomb GR. Hot Corrosion in a Temperature Gradient. Materials and Corrosion. 2000; 51(8): 564–569.

73. Zhang N., Zhu Z. Influence of Exposure Pressure on Oxidation Behavior of the Ferritic – Martensitic Steel in Steam and Supercritical Water. Oxidation of Metals. Springer US; 2016; 86(1–2): 113–124. Available at: DOI:10.1007/s11085-016-9624-1

74. Evans HE., Donaldson AT., Gilmour TC. Mechanisms of Breakaway Oxidation and Application to a Chromia-Forming Steel. Oxidation of Metals. 1999; 52(5–6): 379–402.

75. Halvarsson M., Tang JE., Asteman H. Microstructural investigation of the breakdown of the protective oxide scale on a 304 steel in the presence of oxygen and water vapour at 600°C. Corrosion Science. 2006; 48: 2014–2035. Available at: DOI:10.1016/j.corsci.2005.08.012

76. Schutze M., Tortorelli PF., Wright IG. Development of a comprehensive oxide scale failure diagram. Oxidation of Metals. 2010; 73(3–4): 389–418. Available at: DOI:10.1007/s11085-009-9185-7

77. Shingledecker JP., Pint BA., Sabau AS., Fry AT., Wright IG. Managing Steam-Side Oxidation and Exfoliation in USC Boiler Tubes. Advanced materials and processesdvanced materials and processes. 2013; (January): 23–25.

78. Orvis KH., Grissino-Mayer HD. Technical note: standardizing the reporting of abrasive papers used to surface tree-ring samples. Tree-ring research. 2002; 58: 47–50.

79. Lukaszewicz M., Simms NJ., Dudziak T., Nicholls JR. Effect of Steam Flow Rate and Sample Orientation on Steam Oxidation of Ferritic and Austenitic Steels. Oxidation of Metals. 2013; 79: 473–483. Available at: DOI:10.1007/s11085-013-9358-2

80. Fry AT., Seraffon M., Banks J., Laing D. Comparison of once through and closed loop apparatus for steam oxidation measurements at ambient and elevated pressure. Materials for Advanced Power Engineering 2014. 2014. : 688–697.

81. Betova I., Bojinov M., Kinnunen P., Penttil S. Surface film electrochemistry of austenitic stainless steel and its main constituents in supercritical water. 2007; 43: 333–340. Available at: DOI:10.1016/j.supflu.2007.06.005

82. Z W Liu., M L Zong., C M Tang. Large-scale oxide nanostructures grown by thermal oxidation. IOP Conf. Series: Materials Science and Engineering. 2014; 60. Available at: DOI:10.1088/1757-899X/60/1/012022

83. Kowaka M., Tsuge H. Introduction to Life Prediction of Industrial Plant Materials: Application of the Extreme Value Statistical Method for Corrosion Analysis. Kowaka M (ed.) Allerton Pr; 1994.

84. Pujilaksono B., Jonsson T., Halvarsson M., Svensson JE., Johansson LG.

Oxidation of iron at 400-600°C in dry and wet O2. Corrosion Science. Elsevier Ltd; 2010; 52(5): 1560–1569. Available at: DOI:10.1016/j.corsci.2010.01.002

85. Bertrand N., Desgranges C., Poquillon D., Lafont MC., Monceau D. Iron oxidation at low temperature (260-500°c) in air and the effect of water vapor. Oxidation of Metals. 2010; 73(1–2): 139–162. Available at: DOI:10.1007/s11085-009-9171-0

86. Zhang N qiang., Xu H., Li B rang., Bai Y., Liu D yu. Influence of the dissolved oxygen content on corrosion of the ferritic-martensitic steel P92 in supercritical water. Corrosion Science. Elsevier Ltd; 2012; 56: 123–128. Available at: DOI:10.1016/j.corsci.2011.11.013

87. Zhang N qiang., Zhu Z liang., Xu H., Mao X ping., Li J. Oxidation of ferritic and ferritic-martensitic steels in flowing and static supercritical water. Corrosion Science. 2016; 103: 124–131. Available at: DOI:10.1016/j.corsci.2015.10.017

88. Garza-Montes-De-Oca NF., Colás R., Rainforth WM. High temperature oxidation of a work roll grade high speed steel. Oxidation of Metals. 2011; 76(5–6): 451–468. Available at: DOI:10.1007/s11085-011-9266-2

89. Mongomery M., Karlsson A. Survey of Oxidation in Steamside Conditions. VGB Kraftwerkstechnik. 1995; 75: 235–240.

90. Yi Y., Watanabe Y., Kondo T., Kimura H., Sato M. Oxidation Rate of Advanced Heat-Resistant Steels for Ultra-Supercritical Boilers in Pressurized Superheated Steam. Journal of Pressure Vessel Technology. 2001; 123: 391–397. Available at: DOI:10.1115/1.1373656

91. Monceau D., Pieraggi B. Determination of Parabolic Rate Constants from a Local Analysis of Mass-Gain Curves. Oxidation of M. 1998; 50(516): 477–493.

92. Taneichi K., Narushima T., Iguchi Y., Ouchi C. Oxidation or Nitridation

Behavior of Pure Chromium and Chromium Alloys Containing 10 mass%Ni or Fe in Atmospheric Heating. Materials Transactions. 2006; 47(10): 2540–2546. Available at: DOI:10.2320/matertrans.47.2540

93. Leire del C., Perez-saez R., Tello MJ. Iron oxidation kinetics study by using infrared spectral emissivity measurements below 570°C. Corrosion Science. 2008; 50: 194–199. Available at: DOI:10.1016/j.corsci.2007.05.029

94. Holcomb GR. High pressure steam oxidation of Ni-base superalloys in advanced ultra-supercritical steam boilers and turbines. 8th International Symposium on Superalloy 718 and Derivatives. 2014. : NETL-PUB-830.

95. Quadakkers WJ., Ż J., Hänsel M. Effect of Water Vapor on High-temperature Oxidation of FeCr Alloys. JOM: the journal of the Minerals, Metals & Materials Society. 2009; 61(7): 44–50. Available at: DOI:10.1007/s11837-009-0102-y

96. Oya Y., Kobayashi M., Osuo J., Suzuki M., Hamada A. Effect of surface oxide layer on deuterium permeation behaviors through a type 316 stainless steel. Fusion Engineering and Design. Elsevier B.V.; 2012; 87(5–6): 580–583. Available at: DOI:10.1016/j.fusengdes.2012.01.025

97. Perujo A., Reimann J., Feuerstein H., Mancinelli B. The oxidation kinetics of Incoloy 800 and its deuterium permeation behavior. Journal of Nuclear Materials. 2000; 283–287: 1292–1296.

98. Matsuyama F. Adavanced power plant developments and material experiences in Japan. Materials for Advanced Power Engineering 2006. 2006. : 175–187.

APPENDICES

Appendix A Flex-E-Plant project

Flex-E-Plant (Flexible and Efficient Power Plant), is an EPSRC research program created in 2013, to investigate the key aspects of the new challenges met by the power generation industry:

- Plant efficiency
- Plant flexibility
- Fuel flexibility
- Sustainability

These different issues were gathered in three different work packages, each dealing with a specific scientific aspect of power plants:

1. Plant operations and design
2. Combustion fuels and operability
3. Structural integrity and advanced materials

The consortium gathers six leading UK Universities and several Industrial partners including power generation operators, original equipment manufacturers, government laboratories and companies in the generation sector. The different members of the Flex-E-Plant consortium are listed in Table 7-1.

Table 7-1: List of the different participants in Flex-E-Plant.

Universities	Industrial partners
Loughborough University (project leader) Cardiff University Cranfield University Imperial College London University of Nottingham University of Warwick	Alstom Group EDF Energy Goodwin Plc Rolls-Royce Plc Siemens Doosan Power Systems Eggborough Power Ltd National Physical Laboratory RWE Generation Technology Strategy Board (Innovate UK) E.On Emerson Process Management R-MC Power Recovery Energy (SSE) TWI Ltd

Appendix B Sample preparation procedures

B.1 Cutting procedure to produce tube segment samples

Using a Struers Exotom saw, which uses an oil/water mixture as a lubricant and cooling medium, the tubes were cut into 15 mm high rings. The tubes associated with Sanicro 25 and HR3C alloys possessed a larger diameter requiring some modification of the cutting set up. Indeed, a security captor is present to make sure the cutting disc does not hit the bottom of the working area but the Sanicro 25 and HR3C tubes, the security captor is triggered before the tube is entirely cut. To cut these tubes completely, the security captor was disconnected. The presence of a competent technician is absolutely necessary before disconnecting the captor as it requires extreme vigilance to stop the saw when the tube is cut and before the cutting disc hits the bottom of the cutting area. Once the 15 mm high rings were obtained, these were marked every 15 mm on their outer part. Then radial lines were drawn through those marks to indicate the position where the precision saw ATM Brillant 220 must cut through.

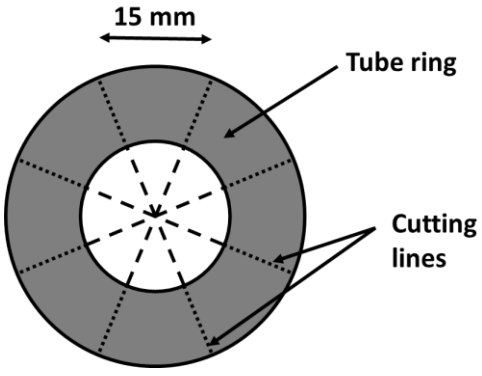

Figure 7-1: Schematic of the cutting positions when creating samples from tubes.

The precision saw was programmed to 0.024 mm/s blade advancing speed and 2000 rpm blade rotation speed. After having cut the samples from tubes they were folded in paper and put into a zip bag to avoid scratches.

B.2 Cutting procedure to produce cotton reel samples

Using the precision saw ATM Brillant 220, the different cylinders were separated as shown on Figure 7-2. After having prepared the cotton reel samples, they were folded in paper and then put into a zip bag to avoid scratches.

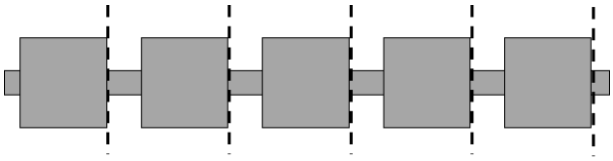

Figure 7-2: Cotton reels geometry and cutting axes.

B.3 Grinding procedure for tube segment samples

The surfaces of the tube segment samples were ground by hand using the polishing machine ATM Saphir 550 with an oil lubricant at 180 rpm. All the surfaces but the concave surface of the samples were ground using consecutively P120, P240, P600, and P1200 SiC papers with an extra step with the P2500 SiC paper for the samples with the P2500 ground surface finish. The SiC papers needed to be changed after every two sample surfaces ground, so the grinding was not altered by the extensive use of a SiC paper. The surfaces were held manually as flat as possible at the surface of the SiC paper. When grinding the convex surface, the sample needed to be tilted along the curve of the sample so that the entire curved surface was ground as homogeneously as possible.

B.4 Grinding procedure for cotton reels

To grind cotton reel samples, a drill was used to hold the samples by the small part of the cylinder (labelled c in Figure 3-1 (a)). SiC papers lubricated with oil were held against the cylindrical surface so that it was ground when the drill was switch on. The cotton reel samples were ground using consecutively P120, P240, P600, and P1200 SiC papers with an extra step with the P2500 SiC paper for the samples with the P2500 ground surface finish. The extremities of the cylinders were manually ground using the polishing machine as described in Section B.3.

B.5 Polishing procedure for cross-sections

The mounted samples presented in Section 3.4 were cut using the precision saw ATM Brillant 220 and were polished to a 1 µm surface finish. For the mounted samples to be analysed using FIB-SIMS (Section 4.5), an extra polishing step was performed using colloidal silica. Nine different mounted samples can be mechanically polished simultaneously using the ATM Saphir 550 polishing machine. The different mounted samples were ground 4 times with each of the SiC papers in the following order: P120, P240, P600, P1200, P2500. SiC papers were removed after each grinding cycle. After being ground, the samples were then polished a single time using consecutively a 6 µm and a 1 µm diamond suspension. For the mounted samples required to the polished with colloidal silica, a single polishing cycle was also performed. The different polishing parameters to be set for the different grinding and polishing media are described in Table 7-2.

Table 7-2: Polishing parameters used for the different polishing media.

Grinding/polishing medium	Parameters for the polishing machine
SiC grinding paper P120 SiC grinding paper P240	• 35 N • Central pressure • Counter rotation • 170 rpm • 3 min 30 sec
SiC grinding paper P600 SiC grinding paper P1200 SiC grinding paper P2500	• 35 N • Central pressure • Complementary rotation • 170 rpm • 3 min 30 sec
Diamond suspension 1 µm	• 30 N • Central pressure • Complementary rotation • 120 rpm • 1 min 30 sec
Diamond suspension 6 µm	• 20 N • Central pressure • Complementary rotation • 80 rpm • 45 sec
Colloidal silica 0.05 µm	• 20 N • Individual pressure • Complementary rotation • 100 rpm • 5 min

B.6 Holding the samples into SEM and XRD

To perform XRD and SEM analyses on the different surfaces of the exposed samples without damaging the oxide layers formed on their concave and convex surfaces, a metallic clamp was used to hold the samples as schematized in Figure 7-3. The metallic clamp holding the sample to be analysed was then fixed at the base of the SEM and XRD devices using conductive carbon tape.

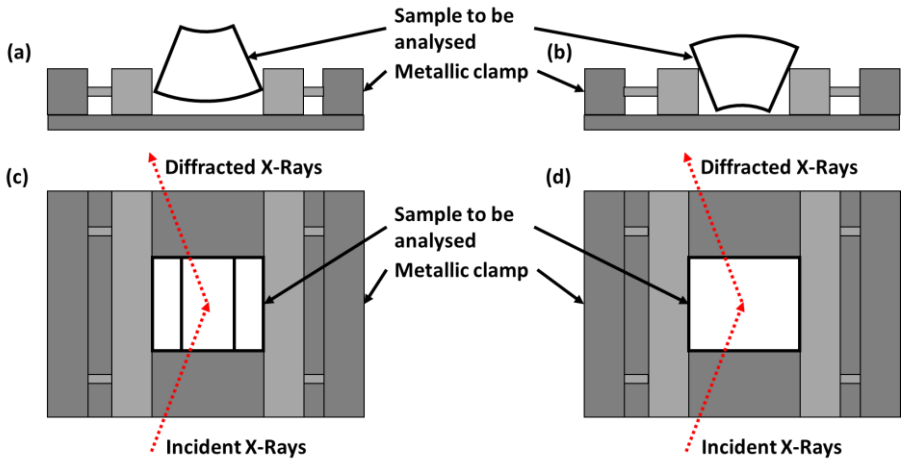

Figure 7-3: Schematics of the metallic clamp used to hold the samples during XRD and SEM analyses of (a) concave surfaces and (b) convex surfaces. Top views show the direction of the samples during XRD analyses for (c) concave and (d) convex surfaces.

Appendix C Publications, conferences and presentations

List of papers published and submitted:

- 22 November 2017, article published at Materials at High Temperatures, “Impacts of temperature and surface finish upon steam oxidation of austenitic steel TP347HFG”, J. BOUVET, J. SUMNER, N.J. SIMMS
- 22 February 2018, paper submitted to publication in NACE journal, “Study of the effect surface finish and pressure upon the steam oxidation of austenitic steels TP347HFG and Sanicro 25”, J. BOUVET, J. SUMNER, A.T. FRY, N.J. SIMMS

List of conferences attended:

- 03, 04 April 2017, Loughborough University, Microscopy of Oxidation 10, poster presentation
- 12 September 2017, Grantham, High Temperature Materials Degradation Workshop, poster presentation
- 09, 10 May 2018, Krakow Poland, NACE conference, oral presentation

Other presentations given:

- 13 January 2016, Cranfield University, 3 month review, report + oral presentation
- 26, 27 January 2016, Cranfield University, Flex-E-Plant meeting, oral presentation
- 12 April 2016, Cranfield University, School of energy research program, oral presentation

- 07 June 2016, Cranfield University, 9 month review, report + oral presentation
- 06, 07 July 2016, University of Nottingham, Flex-E-Plant meeting, oral presentation
- 16, 17 February 2017, Loughborough University, Flex-E-Plant meeting, oral presentation
- 21 April 2017, Doosan Babcock, industrial partnership meeting, oral presentation
- 03, 04 July 2017, Imperial College London, Flex-E-Plant meeting, oral presentation
- 02 August 2017, Cranfield University, 21 month review, report + oral presentation
- 11 September 2017, Cranfield University, Corrosion networking meeting, oral presentation
- 19 February 2018, Cranfield University, pre-submission review, report + oral presentation
- 22 February 2018, Loughborough University, Flex-E-Plant meeting, oral presentation